AD-A277 203

PROCEEDINGS OF THE 1993 ANTENNA APPLICATIONS SYMPOSIUM

DTIC
S ELECTE
MAR 2 2 1994
F D

Paul Mayes, et al

APPROVED FOR PUBLIC RELEASE; DISTRIBUTION UNLIMITED.

94-08982

DTIC QUALITY INC

Rome Laboratory
Air Force Materiel Command
Griffiss Air Force Base, New York

94 3 21 074

This report has been reviewed by the Rome Laboratory Public Affairs Office (PA) and is releasable to the National Technical Information Service (NTIS). At NTIS it will be releasable to the general public, including foreign nations.

RL-TR-94-20, Vol II (of two) has been reviewed and is approved for publication.

APPROVED:

DANIEL J. JACAVANCO
Chief, Antennas and Components Division
Electromagnetics and Reliability Directorate

FOR THE COMMANDER:

JOHN K. SCHINDLER
Director of Electromagnetics & Reliability

If your address has changed or if you wish to be removed from the Rome Laboratory mailing list, or if the addressee is no longer employed by your organization, please notify RL (ERAS) Hanscom AFB MA 01731. This will assist us in maintaining a current mailing list.

Do not return copies of this report unless contractual obligations or notices on a specific document require that it be returned.

PHASED ARRAYS

THURSDAY, SEPTEMBER 23, 1993

ARRAYS AND REFLECTORS

REPORT DOCUMENTATION PAGE

1. AGENCY USE ONLY (Leave blank)	2. REPORT DATE February 1994	3. REPORT TYPE AND DATES COVERED In-House Report

4. TITLE AND SUBTITLE

PROCEEDINGS OF THE 1993 ANTENNA APPLICATIONS SYMPOSIUM

5. FUNDING NUMBERS

PE: 62702F
PR: 4600
TA: 460014
WU: 460014PT

6. AUTHOR(S)

Paul Mayes, et al

7. PERFORMING ORGANIZATION NAME(S) AND ADDRESS(ES)

Rome Laboratory/ERAS
31 Grenier Street
Hanscom AFB, MA 01731-3010

8. PERFORMING ORGANIZATION REPORT NUMBER

RL-TR-94-20
Volume II

9. SPONSORING/MONITORING AGENCY NAME(S) AND ADDRESS(ES)

10. SPONSORING/MONITORING AGENCY REPORT NUMBER

11. SUPPLEMENTARY NOTES

Volume I consists of pages 1 through 276
Volume II consists of pages 277 through 524

12a. DISTRIBUTION/AVAILABILITY STATEMENT

Approved for Public Release; Distribution Unlimited

12b. DISTRIBUTION CODE

13. ABSTRACT (Maximum 200 words)

The Proceedings of the 1993 Antenna Applications Symposium is a collection of state-of-the-art papers relating to phased array antennas, multibeam antennas, satellite antennas, microstrip antennas, reflector antennas, HF, VHF, UHF and various other antennas.

14. SUBJECT TERMS

Antennas	Microstrip	Multibeam Antennas
Satellite Antennas	Reflector	Array Antennas
Broadband Antennas	HF, VHF, UHF	

15. NUMBER OF PAGES

254

16. PRICE CODE

17. SECURITY CLASSIFICATION OF REPORT	18. SECURITY CLASSIFICATION OF THIS PAGE	19. SECURITY CLASSIFICATION OF ABSTRACT	20. LIMITATION OF ABSTRACT
UNCLASSIFIED	UNCLASSIFIED	UNCLASSIFIED	SAR

CONTENTS

WEDNESDAY, SEPTEMBER 22, 1993

DUAL-USE TECHNOLOGY

* NOT INCLUDED IN THIS VOLUME

iii

PHASED ARRAYS

THURSDAY, SEPTEMBER 23, 1993

ARRAYS AND REFLECTORS

ELEMENTS

FRIDAY, SEPTEMBER 24, 1993

ANALYSIS AND MEASUREMENT

DETERMINING NOISE TEMPERATURES IN
BEAMWAVEGUIDE SYSTEMS

W. Imbriale, W. Veruttipong, T. Otoshi, and M. Franco

Jet Propulsion Laboratory

California Institute of Technology

Pasadena, CA 91109

ABSTRACT

A new 34-meter research and development antenna was fabricated and tested as a precursor to introducing beamwaveguide antennas and Ka-band frequencies into the NASA/JPL Deep Space Network. For deep space use, system noise temperature is a critical parameter. There are thought to be two major contributors to noise temperature in a BWG system: the spillover past the mirrors and the conductivity loss in the walls. However, to date, there are no generally accepted methods for computing noise temperatures in a beamwaveguide system. An extensive measurement program was undertaken to determine noise temperatures in such a system along with a correspondent effort in analytic prediction. Utilizing a very sensitive radiometer, noise temperature measurements were made at the cassegrain focus, an intermediate focal point, and the focal point in the basement pedestal room. Several different horn diameters were used to simulate different amounts of spillover past the mirrors. Two analytic procedures were developed for computing noise temperature, one

utilizing circular waveguide modes and the other a semi-empirical approach. The results of both prediction methods are compared to the experimental data.

1. INTRODUCTION

Noise temperature due to a beamwaveguide (BWG) system is one of the major contributors to antenna receive system noise, especially for an ultra-low noise system or a system with high spillover power in the BWG shroud. A reasonably accurate prediction of the BWG noise temperature is essential. Direct analytical computation of the noise temperature of elaborate BWG systems, including all mirrors, is an extremely complex problem and, to date, there is no generally accepted method. This report presents two new techniques—one a purely analytical method and the second a semi-empirical approach.

The analytical method extends the approach of [1], which computes the waveguide modes that are propagating in the oversized waveguides. Reference [1] describes a PO integration procedure of the currents on the BWG mirrors using a Green's function appropriate to the circular waveguide geometry. Once all the modes in the waveguide are known, it is a simple matter to use standard approximations to determine the attenuation constant and thus the conductivity loss if the conductivity of the wall material is known. Also, all energy that propagates toward but spills past a BWG mirror is assumed to be lost in the walls of the BWG as well. The noise temperature is computed assuming both loss components see ambient temperature.

The second method uses a technique that combines an analytical approach with data from measurements to construct a specific expression to compute the BWG noise temperature.

To validate both approaches, a series of measurements were made on DSS-13, the recently completed research and development 34-meter BWG antenna (see Figs. 1 and 2). The experiments consisted of making very accurate noise temperature measurements for different gain horns located at both the cassegrain focus (f1) and the BWG focus of the upper portion of the BWG system (f2) (designed to image the horn at the cassegrain optics focal point). This portion of the BWG optics is enclosed in 2.44-meter (8-foot) diameter tube. By taking measurements at both focal points, the noise temperature of the BWG portion of the optics can be accurately determined. The results of both computation methods are compared to the measured data.

2. WAVEGUIDE MODE THEORY

The BWG tube analysis is conceptually similar to the physical optics (PO) analysis used in reflector antenna analysis.

The currents induced in the BWG mirror are obtained using a standard physical optics approximation of $J = 2\hat{n} \times H_{inc}$ where $\hat{n}$ is the surface normal and H_{inc} is the incident field. The difference from a standard PO analysis is 1) the method by which the incident field on a mirror is calculated, and 2) the method by which the scattered field is calculated.

One approach to calculating the scattered fields is to use a dyadic Green's formulation[1] where the field scattered from a BWG mirror are computed using the Green's function appropriate to the cylindrical waveguide geometry.

While it is conceptually convenient to use Green's functions to discuss the comparison with PO, the actual computation using this approach is rather cumbersome. Rather, a simpler method, based upon the reciprocity theorem, is used to calculate the waveguide fields. The basic problem is to find the fields radiated by an arbitrary current (the PO currents on the reflector) in a cylindrical waveguide. The problem is easily solved by expanding the radiated field in terms of a suitable set of normal modes with amplitude coefficients determined by an application of the Lorentz Reciprocity theorem.

An arbitrary field in a waveguide can be represented as an infinite sum of the normal modes for the guide. Let the normal modes be represented by

$$\overline{E}_n^{(\pm)} = (\overline{e}_n \pm \overline{e}_{zn})e^{\mp \Gamma_n}$$

$$\overline{H}_n^{(\pm)} = (\pm \overline{h}_n + \overline{h}_{zn})e^{\mp \Gamma_n}$$

(1)

where $\overline{E}_n^{(+)}$ represents a mode traveling in the $+z$ direction and $\overline{E}_n^{(-)}$ is a mode traveling in the $-z$ direction. For the basic normal mode description, see for example Harrington[2].

Let the field radiated in the positive z direction by the current be represented by

$$\overline{E}^{(+)} = \sum_n a_n \overline{E}_n^{(+)}$$

(2)

$$\overline{H}^{(+)} = \sum_n \frac{a_n}{Z_n} \overline{H}_n^{(+)}$$

and the field radiated in the negative z direction by

$$\overline{E}^{(-)} = \sum_n b_n \overline{E}_n^{(-)}$$

(3)

$$\overline{H}^{(-)} = \sum_n \frac{b_n}{Z_n} \overline{H}_n^{(-)}$$

Recalling the Lorentz Reciprocity theorem, if $\overline{E}_1$, $\overline{H}_1$, and $\overline{E}_2$, $\overline{H}_2$ are the fields due to $\overline{J}_1$, $\overline{J}_2$, respectively, then

$$\int_s \hat{n} \bullet \left[\overline{E}_1 \times \overline{H}_2 - \overline{E}_2 \times \overline{H}_1 \right] ds = \int_v \left[\overline{E}_2 \bullet \overline{J}_1 - \overline{E}_1 \bullet \overline{J}_2 \right] dV$$

(4)

If we let E_1, H_1 be the fields due to the sources J and $E_n^\pm$, $H_n^\pm$ be the modal (source-free) solutions, substituting in the Lorentz Reciprocity theorem gives

$$-\int_s \left[\overline{E}_n^{(\pm)} \times \overline{H}_1 - \overline{E}_1 \times \frac{\overline{H}_n^\pm}{z_n} \right] \bullet \hat{n} ds = \int_v \overline{E}_n^{(\pm)} \bullet J dV$$

(5)

We choose as our volume that bounded by the perfectly conducting guide walls and the two cross-sectional planes S_1 and S_2 (see Fig. 3). Then

281

$$\int_s = \int_{s_1} (-\hat{z}) \bullet \left[\overline{E}^{(-)} \times \frac{\overline{H}_n^{(\pm)}}{Z_n} - \overline{E}_n^{(\pm)} \times H^{(-)} \right] ds$$

$$+ \int_{s_2} (\hat{z}) \bullet \left[\overline{E}^{(+)} \times \frac{\overline{H}_n^{(\pm)}}{Z_n} - \overline{E}_n^{(\pm)} \times \overline{H}^{(+)} \right] ds \tag{6}$$

Note that the integral along the wall doesn't contribute because on S_3

$\hat{n} \bullet \overline{E}_1 \times \overline{H}_2 = \overline{H}_2 \bullet \hat{n} \times \overline{E}_1 = \overline{H}_2 \bullet$ Tangential $\overline{E} = 0$ for both $E^{(\pm)}$ or $E_n^{(\pm)}$.

Also only transverse fields enter into computations because $\hat{z} \bullet \overline{E} \times \overline{H}$

selects transverse components.

For the normal mode function E_n^+, H_n^+ it is readily found that

$$\int_s = -\frac{2b_n}{Z_n} \tag{7}$$

when the expansion for E^+ and E^- are used in conjunction with the orthogonal property and

$$\int_s \left(\overline{e}_n \times \overline{h}_m \right) \bullet \hat{z}\,ds = \begin{cases} 0 & \text{if } n \neq m \\ 1 & \text{if } m = n \end{cases} \tag{8}$$

Also, if we use the normal mode function $\overline{E}_n^{(-)}$, $\overline{H}_n^{(-)}$ we find that

$$\int_s = -2\frac{a_n}{Z_n} \tag{9}$$

We have therefore shown that

$$a_n = -\frac{1}{2} Z_n \int_v \left[\overline{E}_n^{(-)} \bullet \overline{J} \right] dV$$

$$b_n = -\frac{1}{2} Z_n \int_v \left[\overline{E}_n^{(+)} \bullet \overline{J} \right] dV$$

(10)

Since we have only surface currents, the integral for the PO currents is over the surface of the reflector. If we let

$$c_n = -\frac{1}{2} \int_s J_s \bullet \overline{E}_n^{(-)} ds$$

(11)

where J_s is the physical optics currents on the mirror, then

$$\overline{H}^+ = \sum_n c_n \overline{H}_n^{(-)}$$

$$\overline{E}^{(+)} = \sum_n Z_n c_n \overline{E}_n^{(-)}$$

(12)

and the total power contained in the fields is

$$P = \sum_n z_n |c_n|^2$$

(13)

The physical optics currents induced on the first mirror are computed either in the standard way if the spillover past the mirror is small (i.e., >25 dB edge taper) by utilizing the free-space near-field radiating H field of the horn and $J_s = 2\hat{n} \times H_{inc}$ or by utilizing a technique similar to the one just described to compute the propagating modes from the horn and radiating in the oversized

283

waveguide and also utilizing the appropriate H field derived from these modes as the incident field. Physical optics currents on subsequent mirrors are computed from the H field derived from the propagating waveguide modes. The technique is summarized in Fig. 4, where it should be noted that

$$H = \int_s J_1 \bullet \overline{\overline{G}}_{wg} ds = \sum_n c_n \overline{H}_n^{(-)} \qquad (14)$$

The power loss in the conductor is obtained utilizing the standard technique to compute the power dissipated in the conductor per unit length (see [2]) as

$$P_d(Z) = R \int_0^{2\pi} \left| \overline{H}_t \right|^2 a d\phi \qquad (15)$$

where

$$R = \sqrt{\frac{\omega\mu}{2\sigma}} \qquad (16)$$

and σ is the wall conductivity, a the radius, and $\left| \overline{H}_t \right|^2$ the tangential H field. It should be noted that P_d is a function of Z since $\left| \overline{H}_t \right|^2$ is a function of Z (i.e., it is composed of more than one waveguide mode).

The power loss is computed from

$$P = P_O e^{-2\alpha d} \qquad (17)$$

where d is the distance from Z_1 to Z_2 and the attenuation constant is computed as

284

$$\alpha d = \frac{\int_{Z_1}^{Z_2} P_d(Z)dZ}{2P_f} \qquad (18)$$

where P_f is the power flow in the waveguide.

To compute noise temperature it is convenient to separate the total RF power, originating from the horn aperture (viewed in transmission, for convenience) and propagating into two parts

$$P_{BWG} = P_m + P_{spill} \qquad (19)$$

where P_{spill} is the portion that spills past the mirrors (since the mirrors do not fill the waveguide). P_{spill} can be computed for each mirror by integrating the total power radiated from the induced mirror currents and comparing it to the incident power. Note that the computation uses the induced currents derived from the waveguide modes. It is then assumed that this spillover power sees ambient temperature since it would be lost in the tube due to multiple bounces in a lossy material.

The total noise temperature then is composed of two parts—the noise due to the spillover power added to the noise from the attenuation of P_m due to the conductivity loss.

3. SEMI-EMPIRICAL APPROACH

A noise temperature of elaborate BWG systems including BWG mirrors and shroud can also be computed by using a new technique that combines an analytical approach with data from measurement tests to construct a specific expression to compute the BWG noise temperature. This technique begins by separating the total RF power, originating from a horn aperture (viewed in transmission, for convenience) and propagating through a BWG shroud (P_{BWG}), into two parts (see Fig. 5)

$$P_{BWG} = P_m + P_{spill} \qquad (20)$$

where P_m is the majority of the total power that is always confined inside all BWG mirrors; it does not contact the BWG wall and there are no multiple reflection, diffraction, and creeping wave components. P_m can be computed easily and accurately because all BWG wall and mirror interactions are not included. It should be noted that in the analysis, the mirrors are assumed to radiate in free space. Thus the P_{spill} from this analysis is different from the P_{spill} of the waveguide mode theory. P_{spill} is the sum of spillover powers of each mirror. It creeps and bounces around the BWG walls, mirrors, brackets (behind the mirrors), and edges, etc., and suffers dissipation loss and consequent noise. On an average, the P_{spill} power largely dissipates before a small remainder exits the BWG opening near f1 (see Fig. 2). Even though P_{spill} can be computed accurately ($P_{spill} = P_{BWG} - P_m$), its field distribution and its chaotic behavior inside the lossy BWG is virtually impossible to compute analytically.

From Eq. (20), the corresponding noise temperatures are

$$T_{BWG} = T_m + T_{spill} \tag{21}$$

where T_{BWG} is the total noise temperature (in kelvins) due to the BWG system (including the shroud, mirror, brackets, etc.). The values T_m and T_{spill} are the noise temperature contributions from P_m and P_{spill}, respectively. Because of the simplicity of P_m, its corresponding noise temperature T_m can be computed with acceptable accuracy. For 6061T6 aluminum with conductivity of 2.3×10^7 mho/meter and 270-K physical temperature, the noise temperature T_m at X-band (8.45 GHz) is (see [3])

$$T_m = 0.734 \frac{P_m}{P_{BWG}} = 0.734 \alpha_m \tag{22}$$

where α_m is the P_m fraction of P_{BWG}, dimensionless.

The noise temperature due to spillover power P_{spill} is given in a very simple form as

$$T_{spill} = \left(\frac{P_1}{P_{BWG}} \right) T_1 + \left(\frac{P_2}{P_{BWG}} \right) T_2 = \alpha_1 T_1 + \alpha_2 T_2 \tag{23}$$

where P_1 is the total spillover power of the two mirrors (M5 and M6) in the basement and the value P_2 is the total spillover power of the four mirrors (M1, M2, M3, and M4) above the basement ceiling. The values α_1 and α_2 are the normalized powers (with respect to P_{BWG}) of P_1 and P_2, respectively.

By substituting Eqs. (22) and (23) into Eq. (21), the BWG noise temperature at X-band becomes

$$T_{BWG} = 0.734\alpha_m + \alpha_1 T_1 + \alpha_2 T_2 \tag{24}$$

By performing various measurements at the NASA DSN BWG research station at Goldstone, the coefficients T_1 and T_2 at X-band have been obtained[3].

$$\text{No basement shroud} \qquad \begin{aligned} T_1 &= 300 \pm 10 \text{ K} \\ T_2 &= 240 \pm 45 \text{ K} \end{aligned} \tag{25}$$

$$\text{Full shroud} \qquad \begin{aligned} T_1 &= 280 \pm 20 \text{ K} \\ T_2 &= 230 \pm 45 \text{ K} \end{aligned} \tag{26}$$

Figure 6 shows the comparison between predicted and measured BWG noise temperatures for various total spillover powers at X-band. The results indicate a very good agreement, especially in the operating range $(0.5\% \leq P_{spill} \leq 1.2\%)$.

4. MEASUREMENTS PROGRAM

Figure 1 shows a recent photograph of the 34-m-diameter BWG antenna built at the NASA/JPL Goldstone tracking facility near Barstow, California. This antenna is the first antenna built for NASA of the BWG type and is primarily an R&D antenna. One of the uses of this antenna has been to develop and verify theoretical models that can be used as tools for designing future improved BWG antennas.

Focal points f1, f2, and f3 are depicted in Fig. 2. Focal point f1 is the cassegrain focal point near the main reflector vertex. An intermediate focal f2 lies above the azimuth track, and focal point f3 is the final BWG focal point located in a subterranean pedestal room. Degradations caused by the BWG system mirrors and shrouds were determined from comparisons made of operating system noise temperatures measured at the different focal points.

As discussed earlier, the goal of the experimental technique was to determine the degradations caused by the noise temperature contributions from wall losses and mirror spillovers in the BWG system. The experimental technique that was conceived and implemented involved measurements of operating system noise temperature at f1, f2, and f3. Taking the difference of the noise temperatures measured at f1 and f2 gives the information on the total losses of the BWG system that include (1) dissipative losses due to finite conductivity of four mirrors, (2) spillover losses associated with four mirrors, and (3) shroud wall losses between f1 and f2. Similarly, information of the total losses of the remaining two mirrors, shroud walls, and unshrouded path between f2 and f3 are determined from differencing noise temperatures measured at f2 and f3.

To obtain information on the losses pertaining only to the cassegrain portion of the BWG antenna, the experimental procedure involved making an operating system noise temperature measurement first with the test package on the ground, and then making a measurement with the test package installed at f1. The difference between f1 and ground noise temperatures reveals the amount of degradation casued by spillover of power from the horn into the region between the subreflector and main reflector, scattering from the tripod legs, noise

contribution from illumination of the ground and sky region as seen from the subreflector focus, and leakage through gaps between panels and perforations in the main reflector surfaces, as well as noise temperature due to illuminating the area between the horn aperture and BWG shroud walls.

For the experimental technique to yield the information described above, it was required that the absolute noise temperature at the different test locations be accurate to about ±0.5 K and be repeatable to about ±0.2 K. The accuracy of values obtained for differential measurements is estimated to be ±0.3 K and is more accurate than absolute values due to common errors canceling each other out in the differencing process.

In order to achieve these goals, an ultra-stable radiometer was required and the test package required good mechanical stability after installation at the various focal points. It was shown in a previous report[4] that a number of measurements were made with the test packages installed at the different focal points, then going back to the ground, and then back to the different focal points. Such repeatability tests confirmed that the X-band test package and radiometric system met the accuracy requirements stated above for making absolute and differential noise temperature measurements.

Figures 7 and 8 show the X-band test package installed at f1 and f3. Horns of different gains at f1 and f2 were achieved easily by beginning with the 29-dBi horn and systematically removing horn sections to produce a lower gain horn. At both f1 and f3, test package adjustments were used to align the phase centers for the different gain horns to the desired geometric focal points.

Special radiometric calibration techniques were employed such as (1) correcting for changes in atmospheric noise contributions due to changes in air temperature and relative humidity, and (2) performing periodic real-time calibrations of radiometric system for measuring noise temperatures. Further details of the microwave performance of these test packages and radiometric techniques used to achieve the desired stability and precision have been reported elsewhere[5].

5.   RESULTS

The measurements described above were made at cassegrain focus f1, at the intermediate focus f2, and at the basement focus f3.

For contrasting the two theories, the most interesting measurements were those made at f2, since the shroud surrounds the mirrors. Since there is no shroud in the pedestal room, both methods give the same result for the basement mirrors.

A horn pattern input at f2 is imaged at f1 so measurements made with the same horn gain at f1 and f2 can be differenced to give the noise temperature due only to the BWG portion of the system. A plot of the measured data for the upper BWG (f2 to f1) is compared to both theories in Fig. 9 for horn gains from 25 to 29.8 dB. Obviously the lower gain horn spills more energy past the mirrors and has a higher noise temperature contribution. Interestingly, both methods do a fairly good job of predicting the noise temperatures. For reference, the BWG system was designed to operate with the 29.8-dB gain horn.

6. ACKNOWLEDGMENTS

7. REFERENCES

1. Cha, A.G. and Imbriale, W.A. (1992) A new analysis of beamwaveguide antennas considering the presence of the metal enclosure, IEEE Transactions on Antennas and Propagation, Vol. 40, No. 9, pp. 1041–1046.

2. Harrington, R.F. (1961) Time-Harmonic Electromagnetic Fields, McGraw Hill, Chapter 8.

3. Veruttipong, W. and Franco, M. (1993) A technique for computation of noise temperature due to a beamwaveguide shroud, 1993 IEEE AP-S International Symposium, The University of Michigan, Ann Arbor, Michigan.

4. Bathker, D.A., Veruttipong, W., Otoshi, T.Y., and Cramer, Jr., P.W. (1992) Beamwaveguide antenna performance predictions with comparisons to experimental results, Microwave Theory and Techniques, Special Issue (Microwaves in Space), Vol. MTT-40, No. 6, pp. 1274–1285.

5. Otoshi, T.Y., Stewart, S.R., and Franco, M.M. (1992) Portable microwave test packages for beamwaveguide antenna performance evaluations, Microwave Theory and Techniques, Special Issue (Microwaves in Space), Vol. MTT-40, No. 6, pp. 1286–1293.
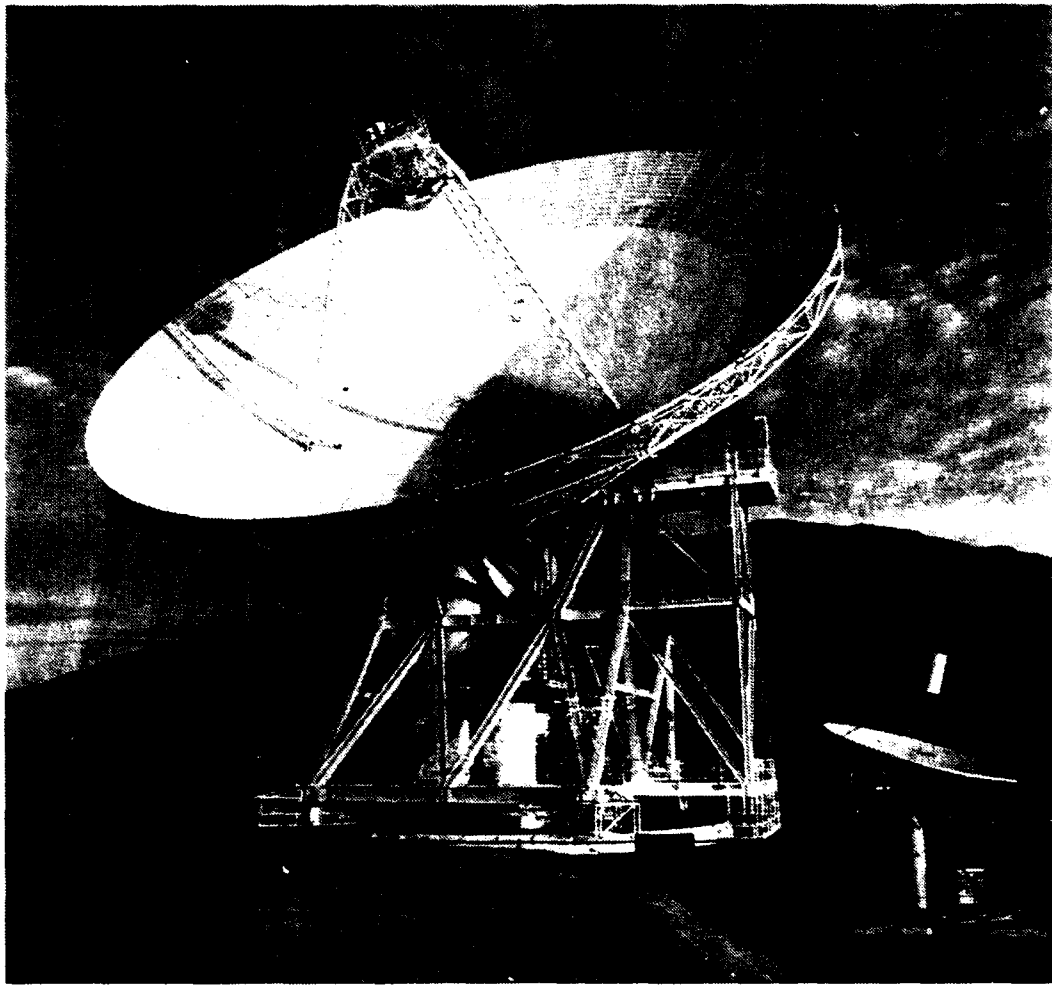
Figure 1. DSS-13 34-meter BWG antenna.

SHAPED-SURFACE
SUBREFLECTOR

34-m SHAPED-
SURFACE
REFLECTOR

TRIPOD

f1

CENTERLINE
BEAM
WAVEGUIDE

f2

AZIMUTH
TRACK

MICROWAVE
TEST
PACKAGE

SUBTERRANEAN
PEDESTAL
ROOM

REAR VIEW

f3
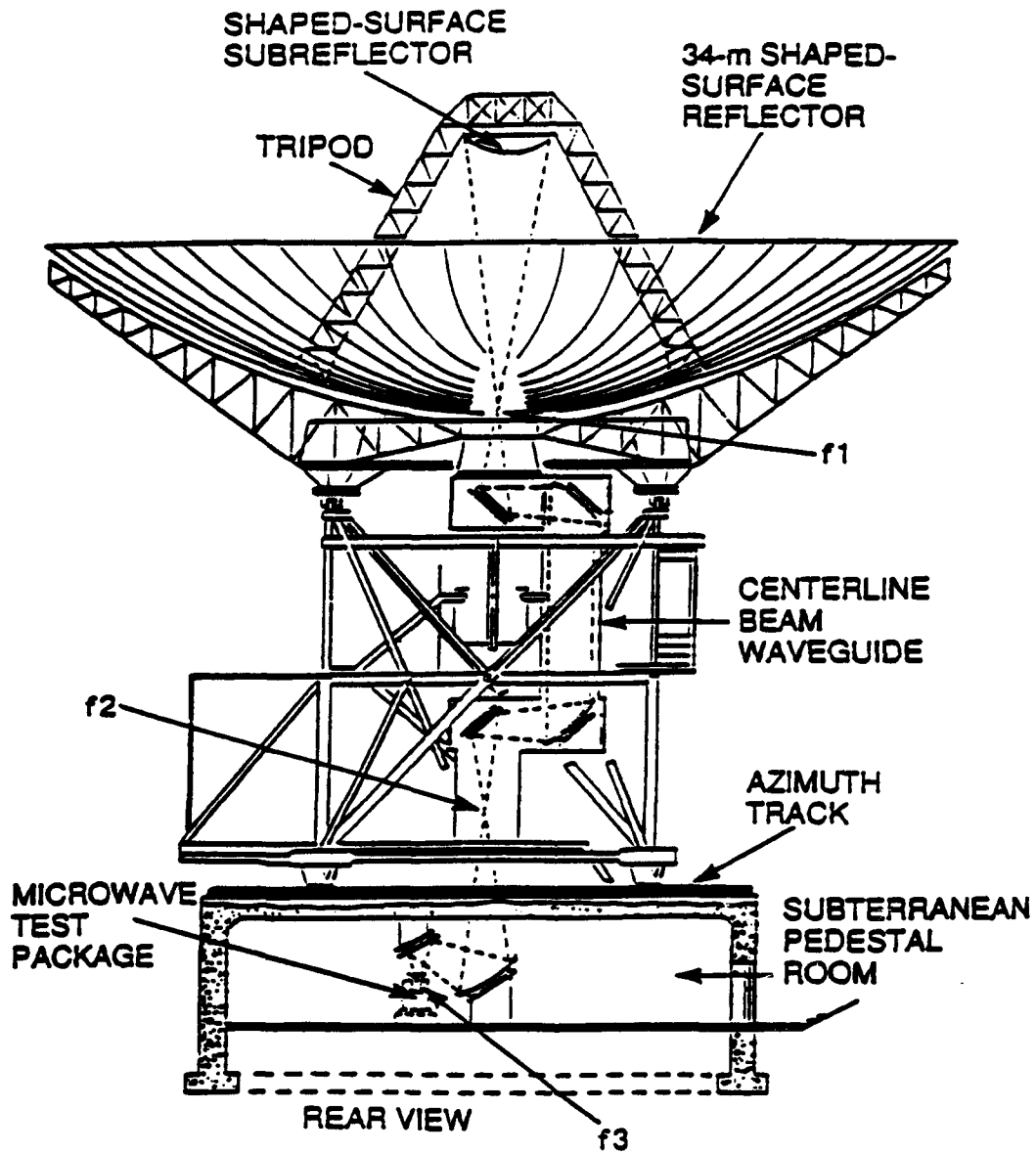
Figure 2. 34-m BWG antenna focal points.
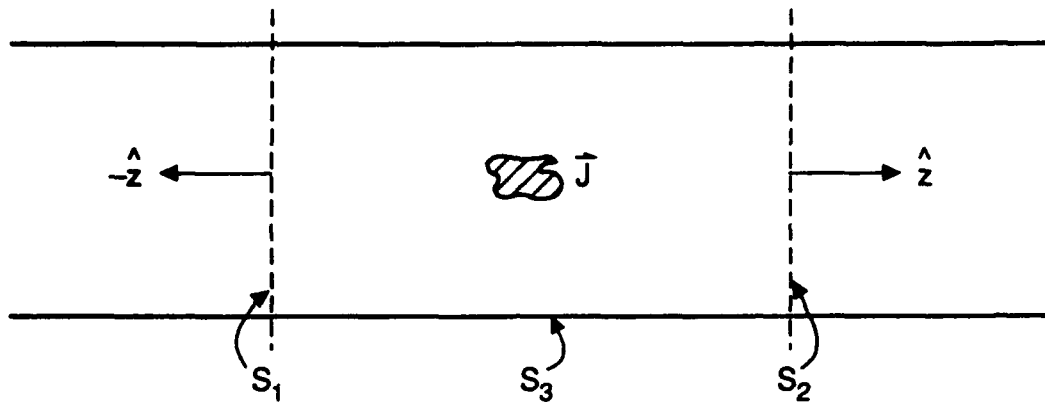
Figure 3. Geometry for computing waveguide modes.
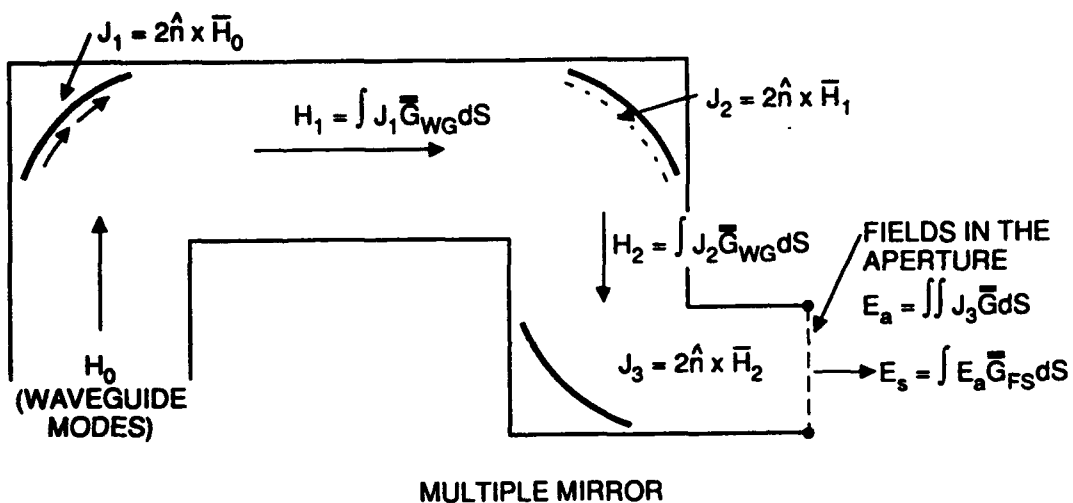
Figure 4. Computation of fields in the BWG system.
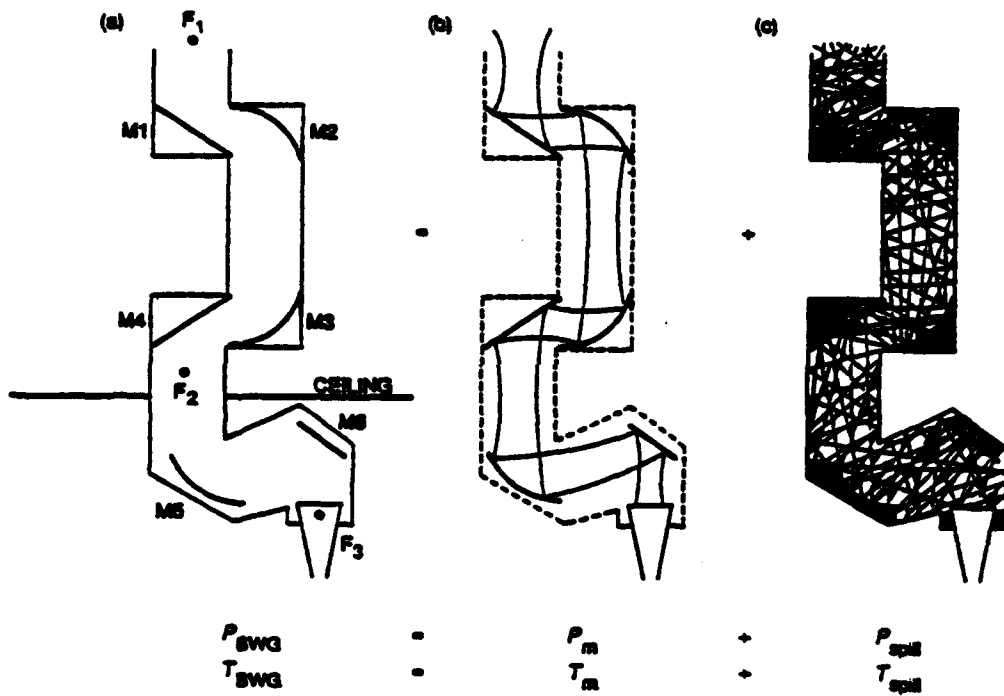
Figure 5. Characteristics of the fields inside a BWG shroud and their corresponding noise temperatures.
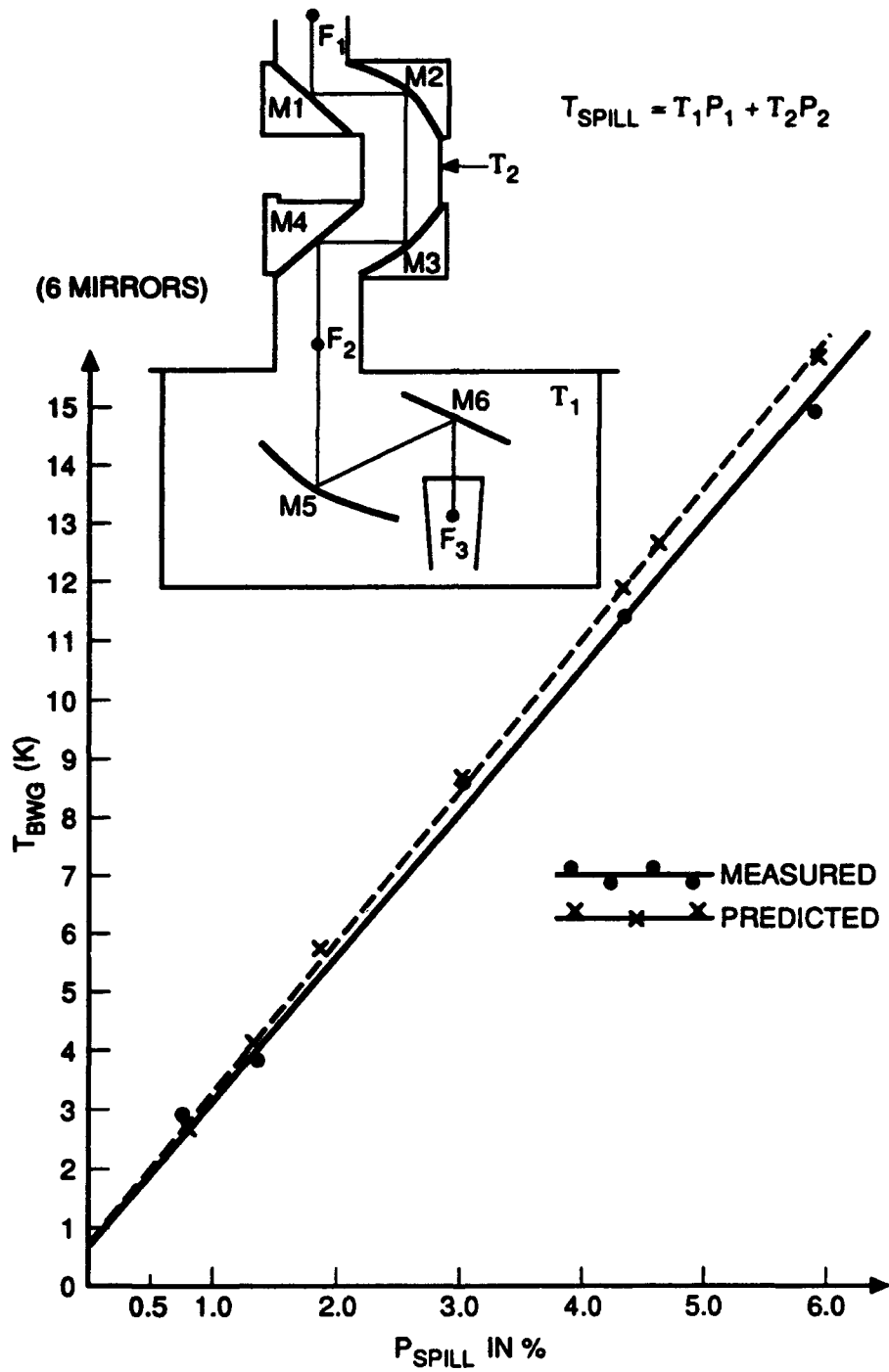
Figure 6. The comparison between predicted and measured BWG noise temperatures at X-band.
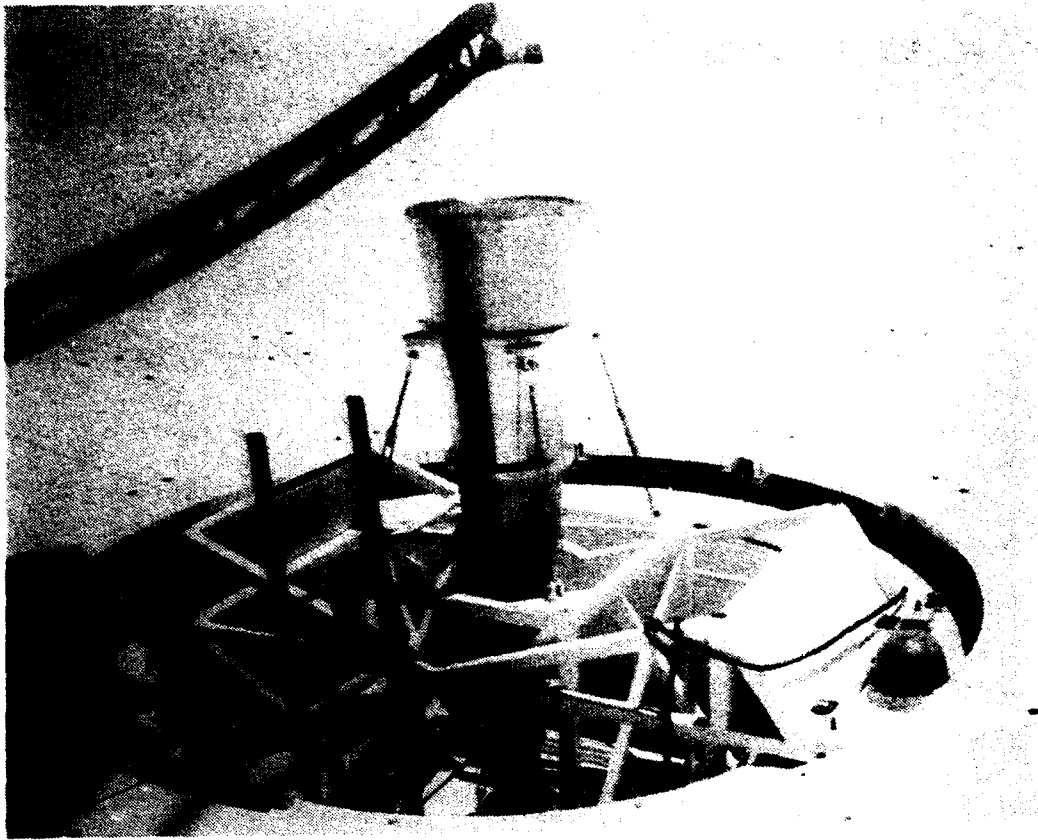
Figure 7. Partial view of the X-band 29-dBi horn test package and mounting
structure installed at the cassegrain focal point f1.

Figure 8. X-band 22-dBi horn test package and mounting table installed in the pedestal room focal point f3.
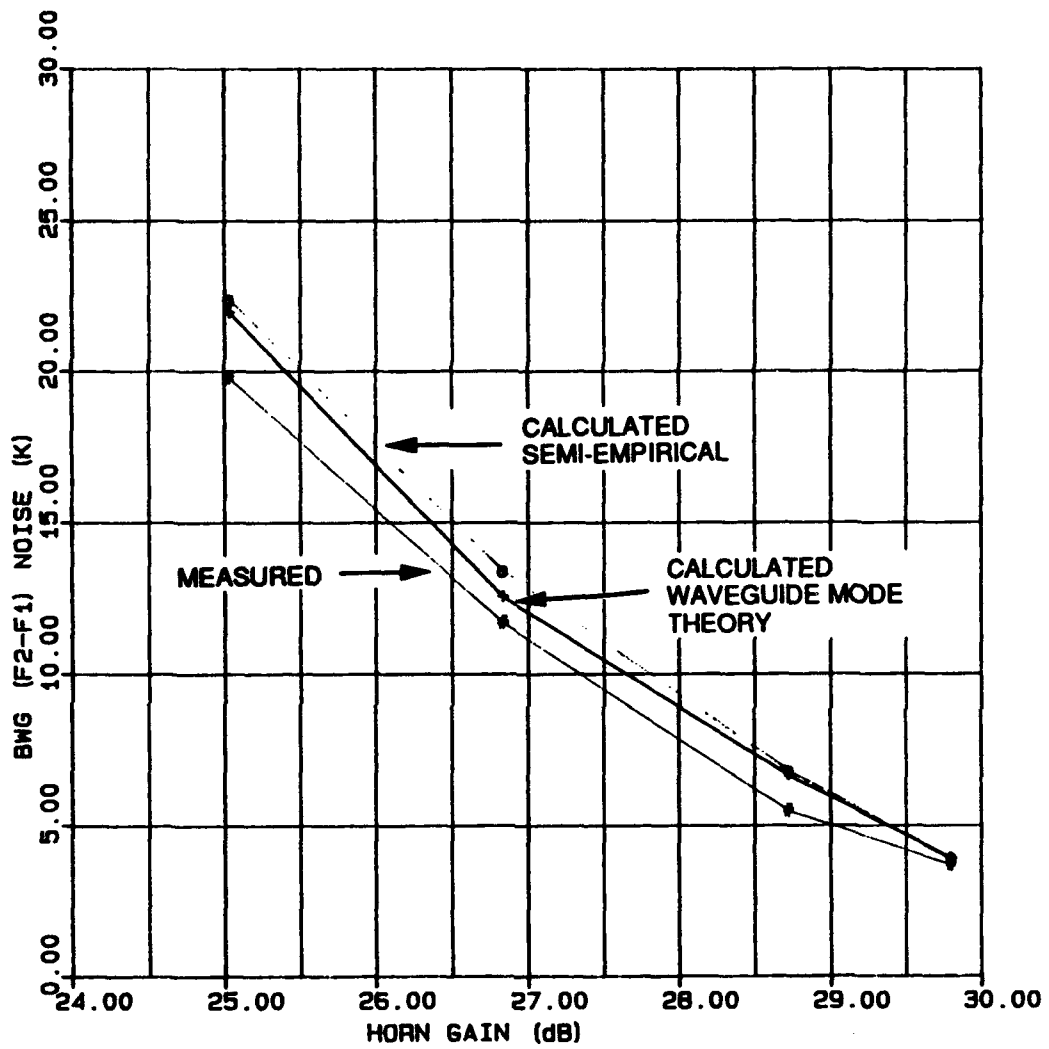
Figure 9. Comparison of computed and measured noise temperatures with different feedhorn gains at f2.

FEED AND SUBREFLECTOR DISPLACEMENT ANALYSIS

OF SHAPED ELLIPTICAL DUAL-REFLECTOR ANTENNAS

M. Im*, Y. Chang, M. Sarcione, F. Beltran

Raytheon Company
Equipment Division
Wayland, MA 01778

ABSTRACT

The effects of feed and subreflector displacements on antenna performance were studied on elliptical-aperture shaped dual-reflectors at millimeter-wave frequencies. The elliptical aperture is required so that the protrusion and intrusion of the antenna system with respect to its platform can be minimized. The motivation of this study is to obtain insight into the effects of dimensional tolerances for this antenna configuration. This insight is needed to optimize the antenna performance and cost, which are very sensitive to tolerances at such high frequencies.

Since conventional designs would produce either a low spillover efficiency or a low illumination efficiency, shaping techniques have been applied to this elliptical antenna. The synthesis approach chosen to produce the dual-reflector surfaces was the one published by Professor Kildal [1]. The main advantage of this approach is that it avoids the solution of nonlinear differential equations. Instead, kinematic and dynamic ray tracing is used to reduce the synthesis procedure to the solution of two sets of linear equations.

In addition to the aperture distributions described by analytical functions, our synthesis program has been expanded to include a general aperture distribution using a linearly piecewise input. An immediate application of this expansion is to synthesize an aperture field with a hole in the middle to reduce the energy loss due to subreflector blockage.

The displacement analysis is performed by tracing the rays with the displaced feed/subreflector to obtain the distorted aperture field, followed by aperture integration for gain and pattern calculation. Results of these analyses for various displacement amounts on several antenna configurations will be shown and compared in this paper.

1. INTRODUCTION

Low cost has become a major design driver for military satellite communication systems. One way of reducing the antenna production cost is to allow for loosest dimensional tolerances consistent with a given required performance. To achieve that, an effective analytical tool for tolerance analysis is required to conduct performance vs. cost tradeoffs. This is especially important at higher frequencies such as millimeter-waves since both performance and cost are very sensitive to relatively tight tolerance requirements. Previous studies on such analysis [2-6] were limited to the cases with conventional parabolic reflectors.

In this paper, the effects of feed and subreflector displacements on antenna performance were studied on an offset elliptical-aperture shaped dual-reflector at 44.5 GHz. The elliptical aperture is required so that the protrusion and intrusion of the antenna system with respect to its platform can be optimized, which is very critical for installation on aircraft. For comparison purposes, results from antennas

302

with other configurations such as shaped center-fed Gregorian are also included.

2. SYNTHESIS OF DUAL-REFLECTORS

The shaping of dual-reflectors to achieve high antenna efficiency has been known for several decades [7]. Recently, various synthesis approaches for shaped dual-reflectors have been reported [1,8,9]. However, earlier methods [8,9] addressed only circular projected apertures. For an elliptical aperture, these methods produce either a low spillover efficiency or a low illumination efficiency unless a feed with an elliptical beam is used. The synthesis approach we chose to generate the shaped dual-reflector surfaces was the one published by P. Kildal [1]. The main advantage of this approach is that it does not require the solution of nonlinear differential equations. Instead, kinematic and dynamic ray tracing is used to simplify the synthesis procedure to the solution of two sets of linear equations. It is also consistent with the use of an arbitrary aperture field distribution.

A synthesis computer program has been developed using Kildal's approach [1], and reflector surfaces for several different shaped dual-reflectors have been generated. Four of these antenna configurations have been selected as examples for this tolerance analysis. All these examples are chosen so that the path lengths between their feed phase centers, the subreflector centers, and the main reflector centers are all the same. All four examples use the same symmetric feed pattern $G(\Theta)$ and the same symmetric aperture field distribution $E(\rho)$ described by [1]

$$G(\Theta) = \cos^n(\Theta/2) \qquad \text{Eq. 1}$$

where Θ is the angle from the feed boresight, and power n is chosen as 57.27 to obtain a -15 Db subreflector edge taper at $\Theta=28$ degrees, and

303

$$E(\rho) = \sqrt{1 - (1 - E_m^2)(\rho/\rho_m)^2}$$

Eq. 2

where E_m is chosen as 0.707 to obtain a -3 dB aperture field taper, ρ is normalized radius and ρ_m is the maximum ρ [1].

Figure 1 shows the synthesized surfaces of a 30"x15" offset shaped Gregorian dual-reflector (Case 1). For comparison purpose, three other configurations have been synthesized and analyzed. One is a 30"x15" center-fed shaped Gregorian (Case 2) as shown in Figure 2 and another is a 24" diameter offset shaped Gregorian (Case 3) as shown in Figure 3. These examples are included to investigate the different displacement effects present in the center-fed vs. offset and circular vs. elliptical configurations. Note that the x and z coordinates of the feed phase center are specified by xf and zf, respectively, in the side view figure. Similarly, the x and z coordinates of the subreflector and main reflector centers are specified by zso, xso, zmo, and xmo, respectively. All the y coordinates are zero in this side view plane. All the linear dimensions are specified in inches.

In addition to the aperture distributions described by analytical functions, our synthesis program has been expanded to include a general aperture distribution using a linearly piecewise input. An immediate application of this expansion is to synthesize an aperture field with a hole in the middle to reduce the energy loss due to subreflector blockage. Figure 4 shows the synthesized surfaces of a 24" diameter center-fed shaped Gregorian reflector (Case 4). The resultant aperture field distribution calculated by the analysis program is shown in Figure 5.

3. ANALYSIS

An analysis computer code was developed to predict the performance of the synthesized dual-reflectors. In this analysis code, geometric optics is used to ray-trace the field from the feed to the main reflector aperture. Once this aperture field is known, individual components of aperture efficiency such as illumination, spillover, phase, and cross-polarization efficiencies can be calculated. Then the aperture integration method is used to determine the gain and far-field patterns of the antenna. This ray tracing and aperture integration approach is also used for the tolerance analysis, except that the ray tracing is done with a displaced feed or subreflector. The following sections describe the details of this approach.

3.1 ANALYSIS WITH NO DISPLACEMENT

The analysis for cases with no displacement is relatively straightforward. Basically, a ray is launched from the feed phase center to every node on the subreflector surface generated by the synthesis program. Every node on the subreflector is defined by its x,y,z position, the principal directions of curvature, the normal to the surface and the curvature values. Knowing the input feed pattern $G(\Theta)$ and the angle Θ between the rays from the feed to the node and the feed boresight axis, the incident field at each node on the subreflector can be calculated. Then the ray is traced from the subreflector node to the corresponding point on the main reflector, which, for the cases of no displacement, is the corresponding main reflector node computed from the synthesis program.

We chose to carry out the aperture integration using a rectangular grid instead of the polar grid generated by the synthesis program for two reasons. The first one is due to fabrication consideration. To machine the reflector surfaces, it

is preferable to work with surface coordinates on a rectangular grid to ensure surface accuracy and easier programming. Secondly, for the far-field gain and pattern calculation, the rotated grid approach [10] can be employed to simplify the integration from two dimensions to one dimension, hence speeding up the calculation significantly. As a result, the aperture fields on a rectangular grid must be linearly interpolated from those on the polar grid.

3.2 ANALYSIS WITH DISPLACEMENT

The approach for analyzing the antennas with displaced components is similar to the forward ray tracing approach mentioned in section 3.1, but the numerical procedures are more complicated. In addition to the required coordinate transformations, there are several tasks needed in the displaced cases:

a. Finding the intersection point on the main reflector

b. Checking if the distorted rays hit the main reflector.

c. Finding the intersection point's associated surface parameters.

A shift in the subreflector or feed position radically alters the path of the ray tracing. As a result, a ray traced from the subreflector in general will not strike the corresponding node on the main reflector as defined in the synthesis program. To find where this ray strike the main reflector, an algorithm is used which can find the intersection point between a ray and the biparabolic expansion of a node on the main reflector. The intersection point with the smallest distance between itself and the node corresponding to the biparabola is taken as the intersection point for the main reflector. However, checking every node on the main reflector for its intersection with each ray from the subreflector takes up excessive computer time. Since the deviations in feed and subreflector position are assumed to be small, the

assumption is made that the ray will strike near the node corresponding to the position where the non-deviated ray would have struck. Thus, only main reflector nodes in the vicinity of the node associated with the given subreflector node are checked for intersection.

After the point is found through biparabolic expansion, verification must be done to check if the ray actually strikes the main reflector. Since the dimensions of the elliptical aperture are known, any rays falling outside the ellipse are assumed not to strike the main reflector and are ignored.

Once the point where the ray reflects off the main reflector is known to be valid, the surface parameters at that point must be determined. Interpolation is required to determine these parameters on the main reflector. The surface parameters of the four nodes nearest to and surrounding the point where the ray strikes the main reflector are used to interpolate the parameters of the point. Each node on the main reflector may be defined in terms of coordinates ρ and Θ. The four nodes surrounding the point of intersection of the ray and the main reflector may be paired in two ways. Nodes 1 and 2 have the same ρ value, as do nodes 3 and 4. Similarly, nodes 1 and 3 have similar Θ values, as do nodes 2 and 4. Thus, for interpolation purposes, the nodes surrounding the point are seen as a rectangle of length Θ_{13}-Θ_{24} and width ρ_{12}-ρ_{34}. The surface parameters of the point are interpolated using weightings which are inversely proportional to the (ρ,Θ) distances to the point from these nearest four nodes.

4. RESULTS

For the purpose of comparison, we use four sample antenna configurations. The first case is that of an offset elliptical aperture dual-reflector antenna (see

Figure 1). The second case is that of a center-fed elliptical-aperture (see Figure 2). The third case is an offset circular aperture dual-reflector (see Figure 3), and the fourth case is a center-fed circular aperture antenna (see Figure 4). Note that all the linear displacements are specified in inches and all the analyses are done at 44.5 GHz.

The key parameters for these cases are described in Section 2. The on-axis circular aperture antenna has been widely studied since the time that dual reflector antennas were first devised. The off-axis elliptical aperture antenna, however, is relatively unstudied, and comparing the effects of feed and subreflector shift on the relative gains of both antennas is quite enlightening.

For the tolerance study, the analysis code is capable of displacing and rotating the feed and/or subreflector. Although the displaced distance and rotation angle have some limitations (see Section 6), they have been found more than adequate for tolerance analysis purposes.

Examples have been chosen that emphasize several interesting points found during this study. For the purpose of comparison, extensive data has been collected for cases with simple shifts in position of the subreflector and feed along the line connecting the feed to the center of the subreflector. Deviations in other directions, as well as tilting the angle of the subreflector relative to the feed, are also demonstrated with limited data.

Another simplification to note is that blockage of the on-axis antenna by the subreflector is ignored for the purpose of this analysis. Although blockage is important and out analysis code can model this effect, we are more concerned with the relative deviation in gain due to shifts in position for this study.

4.1 EFFECT OF FEED SHIFT

The first effect observed is the effect of shifting the feed on the overall gain of the antenna. A degradation in gain is obviously present for both the offset and center-fed cases. From Figure 6, we see that a shift in feed position towards the subreflector (positive shift) causes the gain to deviate slightly more than a shift away from the subreflector. Also seen from this figure is that the shift in feed position for the elliptical aperture cases affect the antenna gain slightly more than the circular aperture cases. This is mainly due to the inherent stability of the circularly-symmetric design.

Figure 7 illustrates the under-illumination of the main reflector aperture due to a 0.2" feed displacement (shift closer to the subreflector) along the feed axis in the offset elliptical case using a subreflector which is not over-sized. The feed displacement causes the main reflector to be under-illuminated in this Gregorian case, in addition to inducing a phase variation over the aperture. On the other hand, if the feed is shifted away from the subreflector, additional spillover occurs for both subreflector and main reflector.

4.2 EFFECT OF SUBREFLECTOR SHIFT

Looking at the effect of feed shift on the antenna and comparing it with that of subreflector shift in Figure 8, we see that all four antennas are much more sensitive to the shift in subreflector position. This makes intuitive sense, since the subreflector provides a "magnification factor" for the equivalent reflector.

The gain degradation is similar whether the subreflector is brought closer to or farther away from the feed. When the subreflector is shifted towards the feed, both the subreflector and the main reflector become under-illuminated. When the

subreflector is shifted away from the feed, spillover increases from the feed to the subreflector, as well as from the subreflector to the main reflector. Thus, the combined loss due to phase variation and spillover or under-illumination is comparable in either direction. Similar to the feed shift, the subreflector shift causes more gain degradation in the elliptical cases than the circular cases.

Note that the amount of gain degradation due to feed or subreflector shift is highly dependent on the initial positions of the feed, subreflector, and main reflector. Those curves in Figures 6 and 8 are not intended to be used as design curves. Instead, they are presented to show sample results of the geometries chosen. To demonstrate the dependence of the degradation on the antenna geometry, we compare two different geometries using offset elliptical configurations. In Case 1 geometry shown in Figure 1, the distance between the subreflector and main reflector centers is 16.2 inches. This distance was shortened to 11.5 inches while the distance between the feed and the subreflector remained the same, and the synthesis and analysis precedures were repeated. A significant increase in the gain degradation due to subreflector shift was observed as shown in Figure 9. This phenomenon can be explained by the increase of the magnification factor in the shortened geometry.

4.3 EFFECT OF OVER-SIZED SUBREFLECTOR

Another capability of the analysis code is to analyze the displacement effect of an over-sized subreflector, which is extended beyond its Geometric Optics (G.O.) rim boundary. The advantages of an over-sized subreflector include the reduction of diffraction effect and spillover loss [11], which are especially significant with feed/subreflector misalignments. As an example, Figure 10 shows the gain

310

degradations due to various feed shifts with an over-sized subreflector compared to the normal subreflector used in Figure 1. For the over-sized case, there is less loss due to feed shift because the amount of under-illumination shown in Figure 7 is reduced. Note that the antenna gain shows a 0.06 dB improvement with a 0.05" feed shift using the over-sized subreflector. This is mainly due to the reduction of the spillover from subreflector. The 0.05" feed shift causes the over-sized subreflector to reflect this spillover energy to the main reflector. This phenomenon is also observed in other examples when the subreflector is shifted slightly away from the feed and an over-sized subreflector is used.

4.4 COMPENSATION OF FEED SHIFT BY SUBREFLECTOR SHIFT

It is desirable to compensate for the feed displacement by moving the subreflector. Typically, the feed is connected to other components such as amplifiers or receivers through waveguide. The built-up tolerance of the feed position can cause significant performance degradations if not properly compensated. Shimming of the waveguide is possible but expensive. On the other hand, moving the subreflector usually is much easier.

Figure 11 shows the amount of gain degradation with a fixed .2" feed shift and various subreflector shifts. One can see that some compensation can be achieved by moving the subreflector in the same direction as the feed shift. Note that the amount of the subreflector shift required for compensation is much smaller than the feed shift. Furthermore, better compensation can be obtained in the circular cases than the elliptical cases.

4.5 OTHER DISPLACEMENTS

Several other examples with various displacements are demonstrated in this

311

section. For the Case 1 antenna (Figure 1) with the feed displaced 0.2" in the X (vertical) direction, the main beam of the antenna scans approximately 0.55 degree in the vertical plane as shown in Figure 12. For the same antenna with a 0.1" subreflector displacement in the Y (horizontal) direction, the main beam scans approximately 0.45 degree to the opposite direction in the horizontal plane as shown in Figure 13.

The dual-reflector configuration also provides the capability of limited scan by tilting the subreflector. For the Case 1 antenna with a 1 degree subreflector tilt in the vertical plane using the subreflector center (-9.3, 0., 8.77) as a pivot point, the main beam scans about 0.35 degree with a gain degradation of 0.35 dB as shown in Figure 14.

5. VERIFICATION OF THE PROGRAMS

Several steps have been taken to verify the accuracy of the synthesis and analysis programs. So far, very good agreements have been obtained.

One of the steps is the ray tracing analysis of the synthesized dual-reflector using surface points with a rectangular grid instead of a polar grid. Identical results in antenna gain and patterns were obtained. This agreement verifies that the surfaces between the synthesized nodes are also good and gives us confidence in the accuracy of both the synthesis and analysis programs.

Another step is to compare results with those available in the literature. The second example in [12], which is a 120 wavelength diameter shaped Gregorian, was repeated using our synthesis and analysis programs, and the results indicate very good agreement.

The ultimate verification is to compare the analysis results against measured

data. Several shaped dual-reflector antennas have been designed and built using these computer codes. However, measured results were not available at the time of this publication.

6. LIMITATIONS

The displacement analysis mentioned above has been found valid for most of the cases. However, it tends to have a singularity problem when there is a large feed or subreflector displacement. This problem is due to a fundamental limitation of the Geometric Optics (G.O.). A key equation in G.O. is for the calculation of the spread factor (S.F.) of rays as defined by

$$S.F. = \sqrt{\frac{\rho_1 \rho_2}{(\rho_1 + s)(\rho_2 + s)}} \qquad \text{Eq. 3}$$

Where s is the distance between points on the referenced surface (subreflector, in this case) and the desired surface (main reflector), and ρ_1 and ρ_2 are the caustic distances of the ray in two principal planes. However, when the value of either factor in the denominator approaches 0, then the spread factor becomes infinite and the result becomes invalid. That is, when $s = -\rho_1$ or $s = -\rho_2$, then the ray convergence causes the value of the field on the main reflector to become singular, and the aperture field is therefore invalid. This problem occurs when there is an excessive subreflector or feed shift that causes a caustic point to be located on or very near to the main reflector, causing the spread factor to be singular.

One possible solution to this problem would be to use a different approach, such as physical optics (P.O.), to computing the aperture field. The main disadvantage of the physical optics is its slow speed. A hybrid approach [7] using

G.O. and P.O. has been proposed to obtain both accurate and fast computations to overcome this caustic problem.

7. CONCLUSIONS

A useful computer modeling tool for the displacement analysis of elliptical or circular shaped dual-reflectors has been developed. This analytical capability has been used extensively for dimensional tolerance analysis as well as other analyses such as limited scan and defocusing.

Using this tool, antenna gain degradations due to feed or subreflector shift in four different configurations have been calculated and compared. It has been found that in general, the elliptical-aperture cases suffer more losses due to feed or subreflector displacement than the circular-aperture cases. The gain degradation is affected significantly by the antenna geometry even with similar configuration. Our analysis also indicates that an over-sized subreflector can be used to reduce the displacement loss and some of the loss caused by the feed shift can be compensated by proper subreflector shift. Various scans of antenna beam were also demonstrated by three examples using lateral displacements of feed and subreflector as well as subreflector tilt.

REFERENCES

1. Kildal, P. (1990) Synthesis of multireflector antennas by kinematic and dynamic ray tracing, IEEE Trans. AP, 38 (No.10): 1587-1599.

2. Ruze, J. (1965) Lateral-feed displacement in a paraboloid, IEEE Trans. AP, 13 : 660-665.

3. Ingerson P.G. and Rusch, W.V.T. (1973) Radiation from a paraboloid with an axially defocused feed, IEEE Trans. AP, 21 (No.1): 104-106.

4. Imbriale, W.A., Ingerson, P.G., and Wong, W.C. (1974) Large lateral feed displacements in a parabolic reflector, IEEE Trans. AP, 22 (No.6): 742-745.

5. Whale, H.A. and Putz E. (1986) Beam steering using feed displacement with a paraboloidal reflector, IEEE Trans. AP, 34 (No.11): 1368-1372.

6. Rahmat-Samii Y. (1988) Antenna Handbook, Reflector Antenna (Chapter 15) Pub. by Van Nostrand Reinhold, Ed. by Lo, Y.T. and Lee, S.W.: 49-61.

7. Galindo, V. (1963) Design of dual reflector antennas with arbitrary phase and amplitude distribution. Paper presented at IEEE APS Int. Symposium, Boulder, CO.

8. Westcott, B.S., Steveens, F.A., and Brickell F. (1981) GO synthesis of offset dual reflectors, IEE Proc. 128, Pt. H, (No.1): 11-18.

9. Galindo-Israel, V., Imbriale, W., and Mittra R. (1987) On the theory of synthesis of single and dual offset shaped reflector antennas, IEEE Trans. AP, 35 (No.8): 887-896.

10. Lee, B.S. and Rudduck, R.C. (1985) Aperture integration and GTD techniques used in the NEC reflector antenna code, IEEE Trans. AP, 33 (No.2): 189-194.

11. Rahmat-Samii, Y. (1986) Subreflector extension for improved efficiencies in Cassegrain antenna using GTD/physical-optics analysis, IEEE Trans. AP, 34 (No. 10): 1266-1269.

12. Galindo-Israel, V., Imbriale, W., and Mittra R. (1992) Examples of synthesis of dual-shaped reflectors, NASA Tech Brief Vol. 16 (No.11), Item #43.

13. Galindo-Israel, V., Veruttipong, T., Rengarajan, S., and Imbriale, W. (1990) Inflection point caustic problems and solutions for high-gain dual-shaped reflectors, IEEE Trans, AP, 38 (No.2): 202-211.

(a) Angle View
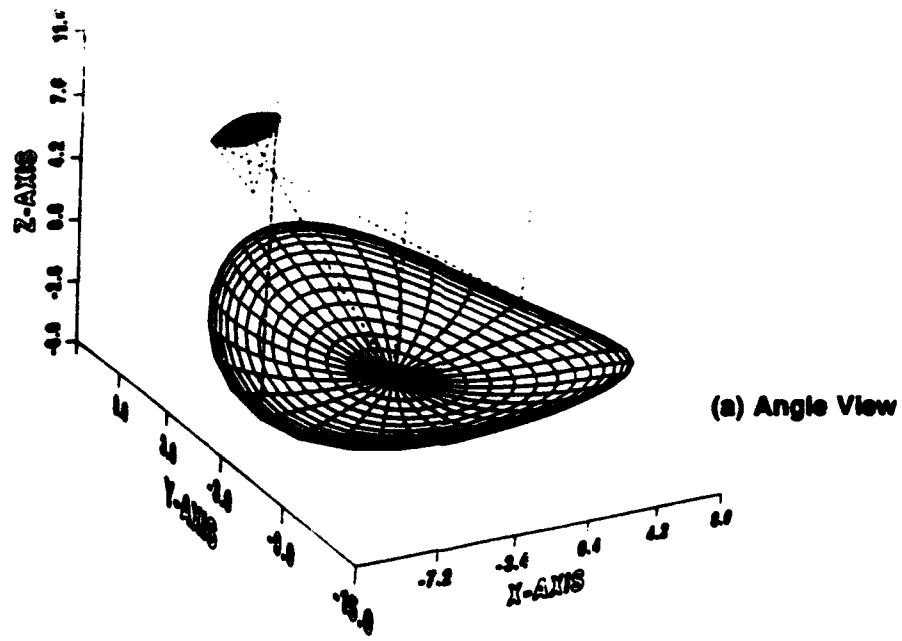
zf - 5.270	xf - -8.500	
zso- 8.770	xso- -9.300	
zmo- -4.500	xmo- 0.000	
zsl- 7.687	xsl- -10.592	
zsu- 8.965	xsu- -7.501	
zml- -5.751	xml- -7.500	
zmu- -1.020	xmu- 7.500	

rho= 7 5t
e 2.00
theta (deg) 28.00
n (dB) 15.0
Co (dB) -3.00

(b) Side View

(c) Front View
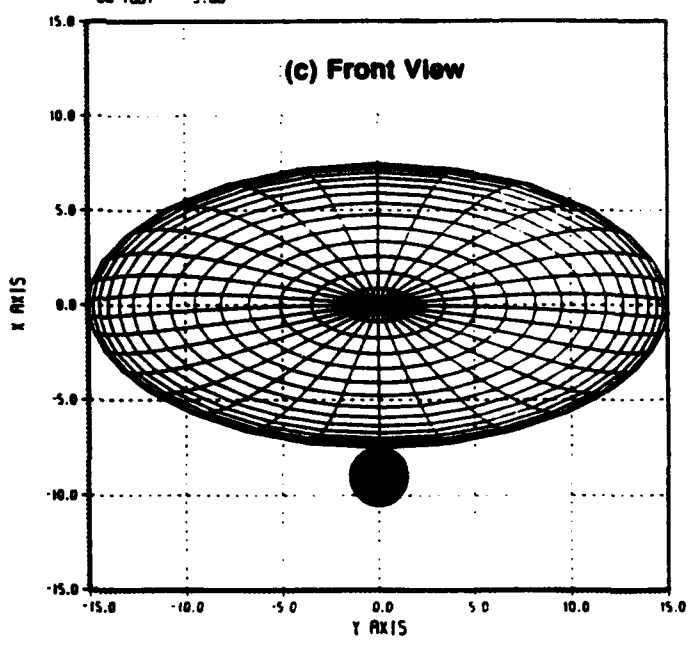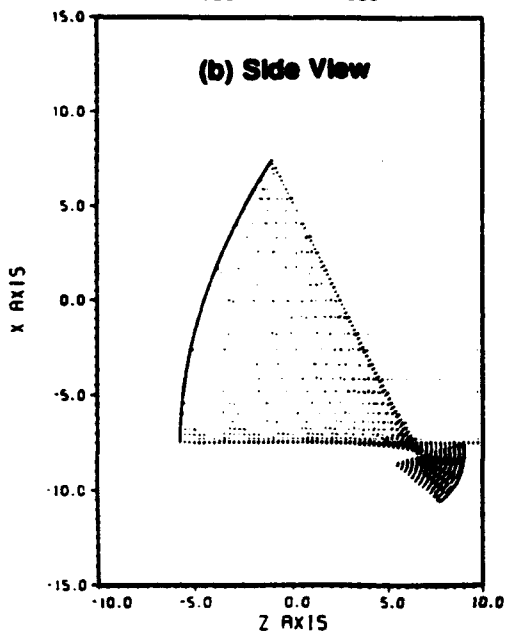
Figure 1.   Synthesized surfaces of a 30"x15" offset shaped dual-reflector.

316

(a) Angle View

Z-AXIS

X-AXIS

zf = 8.100   xf = 0.000
zso= 11.700   xso= 0.000
zmo=-4.500   xmo= 0.000
zsl= 11.205   xsl= 1.651
zsu= 11.205   xsu= 1.651
zml=-3.480   xml=-7.500
zmu=-3.480   xmu= 7.500

rhom   7.50
a   2.00
theta(deg) 28.00
.. (dB)   -15.00
Ce (dB)   -3.00

(b) Side View

X AXIS

Z AXIS

(c) Front View

X AXIS

Y AXIS
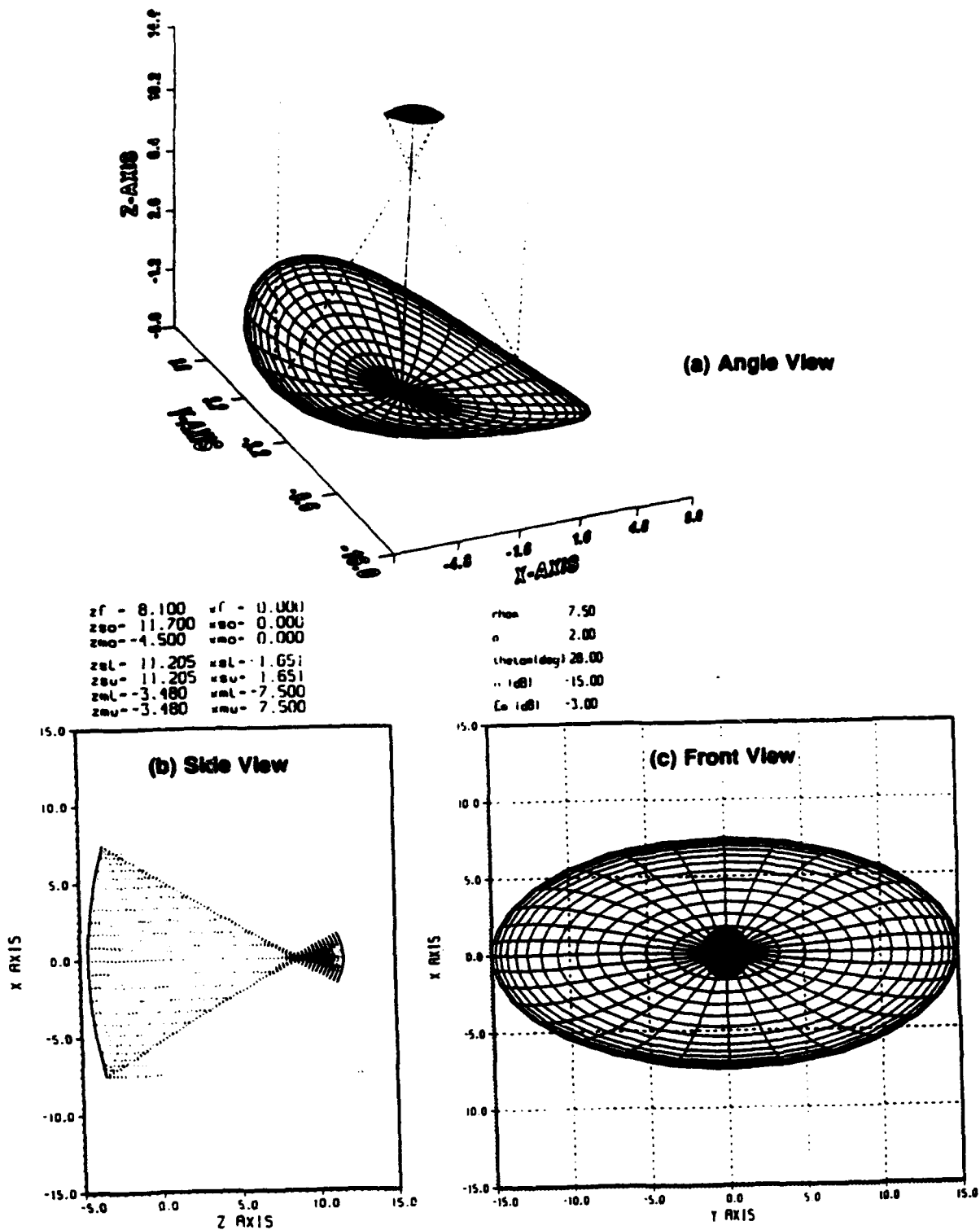
Figure 2.   Synthesized surfaces of a 30"x15" center-fed shaped dual-reflector.

317

(a) Angle View

Z-AXIS

Y-AXIS

X-AXIS
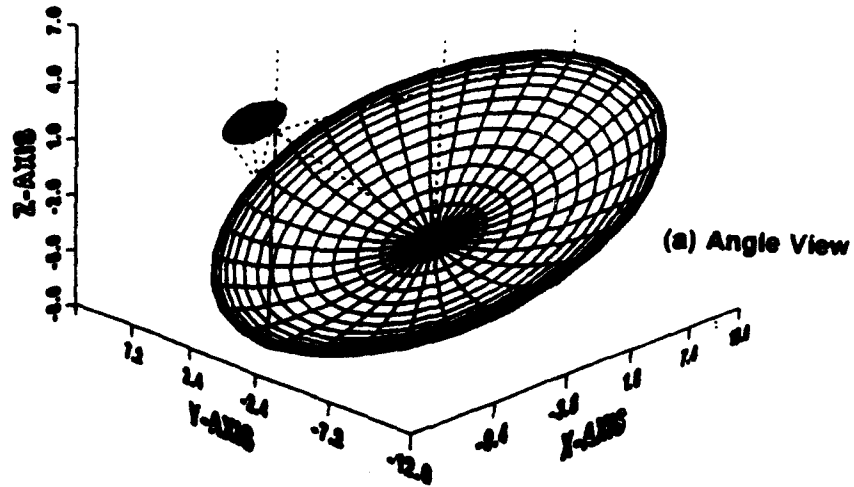
zf - 0.500	xf --13.000
zso- 1.000	xso--13.800
zmo--4.500	xmo- 0.000
zsl- 2.586	xsl--14.806
zsu- 1.353	xsu--11.959
zml--7.977	xml--12.000
zmu- 5.416	xmu- 12.000

rhom	12.00
a	1.00
theta(deg)	28.00
n (dB)	-15.00
Ce (dB)	-3.00

(b) Side View

X AXIS

Z AXIS

(c) Front View

X AXIS

Y AXIS
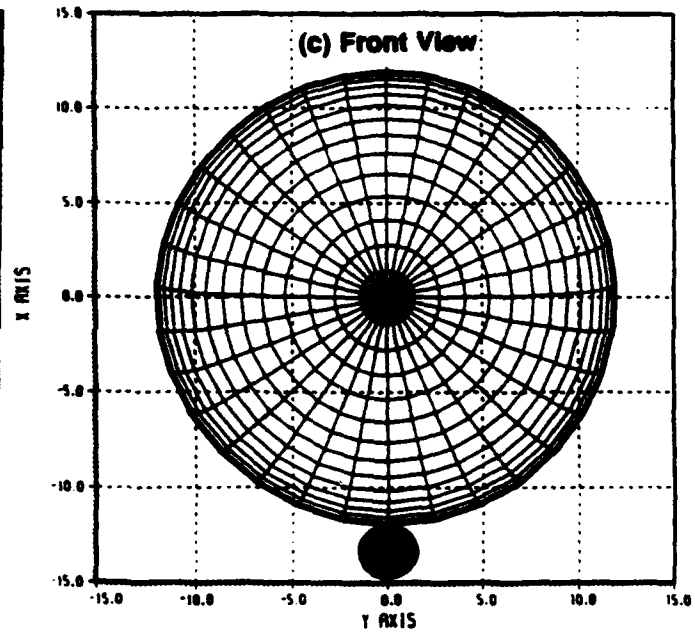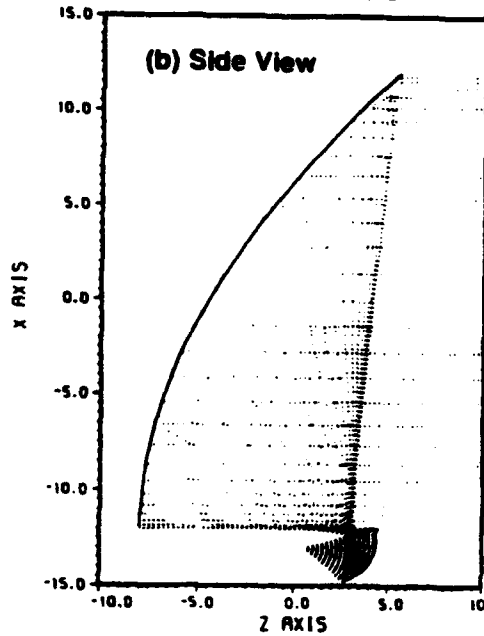
Figure 3.   Synthesized surfaces of a 24" diameter offset shaped dual-reflector.
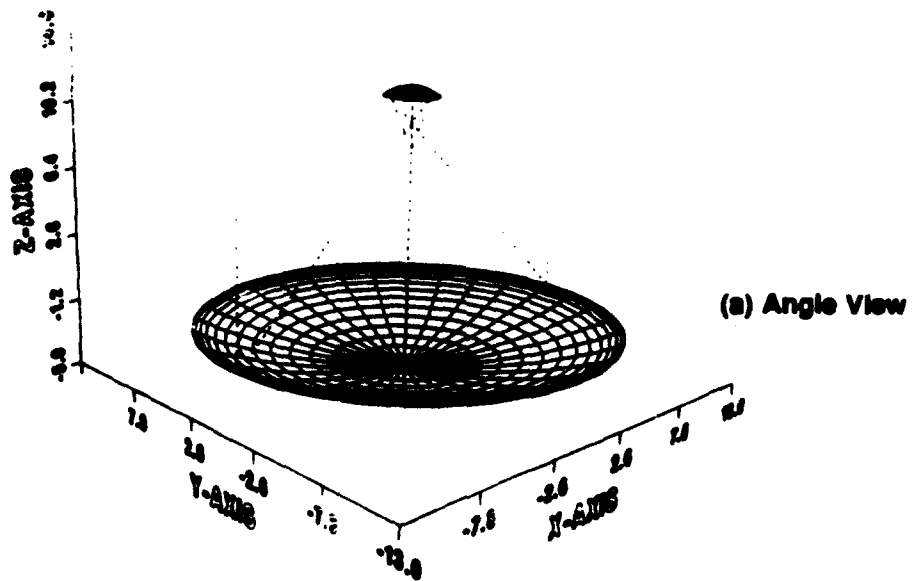
318

(a) Angle View

Z-AXIS

Y-AXIS

X-AXIS

zf = 0.100   xf = 0.000
zso= 11.700   xso= 0.000
zmo= -4.500   xmo= 0.000

zsl= 11.081   xsl= 1.585
zsu= 11.081   xsu= 1.585
zml= -2.038   xml= 12.000
zmu= -2.038   xmu= 12.000

rhom   12.00
e   1.00
thetm(deg) 28.00
n (dB)   -15.00
Ea (dB)   -3.00

(b) Side View

X AXIS

Z AXIS

(c) Front View

X AXIS

Y AXIS
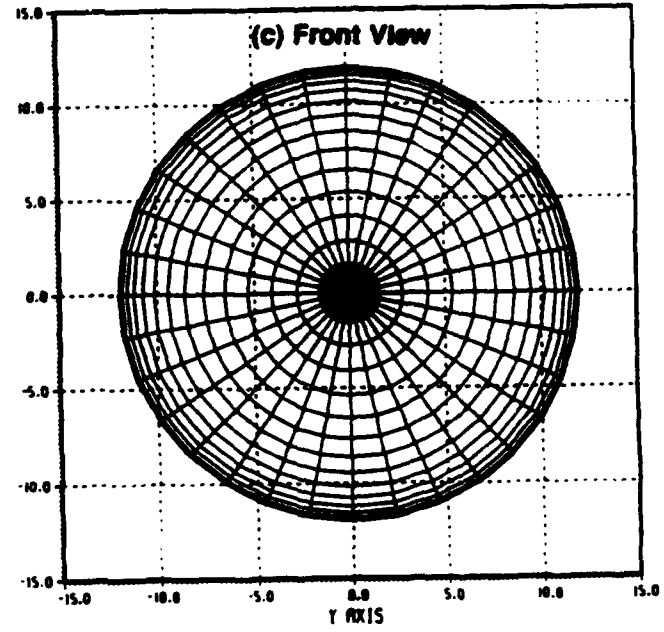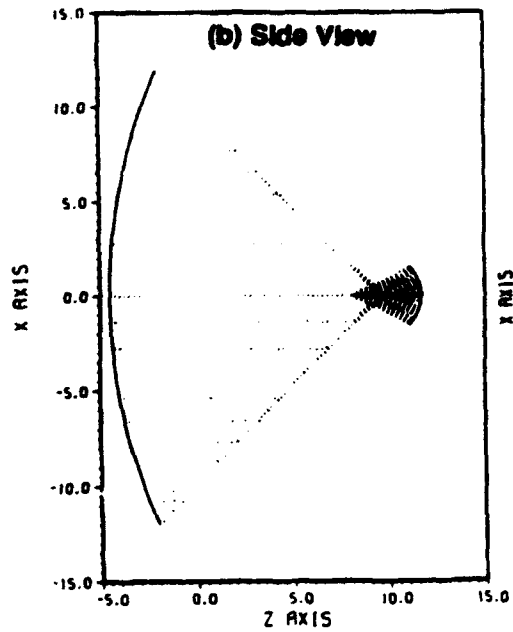
Figure 4. Synthesized surfaces of a 24" diameter center-fed shaped dual-reflector.

319

APERTURE FIELD DISTRIBUTION
FOR CENTER-FED DUAL-REFLECTOR
24 INCH DIAMETER
PRINCIPAL PLANE CUT
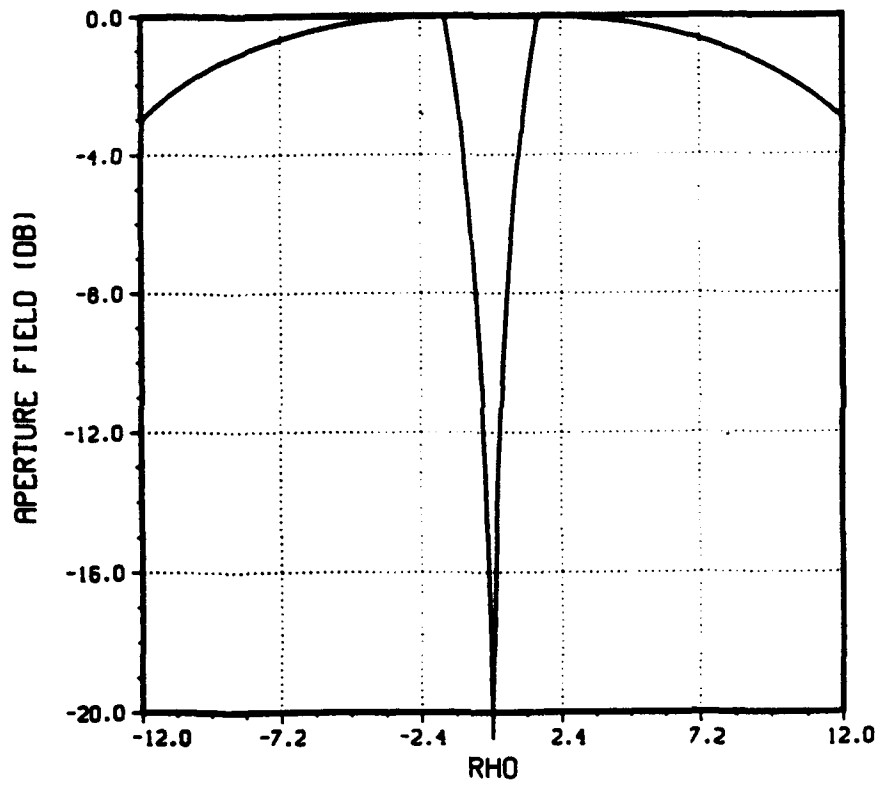
Figure 5.   Resultant aperture field distribution for the 24" diameter center-fed antenna.

GAIN DEGRADATION VS. FEED SHIFT
SHIFT ALONG ZF FEED AXIS

Figure 6.   Gain degradation due to feed shift.

321

(a) Side View

(b) Front View
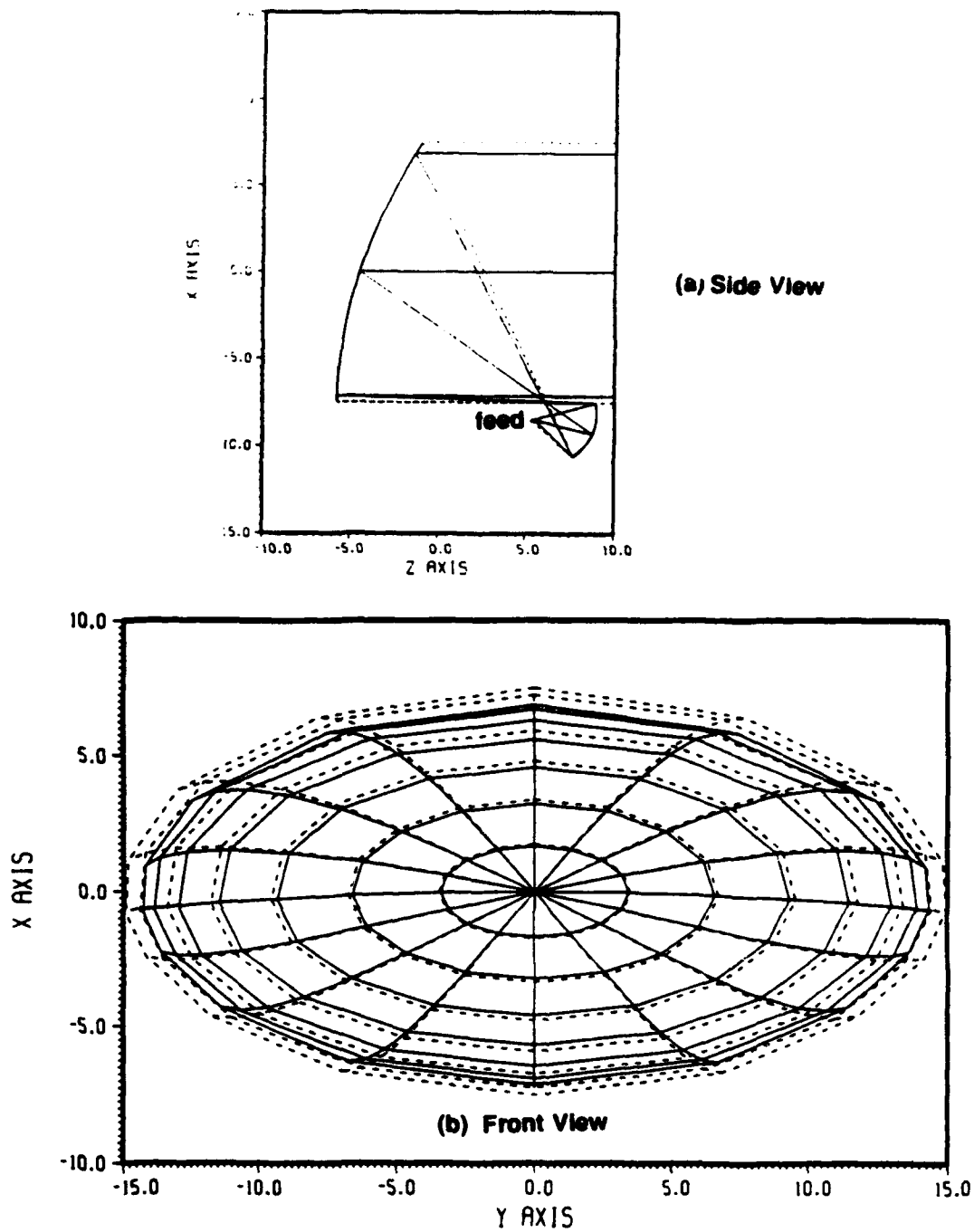
Figure 7. Under-illuminated reflector due to a 0.2" feed shift toward subreflector. The dashed lines indicate the original rays and grids, and the solid lines show the distorted rays and grids.

322

GAIN DEGRADATION VS. SUBREFLECTOR SHIFT
SHIFT ALONG ZF FEED AXIS

SYMBOLS:
o   30x15 offset
△   30x15 center-fed
+   24 dia. offset
x   24 dia. center-fed
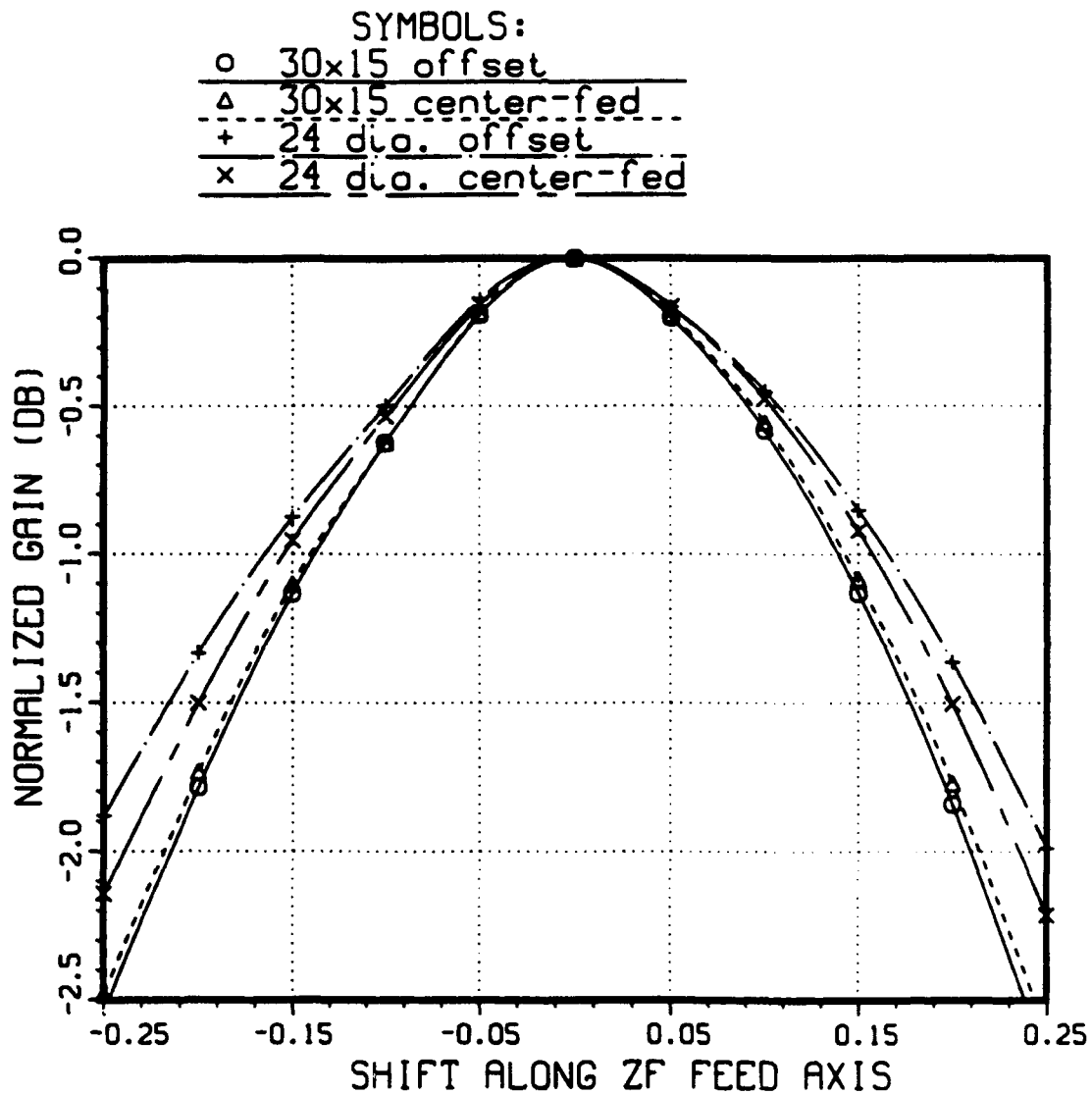
Figure 8.   Gain degradation due to subreflector shift.

EFFECT OF SUBREFLECTOR TO MAIN REFLECTOR PATH LENGTH SHIFT ON GAIN DEGRADATION
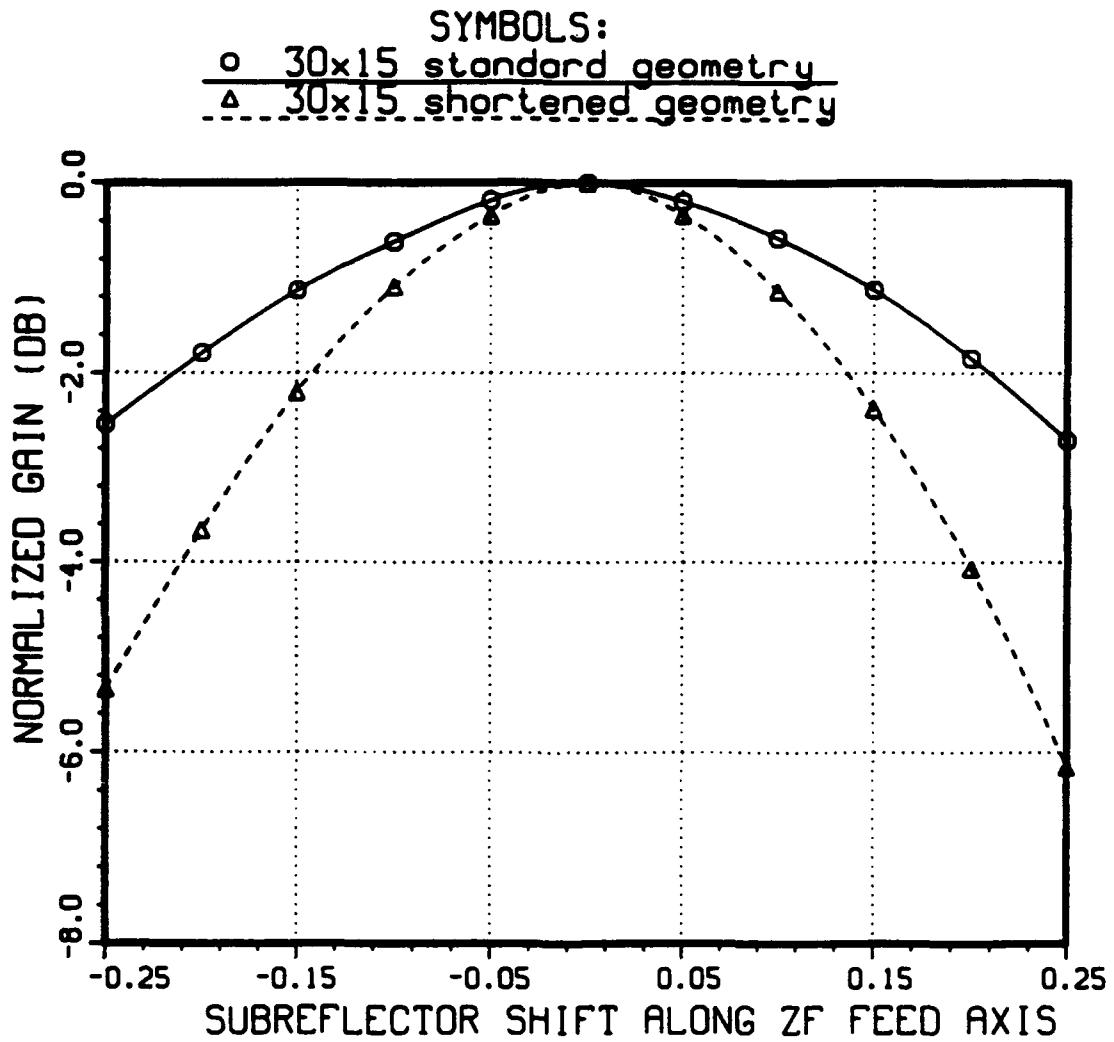
Figure 9.   Effect of geometry on degradation due to subreflector shift.

GAIN DEGRADATION VS. FEED SHIFT
NORMAL VS. OVER-SIZED SUBREFLECTOR

SYMBOLS:
o   30x15 standard subreflector
△   30x15 over-sized subreflector
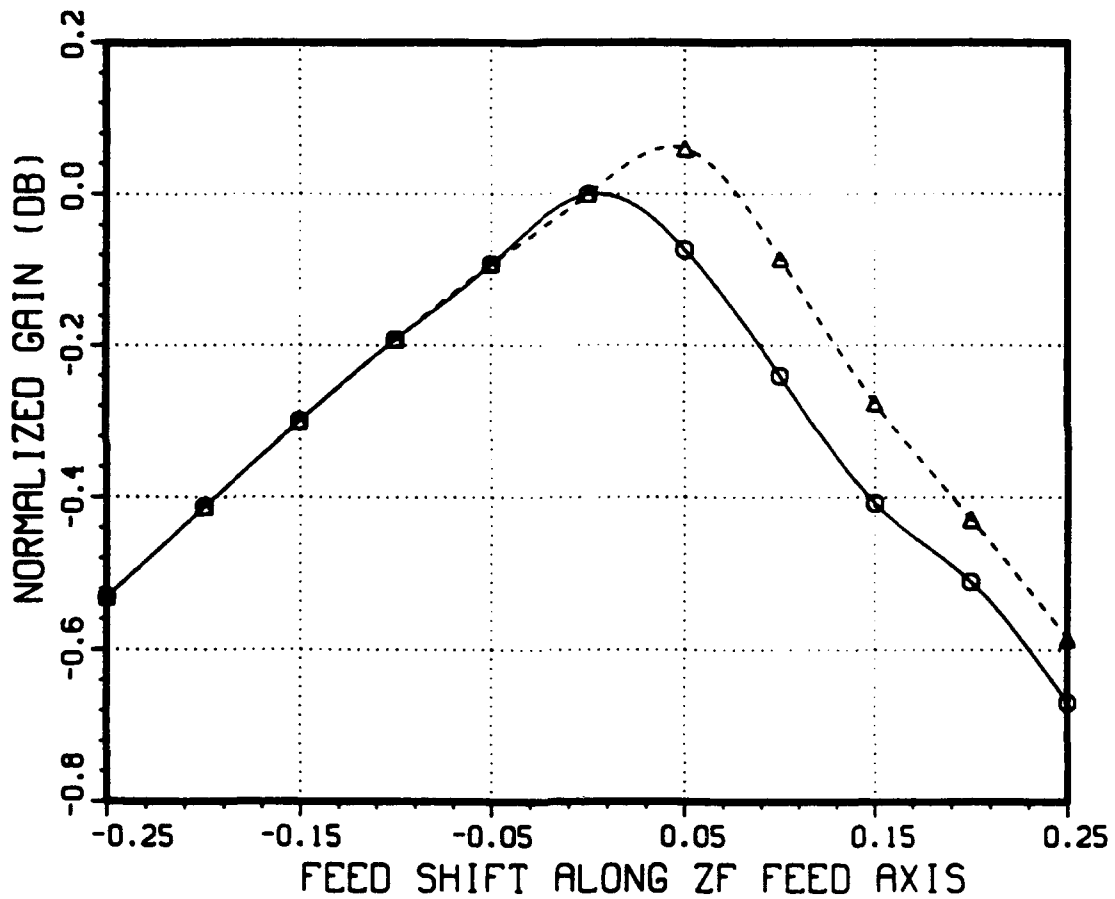
Figure 10.   Gain degradation due to feed shift with over-sized subreflector.

GAIN DEGRADATION VS. SUBREFLECTOR SHIFT
WITH A FIXED 0.2 INCH FEED SHIFT

SYMBOLS:

o	30x15 offset
Δ	30x15 center-fed
+	24 dia. offset
x	24 dia. center-fed

Figure 11.   Gain degradation with a fixed .2" feed shift and compensating subreflector shift.

PATTERNS IN VERTICAL PLANE
FEED SHIFT - (0.2,0.,0.)
SOLID LINE: W/ DISPLACEMENT
DASHED LINE: W/ NO DISPLACEMENT
MAX- 47.83
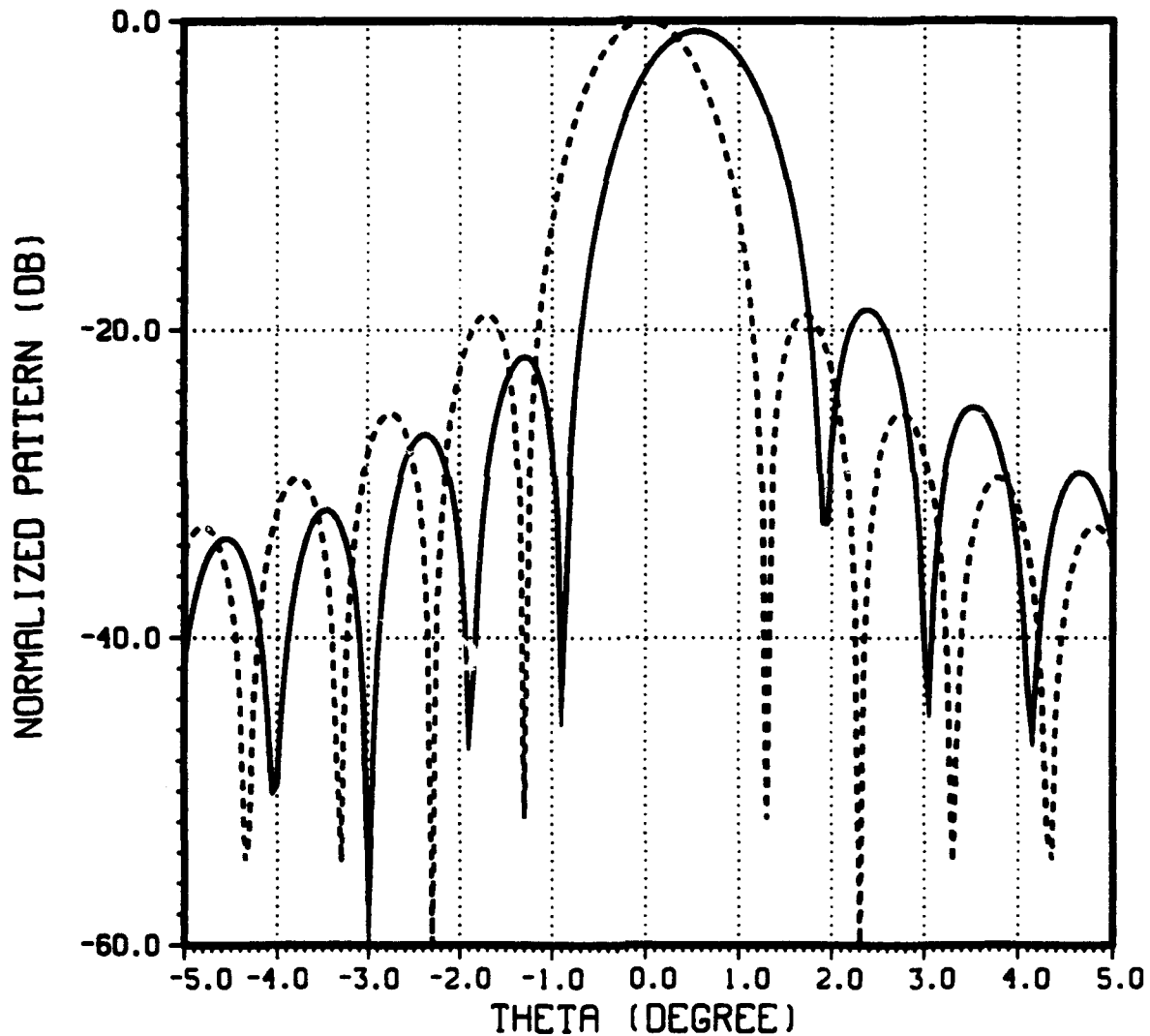
Figure 12. Effect on antenna pattern due to a .2" feed shift in the X (vertical) direction.

PATTERNS IN HORIZONTAL PLANE
SUBREFLECTOR SHIFT - (0.,0.1,0.)
SOLID LINE: W/ DISPLACEMENT
DASHED LINE: W/ NO DISPLACEMENT
MAX- 47.83
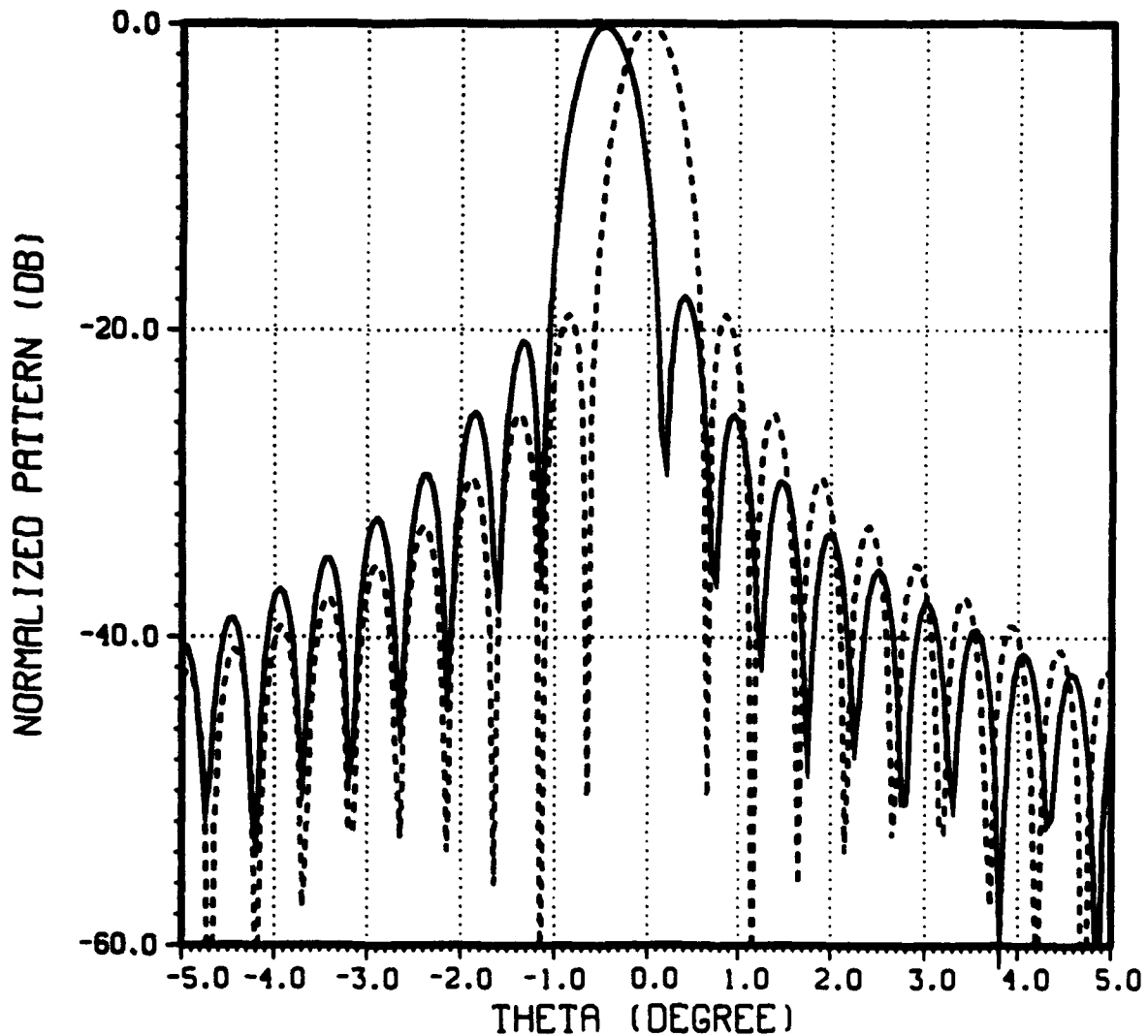
Figure 13. Effect on antenna pattern due to a .1" subreflector shift in the Y (horizontal) direction.

PATTERNS IN VERTICAL PLANE
1 DEGREE SUBREFLECTOR TILT
SOLID LINE: W/   TILT
DASHED LINE: W/ NO TILT
MAX- 47.83
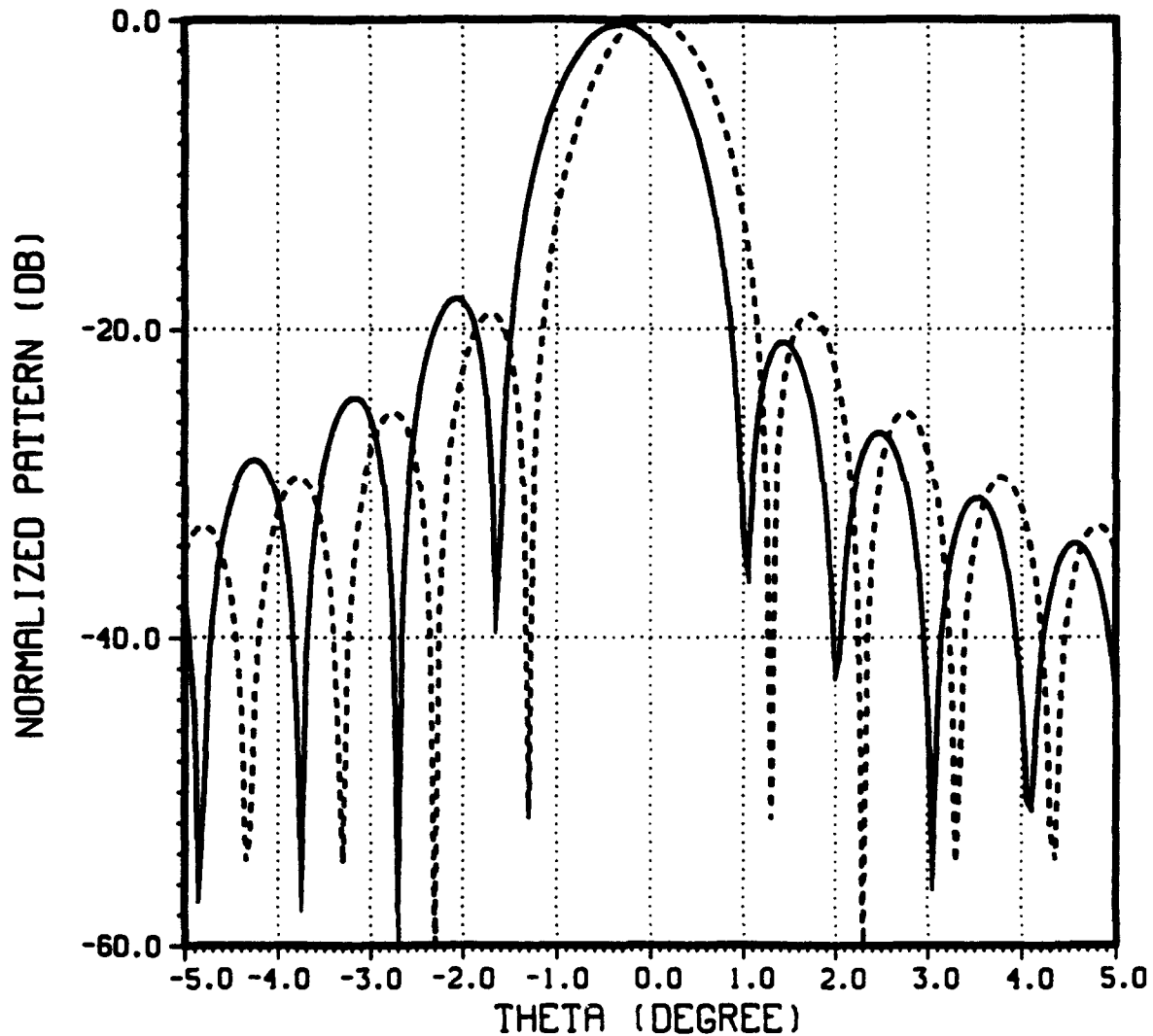
Figure 14.   Effect on antenna pattern due to a 1 degree subreflector tilt.

The New Monopulse Feed Optimised with Antenna Performance

Cai Ming

Beijing Institute of Radio Measurement

Abstract

The paper describes a new wide band monopulse feed which is consisted of four H-plane large sectorial angle horns, each of them is with a dielectric lens to correct the phase in aperture in order that the feed could practice the small illustration angle requirement. All of the horns are laminated together with different sizes between inner two horns and outer two. There are five parameters in feed, the four sizes in aperture and the mode ratio, all of these can be selected to satisfy the necessity of antenna that has five performances, the sum efficiency η_Σ, the azimuth difference efficiency η_H and the slop K_H, the vertical difference efficiency η_E and the slop K_E. The lens introduced into the horn has evidently influence on the monopulse multimode ratio in both the phase and the amplitude. However, this problem has been resolved with the computer aided analysis and experiment test. By the careful design, the laminated four horns monopulse feed has a compact structure as the feeding network. After adjustment, the feeding network has perfect matching and isolating situations that could be compared with the most monopulse feeds worked in the wide frequency band. The detailed mathematic models, described the relationship between antenna and feed, are derived and used in optimizing the performances of antenna with the restrain conditions of side lobes, by the Nelder-Mead method, one of the directive optimization methods. Finally, the optimum process and results are discussed, and compared with the experiment results in both feed and antenna system individually. The comparison is satisfying.

1. Introduction

The monopulse performances in scanning or in tracking are always necessary in the modern radar and communication system. It is important to design a monopulse feed used in space fed array or other antenna. General speaking , the feed is independently designed, only considered the illumination level on the antenna. But, the distributions in the aperture of antenna are different for the various feeds, then the illumination levels in antenna are also different. For the optimum radiation characteristic of antenna, it is necessary to combine the design of feed with the performance of antenna system, as an unit.

In the past , many design methods of the monopulse feeds have been discussed efficiently and implemented continuously. In these feed models, the feed proposed by Hannan [1] is considered as the best one in compromising the monopulse performances

of feed. But, the feed network is complexed. The new feed presented in this paper, could overcome the problem, with the same advantages.

2. The mathematical model for calculating the radiation pattern of feed

The monopulse feed is consisted of four H-plane sector horns, as shown in Fig.1, two of them in the medial are worked with multimode, two in the outside are only with TE10 mode. In order to produce sum beam, only the medial two horns are excited by the mode producer with TE10 and TE30. The H-plane difference is also formed by the medial horns worked in TE20 mode. The network of forming E-plane difference is complexity. The two signals of medial horns are subtracted and the two signals of outside horn are also subtracted. The two subtracted signals are added to form the E-plane difference which distribution is weighted by the different sizes and power divided coefficients. In order to satisfy the monopulse requirement of antenna in wide frequency band, the H-plane dielectric len has been put in the the horn. The phase distribution may be uniform in the H-plane aperture. Since the size of horn on E-plane is nearly 1λ, the phase distribution in E-plane is also considered as uniform. The monopulse radiation characteristic of feed may be expressed as following:

In the sum condition:

$$E_{\Sigma}(\theta,\phi)=\sqrt{\frac{A_1B_1}{1+\alpha_{30}^2}}\frac{2(1+\cos(\theta))\sin(K_2B_1)}{\pi K_2B_1}\left[\frac{1}{1-(\frac{K_1A_1}{\pi})^2}-\frac{\frac{\alpha_{30}}{3}}{1-(\frac{K_1A_1}{3\pi})^2}\right]\cos\left(\frac{K_1A_1}{2}\right)$$

--------(2-1)

In the H-plane difference condition:

$$E_{\Delta H}(\theta,\phi)=\sqrt{A_1B_1}\frac{2(1+\cos(\theta))\sin(K_2B_1)}{\pi K_2B_1}\frac{\sin\left(\frac{K_1A_1}{2}\right)}{1-(\frac{K_1A_1}{2\pi})^2}$$

--------(2-2)

In the E-plane difference condition:

$$E_{\Delta E}(\theta, \phi) = \{E_{B0} \frac{4A_1 B_1}{\pi} \sin\left(\frac{K_1 B_1}{2}\right) \frac{\sin\left(\frac{K_2 B_1}{2}\right)}{K_2 B_1} \cos\left(\frac{K_1 A_1}{2}\right)$$

$$\left[\frac{1}{1-(\frac{K_1 A_1}{\pi})^2} \frac{\frac{\alpha_{30}}{3}}{1-(\frac{K_1 A_1}{3\pi})^2}\right] + E_{E1} \frac{4A_2 B_2}{\pi} \sin\left(K_2(B_1 + \frac{B_2}{2})\right)$$

$$\frac{\sin\left(\frac{K_2 B_2}{2}\right) \cos\left(\frac{K_1 A_2}{2}\right)}{K_2 B_2} \frac{}{K_1 A_2}\}(1+\cos(\theta))$$

——(2-3)

where $K_1 = \frac{2\pi}{\lambda} \sin(\theta)\cos(\phi)$, $K_2 = \frac{2\pi}{\lambda}\sin(\theta)\sin(\phi)$ and the coefficients E_{B0} and E_{E1} are determined by the energy conservation law.

3. The mathematical model for antenna system

The antenna is considered as a circular phased array antenna, as shown in Fig. 2.

For the space fed circular array, the coordination relationship between antenna and feed is shown in the Fig.2, the radiation field of the antenna may be derived from the radiation formula [2]:

$$E_f(\eta, \xi) = \frac{1+\cos(\eta)}{2} \frac{D}{\sigma} \int_0^{2\pi} \frac{E(\rho, \phi)}{L}$$

$$[jk(\quad (\phi)\sin(\;)\quad (\xi)\quad \sin(\phi)\sin(\;)\sin(\xi)\; L]\; d\;d\phi \qquad ----(3-1)$$

By adjusting the phase shifter to make $kL=0$, where $K = \frac{2\pi}{\lambda}$. $E(\rho, \phi)$ is the illumination function of antenna. For the convenience, the coordination (ρ, ϕ) may be transformed into (θ, ϕ) by the following expression:

$$\rho = F\tan(\theta), \quad L = \frac{F}{\cos(\theta)} \qquad -----(3-2)$$

Substituting the radiation functions (2-1), (2-2) and (2-3) into (3-1) individually, the far field radial pattern of the antenna can be obtained.

In order to optimize the antenna performance, the aperture efficiency and the relative difference slop are selected to express as following:

The sum aperture efficiency:

$$\eta_{\Sigma} = \frac{1}{S} \frac{\left| \int_0^{\frac{D}{2}} \int_0^{2\pi} \frac{E_{\Sigma}(\rho, \phi)}{L} \rho d\rho d\phi \right|^2}{\int_0^{\frac{D}{2}} \int_0^{2\pi} \left[\frac{E_{\Sigma}(\rho, \phi)}{L} \right]^2 \rho d\rho d\phi} \qquad \text{----(3-3)}$$

The H-plane difference aperture efficiency:

$$\eta_H = \frac{4}{S} \frac{\left| \int_0^{\frac{D}{2}} \int_0^{\pi} \frac{E_{\Delta H}(\rho, \phi)}{L} \rho d\rho d\phi \right|^2}{\int_0^{\frac{D}{2}} \int_0^{2\pi} \left[\frac{E_{\Delta H}(\rho, \phi)}{L} \right]^2 \rho d\rho d\phi} \qquad \text{-----(3-4)}$$

The E-plane difference aperture efficiency:

$$\eta_E = \frac{4}{S} \frac{\left| \int_0^{\frac{D}{2}} \int_0^{\pi} \frac{E_{\Delta E}(\rho, \phi)}{L} \rho d\rho d\phi \right|^2}{\int_0^{\frac{D}{2}} \int_0^{2\pi} \left[\frac{E_{\Delta E}(\rho, \phi)}{L} \right]^2 \rho d\rho d\phi} \qquad \text{-----(3-5)}$$

where $S = \pi \left(\frac{D}{2\lambda} \right)^2$ $\qquad$ -----(3-6)

$E_{\Sigma}(\rho, \phi)$, $E_{\Delta H}(\rho, \phi)$ and $E_{\Delta E}(\rho, \phi)$ are respectively the sum, the H-plane difference and the E-plane difference aperture distributions of antenna, expressed in (2-1), (2-2), and (2-3).

The H-plane relative differency slope is defined by the following formula,

$$K_H = \frac{1}{\sqrt{G_{\Delta H}}} \left[\frac{\partial E_{f\Delta H}}{\partial \eta} \right]_{\substack{\xi=0 \\ \eta=0}} \qquad \text{-----(3-7)}$$

where $E_{f\Delta H}$ can be derived by substituting the $E(\rho, \phi)$ of (3-1) with (2-2),

$$K_H = \frac{\lambda}{\pi D} \int_0^{\frac{D}{2}} \int_0^{2\pi} \frac{E_{\Delta H}(\rho, \phi)}{L} [jk\rho\cos(\phi)]\rho d\rho d\phi \qquad \text{-------(3-8)}$$

The E-plane relative differency slop is defined by the following formula:

$$K_E = \frac{1}{\sqrt{G_{\Delta E}}} \left[\frac{\partial E_{f\Delta E}}{\partial \eta} \right]_{\substack{\xi=0 \\ \eta=0}} \qquad \text{------(3-9)}$$

where $E_{f\Delta E}$ can be derived by substituting the $E(\rho, \phi)$ of (4-1) with (3-3),

$$K_E = \frac{\lambda}{\pi D} \int_0^{\frac{D}{2}} \int_0^{2\pi} \frac{E_{\Delta E}(\rho, \phi)}{L} [jk\rho\sin(\phi)]\rho d\rho d\phi \qquad \text{------(3-10)}$$

Now , all of the mathematical function models, that can assure the optimum monopulse requirement of antenna system, have been established.

4. The design process of optimization

4.1 The object function

There are five variable parameters in the monopulse feed consisted of four H-plane sector horns: A1, B1, A2, B2, and the mode ratio α_{30}.

The objective function are the radiation parameters η_Σ, η_H, η_E, K_H and K_E, that can be expressed in the mathematical formula. It is necessary to combine these indexes with the weighted coefficients pi, according to the requirement of the antenna. It is important that the different combinations of these indexes would satisfy the various conditions. The antenna gain can be determined by the sum aperture efficiency η_Σ and the constraint of the sidelobe level. The H-plane difference slope and the contrariety between sum and difference can be determined by the combination of η_H and K_H. It is the same for the E-plane difference. All of the objective functions are linearly added with the weighted coefficient pi (i=1, 2, ..., 5):

$$g = p_1\eta_\Sigma + p_2\eta_H + p_3\eta_E + p_4 K_H + p_5 K_E \qquad \text{------(4-1)}$$

where η_Σ, η_H, η_E, K_H and K_E are introduced by (3-3), (3-4), (3-5), (3-8) and (3-10).The sidelobe level is set as one of the constraints. There are also some constraints for variable parameters, such as the mode ratio α_{30} must be in the range (0, 1).

4.2 The optimization

Because the objective function is the combination of five integration expressions which are difficulty to derive, those derived optimum methods are not suitable. The Nelder-Mead optimization that is one of the directive methods is powerful to the stabalility objection.

The essential block diagram of optimum design of antenna is shown in Fig.3. The block diagram of Nelder-Mead method is referenced to [3].

In the calculation, the initial parameters must be selected carefully, because that would increase the optimum speed. The weighted coefficient pi in the objective functions need to be adjusted, according to the optimum compromise results. In the search beginning, the effectiveness of this method is approaching to the optimum point.

5. The comparison between the calculation and the measurement

Because of the len introduced, the amplitude distribution in H-plane aperture, need to be modified. After modified, the pattern of feed is identical with the computing results, so the optimum compromises result of calculation from (4-1) may illustrate the experiment results of antenna system.

When the phased array antenna does not scan, the contrariety of sum and difference is measured better than 3dB, the difference slop is measured better than 1.5. Both f them are coincided with the calculation results of optimum compromised results.

6. Conclution

This paper describes the optimum design of the monopulse antenna system that is consisted of the four H-plane sector horns and the space fed phase array. The multiple objective function are established by the mathematical models of antenna parameters, and processed optimistically by the Nerls-Mesd method. The results of optimization are compared with the experiments. This optimization is suitable to any other antenna system, that only required to substitute the feed or antenna subprogramme with the special one, according to the special necessity.

Acknowledgment

References
1. Hannan, P. W. and Loth, P. A. (1961) A monopulse antenna having

independent optimization of the sum and difference modes. IRE Int. Convention Rec., pt 1, 57- 60

2. Elliott, R. S. (1981)   Antenna Theory and Design, Englewood Cliffs NJ: Prentice Hall, Charpter.3

3. Yie, Qing Kai and Wang, Zhao Ming (1986) The Computation Methods in Optimum Control (Chinese), Science Published House, Charter .3
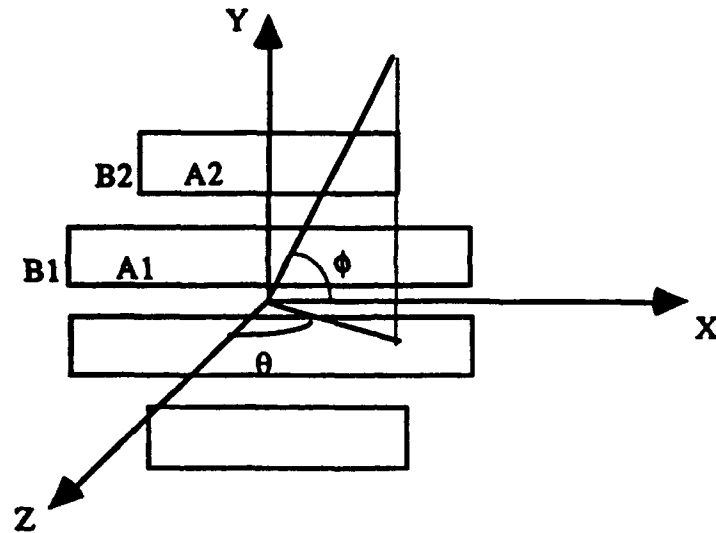
Fig. 1 The Coordination of Feed
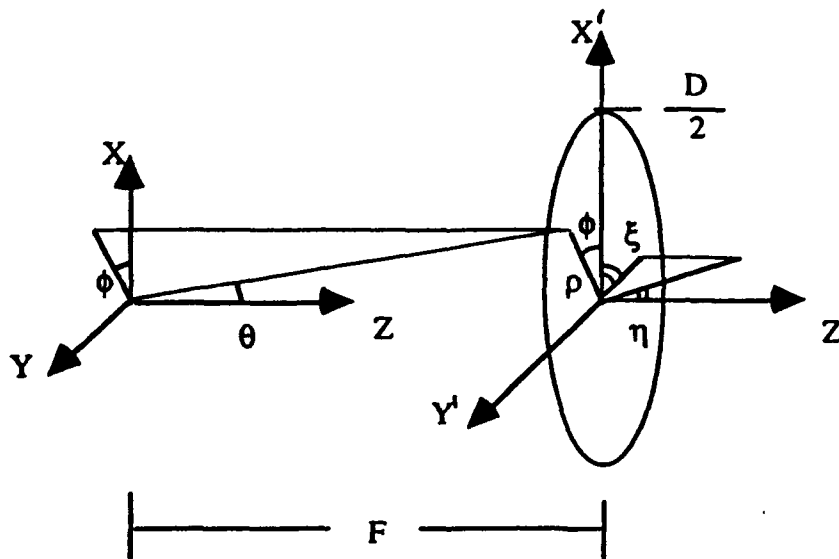
Fig. 2 The coordination relationship between antenna and feed
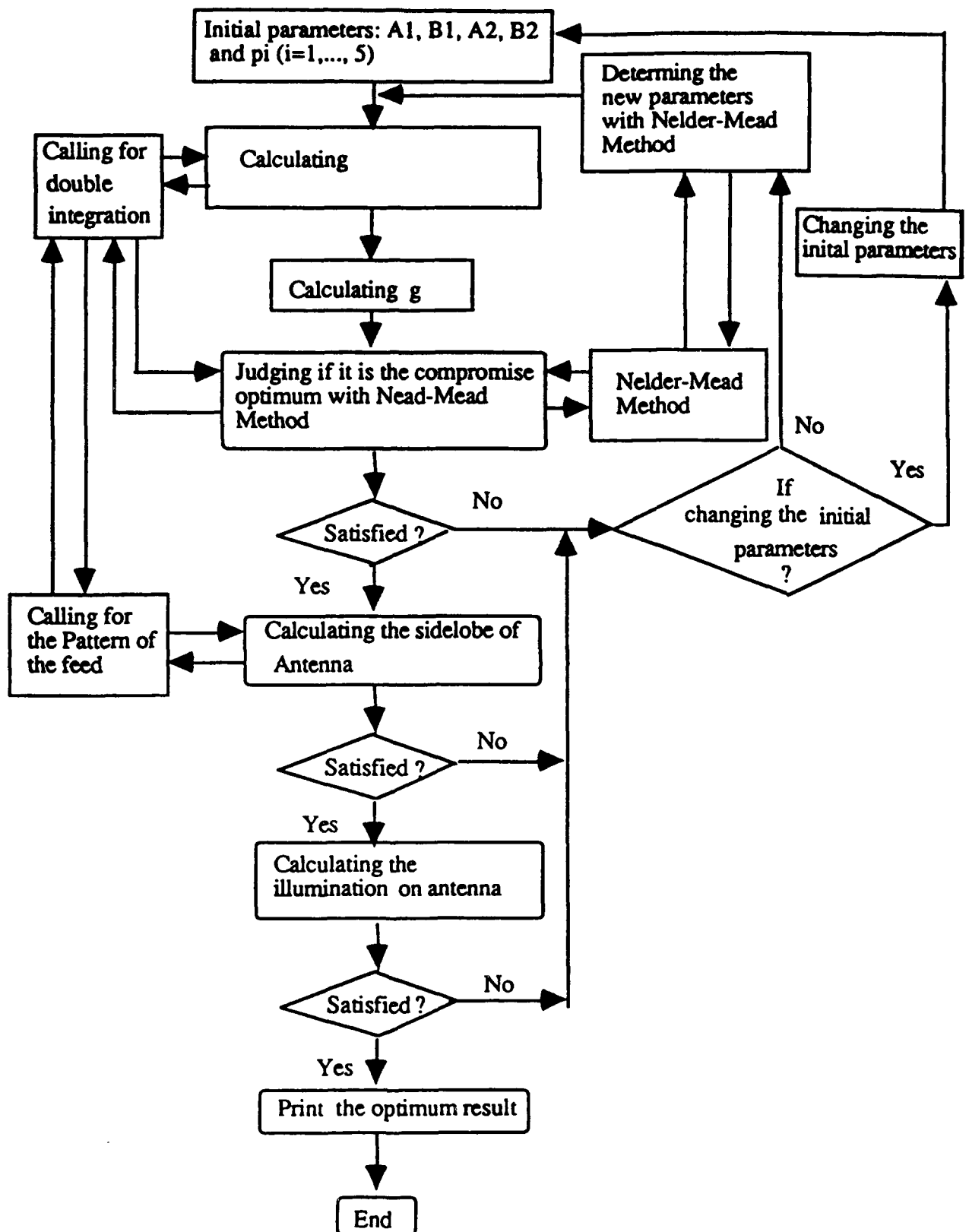
Fig.3 The block diagram of optimum design of antenna and feed system

VIVALDI ANTENNA ELEMENTS FOR MICROWAVE NEURAL NETWORKS

A.D. MACEDO FILHO ⚓ ▱

M.M.MOSSO ∅

A.PODCAMENI ∅

⚓ - Brazilian Navy

▱ - UCL -University College London

∅ - CETUC/PUC RJ - Catholic University of Rio de Janeiro

ABSTRACT

The performance of slotline printed antennas, as the vivaldi, is shown to be shaped by the placement of dielectric overlays and magnetic disks. A survey of those developments is provided and neural systems based on such capability are suggested.

1 - VIVALDI ANTENNAS AND ESM SYSTEMS

The vivaldi antenna has been the topic of several investigations during the past years [1-2]. It presents a series of advantages for phased-array applications, as it it a small, lightweight and easy to manufacture element. However, the main feature that turns such element particularly attractive for ESM systems is its wideband response, typically over 1 octave.

Recently, microwave neural networks have been introduced with the aim to carry out clustering of intercepted radar signals directly through microwave devices [3]. Vivaldi aerials seem to be a natural choice for those adaptive systems; nevertheless, some special features should be investigated in order to allow them to be integral part of the processing structure and not only a receiving element.

For ESM purposes,it is important to determine the polarisation of an incoming radar wave, since the effectiveness of a jammer with improper polarisation is reduced. Furthermore, polarisation measurements can aid the understanding of the radar function, and in the analysis of the received data. Detection of a rotating linear-polarisation may lead to the conclusion that the radar has a conical scan mode, being so a high priority threat. Nonetheless, vivaldi elements are typically linear polarized. this constraint restricts its use and compactness if they are assembled in an eggcrate structure.

This paper provides an insight to the enhancements in the typical vivaldi elements achieved by the authors and introduces its applications to neural systems.

2 - THE VIVALDI AND THE MONZA ELEMENTS

The exponential deigned slotline antenna, the Vivaldi element, was introduced in 197 by Gibson [4]. Nonetheless, a serious problem concerning these elements is their feeding structure. The feeder,

usually a balun, should present an extremely large band. In practice, the problems due to the feeder implementation are most time more critical than those of mounting the antenna itself. This was investigated by comparing a typical exponential element with a parabolic shaped one, denominated Monza, as seen in Fig 1. The performance of both elements were compared using the same feeding device [5].

The first experiment compared the main axis response of four prototypes. Two of them, one vivaldi and one monza were photo-etched over a substrate with ε_r = 4.4 and hight H = .8 mm. The feeders for first two elements were simple coax-to slotline transitions as described by Knorr [6]. In the present case the necessary tuning of this transition was centered in 10 Ghz. Fig 2 shows the response of both elements and it is seen that in spite of the monza aerial have a slightly lower maximum gain, their performance is very close over all the frequency band. If a typical figure of 8 dB gain is searched, an octave coverage from 7 to 14 Ghz is obtained by the two antennas, despite the use of the simple feeder.

The next two prototypes were basically the same, but printed over a higher quality substrate with ε_r = 2.2 and H = .26 mm. The slotline parameters were all obtained empirically as no adequate design procedure was available for slotlines over such low dielectric constant value. Low ε_r dielectrics tend to cause irradiation of the bounded wave on the slotline, this is not desired for circuit applications but is quite useful for antennas.

The feeding structure is the biggest change on these last two prototypes. Now, a broadband microstrip-to-slotline transition with parameters calculated to simulate a Marchand-balun [7] was designed.

The measured results are in Fig 3. Again both devices presented similar performances. for the 8 dB gain threshold, the vivaldi element presents a 6 to 18 Ghz bandwidth while the Monza, in spite of its theoretically less effective design, reaches a 5 to 20 Ghz bandwidth.

3 - GAIN ENHANCEMENT BY DIELECTRIC COMPENSATION

In the original paper, Gibson mentioned that the main requirement for obtaining gain from a vivaldi aerial is that the phase velocity of the bounded wave on the conductors should exceed that in the surrounding medium. in fact, when the dielectric constant of the substrate decreases, meaning larger phase velocity, the gain seemed to increase as well. Then, it is natural to try the other way around and decrease the phase velocity of the environment.This can be done placing a dielectric overlay on these printed elements. So, it was suspected that by covering the antennas with these layers, provided that they are made of low loss materials, there would be a considerable improvement of their performances.

Hence, the two narrow band prototypes, previously described, were covered with teflon and presented the results in Fig 4. A 4 dB gain increment was achieved. Further, a small shift towards frequency was noted. By the same criteria applied before, a 3 to 15 Ghz band is now observed, still maintaining a similar performance.

The remaining pair, was also dielectric loaded and the measured results obtained are in Fig 5. A 3dB increment was verified and by the adopted criteria the bandwidth of both elements surpasses the decade.

Analysing this results, one may find out that the design of those antennas may not be critical , and

positively, the dielectric loading increases the maximum gain of these antennas.

4 - THE ORTHO-MODE QUADRIDGED VIVALDI

Investigations in order to achieve multi-polarisation performances on these elements were conducted next. The simple ortho-mode vivaldi (OMV) antenna was the first result of such efforts [8].

The OMV prototypes were able to cope with all kinds of polarisation since it was composed by a set of two orthogonal vivaldi elements suitably fed by an Ortho-mode Tee (OMT).

The ortho-mode tee applied was a quadridged output port OMT described by Schlegel and Fowler [9]. In the schema of Fig 6, the top ridge of input port 1 is electrically attached to quadridges 1 and 2 of port 3; while the bottom ridge is electrically attached to quadridges 3 and 4. In a similar way, the two ridges of port 2 are electrically connected to quadridges 2 and 3; and 1 and 4 of port 3. This provides two spatially orthogonal E vectors of equal amplitude. A 90 degree phase shift is assured between them by internal construction of the OMT [10].

Such feeder avoids the disadvantages of both microstrip and coax feeders as each element feeding doesn't need to cross the other element's aperture, which would disturb the fields at the cross-over point. An additional advantage is that whatever traditional feeding structure is applied it is necessary to impose a physical off-set between both elements, which would cause distortions in the axial ratio.

Observing the fields in the quadridged port 3, it can be seen that opposite quadridges can be slowly separated just like the vivaldi elements. In fact these ridges can be considered slotlines over air substrate, which has the advantage of having dielectric constant 1.

Two prototypes were assembled. The first one was a fixed structure comprising four aluminium half-vivaldis. This material; has the advantages of being easily machined providing practically no discontinuities and a good exponential shape, its is low weighed and low cost as well. However, aluminium is very difficult to weld, therefore, the solution was to etch the pieces with industrial glue ensuring pressure contact only in the quadridges. the results presented by this prototype are shown in Fig 7

One should note that:

a) the antenna has a better response up to 8.5 Ghz when the mica dielectric overlay was placed. this material is rather lossy for higher frequencies and it was chosen only because of its light-weight compared to teflon and due to the mechanic fragility of this prototype.

b) For a 8 dB gain figure, an operating band larger then 2 to 17 Ghz was obtained.

The second prototype was quite more robust, and was built up using four independent brass parts. the results are shown in Fig 8

One should note that:

a) both responses for prototype 2 are better for f>6 Ghz.

b) the effect of the mica dielectric are quite sensible in the 6 to 11 Ghz band

These prototypes were quite promising, however, the OMT was still a heavy and large block for large array applications. As the dielectric overlay confirmed its usefulness, in spite of the problems concerning to mica, the next step was to apply magnetic overlays.

340

5 - MAGNETIC OVERLAYS FOR VIVALDI ELEMENTS

An alternative method for achieving multi-polarisation performance was investigated inspired by an article of Vartanian [11]. This work suggests that in a traditional rectangular waveguides locally filled with anisotropic ferromagnetic material, the propagation modes became distorted if under a DC transverse magnetic field, becoming into the form

$$E_x(y) = \left\{ \begin{array}{c} \sin \\ \cos \end{array} \right\} (ny) \left\{ \begin{array}{c} \sin \\ \cos \end{array} \right\} (my) \tag{1}$$

The fields in a slotline are very close to those in usual rectangular waveguides. Thus, some similar effect may arise by placing a strong magnet near to one of the edges of the element. The local distortion should disturb the cross-polarisation response of the printed antenna element either by enhancing or suppressing it even more.

The results obtained by practical experience are given in Fig 9 [12] and confirm that the x-pol response is indeed influenced by the placement of a physically small magnet disks close to the border at the front-end edge or at the feeding point. The co-pol response was degraded by less than 1 dB over all the operating bandwidth. the element used in this test was the first $\varepsilon_r=4.4$ coax fed vivaldi element. no law was found to describe the behaviour such performances.

6 - THE MAGVIV ELEMENT

The following move was to verify the performance of a vivaldi element printed over a ferrite substrate [13]. The magviv element, as it was called, has a more accurate design to compensate the intrinsic drawbacks of the substrate. The boundaries of this aerial, shown in Fig 10, are double exponential curves and the wide-open edge covers all the dimension of the substrate, thus, avoiding charge densities that increases the element VSWR. The response of this prototype is given in Fig 11.

7 - VIVALDI ANTENNAS AND NEURAL SYSTEMS

The vivaldi elements were seen to have their performance affected by the placement of dielectric overlays and magnetic materials close to their fringes. This feature may be explored to achieve neural processing in order to cluster radar signals.

These elements can be biased by such simple ancillary devices to weight the incoming signals. in this way, the slotline antennas are now integral part of the signal processing itself. Fig 12 portraits this conceptual subsystem.

The training of such structures is rather clumsy, as the parameters are not constant over the entire frequency band, and changes are not well described mathematically and so a numerical approach is necessary. There are many local maximums for the empirical function to be optimised, hence, a procedure based on genetic algorithms [14] are likely to overcome this problems and is currently under investigation. The size, place and dielectric constant of the overlay ,besides, the position and the

strength of the magnetic disks are typical variables. Moreover, several overlays or magnetic disk can be applied.

8 - CONCLUSION

Vivaldi antenna elements are shown to be quite easy and simple to assembly. Octave, and even decade, bandwidths were achieved using dielectric overlays. Their shape has also been verified not to be critical.

It was also verified that their performance is quite easy to be shaped, although being quite difficult to tune exactly to desired figures. Nonetheless, with the development of model-free optimization procedures, as genetic algorithms,in which no a priori knowledge or mathematical formulation about the diverse parameter interactions are necessary, is promising.

9 - ACKNOWLEDGMENTS

10 - REFERENCES

1. Schaubert, D.H. (1969) Endfire Tapered Slot Antenna Characteristic. Paper presented at the ICAP Conference-IEE, London U.K.
2. Yngvesson, K.S.; et alli (1989) The tapered Slot antenna- a new integrated element for millimeter-wave applications, IEEE Transactions MTT 37 (no. 2): 365-374
3. Macedo F., A.D.; & Griffiths, H.D. (1993) High performance microwave neural net-antenna array for radar signal clustering. Paper presented at the Antenna Application Symposium, Allerton Park Monticello Illinois USA.
4. Gibson, P.J. (1979) The vivaldi aerial. Paper presented at the 9[th]European Microwave Conf., Brighton U.K.
5. Macedo F., A.D.; Podcameni, A.; & Mosso, M.M. (1986) A dielectric overlay slotline printed antenna. Presented at the JINA, Nice France
6. Knorr, K.B. (1974) Slotline transitions, IEEE Transactions MTT 22 pp:548-554
7. Marchand, N. (1944) Transmission Line Convertion, Electronics (Dec) pp:142-145
8. Macedo F., A.D.; & Mosso, M.M. (1989) Ortho-mode vivaldi antennas for agile polarization systems. Presented at the ICAP, London U.K.
9. Schlegel, H.; & Fowler, W. D. (1984) The ortho-mode transducer offers a key to polarisation diversity in EW systems, MSN (Sept) pp: 65-70
10. Boifot, A.M.; Lier, E.; & Schaug-Pettersen, T. (1990) Simple and broadband orthomode transducer, IEE Proceedings 137 pt H (No 6) pp:396-400
11. Vartanian, P.H.; & Jaynes, E.T. (1956) Propagation in ferrite-filled transversely magnetized waveguide, IRE Proceedings pp:140-143

12. Macedo, A.D.; & Mosso, M.M. (1991) Cross-polarization performance of vivaldi antennas in DC transverse magnetic fields. Paper presented at the 21StEuropean Microwaves Conf., Stuttgart Germany

13. Macedo F, A.D.; & Mosso, M.M. (1992) The design of printed slotline antennas over ferrite substrates and their performance under DC magnetic fields. Paper presented at the JINA Conf., Nice France

14 Goldberg, D.E. (1989) Genetic algorithms in search, optimization & machine learning, Addison-Wesley, Reading MA USA

(a)   **(b)**
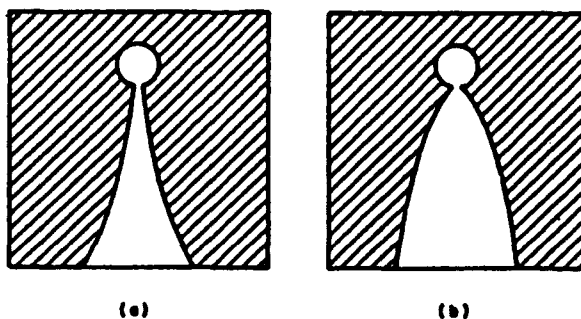
Fig. 1 - Slotline Printed Antennas

    (a) - Classical Vivaldi Aerial with Exponential Design

    (b) - Suggested Monza Aerial with Parabolic Design.
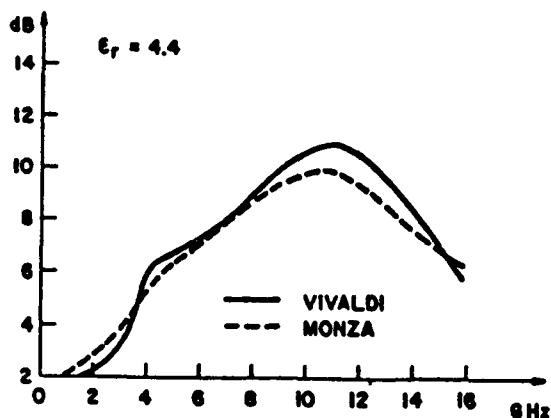
Fig. 2 - Comparison Between the Maximum Gain Obtained from a Vivaldi and a Monza Aerial Using a Narrow-Band Balun Feeder.
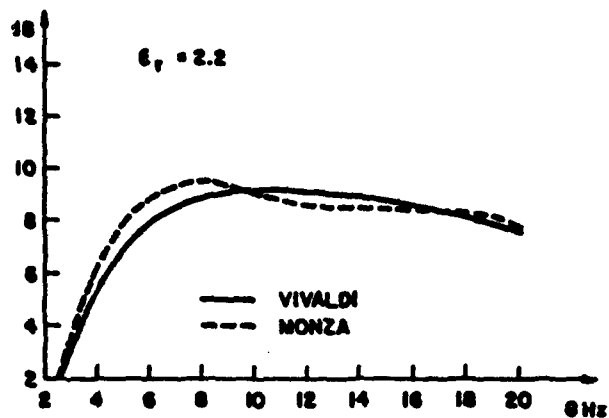
Fig. 3 - Comparison Between the Maximum Gain
Obtained from a Vivaldi and a Monza
Aerial Using a Broad-Band   Balun
Feeder.
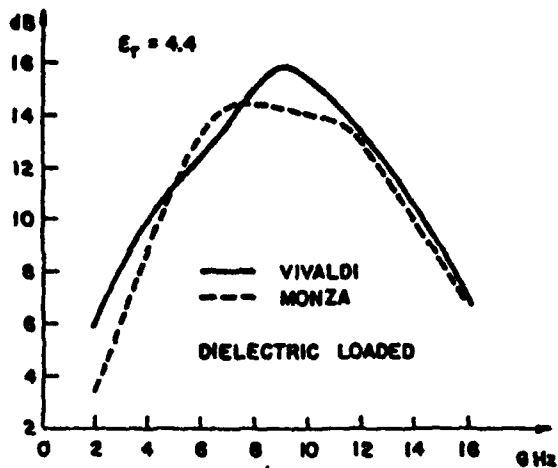
Fig. 4 - Printed Narrow Band Antennas Covered
with Teflon-Gain Obtained
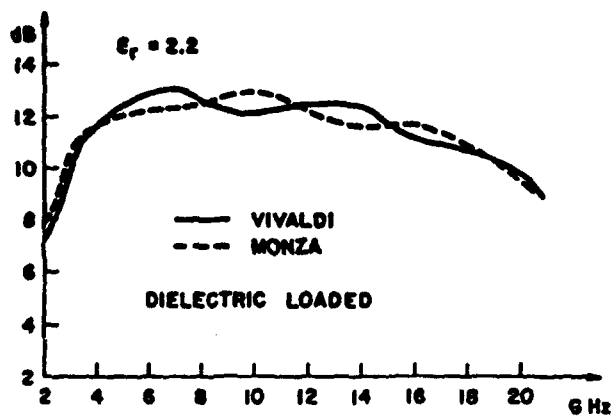
Fig. 5 - Printed Broad-Band Antennas Covered
with Teflon-Gain Obtained

344

VIVALDI
AERIALS

OUT 3
IN 1

OUT 3
IN 2

PORT 1   PORT 3
    TOP RIDGE   QUADRIDGE 1

    BOTTOM RIDGE   QUADRIDGE 2

PORT 2
    TOP RIDGE   QUADRIDGE 3

    BOTTOM RIDGE   QUADRIDGE 4
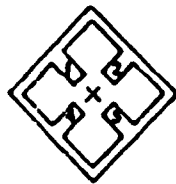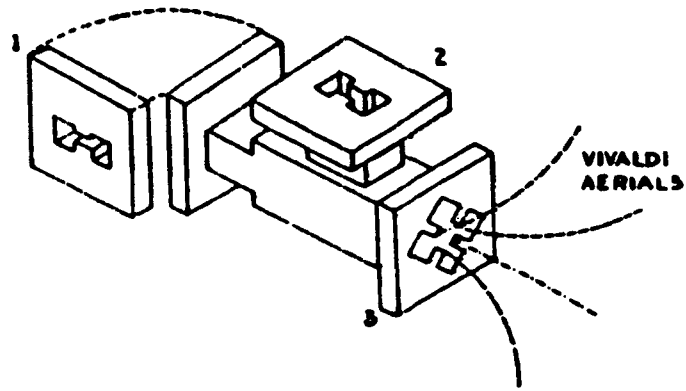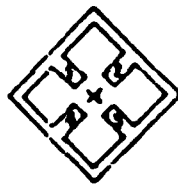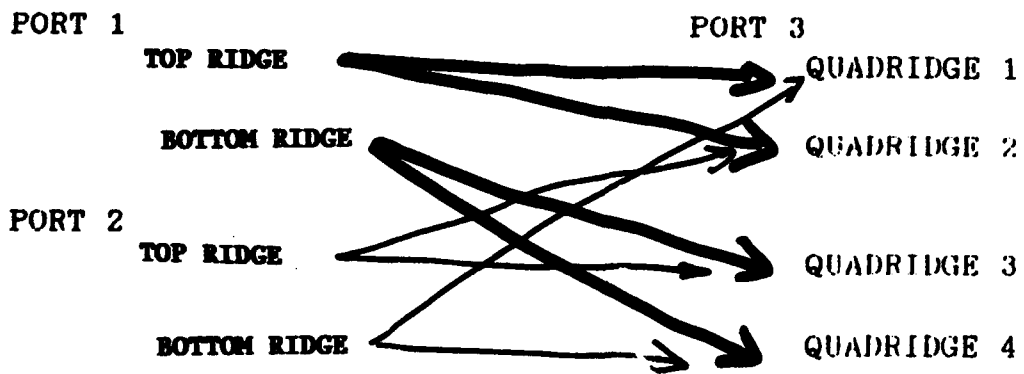
Fig 6-   The Ortho-Mode Vivaldi Aerial (adapted from [9])

gain (dB)

pure
w/mica

freq

gain (dB)

pure
w/mica

freq

return loss (dB)

20

10

freq

return loss (dB)

20

10

freq
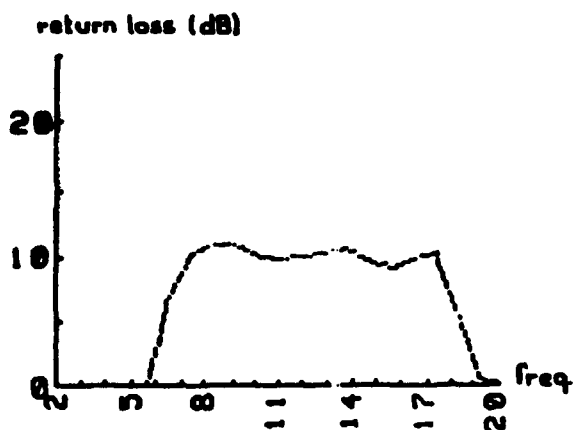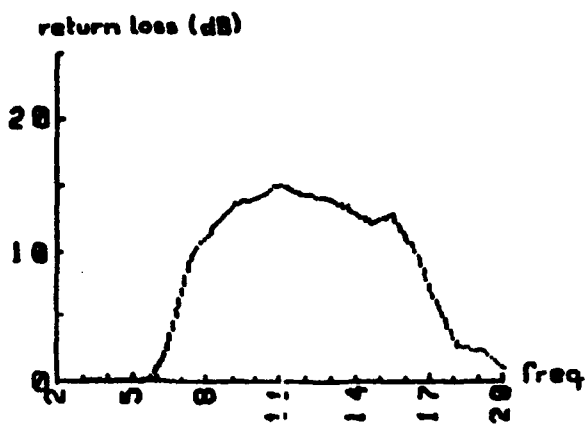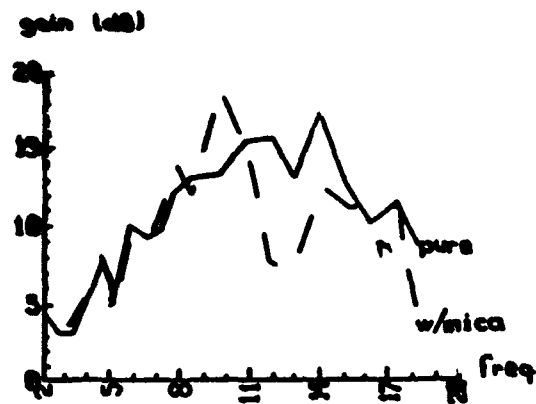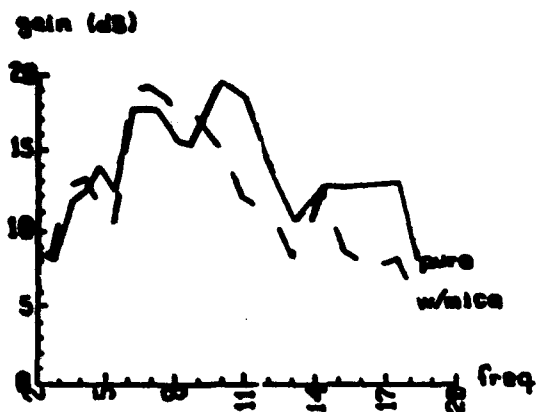
Fig 7-   Results of Prototype 1   Fig 8 -   Results of Prototype 2

Gain Increment for 2 Magnetic Disks
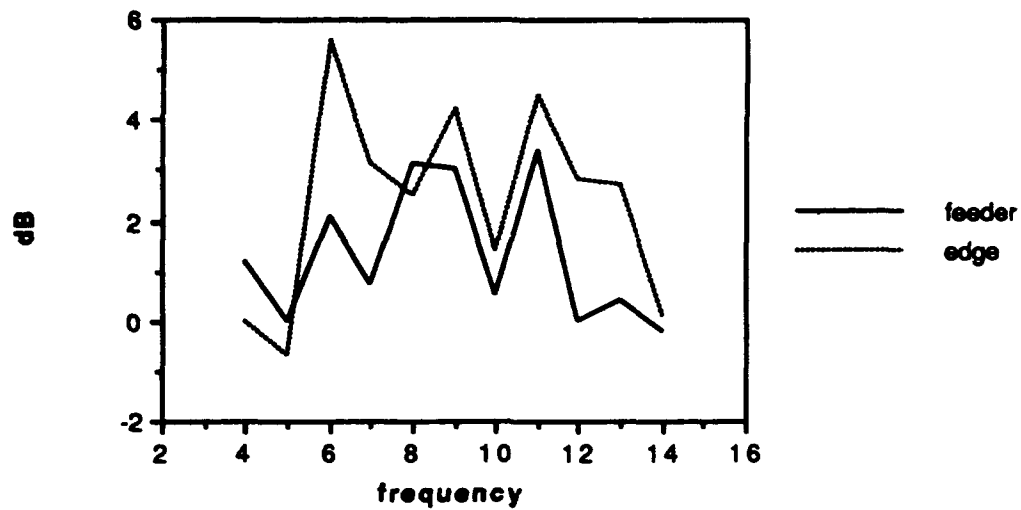
Gain Increment for 3 Magnetic Disks

DISCO MAGNÉTICO

LINHA COAXIAL
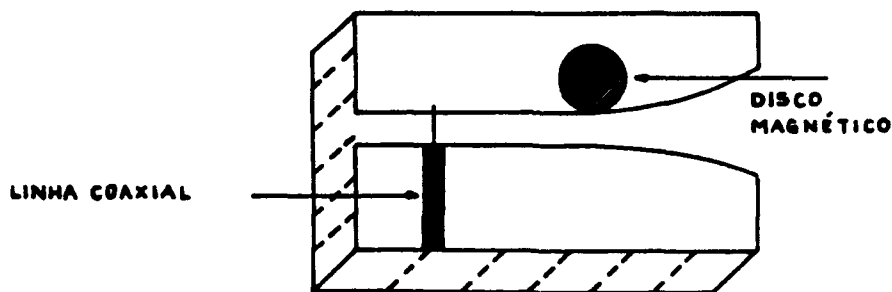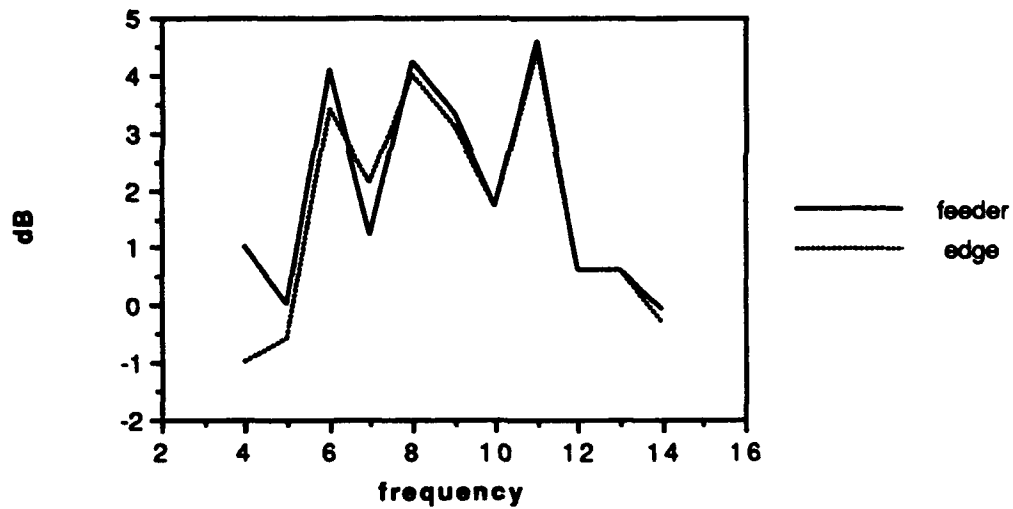
Fig 9- Results Obtained by Simple Vivaldi Element printed over 4.4 dielectric constant substrate and feeded by coax cable when under DC magnetic field

347
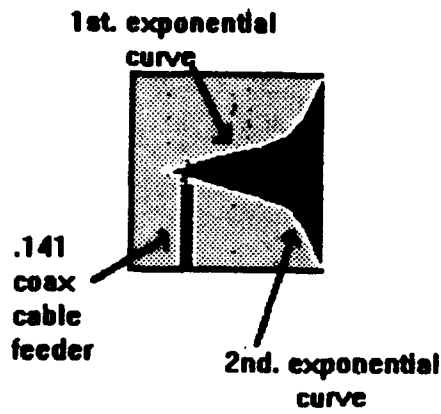
Fig 10- Magviv Element Design
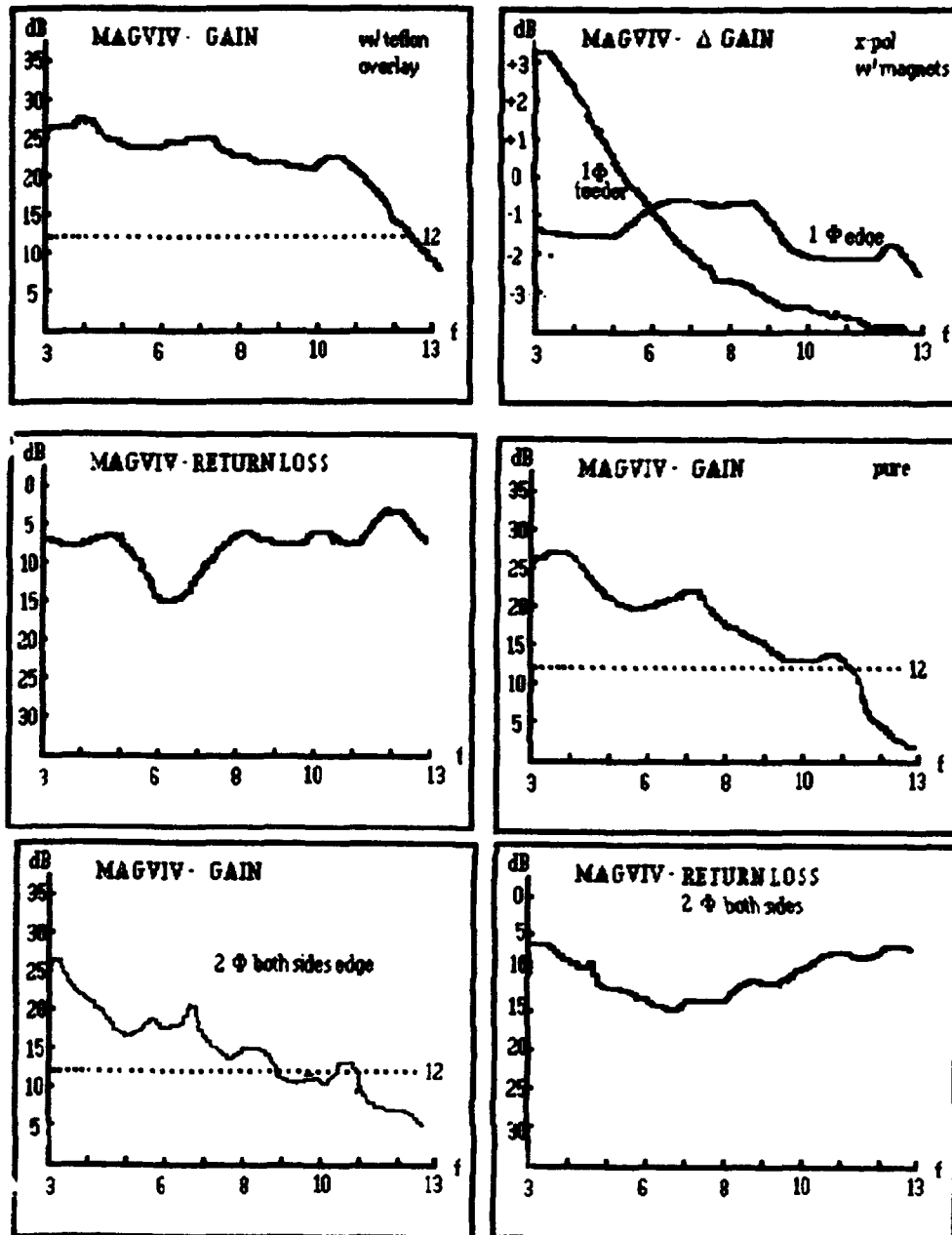
Fig 11--Magviv Element Results

LINEARLY TAPERED SLOT ANTENNAS AND FEED NETWORKS

Richard Q. Lee and Rainee N. Simons

NASA Lewis Research Center

MS 54-8

Cleveland, OH 44135

ABSTRACT

Linearly tapered slot antennas (LTSAs) have been demonstrated to have higher element gains and broader bandwidths than patch antennas, and are therefore more suitable for use in arrays of 'brick' configurations. Recently, the LTSA has been studied for possible communications applications. This research efforts involve the evaluation and enhancement of the performance of both the planar and non-planar LTSAs. Specifically, the effects of superstrates and the antenna dimensions on the radiation characteristics of the LTSA have been experimentally investigated. New feeding techniques with coplanar waveguide feeds have also been developed and demonstrated on arrays with LTSA elements. In the paper, we will present and discuss our experimental findings.

1.0 INTRODUCTION

Linearly tapered slot antennas have been developed for potential millimeter-wave applications; e.g., as radiating elements for reflector or lens antennas. Compared to patch antennas, the LTSA has higher element gain, broader bandwidth and less spatial constraint for solid state device integration [1]. Although LTSA has been studied by several investigators [2,3], most of these studies are on LTSA of planar geometry excited through a microstrip-to-slotline transition. The microstrip feeding approach generally has very limited bandwidth promting the need to develop new feeding techniques. Recently, coplanar waveguide (CPW) has emerged as an alternative to microstrip line because of its many advantages [4]. In this paper, we introduce four new techniques: three for exciting planar LTSAs with coplanar waveguide and one for exciting non-planar LTSAs with balanced microstrip feed. This paper will summarize the study results including the effects of various feeding techniques, superstrate and antenna dimensions on the performance characteristics of both planar and non-planar LTSAs. To investigate integration of MMICs with LTSAs, a 1x4 array and a 3-element active space-fed array with non-planar LTSA elements have also

been studied.

2.0 ANTENNA AND FEED DESIGN

The three CPW feeds developed for exciting the planar LTSAs are shown in Figures 1-3. As indicated in Fig. 1, the planar LTSA is excited with a finite coplanar waveguide feed (FCPW) [5]. The LTSA and the FCPW are etched on opposite sides of the substrate with the finite ground plane of the CPW tapered and connected to the antenna ground plane through via holes to ensure good impedance match and odd mode operation. The LTSA with length L=6.6 cm and taper angle $2\alpha=11.2°$ is formed by gradually increasing the width of the slotline from its feed end to an open end of width H. Power is coupled to the antenna through the center conductor of the CPW which is extended to form a CPW-to-slotline transition with the LTSA. To provide a smooth transition, the slotline at the feed end has a circular bend instead of a right angle bend.

Fig. 2 illustrate another feeding approach with the FCPW placed at a right angle to the slotline of the LTSA. To improve coupling, two notches of width W and lengths L_1 and L_2 are cut out from the FCPW ground plane located right above the slotline of the LTSA. A

pair of bond wires are attached to both sides of the notch to suppress any spurious slotline modes generated at the discontinuity. The FCPW and the slotline are terminated in short circuits.

Figure 3 shows a third approach for exciting a planar LTSA with an air bridge. Power is coupled to the antenna through a 0.00508 cm wide gold ribbon which bridges over the slotline connecting the open end of the CPW to the opposite edge of the slotline. The LTSA is same as the one shown in Fig. 1.

One disadvantage of planar LTSA is that the slotline feeding the antenna is difficult to fabricate for matching to a 50 Ohms input, especially if the substrate is of low dielectric permittivity [6]. Unlike the slotline, the balanced microstrip is relatively easy to realize wideband impedance matching. Figure 4 shows a non-planar LTSA excited by a balanced microstrip. The non-planar LTSA is formed by gradually flaring the strip conductors of the balanced microstrip on opposite side of the substrate by an angle $\alpha=5.3°$ with respect to the antenna axis. The feed structure consists of a conventional microstrip on a dielectric substrate of thickness D with the ground plane tapered to the strip width W (0.071cm) to form a balanced

microstrip. The characteristic impedance of the balanced microstrip is chosen to be the same as the input impedance of the LTSA which is approximately 160 Ohms. The electric field distributions at various cross sections are shown in Fig. 5.

Using of non-planar LTSA as array elements has never been attempted, and little is known about its peformance. In our experiment, we studied the performance characteristics of two non-planar LTSA arrays: a 4-element linear array (Fig.6) and a 3-element active spaced-fed array (Fig.7). The active array is formed by integrating MMIC amplifiers (10 dB gain) with the non-planar LTSA elements.

3.0 RESULTS AND DISCUSSIONS

The measured return losses and input impedance for the planar LTSA excited by coupling to the center strip of the FCPW is shown in Fig. 8. which indicates a 2:1 VSWR bandwidth of 20 GHz over a frequency range of 10-30 GHz. Similar return loss results were obtained for the planar LTSAs excited with an air bridge and notch electromagnetic coupling. These results are displayed in Fig. 9. The measured E- and H-plane patterns for the planar LTSA with center strip coupling and those with

air bridge and notch electromagnetic coupling are shown in Figures 10 and 11 respectively. These results indicate that the LTSA excited by FCPW feed has ultra wideband characteristics and excellent far-field patterns.

For the planar LTSA, the effects of superstrate and antenna lengths on the directivity have also been studied. In the experiment, a superstrate was placed over the LTSA and the beamwidths were measured as a function of frequencies and antenna lengths. The results as indicated in Fig. 12 show that the superstrate improves the directivity by increasing the electrical length and effective aperture of the antenna. Thus, the use of a superstrate can reduce the physical length of the antenna without compromising its directivity.

The measured return loss for the non-planar LTSA is shown in Fig. 13. The return loss is observed to be better than -10 dB (2:1 VSWR) over a frequency range extending from 8 to 32 GHz, a significant improvement over the LTSA reported in reference [7]. As with the planar LTSA, the directivity of the non-planar LTSA was experimentally observed to be inversely proportional to its length. The measured radiation patterns for three different frequencies are shown in Fig. 14. The patterns appear symmetrical over a wide frequency band.

The H-plane cross-polarized radiation was found to be -16 dB below that of the copolarized radiation.

In the array experiment,we have demonstrated the non-planar LTSAs in two different configurations. Figure 15 shows the measured radiation patterns for a 4-element linear array fed by a microstrip corporate feed network. As shown, the array exhibits excellent pattern characteristics with sidelobe levels of -14 dB for the E-plane and -18 dB for the H-plane. In the second experiment with the 3-element active space-fed array, the non-planar LTSA elements at the input terminals are space-fed from a horn while those at the output terminals radiate into free space. The free space radiation is picked up by a second horn in the far field. In the setup, the two horns are orthogonally polarized but the LTSAs are oriented to have the same polarization as their respective horn antennas. Thus, good isolation between the transmitting and the receiving horn antennas is established. The measured radiation patterns are shown in Fig. 16 with the amplifiers turned ON and Off. Results indicate an increase in gain of more than 30 dB for the H-plane pattern and over 25 dB for the E-plane pattern with the amplifiers turned ON. These values are in good agreement with the mea-

sured gain of the amplifiers. The gain is lower for the E-plane case because the LTSAs on either side of the center element are excited with a lower amplitude due to the amplitude taper of the electrical field distribution of the transmitting horn. We have also demonstrated harmonic generation with the 3-element active space-fed array by driving the amplifiers to operate in the nonlinear region. The transmit horn radiates at the fundamental frequency of 8.95 GHz. To receive the second harmonic power, we used a horn which cuts off at the fundamental frequency. Fig. 17 shows the measured pattern at 17.9 GHz with the amplifiers turned ON and OFF. With the amplifiers OFF, the horn measured only the noise pattern. The second harmonic signal is 50 dB above the noise.

4.0 CONCLUSION

This paper presents four new feeding techniques, three for exciting planar LTSAs with CPW feeds and one for exciting non-planar LTSAs with balanced microstrip feeds. LTSAs excited by these new feeding techniques were found to have ultra wide-band characteristics and excellent radiation patterns. The directivity of the LTSAs was found to increase with superstrates and

decrease with reducd antenna lengths. Two arrays, a 4-element linear array and a 3-element active space-fed array, with non-planar LTSA elements have been demonstrated and found to have excellent radiation characteristics.

REFERENCES

1. Yngvesson,K.S., Korzeniowski, T.L., Kim, Y.S., Kollberg, E.L. and Johnson J.F. (1992) The tapered slot antenna-anew integrated element for millimeter-wave applications, IEEE Trans. MTT., 37 (No. 2): 365-374.

2. Kim, Y.S. and Yngvesson, K.S. (1990) Characteriza tion of tapered slot antenna feeds anf feed arrays, IEEE Trans Ant. & Propagation, 38 (No.10): 1559-1564.

3. Kooi, P.S., Yeo, T.S. and Leong, M.S. (1991) Para metric studies of the linearly tapered slot antenna (LTSA), Microwave & Optical Tech. Lett., 4 (No. 5): 200-207.

4. Wen, C.P. (1969) Coplanar waveguide: A surface strip transmission line suitable for nonreciprocal gyro magnetic device applications, IEEE Trans. Microwave Theory Tech., Mtt-17 (No. 12): 1087-1090.

5. Simons, R.N. and Lee, R.Q. (1992) Coplanar waveguide aperture coupled patch antenna with ground plane/ substrate of finite extent, Electronics Lett. 28 (No. 1): 75-76.

6. Gazit E. (1988) Improved design of the vivaldi antenna, IEE Proceedings pt. H, 135 (No. 2): 89-92.

7. Nesic, A. (1991) Enfire slot line antennas excited by a coplanar waveguide, IEEE AP-S Inter. Symposium Digest, 700-702
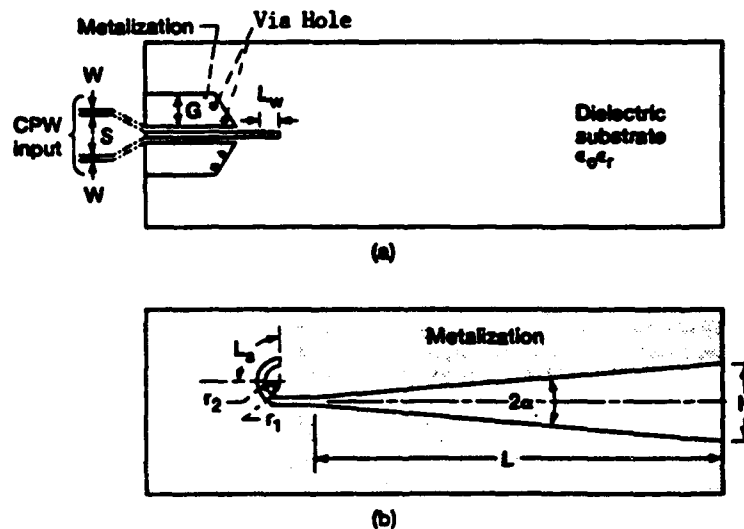
Figure 1. Schematic for the LTSA and the FCPW feed circuit: (a) top metalization /feed layer, S=0.762 mm, W=0.254 mm, G=5.08 mm, L_w=2.951 mm ϵ_r=2.2, and (b) bottom metalization/antenna layer, r_1=2.171 mm, r_2=2.425 mm, L_s=3.43 mm.
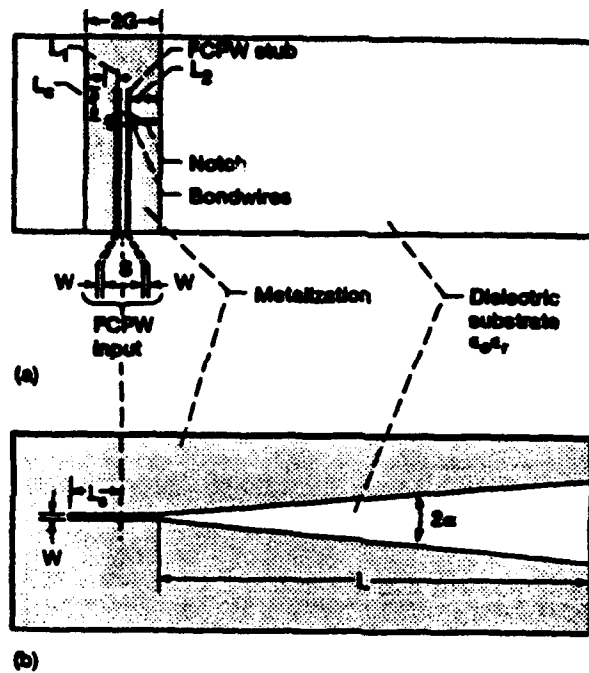
Figure 2. Schematic for the LTSA and the electromagnet
ically coupled FCPW feed:
(a) top metalization, S=0.762 mm, W=0.254 mm
$L_2=3L_1=\lambda_{g(slot)}/4$, $2G=0.65\lambda_{g(cpw)}$, $L_c=0.4\lambda_{g(cpw)}$
(b) bottom metalization.
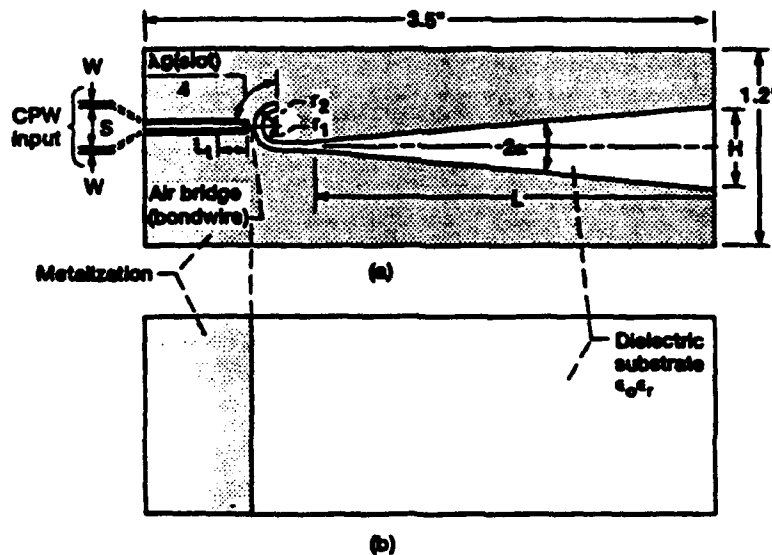
Figure 3. Schematic for the LTSA with an air bridge/CPW
feed: (a) top metalization, S=0.762 mm,
W=0.254 mm, and (b) bottom metalization.
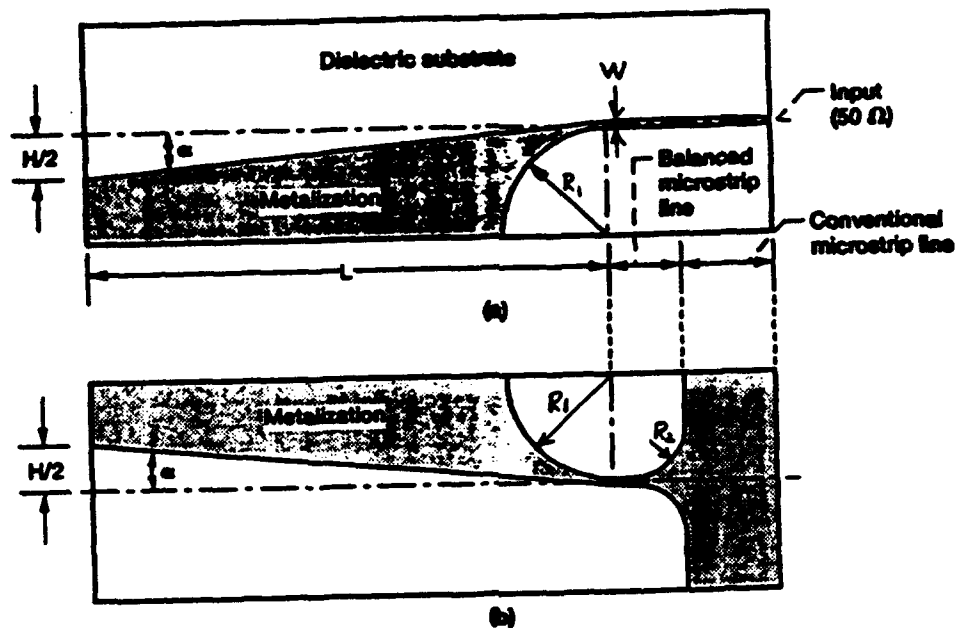
Figure 4. Non-planar LTSA and feed network: (a) top metalization, $L=4.3\ \lambda_o$, $H=0.75\lambda_o$, $\epsilon_r=2.2$, and (b) bottom metalization, $R_1=0.9\lambda_o$, $R_2=0.5\lambda_o$.
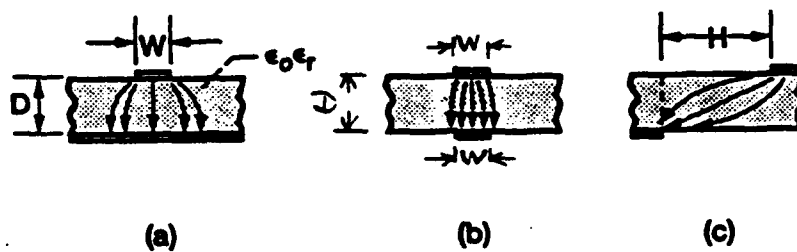
Figure 5. Electric field distributions at various cross sections: (a) Conventional microstrip, (b) balanced microstrip and (c) antenna radiating edge.
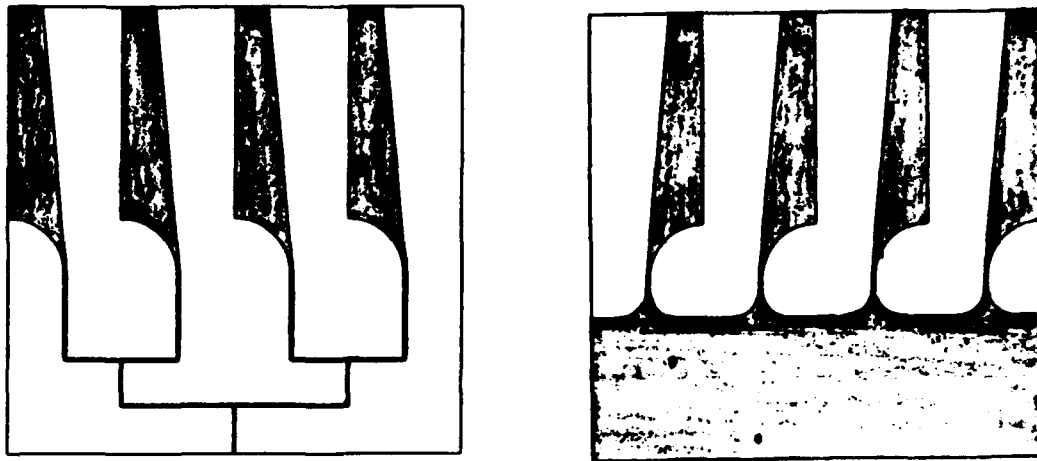
(a)

(b)

Figure 6. 1x4 array with non-planar LTSA
(a) Top metalization
(b) Bottom metalization
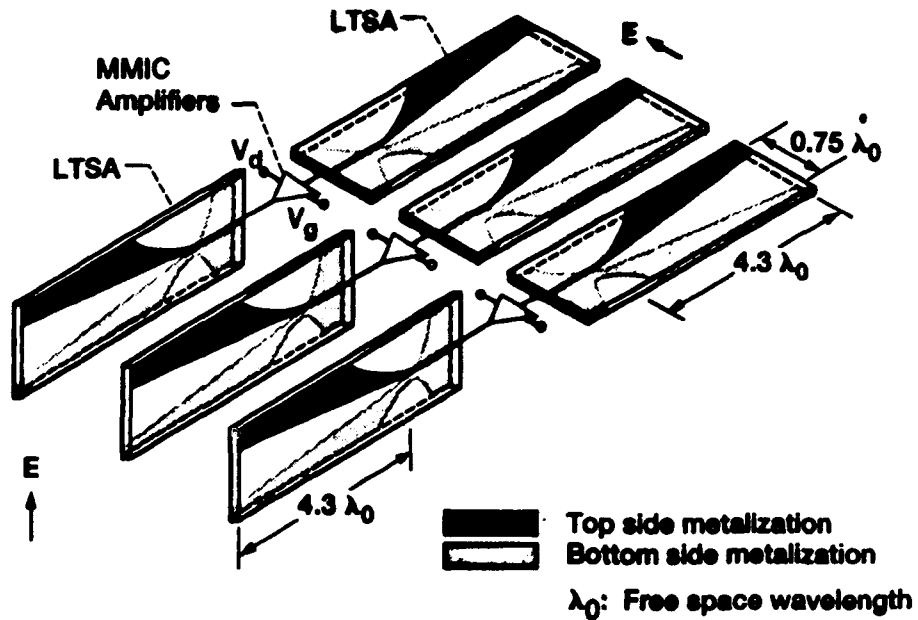
Figure 7. Schematic illustrating the 3-element active
array with non-planar LTSA elements (λ_o: free
space wavwlength).
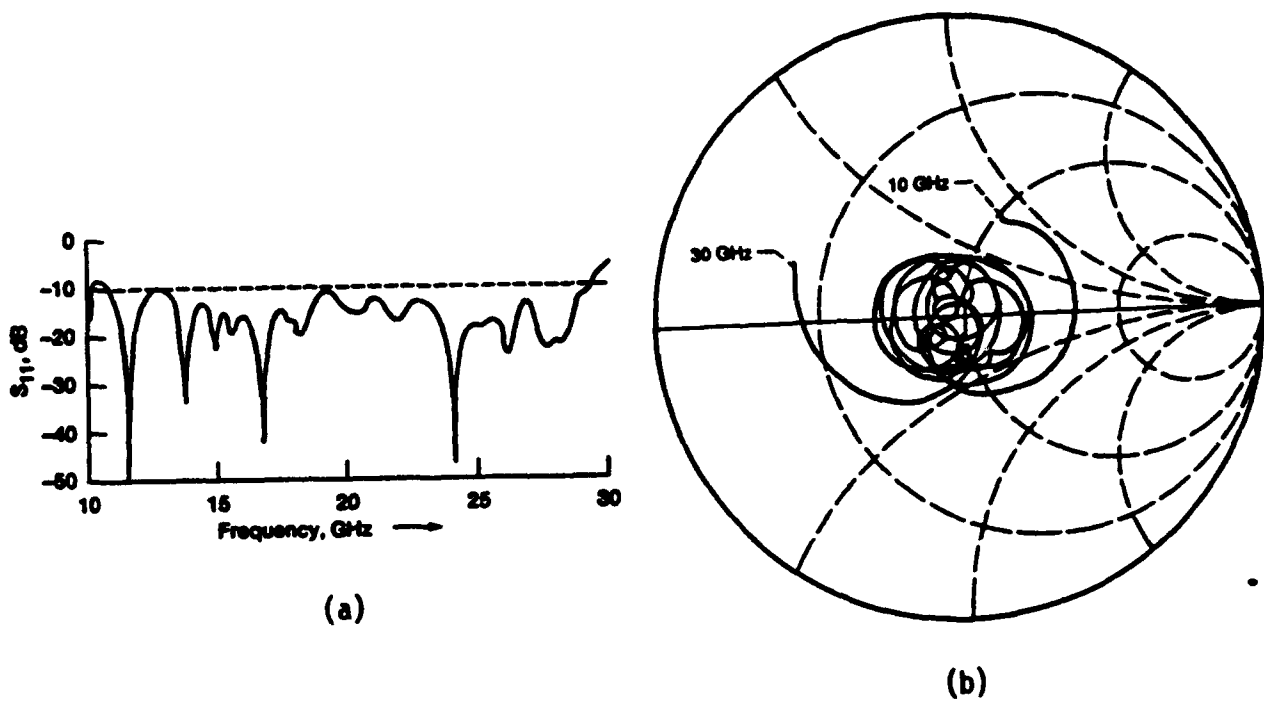
Figure 8. Measured return loss and input impedance for center strip coupled LTSA:
(a) S_{11} magnitude vs. frequency.
(b) Smith chart plot of input impedance vs. frequency.
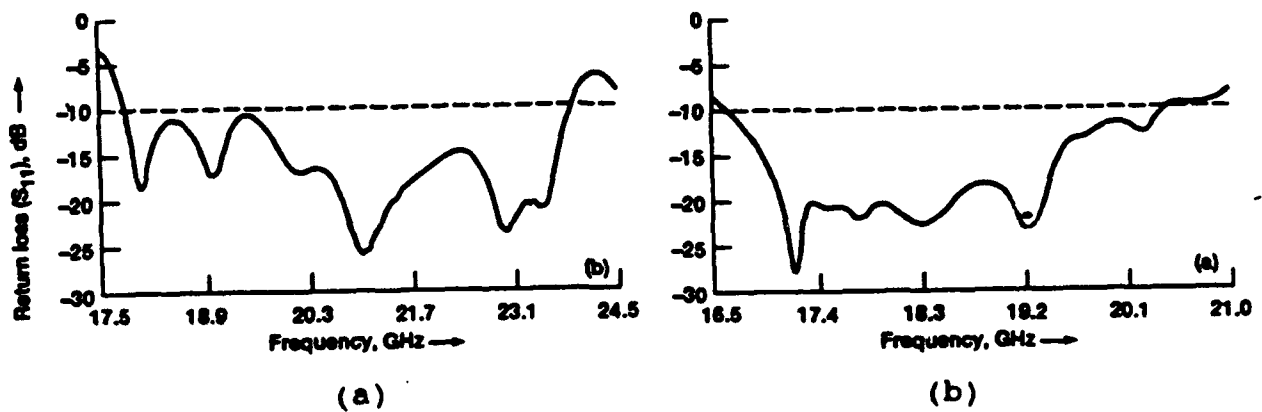
Figure 9. Measured return loss at the CPW port
(a) Air bridge feed.
(b) Electromagnetically coupled feed
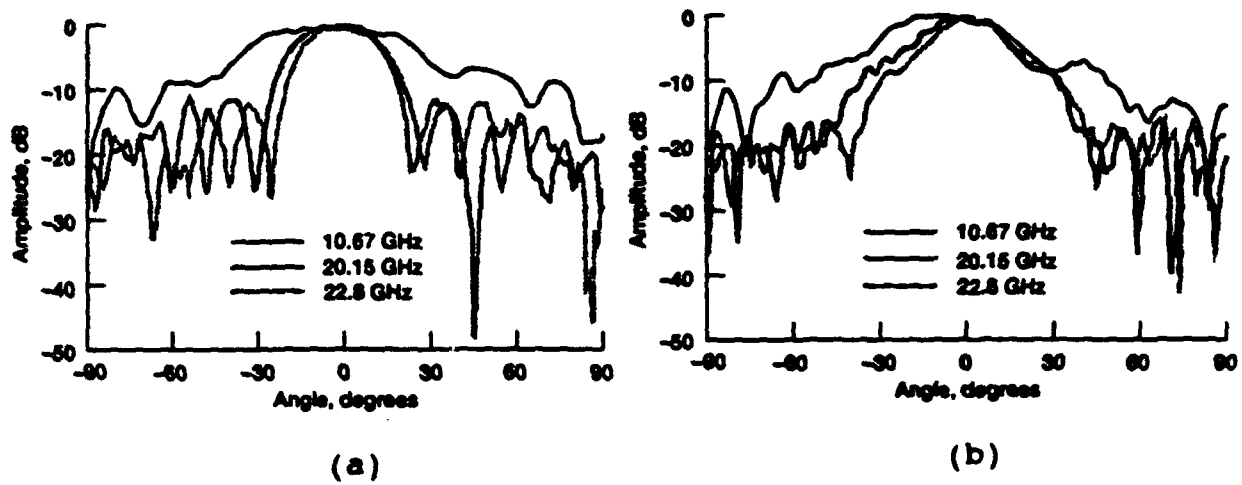
Figure 10. Measured radiation patterns for the LTSA
with center strip coupled feed.
(a) H-plane
(b) E-plane
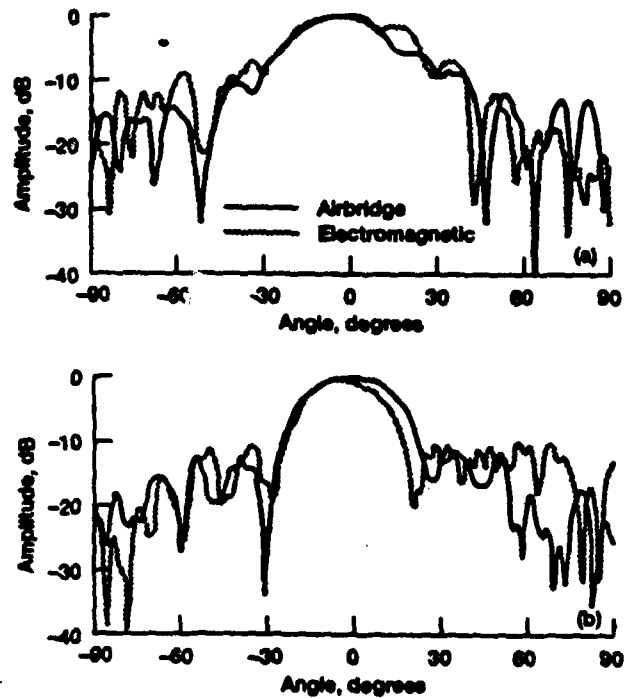
Figure 11. Measured radiation pattern of the LTSA with
air bridge and electromagnetically coupled
feed.
(a) E-plane
(b) H-plane
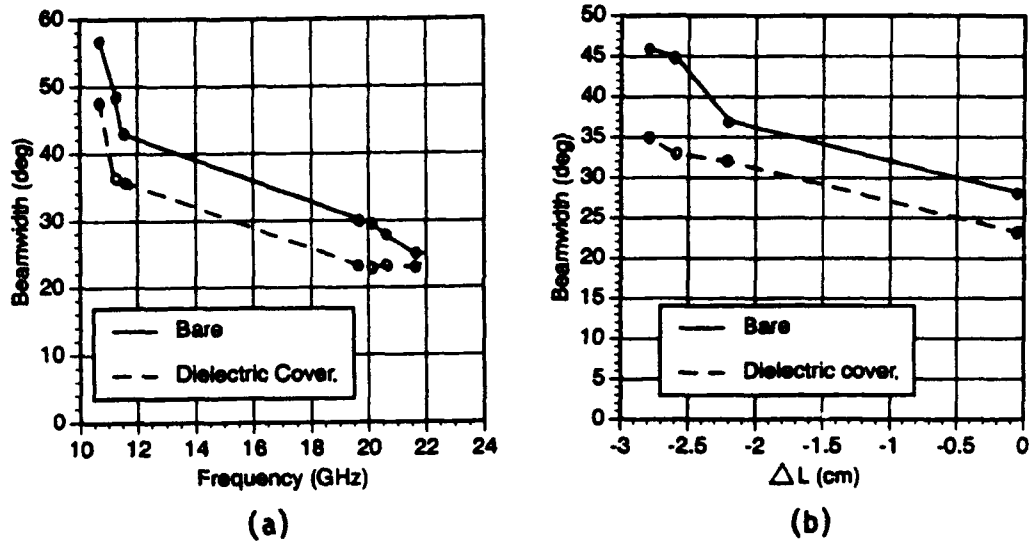
Figure 12. Measured beamwidth vs. (a) frequency and (b)
reduced lengths (11 GHz) for the LTSA with
and without superstrate.
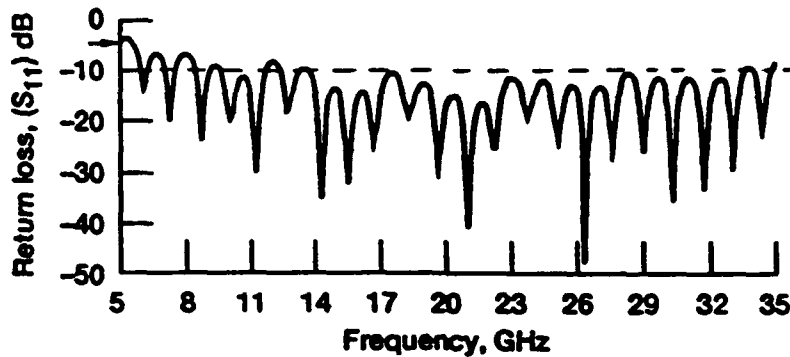
Figure 13. Measured return loss for the non-planar LTSA
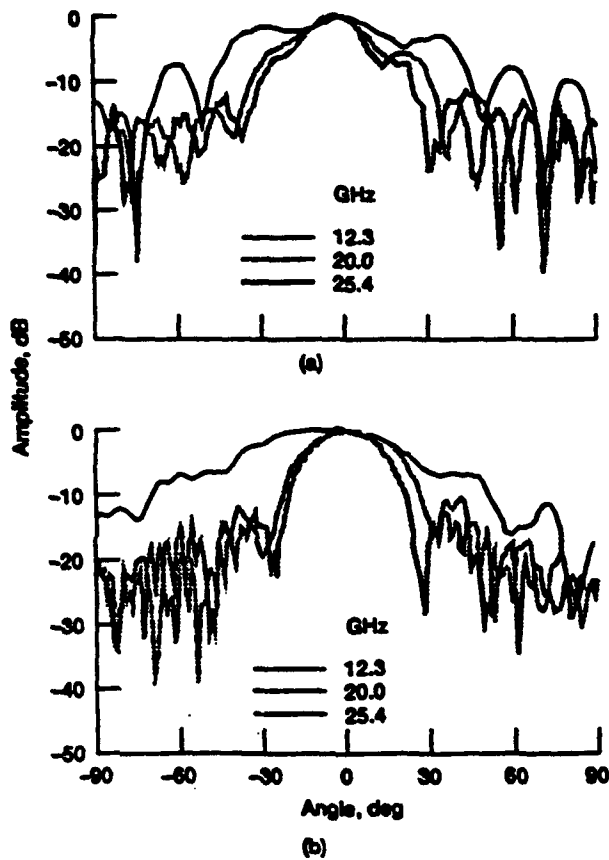
Figure 14. Measured radiation patterns for the non-
planar LTSA:
(a) E-plane
(b) H-plane
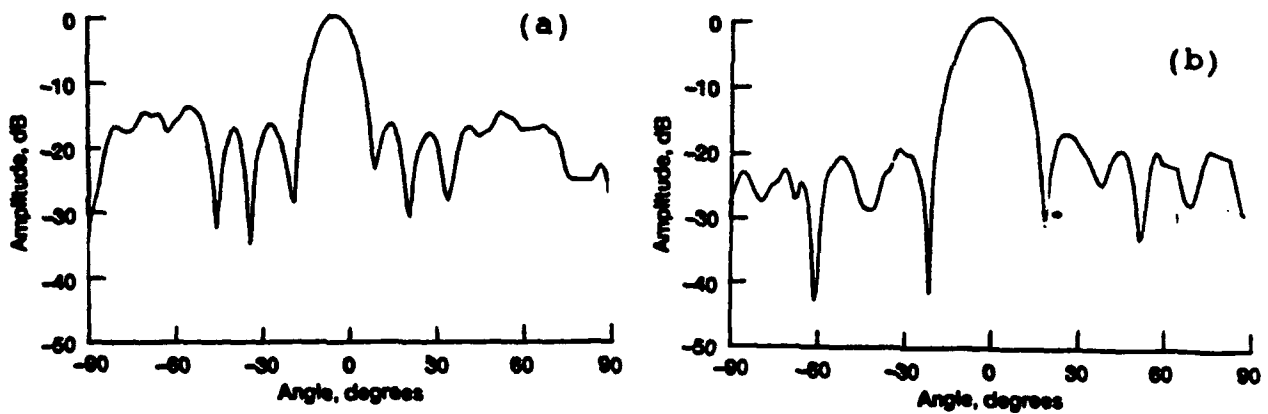
Figure 15. Measured radiation patterns for a 1x4 array
with non-planar LTSA elements:
(a) E-plane
(b) H-plane
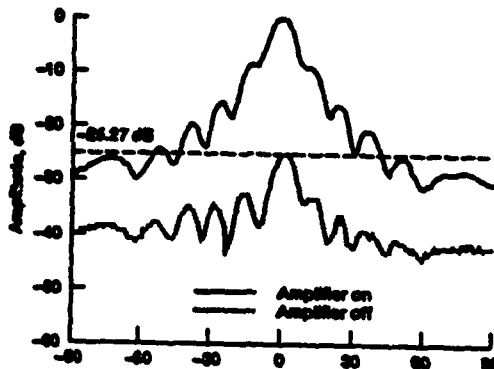
Figure 16. Measured radiation pattern of the horn antenna showing space power amplification.
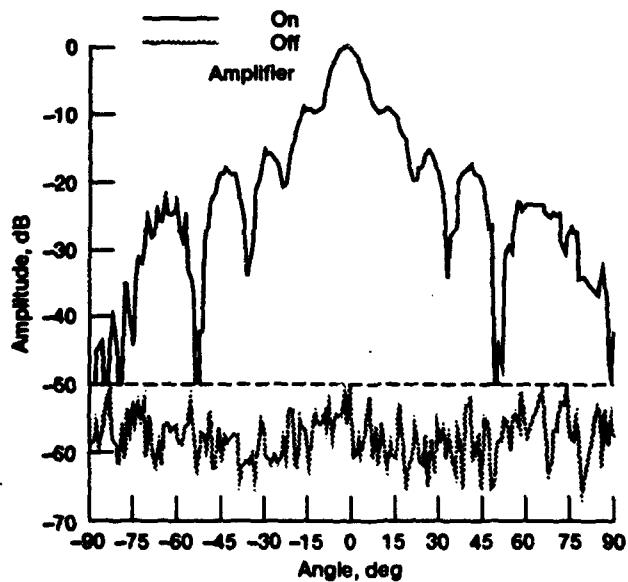
Figure 17. Measured radiation pattern of the horn antenna showing second harmonic generation.

LAND MOBILE SATELLITE VEHICULAR ANTENNA DEVELOPMENT AT JPL

A. Densmore, V. Jamnejad, A. Tulintseff, J. Huang,
R. Crist, K. Lee, L. Sukamto and W. Chew

Jet Propulsion Laboratory
California Institute of Technology
Pasadena, CA 91109
(818) 354-4733

ABSTRACT   This paper describes the design and performance of a series of vehicle antennas developed at JPL for mobile communications with geostationary satellites. Several antennas have been developed, both in support of an emerging L-band U.S. Land Mobile Satellite Service (LMSS) system and most recently in support of K- and Ka-band mobile communications studies using NASA's Advanced Technology Communications Satellite (ACTS). The designs and performance measurements of the antennas are presented. The developments are presented chronologically.

1. INTRODUCTION

The emerging L-band LMSS system will provide telephone and data services for a variety of users across the Continental United States (CONUS), supplementing the existing cellular telephone service. Vehicle antennas of significantly higher performance than the simple whip antenna used for cellular telephones are needed to establish the communications link between a mobile vehicle on the ground and an LMSS satellite. JPL has been sponsored by NASA to conduct research in this field, to demonstrate system capabilities, and to transfer this technology to U.S. industry. Since the early 1980's JPL has developed a family of L-band vehicle antennas to meet the requirements of diverse potential users of such a LMSS system. These antennas are required to be circularly polarized and provide coverage from 20-60 deg elevation above the horizon and continuous azimuth coverage (360 deg). Circular polarization alleviates polarization misalignment due to Faraday rotation and geographically dependent orientation. The antennas are required to operate in the L-band frequency bands of 1.5450-1.5590 GHz (downlink) and 1.6465-1.6605 GHz (uplink). Several low-

gain omni-directional and medium-gain steerable antennas have been developed and tested in field trials. JPL has equipped a van and a sedan for installation of these antennas along with a communications terminal to conduct the field trials. The field trials have been conducted across the U.S. and in Australia with the cooperation of other institutions such as the Australian Satellite organization (AUSSAT), the Federal Communications Commission (FCC), the International Maritime Satellite organization (INMARSAT) and several American universities. Aided by the research and field trials conducted by JPL, a commercial market has evolved, and the FCC has granted operational licenses to companies such as the American Mobile Satellite Corporation (AMSC) and Westinghouse. In 1992 Westinghouse issued a request for proposals for a commercial vehicular antenna system.

Now that the L-band LMSS system concept has commercialized, JPL has subsequently addressed the technologies required of future systems which may eventually supersede the L-band LMSS system with even higher performance capabilities. JPL has studied the K- and Ka-bands for application to satellite mobile and personal communications because of the greater bandwidth available compared to L-band, and the significant antenna size reduction that these higher frequencies allow. The most recent developments at JPL are two antennas designed for 20 and 30 GHz communications experiments using NASA's Advanced Communications Technology Satellite (ACTS) in a program at JPL titled the ACTS Mobile Terminal (AMT). These antennas are substantially smaller than their L-band cousins.

2. ANTENNA DEVELOPMENTS

2.1. Low Gain- Omni

Of the antennas discussed in this article, omni-directional antennas are the simplest, most reliable and least expensive; although, they provide the least performance. Here "omni-directional" means, more accurately, azimuthally-omni-directional, since the elevation coverage is typically contoured to maximize the gain in the 20-60 deg range, unlike the cellular telephone whip which is truly omni-directional. Note also that the whip antenna used for cellular telephone provides linear, not circular, polarization. Circularly polarized omni designs developed by JPL include the crossed drooping-dipole, quadrifilar helix, and circular microstrip patch. These designs and test results have been reported in Ref. 1. These antennas were found to provide 3.5-6.0 dBic gain at L-band for CONUS coverage. Figure 1 presents pictorial views and measurements of early prototypes of the three different designs.

2.1.1. Crossed Drooping-Dipole

The crossed drooping-dipole proved to be the most versatile in the JPL field trials. It consists of a pair of inverted-V dipoles, oriented orthoganally but sharing a common central feed point at the top of a mast which doubles as a balun. Non-equal dipole lengths establish the phase relationship required for circular polarization. The azimuthal pattern is slightly elliptical, so it is not purely omnidirectional (i.e. circular azimuth pattern). Its elevation coverage is generally rather broad, and if the elevation coverage is required to be optimized for the satellite look angle of a particular geographical region, this is done by adjusting the height of the antenna above its ground plane (the vehicle roof). A left-hand circular polarized version used for experiments in Australia provided a peak gain of 5.3 dB at an elevation of 55 deg above the horizon. Its height is 8 cm.

2.1.2. Quadrifilar Helix

The quadrifilar helix has the best circularly symmetric azimuth coverage and a unique method for elevation tracking, but it presents the most vehicle protrusion of these three antenna designs. It has four filaments, 90 deg apart, wound at a constant pitch about a cylindrical mast. The units built for L-band operation have a cylinder diameter of about 2 cm and height about 20 cm. The resonant frequency is generally set by filament length, and the elevation angle coverage is set by the winding pitch (or overall height). Reducing the winding pitch (thus increasing the overall height) directs the antenna beam lower in elevation, toward the horizon. The helix antenna is able to provide up to about 5 dBic peak gain. Such an antenna is now sold commercially for satellite communication; it is trunk-mountable and uses an electric motor to stretch and compress the helix to set the desire elevation coverage. The antenna and mechanism which protrude from the vehicle are contained within a capped cylindrical tube of fixed height mounted to the vehicle.

2.1.3. Microstrip Disk

The microstrip disk is the most conformal of these three antenna designs. The peak elevation angle of the antenna beam can be varied over a wide range by exciting the disk at different higher order modes and/or by loading the substrate material with different dielectric constants[2]. By suppressing higher order modes the beam symmetry and good ellipticity is preserved. The disk is suspended on a thick honeycomb substrate and driven at four points to excite higher order modes to generate a circularly polarized broadside pattern (null at broadside, or zenith). The TM_{41} mode provides peak coverage near 30 deg elevation, the TM_{31} mode peaks near 45 deg, and the TM_{21} mode peaks near 60 deg. The microstrip disk is able to provide up to 6 dBic peak gain. Its height is less than 3 cm.

2.2. Medium Gain-Steerable, L-band

Medium-gain steerable antennas were developed for mobile vehicles. the purpose of the development is two-fold: (1) to provide higher antenna gain for the mobile terminal, and (2) to provide a directive beam to effect sufficient intersatellite isolation for interference-free communications. The goals are to achieve: (1) a minimum of 10 dBic gain over the elevation angle range of 20-60 deg above the horizon, and (2) 20 dB intersatellite isolation for two satellites with opposite polarization placed approximately 30 deg apart in the geostationary orbit. With higher gain comes a smaller antenna beamwidth, and thus the need for satellite tracking. (A CW signal is assumed to be sent by the satellite for the purpose of satellite tracking by the vehicle antenna.) Two classes of steerable antennas have been designed and breadboarded. These are the electronically steered phased-array antennas and the mechanically steered tracking antennas. Low cost and low profile were the two principal drivers in designing these antennas.

2.2.1. Phased Array, Electronically Steered

Phased array antennas were developed primarily to provide a thin antenna that can be installed conformal to the top of the vehicle for aesthetic or security reasons. these antennas are well known to be complex and expensive. As a result, emphasis was placed methods of reducing costs in addition to meeting the RF and pointing requirements.

Two right-hand circularly polarized (RCP) phased array antennas were separately developed by Ball Aerospace Systems Division[3] and Teledyne Ryan Electronics[4] under contract with JPL. The antennas developed by these two companies, shown in Figure 2, exhibit several common features. Both antennas use 19 radiating elements with 18 3-bit diode phase shifters. The RF construction of both antennas employ the "tile" approach. Satellite tracking is accomplished in elevation and azimuth dimensions independently, with fast-rate sequential lobing used for azimuth tracking and a slow amplitude search routine for elevation tracking. The tracking systems of both antennas are augmented by an inertial vehicle yaw rate sensor to combat short signal outages.

There are also several distinct differences in technology and design between the two antennas developed by the contractors. Ball uses a dual-resonant stacked 13 mm-thick circular microstrip element to cover both the transmit and receive bands, while Teledyne employs a 6 mm-thick stripline cavity-backed crossed-slot radiator. The overall height of the Ball antenna is 3.3 cm (61 cm diameter), while the Teledyne antenna achieved an overall height of only 1.8 cm (54 cm diameter). The microstrip element has a 3-dB beamwidth of about 90 deg, and the crossed-slot element 140 deg. The crossed-slot element is thinner and allows the array beam to scan lower in elevation due to its wider element beamwidth. The dual stacked

microstrip element is lower in cost because of its simplicity and the use of low-cost foam material. Another difference between the two antennas is that Teledyne uses the switched-line 3-bit diode phase shifters, while Ball employs the hybrid reflection/loaded line type 3-bit phase shifters. The former use 6 diodes each, while the latter require 12 diodes each. The hybrid phase shifter has slightly higher insertion loss and phase error as compared to the switched-line design.

In addition to the RCP phased arrays developed by Ball and Teledyne, an LCP unit was also produced by Teledyne under a follow-on contract with JPL. This LCP unit was successfully tested in JPL communication tests conducted in Australia, using the Japanese ETS-V satellite. The performance of the RCP and LCP antennas are very similar because the only difference in their design is the sense of polarization. The measured far-field patterns of the LCP phased array are shown in Figure 3.

2.2.2. Mechanically Steered

Mechanically steered tracking antennas were developed for the purpose of providing tracking antennas with considerably lower cost than the phased array antenna. The challenge is to achieve a low-profile, low-cost design in addition to meeting the RF and pointing requirements.

Four mechanically-steered, L-band tracking antennas were developed. The original design was a tilted linear array[5]. The second is a revision of the first antenna, of lower-profile and lower-weight, accomplished by redesigning the pointing mechanism and employing integrated stripline feed circuitry[6]. The third antenna is a hybrid mechanically/electronically steered antenna built by Teledyne under contract with JPL[7]. The fourth antenna is a novel planar microstrip array which achieves the most attractive combination of performance, cost and low profile[8]. All but the hybrid design incorporate a fixed broad elevation beamwidth to alleviate the need for elevation tracking and reduce the satellite tracking system to simply that of azimuth tracking.

2.2.2.1. Original Tilted Patch Array and Reduced-Height Version

Figure 4 presents a pictorial view of the original antenna and the subsequent design, similar to the first but of reduced height. Both antennas have a diameter of 51 cm, and heights of 23 and 15 cm, respectively. They employ the same single-channel monopulse technique for tracking the satellite in azimuth. There is no need for satellite tracking in elevation angle since the antenna elevation beamwidth spans the entire 20-60 deg range.

The array used in both antennas is designed for the simultaneous transmission and reception of communication signals, and the far-field patterns are shown in Figure 5. The patterns are very similar for both the original antenna and the reduced-height version. The array is divided into two identical subarrays, each

composed of two radiating square microstrip patch elements, tilted so the broadside peak is set at 45 deg.

The classical single-channel monopulse technique is used to detect antenna azimuth pointing error. The signals from the left and right subarrays pass through a sum/difference hybrid circuit, whereby their sum and difference are obtained. The difference, or pointing error signal, is modulated by a 1-bit, 180 deg phase shifter at a rate of about 2 KHz and coupled into the main communications (sum) signal path via a -10 dB coupler. The combined output of the coupler is then passed through a single-channel rotary joint. Thus, since the difference signal is modulated before addition to the sum signal, it can be extracted from the composite baseband signal at the receiver output with coherent demodulation with a 2 KHz square wave. After extracting the difference signal and normalizing it to the sum signal, it proportionately represents the antenna pointing error.

The antenna maintains closed-loop tracking of the satellite using this error signal as feedback, as long as the received signal strength exceeds a preset threshold. About 1 KHz bandwidth of antenna pointing error is obtained from the "error" signal. When the signal falls below the preset threshold, tracking is accomplished using an inertial vehicle yaw rate sensor, which is accurate enough to maintain point during signal outages as long as 10 sec.

The original design performed well in several field trials, and its success led to additional development aimed at reducing the antenna height as well as further integration of the RF monopulse components into the array assembly. Two stripline layers flush-mounted behind the microstrip patch array provide most of the required RF circuitry. The quadrature hybrids for four microstrip patches are on one layer, while the array feed power-divider network, the sum/difference hybrid and the -10 dB coupler are all integrated on a second layer. Discrete components were still used for the phase modulator and an isolator which protects the modulator from the transmit signal energy. In addition to somewhat improved RF performance, the revised design is lighter and less expensive. The major modification to the pointing mechanism in the reduced-height design involved the use of a pancake stepper motor of only 13 mm height with which to drive the azimuth angle of the antenna. The modifications made to the pointing mechanism reduced its height from to 10.5 to 2.5 cm.

2.2.2.2. Hybrid Phased Array/Mechanical Steering

In pursuit of antenna height reduction, a low profile planar hybrid mechanically and electronically steered tracking antenna was fabricated by Teledyne under contract with JPL. It has a height of 4 cm and a diameter of 69 cm, but this development did not achieve the RF performance goals. It uses 32 crossed-slot stripline radiating elements, phased to accomplish elevation angle tracking, and pancake stepper motor drive for azimuth angle tracking. The array elements are

arranged with complete symmetry about the two major axes of the array. Two phase shifters connect to the two identical halves of the array to provide sequential lobing in azimuth. Another two pairs of phase shifters are used for beam switching in elevation. With the independent azimuth and elevation tracking functions, this antenna utilized essentially the same satellite tracking scheme as the Teledyne phased array, except that azimuth angle is steered mechanically.

This hybrid-scanned antenna did not achieve the RF performance goals. Factors such as high circuit losses, array grid configuration, and mutual coupling effects contributed to serious performance degradation. The design, however, seems basically sound, and a more careful implementation may provide success.

2.2.2.3. Planar Microstrip Yagi Array

One final effort was made to achieve a low profile with a low-cost mechanically steered antenna using a novel planar microstrip Yagi array concept. This concept incorporates microstrip patches on a 6 mm thick dielectric substrate in a configuration similar to a classical Yagi-Uda array; although, in the microstrip topology the Yagi effect is used to direct the array antenna beam away from the array broadside and toward the horizon, unlike the classical Yagi dipole array which provides gain enhancement along the dipole array axis. Successful height reduction required integration of all of the antenna components, including the phase modulator and ferrite isolator that were not integrated in the reduced-height version of the original mechanical antenna design. A pictorial view of the planar microstrip Yagi array antenna is shown in Figure 6.

The array of 16 microstrip patches consists of 4 columns (Yagi arrays) of 4 patches each. Each column consists of a single driven patch with two feed points to excite circular polarization, a reflector patch of larger dimension, and two director patches of smaller dimension. Optimum axial ratio is not obtained with the traditional 90 deg feed phase differential, but rather 115 deg for this design. The reactance of the directors and reflector, along with the inter-element coupling determines the antenna patterns, shown in Figure 7. With only one patch per column requiring direct electrical connection (two feed points), the complexity of the feed circuitry and thus the insertion loss is substantially reduced, optimizing the power efficiency of the array.

The reduced-height pointing mechanism of the reduced-height tilted linear array antenna was inherited, and all of the antenna RF feed and monopulse components, other than the array itself, were integrated into a 3 mm-thick stripline "beamformer" circuit mounted flush against the bottom of the array.

The design of the thin "beamformer" circuit solved all of the significant problems encountered with the tilted linear array antennas. A bulky ferrite isolator used in the tilted linear array monopulse circuit was replaced with a negligibly thin stripline resonator filter in the microstrip Yagi monopulse circuit, providing

spectral rather than spatial isolation of the transmit signal power from the sensitive receive monopulse components. A binary PIN-diode phase modulator in stripline topology replaced a bulky, packaged unit. The slew rate of the modulator was optimized to avoid receiver desensitization due to spectral splatter of the transmit signal generated by the monopulse phase modulator at high transmit power levels. The modulator is designed to be powered and controlled by only a single DC line, supplying all power supply and binary modulation information. The one DC line is routed through the same coaxial rotary joint through which the RF is carried. Thus, by simplifying the monopulse phase modulator circuit, the DC slip rings, which supply power to the modulator in the tilted linear array antenna designs, were eliminated. With the absence of the slip rings the friction in the mechanism is significantly reduced and the torque requirements on the drive motor thereby reduced.

The overall height achieved with the Microstrip Yagi array is 38 mm. Its diameter is 51 cm. This antenna outperformed all the others in almost every category. The antenna insertion loss (directly affecting receive noise temperature and transmit power efficiency) is the lowest of all the L-band tracking antennas developed, at 0.8 dB, especially compared to the phased arrays. Its height is one of the lowest and directly comparable with the phased arrays. It construction is the simplest, made mainly of planar, printed circuits, and as a result its manufacturing cost is the lowest. It has lasted longer than any other tracking antenna during field trials, proving a superior durability.

2.3. High Gain, K/Ka-band

The benefits of K/Ka-band compared to lower frequencies such as L-band include a much larger available bandwidth and higher antenna gain and/or a substantial size reduction. Reaping these benefits requires overcoming disadvantages of higher RF component losses, significant rain attenuation, greater Doppler and the need for more a accurate satellite-tracking system to accommodate a narrower antenna beam.

A K/K_a-band mobile vehicle antenna system has recently been developed for use with NASA's Advanced Communications Technology Satellite (ACTS) by the JPL. The ACTS satellite is scheduled for launch into its geostationary orbit at 100 deg West longitude (above the mid-Western US) in late1993. The new mobile vehicle antenna system development is for NASA's ACTS Mobile Terminal (AMT) project. Soon after the satellite is operational, the AMT project will demonstrate the first experimental use of ACTS, with direct-dial voice, video and data communications from a mobile vehicle while traveling in the Southern California area[9], using the land-mobile antennas developed by the AMT project.

Two mechanically-steerable antenna concepts have been developed, one based on a small offset reflector[10], using more traditional technologies, and the other

based on a printed circuit slot/dipole shared aperture active array[11], using state-of-the-art solid-state technologies. These antennas are substantially smaller than the L-band antennas. The two antennas are designed to operate within the AMT frequency bands of 19.764-20.064 GHz (downlink) and 29.484-29.784 GHz (uplink). These bands represent only a portion of the ACTS frequency bands. The ACTS satellite uses linear polarization, and so the AMT antennas are designed with linear polarization. The AMT antennas are required to provide an elevation beamwidth of 12 deg to reduce satellite tracking to only azimuth, at least for operation within a particular geographical region, accommodating the pitch/roll variations of a vehicle while traveling along paved roads.

2.3.1. Small Offset Reflector Antenna

Figure 8 is a picture of the AMT reflector antenna shown with a transparent mock radome; the actual radome has the same hemi-ellipsoidal shape but is optically opaque. The external dimensions of the radome are 23 cm in diameter and 10 cm in peak height. It uses a single reflector and feed horn for both uplink and downlink. A low noise amplifier (LNA) and traveling-wave tube amplifier TWTA) are mounted within the vehicle cabin below the antenna to establish the required receive noise sensitivity and provide the required transmit RF power, respectively. A thin but sturdy radome protects the antenna from the environment.

Figure 9 presents the measured elevation and azimuth co- and cross-polarization 20 and 30 GHz patterns of the overall antenna, including the radome. The patterns show the elevation coverage centered at 46 deg, the southern California ACTS elevation look angle. Over a 12 deg elevation range centered at 46 deg the 30 GHz gain is a minimum of 19.6 dBi with a peak of 23.0 dBi, and the 20 GHz gain is a minimum of 19.0 dBi with a peak of 22.5 dBi. Antenna gain is referenced to the output ports of the diplexer below the rotary joint. Peak transmit EIRP is 33 dBW, and peak receive sensitivity is -2.5 dB/K. The elevation and azimuth sidelobes are more than 20 dB down from the main lobe. Peak cross-polarization is no greater than -15 dB.

The antenna incorporates an offset reflector configuration to avoid feed horn aperture blockage. The reflector is constrained to fit with the feed horn under the radome and is relatively small, only about four by ten wavelengths at K-band. The basically elliptical reflector shape maximizes gain while providing a relatively wide elevation beamwidth to relax the need for satellite elevation tracking. The shape of the reflector is the intersection of a paraboloid and an elliptical cylinder, with the cylinder oriented so the projection of the reflector surface is nearly a simple ellipse as viewed from both the feed horn and the satellite directions; this orientation is important to ensure good illumination of the reflector by the feed horn and a reasonably symmetrical antenna elevation pattern -- it also contours the shape of the reflector to fit well under the radome. The reflector mounts to a manually

375

adjustable fixture used to set the elevation angle of the antenna beam to potentially allow operation with ACTS in any region of the continental United States (30-60 deg elevation satellite look angle). Only the reflector adjusts; the feed horn remains fixed.

All of the antenna RF components are integrated into a single rigid assembly, except for the reflector and rotary joint, to reduce RF losses and increase the mechanical integrity. Figure 8 shows the feed horn, orthomode transducer and upper diplexer (the components above the rotary joint in Figure 6) all integrated into a single feed horn assembly. The feed horn assembly is a waveguide system that distributes both the 20 and 30 GHz signals from the rotary joint to the feed horn. The one feed horn is used for both frequency bands, with vertical polarization for the 20 GHz downlink and horizontal polarization for the 30 GHz uplink. Immediately behind the feed horn is the orthomode transducer. The orthomode transducer combines the two frequency bands from two different ports and channels them to the feed horn after orienting them with the proper polarizations. The upper diplexer spatially separates the two frequency bands and distributes them to the respective ports of the orthomode transducer. The diplexer makes up most of the lower portion of the assembly and consists of a tee-junction of a lowpass filter for 20 GHz and a highpass filter for 30 GHz. The feed horn assembly also includes a coax-to-waveguide transition, to adapt directly to the coaxial rotary joint connector, and a section of flexible waveguide that connects the coax transition to the rest of the waveguide structure and accommodates any misalignment of the rotary joint and motor axes as the motor turns. The RF losses through the entire antenna, including the rotary joint and the diplexer below the rotary joint, are 1 dB at 20 GHz and 1.5 dB at 30 GHz.

2.3.2. Active Array with Electromagnetic Coupling

Figure 10 is a diagram of the AMT active array layout. The active array incorporates a multi-layered microstrip, electromagnetically-coupled slot and dipole element design with shared receive/transmit aperture (20/30 GHz), and monolithic microwave integrated circuit (MMIC) LNAs and high-power amplifiers (HPAs). Because the active array is flat, much shorter than the reflector and mounted horizontally, a shorter radome than that used for the reflector antenna may be used for the active array. The active array, not including the motor or radome, is 16 cm long, 13 cm wide and 2 cm tall -- it mounts flat to the same motor used in the small reflector antenna and radiates a fixed beam 46 deg in elevation from the horizon. A TWTA is not needed because the transmit RF power is generated by the MMIC HPAs within the array; only a small transmit signal level is required through the rotary joint to drive the HPAs, about 0 dBm. A thin, conformal radome protects the antenna from the environment.

The array, currently under development, is a multi-layered assembly in which a receive array of radiating slots and a transmit array of microstrip dipoles are interleaved such that they share the same aperture and provide a compact, dual frequency antenna. The slots are electromagnetically coupled to MMIC LNAs, and the dipoles are electromagnetically coupled to MMIC HPAs. Due to a lack of funding for transmit array development, the active array has been implemented with only receive capability.

The interleaved transmit and receive planar arrays both consist of linear subarrays which determine the elevation radiation patterns. The receive linear subarray is a series-fed array of slots, transversely coupled electromagnetically to a microstrip transmission line, as shown in the top of Figure 11. The transmit linear subarray is a series-fed array of dipoles, transversely coupled electromagnetically to a microstrip transmission line, as shown in the bottom of Figure 11. Each dipole of the transmit array represents a shunt impedance to the transmission line, where the impedance is a function of dipole offset distance from the line, and the width and length of the printed dipole. Similarly, each slot of the receive array represents a series impedance to the transmission line. The amplitude distribution is tapered to meet the sidelobe level requirement of -13 dB. The proper elevation scan angle (fixed) is set by the phase distribution, obtained by adjusting the path length of the interconnecting transmission lines.

The linear subarrays for both the transmit and receive antennas consist of eight elements each, with an inter-element spacing of approximately 0.47 free-space wavelength. The transmit array consists of 10 linear subarrays of dipoles, spaced 0.96 free-space wavelength apart, and the receive array consists of 14 linear subarrays spaced 0.65 free-space wavelengths apart.

The active array antenna design includes a receive module of MMIC LNAs and a transmit module of MMIC HPAs. One MMIC circuit connects to each of the array's linear subarrays: one LNA for each receive linear slot array, and one HPA for each transmit linear dipole array. Figure 10 diagrams this relationship.

All the MMIC circuits are assembled into a single module that attaches to the array via bonding straps. The transmit and receive modules are mechanically assembled back-to-back, as shown in the sidebar of Figure 10, such that the antenna feed lines align properly with the module microstrip interconnects. A ribbon bond connects the modules electrically to the antenna. The DC power for the MMIC circuits is passed through the rotary joint along with the RF signals.

The transmit module provides greater than 1 Watt of RF power to the dipole array at the 30 GHz transmit frequency band. Ten MMIC pseudomorphic HEMT (PHEMT) amplifiers provide 125 mW each to ten subarrays. Each MMIC is mounted in a package, as shown in Figure 12, with a kovar base with metallized ceramic walls. The transmit modules are designed to maintain gate junction

temperatures below 125 deg C. Each package is mounted in the transmit module, which also contains the transmit power divider circuit.

The receive module consists of 14 MMIC PHEMT LNAs. Each LNA has a noise figure less than 3 dB and greater than 20 dB gain (at 20 GHz). The LNAs are specified such that the coupling of the transmit signal into the receive antenna does not desensitize the receiver. Each LNA is individually packaged, as shown in Figure 12, and mounted in the receive module, which also contains the receive power combiner.

Figure 13 presents the calculated elevation patterns at 20 and 30 GHz for the overall antenna. The measured far-field patterns of linear arrays of the slots and dipoles agree very well with the calculations. The patterns show the elevation coverage centered at 46 deg, the southern California ACTS elevation look angle. Over a 12 deg elevation range centered at 46 deg the 20 GHz directivity is a minimum of 22.5 dBi with a peak of 24 dBi, and the 30 GHz gain is a minimum of 23 dBi with a peak of 24.5 dBi.

3. CO᠎᠎LUSIONS

From the decade of experience JPL has had in the development of vehicular antennas for land mobile satellite service, the following observations are made. Refer to Table 1 for an overview of the performance achieved with the L-Band antennas, and to Table 2 for the performance of the K/Ka-band ACTS Mobile Terminal antennas.

L-band Mobile SATCOM Antennas

For applications requiring only the modest antenna performance that an omni-directional provides, the crossed drooping-dipole antenna is small, simple, reliable and low cost. It is adequate for low rate data communications and does not require a satellite tracking system.

The electronically steered L-band phased arrays are conformal and thereby aesthetically pleasing. At this stage though, they are of high cost. The cost drivers are assembly labor, phase shifting components and beam-pointing electronics. Much development is still required before the phased array manufacturing costs become directly competitive with more traditional antenna technologies.

The mechanically steered L-band tracking antennas offer similar RF performance as the L-band phased array antennas, and they are considerably lower in cost. The height reduction recently achieved by the planar microstrip Yagi array makes its profile directly comparable to the phased arrays. The reliance on printed-circuit techniques in the microstrip Yagi design significantly reduces the labor cost associated with its fabrication and thereby significantly reduces its overall cost. The cost of the microstrip Yagi is the lowest of all the tracking antennas considered.

Comparing the relative merits of the L-band tracking antennas, the mechanically-steered, planar microstrip Yagi provides the best combination of performance, low profile and low cost. Phased array antennas could provide unique commercial applications if the cost is brought down.

K and Ka-Band Mobile SATCOM Antennas

The two antenna systems developed for NASA's ACTS Mobile Terminal program will demonstrate the increase in performance and the reduction of size afforded by the move to Ka-band from L-band. The small reflector and the active array antennas will enable propagation experiments to be conducted using NASA's ACTS satellite..

The small reflector antenna utilizes traditional technologies and is very robust. The receive sensitivity is exceptional at a peak G/T of -2.5 dB/K. This antenna will be used for mobile satellite communication experiments across the U.S. using the ACTS satellite.

The active array antenna utilizes state-of-the-art antenna array and solid-state technologies. Printed-circuit techniques along with the multi-layered design allow a very high degree of integration and afford commercial mass production for future applications. The use of MMIC LNAs and HPAs within the array itself alleviate the need for a transmit TWTA, increasing the overall power efficiency of the antenna, and enhance the receive performance as well. With active circuitry, but without electronic phase steering, the active array provides the advantages of low profile and performance of a phased array but at a mid-range cost less than that of a phased array.

Table 1. Comparison of L-band Vehicle Antennas Designed for CONUS Coverage

Antenna (All RCP)	XMT Gain[1] (dBic)	RCV G/T[2] (dB/K)	Intersatellite Isolation[3] (dB)	Height (cm)	Diameter (cm)	Cost[4] ($)
Mechanically Steered						
Microstrip Yagi	9.5	-14.7	21	3.5	51	450
Reduced-Height Tilted Linear Array	10.0	-15.6	24	15	51	600
Original Design Tilted Linear Array	10.0	-15.7	24	23	51	600
Phased Arrays						
Ball Aerospace	8.0	-17.8	19	3.3	61	1600
Teledyne Ryan	8.0	-17.9	25	1.8	54	1800
Omni-Directional						
Crossed, Drooping-Dipole	4.0	-19.9	10	12	8	50

[1] Minimum over the elevation angle range of 20-60 deg from horizon.
[2] G/T calculations assume a 2.2 dB receiver noise figure.
[3] Assumes two geostationary satellites with opposite polarization separated by 30 deg.
[4] Estimated cost, based on producing 10,000 units per year over a five-year period.

Table 2. Performance of the K/Ka-Band ACTS Mobile Terminal Antennas

Antenna (Linearly Polarized)	XMT EIRP[1] (dBW)	RCV G/T[2] (dB/K)	Height (cm)	Diameter (cm)
Small Reflector[3]	29.6	-6.0	10	22
Active Array[4]	22.0	-8.0	6	22

[1] Minimum over a 12 deg elevation range when centered 46 deg from horizon. The antenna beam, with a fixed elevation beamwidth of 12 deg, may be manually set within the range of 30-60 deg in elevation for operation within the CONUS.
[2] G/T calculations assume a 2.7 dB receiver noise figure.
[3] The XMT EIRP specification for the Small Reflector assumes use of the maximum transmit power level that the antenna is rated for, 10 Watts.
[4] Estimated performance, using measurements of antenna components not yet integrated.

4. ACKNOWLEDGMENT

5. REFERENCES

1.	Woo, K., 1988.	Vehicle Antenna Development for Mobile Satellite Applications, Proceedings of the IEEE Fourth International Conference on Satellite Systems for Mobile Communications and Navigation, pp. 23-27.

2.	Huang, J., 1984.	Circular Polarized Conical Patterns from Circular Microstrip Antennas, IEEE Trans. Antennas Prop., Vol. AP-32, No. 9, pp. 991-994, Sept. 1984.

3.	Schmidt, F. et al. 1988.	MSAT Final Report, Ball Aerospace Systems Division. JPL Contract No. 957467.

4.	Peng, S. Y., et al. 1988.	Final Report: Vehicle Antenna for the Mobile Satellite Experiment, Teledyne Ryan Electronics, JPL Contract No. 957468.

5.	Jamnejad, V. 1988. A Mechanically Steered Monopulse Tracking Antenna for PiFEx, MSAT-X Quarterly, No. 13, JPL Publication 410-13-13, pp18-27.

6.	Bell, D. et al. 1989.	Reduced-Height Mechanically Steered Antenna Development, MSAT Quarterly, No. 18, JPL Publication 410-13-18, pp. 3-10.

7.	Francian, et al. 1989.	A Hybrid Scanned Conformal Planar Array for Mobile Satellite Communications, IEEE APS Symposium Digest, pp. 686-689.

8.	Huang, J. and A. Densmore, 1991.	Microstrip Yagi Array Antenna for Mobile Satellite Vehicle Application, IEEE Trans. Antennas Propagat., Vol. AP-39, pp. 1024-1030, July 1991.

9.	Dessouky, K. et. al., 1991.	The ACTS Mobile Terminal, JPL SATCOM Quarterly, July 1991.

10.   Densmore, A. and V. Jamnejad, 1993 K/Ka-band Antenna System for Mobile Satellite Service, _IEEE APS Symposium Digest_, Vol. 1, pp. 124-127, July 1993.

11.   Tulintseff, A., 1993. Series-Fed-Type Linear Arrays of Dipole and Slot Elements Transversely Coupled to a Microstrip Line, _IEEE APS Symposium Digest_, Vol. 1, pp. 128-131, July 1993.
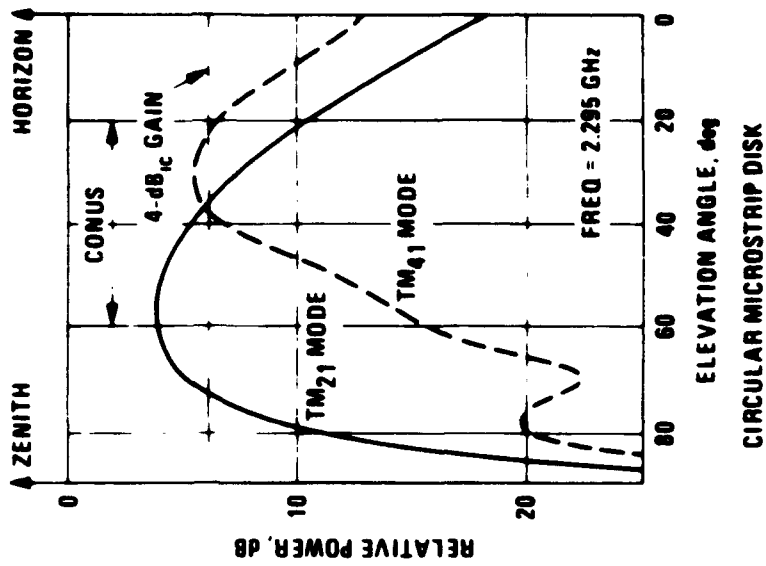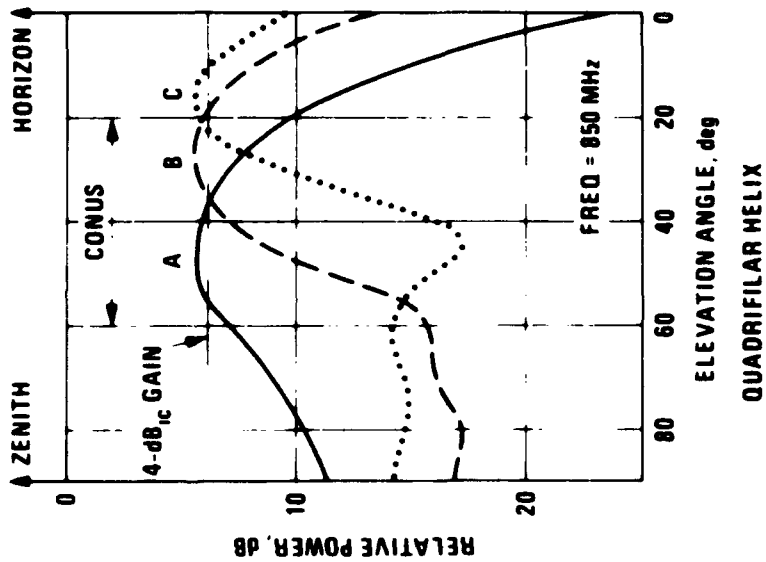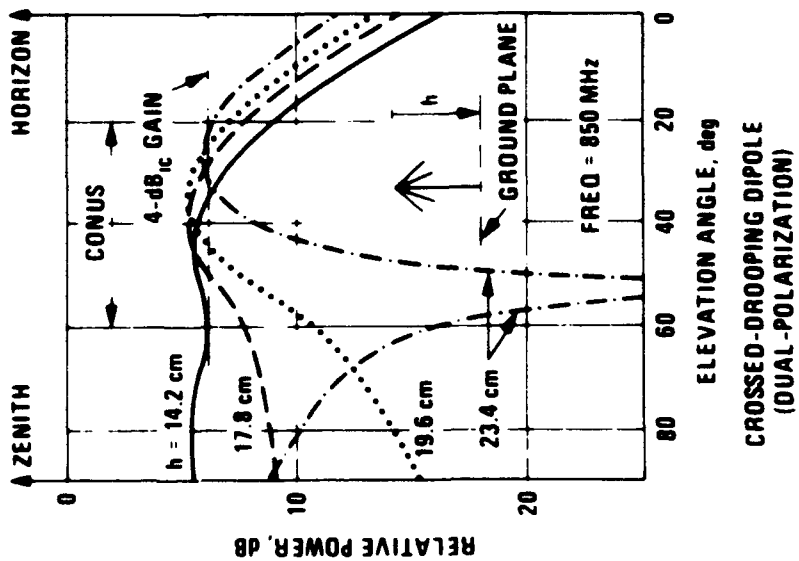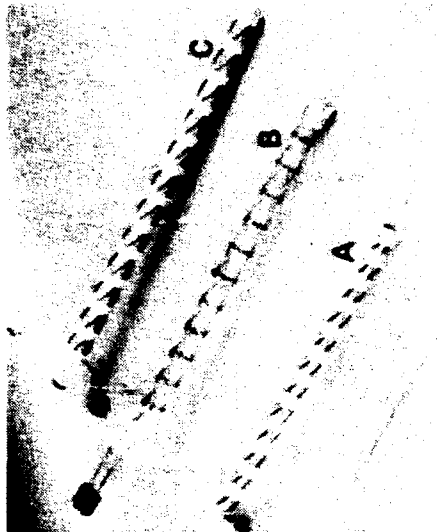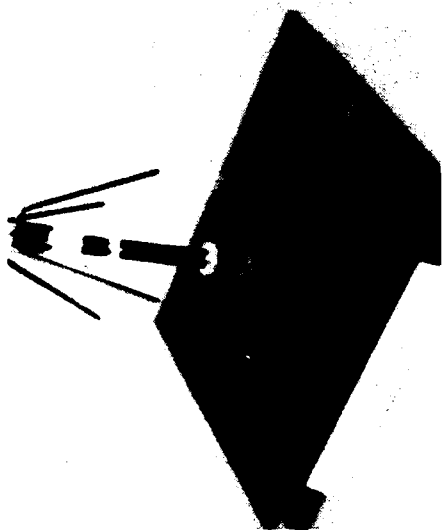
Figure 1. Omni-Directional, Circularly Polarized Antennas.
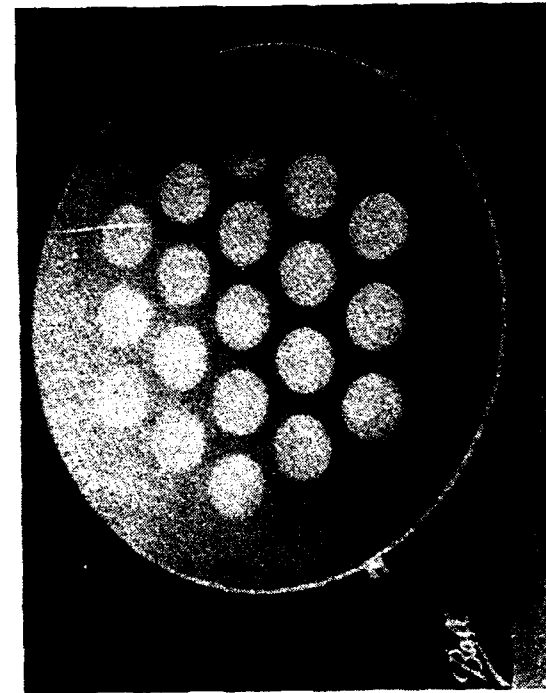
BALL
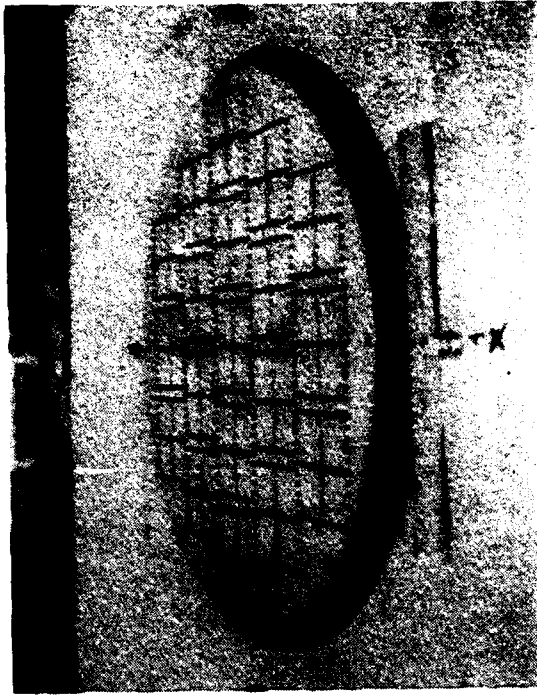
TELEDYNE

Figure 2. Ball Aerospace and Teledyne Ryan L-band Phased Array Antennas.

FREQ = 1.55 GHz

GAIN = 11.1 dB$_{ic}$

60°

40°

20° ABOVE THE HORIZON

RELATIVE POWER, dB

0
5
10
15
20
25
30

ANGLE (deg)

-36   0   36   72   108

ELEVATION PATTERNS

90° BEAM

45° BEAM

11.2 dB$_{ic}$

0° BEAM

x   0°

y   90°

270°

180°

AZIMUTH PATTERNS AT 55° ABOVE THE HORIZON

Figure 3. Co-pol patterns of Teledyne phased array antenna, LCP

REDUCED-HEIGHT DESIGN

12"

1"

ORIGINAL DESIGN
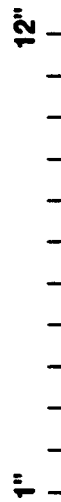
Figure 4. Original and Reduced-Height Versions of Tilted Linear Array

FREQ. = 1.55 GHz

GAIN = 11.3 dB$_{ic}$ AT 55° ABOVE THE HORIZON

————— CO-POL
– – – CROSS-POL

11.6 dB   DIFFERENCE (Δ)
SUM (Σ)
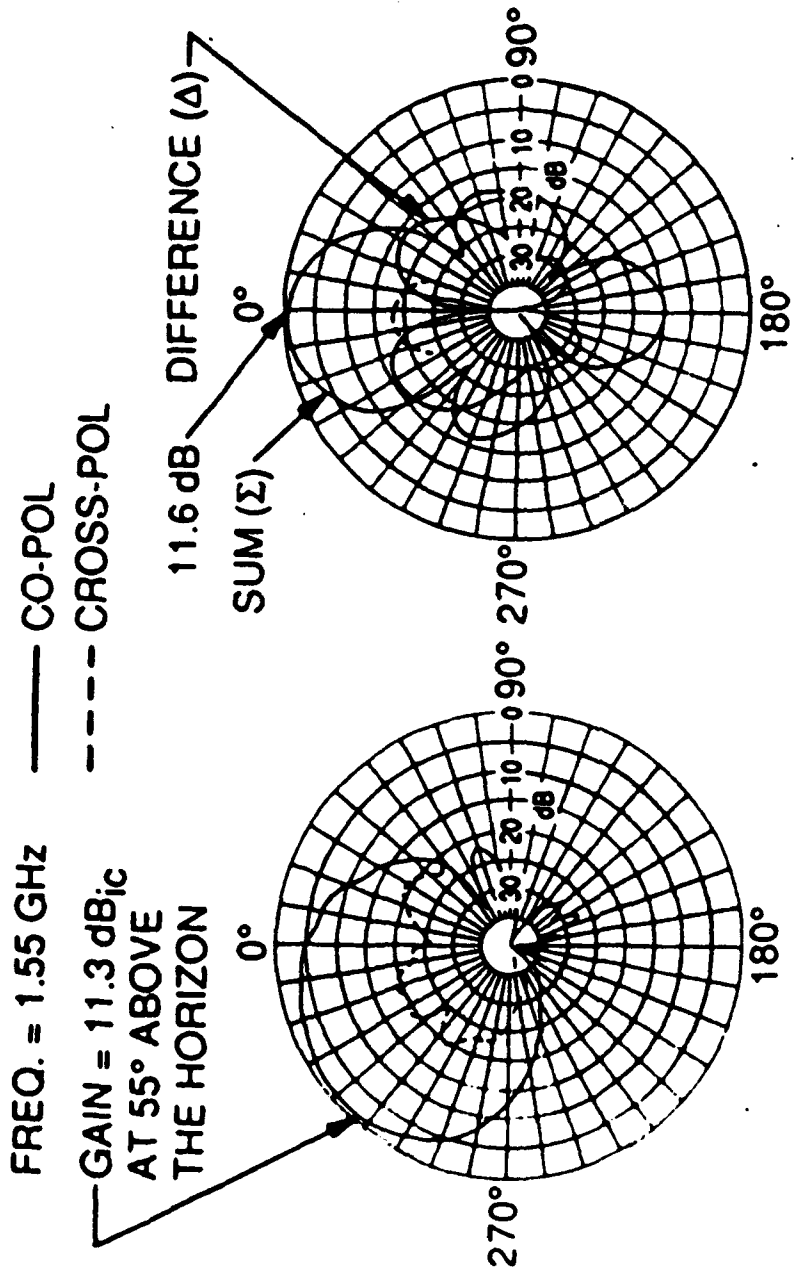
ELEVATION PATTERNS

AZIMUTH PATTERNS AT 55° ABOVE THE HORIZON

Figure 5.   Radiation patterns of reduced-height mechanically steered tilted array antenna, LCP

387
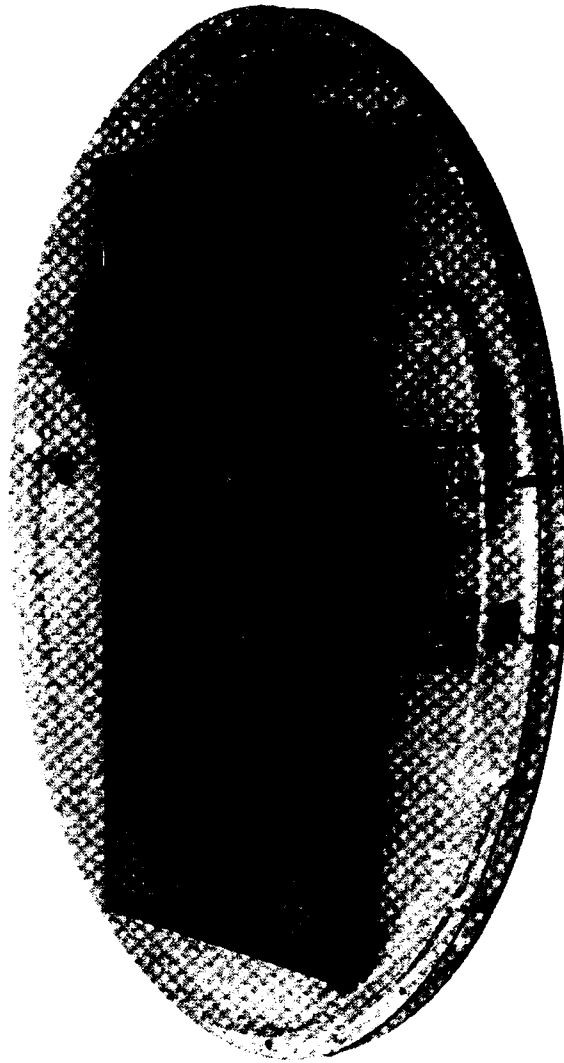
Figure 6. Microstrip Yagi Array with Transparent Radome.

FREQUENCY = 1552 MHz
CO-POL
X-POL

17 dBiC

ELEVATION PATTERNS

FREQUENCY = 1552 MHz
ELEVATION = 40°
SUM
DIFFERENCE
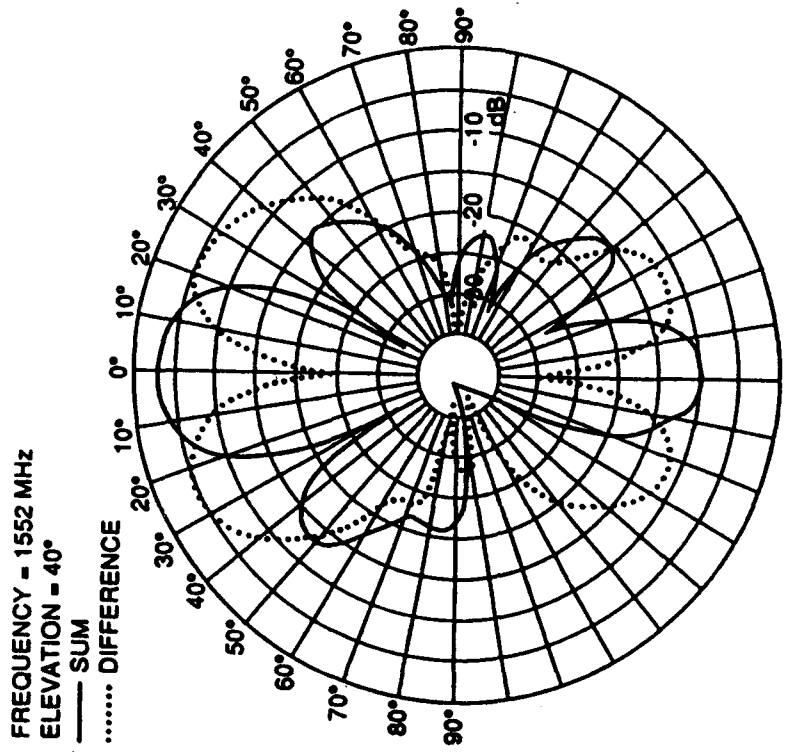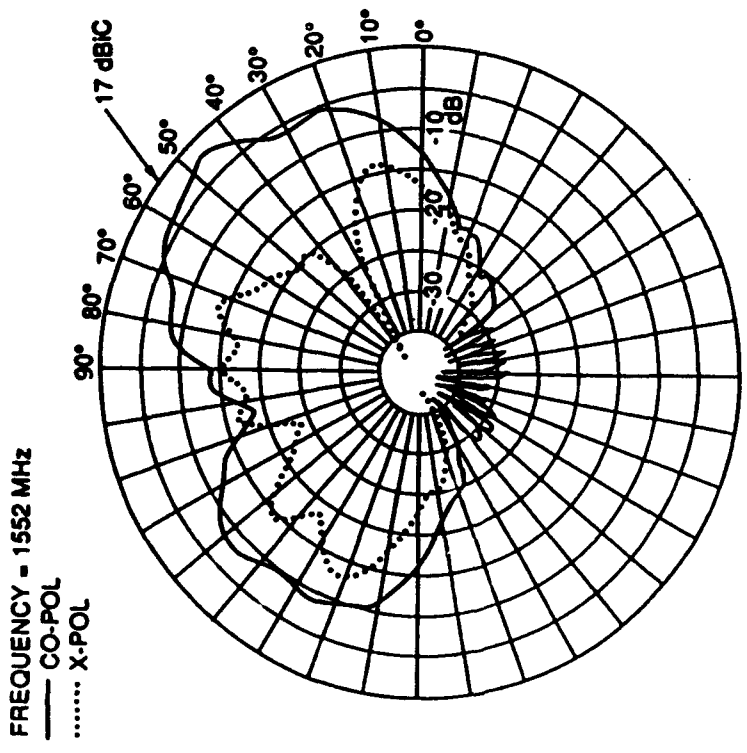
AZIMUTH PATTERNS

Figure 7. Radiation Patterns of Microstrip Yagi Array, RCP

389

Figure 8. Reflector antenna assembly.

Elevation Pattern, 20 GHz, Co- and X-pol.

Elevation Pattern, 30 GHz, Co- and X-pol.

Azimuth Pattern, 20 GHz, Co- and X-pol.

Azimuth Pattern, 30 GHz, Co- and X-pol.
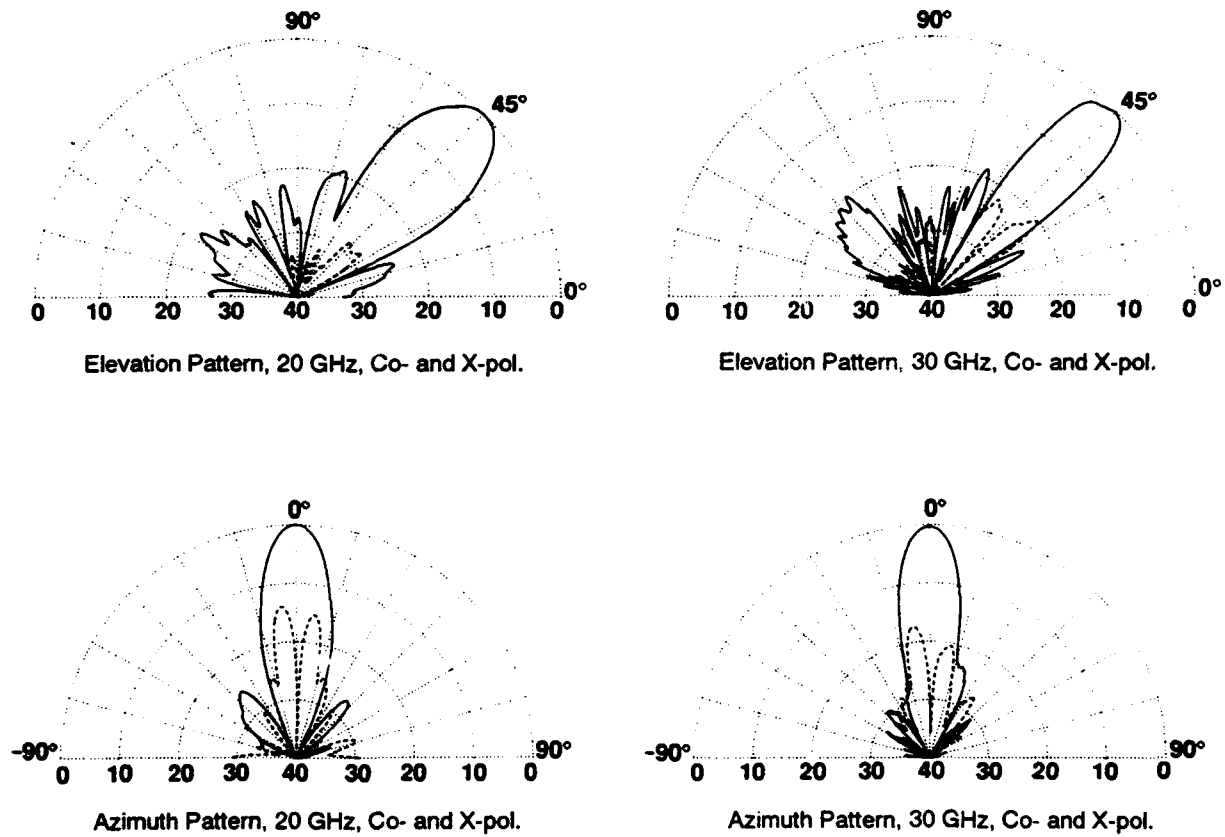
Figure 9. Measured patterns of reflector antenna.

390
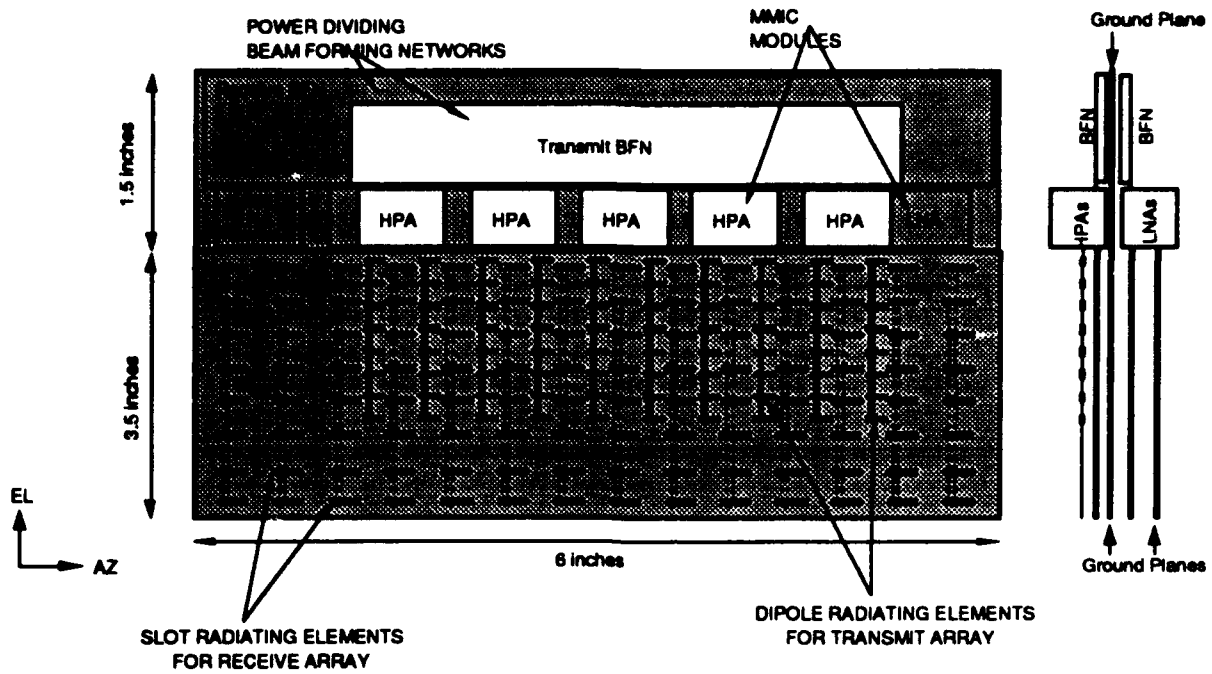
Figure 10. Active array antenna layout.
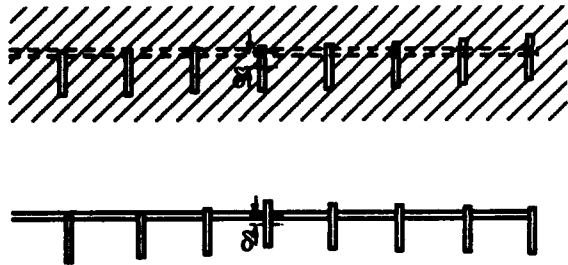
Figure 11. Array element coupling.
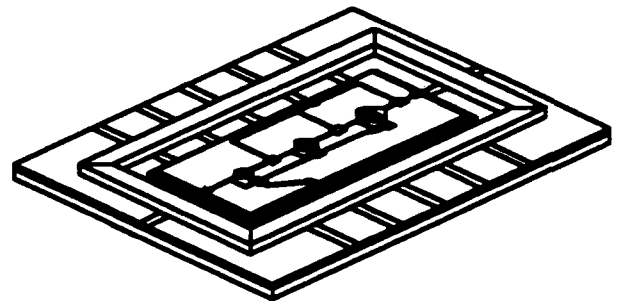
Figure 12. Packaged MMIC circuit.
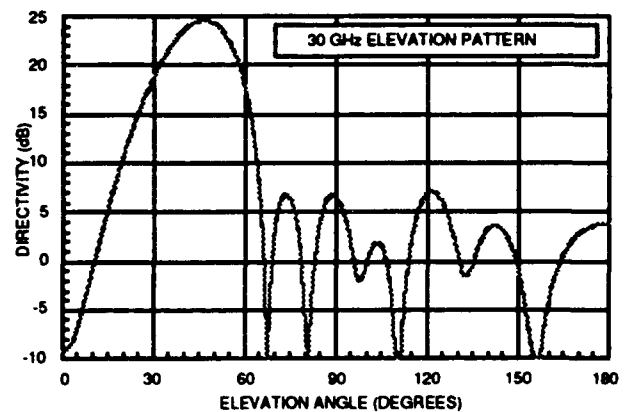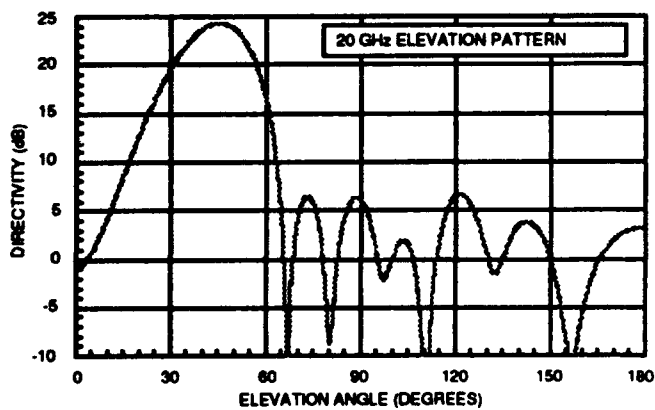
Figure 13. Calculated patterns of the active array antenna.

391

DIRECTION FINDING WITH AN ELECTROMAGNETICALLY COMPLETE FIELD SENSOR

Jeffrey F. Bull
Flam & Russell, Inc.
P.O. Box 999
Horsham, PA 19044
215-674-5100

Abstract

An electromagnetically complete field sensor simultaneously measures the complete electric and magnetic fields at a single point in space. It comprises an array of electrically small antennas in a colocated geometry. Three orthogonal dipoles measure the components of the electric field while three orthogonal loops measure the components of the magnetic field. Thus, the electromagnetically complete field sensor is isotropic to polarization and angle-of-arrival (AOA). For Direction Finding (DF) it is the ultimate small aperture providing the most information about the signal scenario in the smallest physical space. Furthermore, it is inherently broadband since the spatial response of the electrically small elements are independent of frequency and the array geometry is colocated.

In this paper we will describe an Electromagnetically Complete Sensor designed and built for operation in the High Frequency (HF) band, i.e 2 to 30 MHz. Additionally, we will discuss the multisignal DF performance of this sensor when utilized with modern superresolution DF algorithms in both ideal and realistic electromagnetic environments.

1.0 Introduction

Superresolution direction finding algorithms provide greater resolution than conventional techniques and are able to determine the angle-of-arrival (AOA) of several signals simultaneously. Greater resolution implies that system designers can reduce the size of their aperture, as much as an order of magnitude, and still obtain the bearing error that conventional techniques provide. These techniques are well suited to the lower frequencies where the wavelengths are long and large apertures require a lot of real estate.

Electrically small antennas are useful sensors for direction finding systems that operate at the High Frequencies (HF) because their radiation patterns are constant with frequency, i.e. they are broadband, and they are physically compact. Furthermore, up to six electrically small elements may be colocated providing a compact and broadband sensor that is electromagnetically complete.

In this paper we will describe a broadband superresolution direction finding system that utilizes a six element colocated antenna array that operates at HF. It provides the ability to DF on up to four incident signals simultaneously and fits within a two meter diameter sphere. We will also show computer simulations that verify its multisignal performance. Additionally, we will present DF results on real signals illustrating the systems ability to DF on a direct signal as well as reradiation of this signal by local scatterers.

2.0 Antenna Array Description

The antenna array comprises six electrically small antennas: Three orthogonal dipoles and three orthogonal loops. The antenna elements are arranged symmetrically about three orthogonal axes yielding coincident phase centers for all elements. Thus, the array is inherently broadband since the electrically small antenna elements possess frequency independent radiation characteristics and all array elements have the same phase center.

The open circuit voltage induced at the feed point of an electrically small dipole aligned along the z axis as a result of excitation by a vertically polarized plane wave is expressed as:

$$V_{oc} = K_1 \sin \Theta \qquad (1)$$

where Θ is one of the two spherical coordinate angles. The factor K_1 is dependent upon the amplitude of the incident plane wave, wavelength, directivity and radiation resistance. This factor is independent of frequency provided the dipole is electrically small. Thus, we note that the electrically small dipole is a broadband voltage source with its open circuit voltage proportional to an incident plane wave's electric field strength. In effect, this antenna element is an electric field probe.

The short circuit current induced in an electrically small loop aligned in the x-y plane as a result of excitation by a horizontally polarized incident plane wave is expressed as:

$$I_{sc} = K_2 \sin \Theta \qquad (2)$$

The factor K_2 is also dependent upon the amplitude of the incident plane wave, wavelength, directivity, radiation resistance as well as reactance. All frequency dependent terms cancel if the loop is electrically small. Thus, we note that the electrically small loop is a broadband current source with its short circuit current proportional to an incident plane wave's magnetic field strength. In effect, this antenna element is a magnetic dipole or magnetic field probe.

The antenna array is made up of electrically small dipoles and loops oriented orthogonally. This geometric configuration minimizes mutual coupling between elements. It also provides an electromagnetically complete sensor since it possesses probes to measure the three orthogonal electric field components and three orthogonal magnetic field components of the electromagnetic field it is immersed in. The spatial response of all six elements in the array are listed in Table 1 to both the vertical and horizontal polarization components of the electric field of an incident plane wave of arbitrary polarization.

Table 1

Spatial Response of Array Elements

Antenna Elements	Vertical Polarization	Horizontal Polarization
z dipole	$\sin \Theta$	0
y dipole	$-\cos \Theta \sin \Phi$	$-\cos \Phi$
x dipole	$-\cos \Theta \cos \Phi$	$\sin \Phi$
x-y loop	0	$-\sin \Theta$
z-x loop	$-\cos \Phi$	$\cos \Theta \sin \Phi$
z-y loop	$\sin \Phi$	$\cos \Theta \cos \Phi$

A photograph of the array is shown in Figure 1. Each loop is square and fed at each of its four corners. Step down transformers are utilized at each feed point to match the gain versus frequency characteristic of the loops with the dipoles. Each dipole is fed at two points at symmetric distances from the center of the array. Step up transformers are utilized at each feed point to match the gain versus frequency characteristic of the dipoles with the loops. Six coaxial cables run down the inside center of the supporting mast to provide the signals to the receiving equipment.
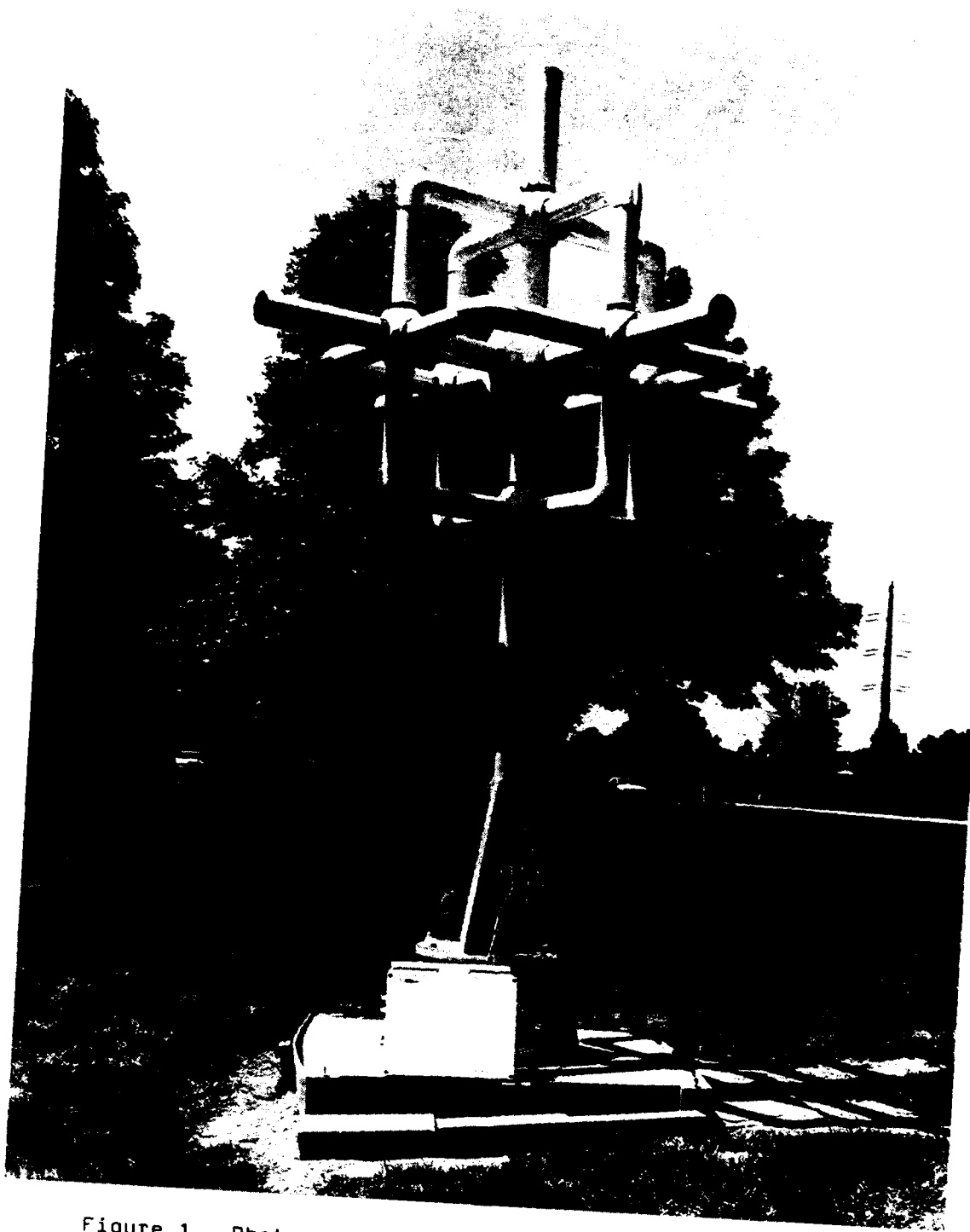
Figure 1. Photograph of an Electromagnetically Complete
Antenna Array

3.0 Superresolution Direction Finding (DF) Algorithms

Superresolution DF algorithms are model based techniques that utilize prior knowledge of the array's response to an incident plane wave of arbitrary AOA and polarization to determine the incident signals' AOAs. The number of uncorrelated signals that a superresolution DF system can determine the AOA of simultaneously is called its "degrees of freedom". A DF system's degrees of freedom is determined by the antenna array. An upper bound on the number of degrees of freedom is one less than the number of antenna elements that the antenna array comprises.

Determination of the AOA's of incident signals with a superresolution DF system involves four basic steps. They are:

1. Acquisition of Data

2. Formation of the Covariance Matrix

3. Operation on the Covariance Matrix

4. Computation of the Spatial Spectrum

Acquisition of data typically requires a multichannel receiver that downconverts a narrowband portion of the RF spectrum to complex (I and Q) baseband. Typically, the outputs of this multichannel receiver are simultaneously digitized and the samples stored in memory.

The second step, formation of the covariance matrix, requires construction of an N by N, for an N element array, complex matrix. This matrix represents the correlation of each antenna element in the array with all other elements over the

length of time the data was acquired. It is an expectation over the outer product of a vector representing the voltages at each antenna element. It is expressed mathematically as:

$$\mathbf{R} = E\left[\mathbf{x}\,\mathbf{x}^H\right] \approx \frac{1}{p}\sum_{i=1}^{p}\mathbf{x}_i\,\mathbf{x}_i^H \qquad (3)$$

where $\mathbf{x}$ is the vector of voltages at the antennas. It may be approximated by the summation of the outer product of p snapshots, i.e. $\mathbf{x}_i$, of the voltages at the antenna elements.

The covariance matrix must be operated upon in order to determine another matrix that is utilized in the final step, i.e. computation of the spatial spectrum for determining the AOAs of incident signals. The specific operation is determined by the particular superresolution DF algorithm utilized. The MUSIC algorithm[1] requires one to determine the eigenvectors of the noise subspace of $\mathbf{R}$. We will limit our discussion to this algorithm since its asymptotic performance is best. It can be decomposed into its orthogonal signal and noise subspaces as:

$$\mathbf{R} = \mathbf{E}_s\Lambda_s\mathbf{E}_s^H + \mathbf{E}_n\Lambda_n\mathbf{E}_n^H \qquad (4)$$

where E_S and E_n are matrices of eigenvectors for the signal and noise subspaces respectively. Similarly, Λ_s and Λ_n are diagonal matrices containing the signal and noise eigenvalues respectively. The AOA's of incident signals are indicated by peaks in the spatial spectrum. The spatial spectrum may be calculated for the MUSIC algorithm, modified for a polarization diverse antenna array[2], in terms of the spatial variables Θ and Φ as:

$$S[\Theta,\Phi] = \frac{k_{min}^{H} k_{min}}{k_{min}^{H} A^{H} E_n E_n^{H} A\, k_{min}} \qquad (5)$$

where k_{min} is the polarization which minimizes the spatial spectrum and:

$$A = \begin{bmatrix} a_v & a_h \end{bmatrix} \qquad (6)$$

is a six by two dimensional matrix of the vertical and horizontal polarization response of the antenna array to an incident plane wave. These responses were given in Table 1. The MUSIC spatial spectrum represents the inverse of a summation of array responses where each response has a null at the AOA and polarization of each incident plane wave.

4.0 Computer Simulations

A superresolution DF system utilizing the six element antenna array described has been modeled on a computer. Four uncorrelated signals are incident upon the array, each having a signal-to-noise ratio of 40 dB. Five hundred snapshots were utilized in the construction of the covariance matrix. The signals are separated in increments of thirty degrees in Φ and all arrive at Θ equal to 86 degrees. The polarization of each signal is different. A contour plot of the spatial spectrum is shown in Figure 2 and a three dimensional plot in Figure 3. All four signals are resolved at their proper angles and their locations are unique. This illustrates the ability of the array to DF on as many as four signals simultaneously when used with superresolution algorithms.

5.0 DF Results on Measured Data

The antenna array and superresolution algorithm has been tested on signals of opportunity. The antenna array was located in the center of a 500 foot radius ground plane 2 meters off the ground. The effect of an infinite ground plane was included in the array's spatial response. Figure 4 illustrates the spatial spectrum that resulted from processing 15 milliseconds of data when receiving WWV at 15 MHz. Three noise eigenvalues were used. The spectrum shows two peaks. One is located at approximately 300 degrees in azimuth and approximately 20 degrees off the horizon plane. This is due to the direct skywave path of WWV. Another peak occurs at approximately 50 degrees azimuth and in
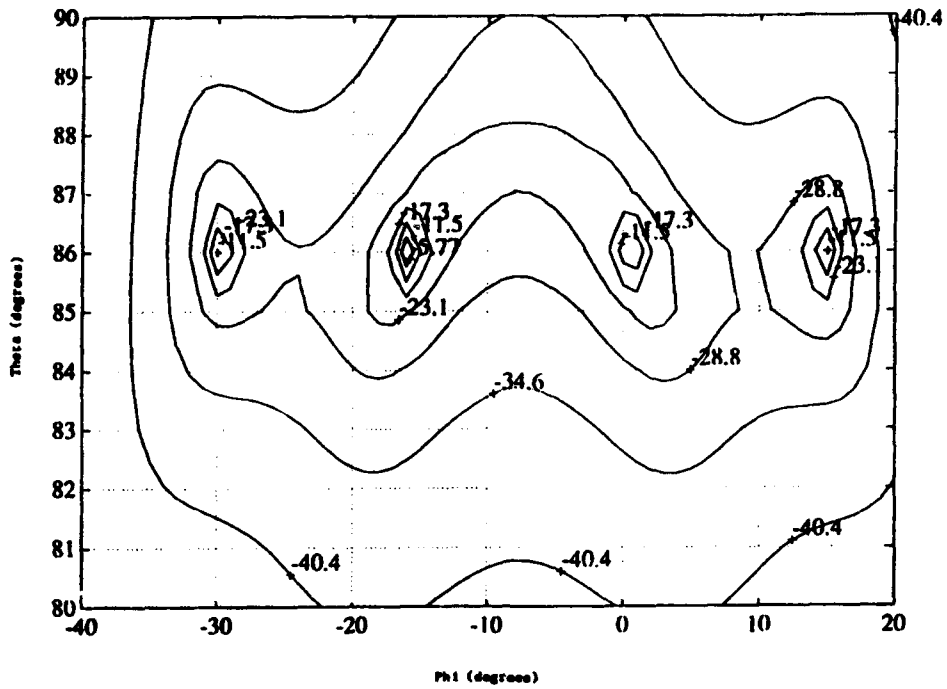
Figure 2. Computer Simulation of MUSIC Spacial Spectrum
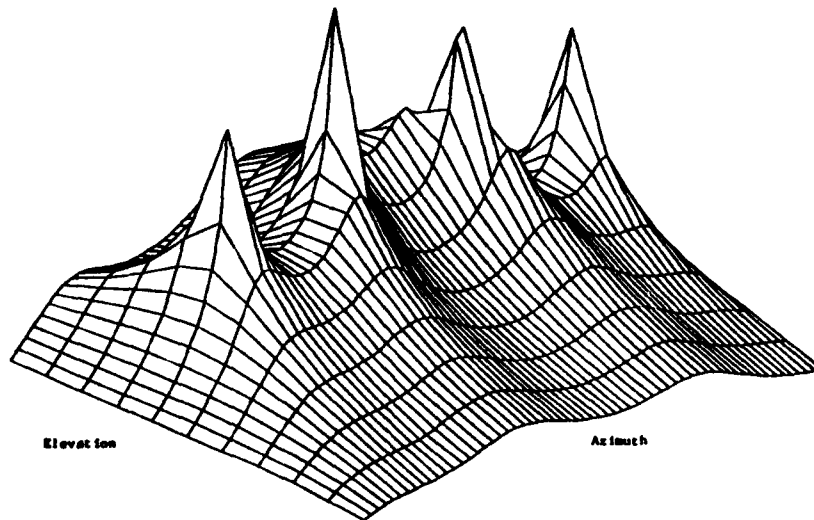
Figure 3. Three Dimensional Plot of MUSIC Spacial Spectrum
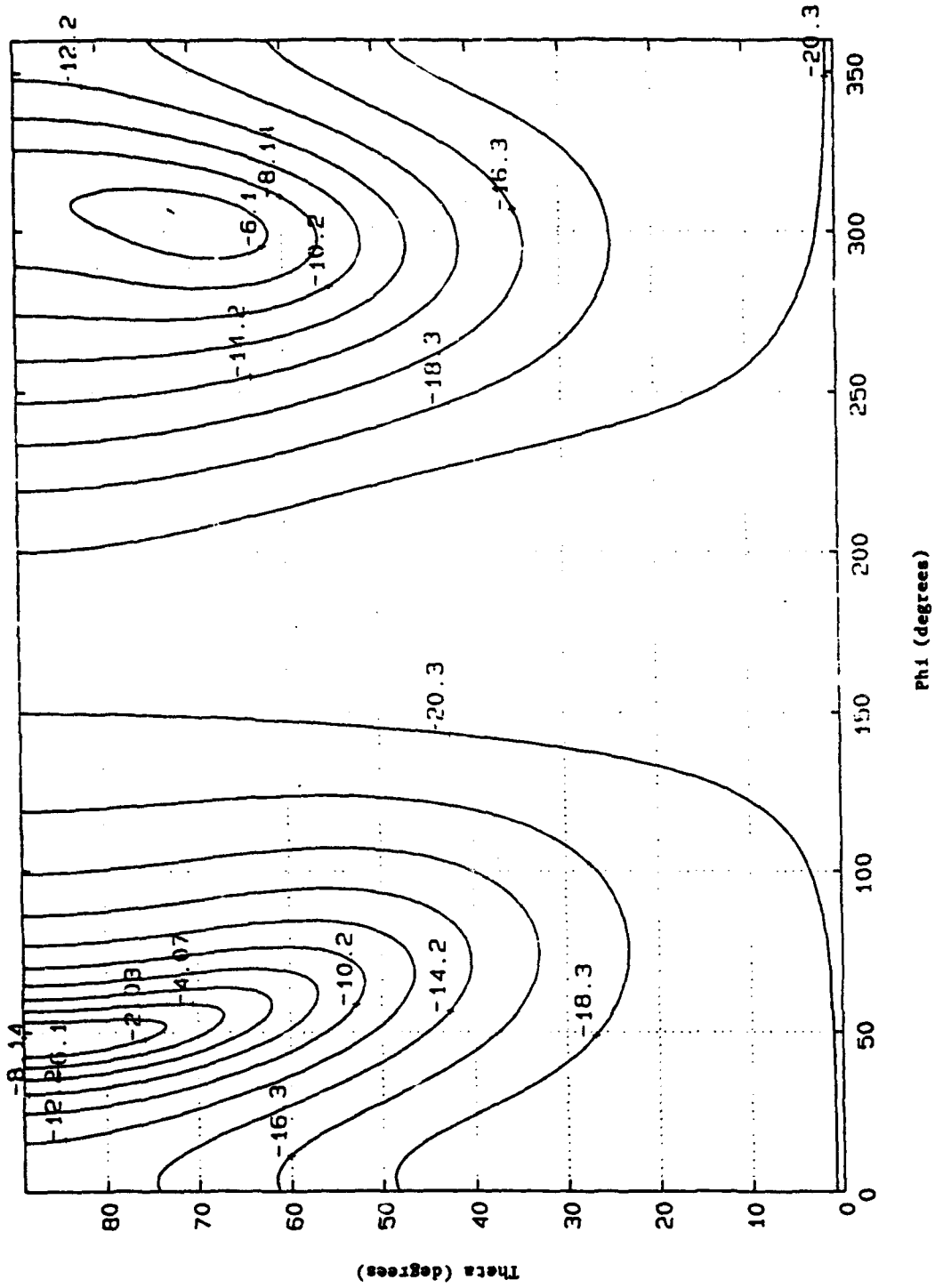
Figure 4. MUSIC Spacial Spectrum of Measured WWV Data

the horizon plane. This peak is due to reradiation of the direct signal by a group of towers located approximately 1000 feet from the receive site. While not extremely rigorous, these results suggest the ability of the array to DF skywave propagated signals. Skywave signals typically give small aperture DF systems difficulty because their polarization can change over time. Additionally, DF of reradiated signals is also demonstrated.

VI. Conclusions

An electromagnetically complete antenna array has been designed and built for use in the HF band. It is inherently broadband because it utilizes electrically small antenna elements in a colocated geometry. Furthermore, it is physically compact and isotropic to AOA and polarization when utilized as a receive antenna. Computer simulation indicates it can DF on up to four signals simultaneously when modern superresolution algorithms are utilized. Its ability to DF on a skywave propagated signal, as well as reradiation of this signal by local scatterers, has been demonstrated experimentally. Other possible uses of the array include spatial filtering for discriminating cochannel signals based upon their AOA and polarization. Additionally, the array can be utilized as an element in an array for more degrees of freedom. Finally, it can be used as a field probe for measurement of either the average or instantaneous Poynting vector.

REFERENCES

1. Schmidt, R.O., "Multiple Emitter Location and Signal Parameter Estimation", in Proc. RADC Estimation Workshop, Rome Air Development Center, Rome, NY, October 1979.

2. Ferrara, E. and T. Parks, "Direction Finding with an Array of Antennas having Diverse Polarizations," IEEE Trans. on Antennas and Propagation, Vol. 31, March 1983, pp. 231-236.

Summary of
THE MONOPOLE AS A WIDEBAND ARRAY ANTENNA ELEMENT

Don Collier and Harold Shnitkin
Norden Systems, Inc.
P.O. Box 5300
Norwalk, CT. 06856
(203)852-6339/FAX (203)852-7721

ABSTRACT

An inexpensive, wideband array antenna element has been developed for application in the frequency range utilized by airport ground-to-air beacon systems. The element operates over a 2.7-to-1 bandwidth, making it useful in both civilian and military applications. This novel design is a variant of the monopole above a ground plane, but with higher gain and wider bandwidth than the traditional monopole. Measured far-field patterns taken in the Norden compact range and photographs of working models will be presented.

1. BACKGROUND

In recent years, ground-based and sea-borne aircraft identification systems have utilized an increasing portion of the electromagnetic spectrum. Consequently, civilian and military beacon systems have been forced to broaden their operating bandwidths, requiring, in turn, antennas with wider band transmit and receive capabilities. In addition, these antennas, usually designed as linear arrays, have dimensional limitations dictated by their physical location. Whether at sea or near the edge of an airport runway, they are normally required to rotate in azimuth at a fixed rate without excessive wind loading. The array element design described

below is the product of a two-year R&D effort oriented toward production of an economical, wideband device having maximum gain, minimum VSWR, and size commensurate with the dimensions imposed by the beacon user agency.

2. DESCRIPTION

The overriding considerations of the just-completed R&D investigation were electrical performance within the volume constraint, as well as simplicity, manufacturability and low weight. The major electrical performance parameters were gain throughout the required frequency band and low VSWR.

Four candidate array element designs were selected, constructed and tested to determine which would best meet the array user's needs. A log periodic, a microstrip flared notch, a bowtie horn and a quarter wave stub were all built, optimized, and range tested. All four approaches were breadboarded (Figures 1 through 4) and extensively evaluated.
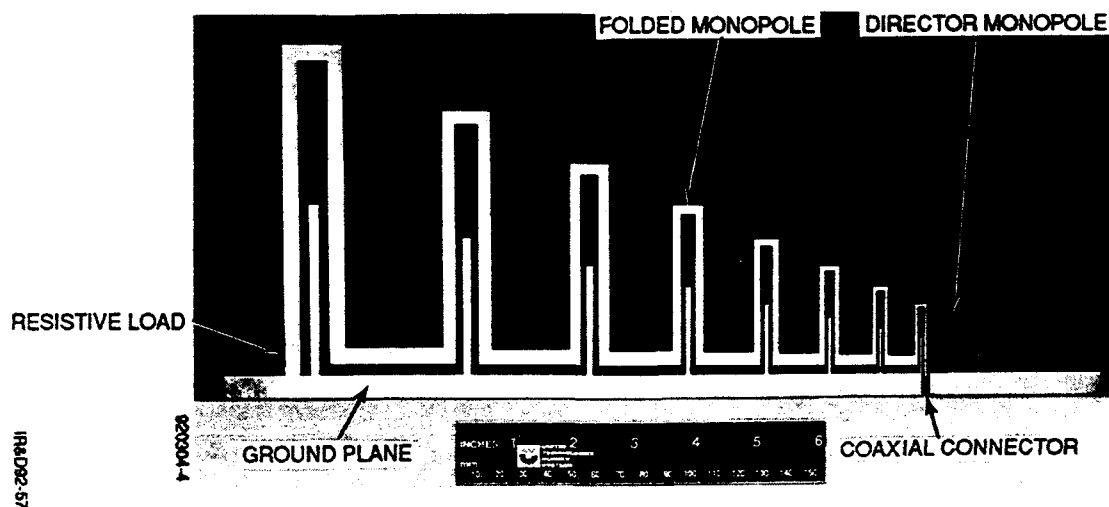
Figure 1. Log Periodic Antenna Element

1/4 WAVE SHORTED
PARALLEL PLATE
WAVEGUIDE SECTION

BOWTIE
RADIATING ELEMENT

METALLIC GROUND PLANE
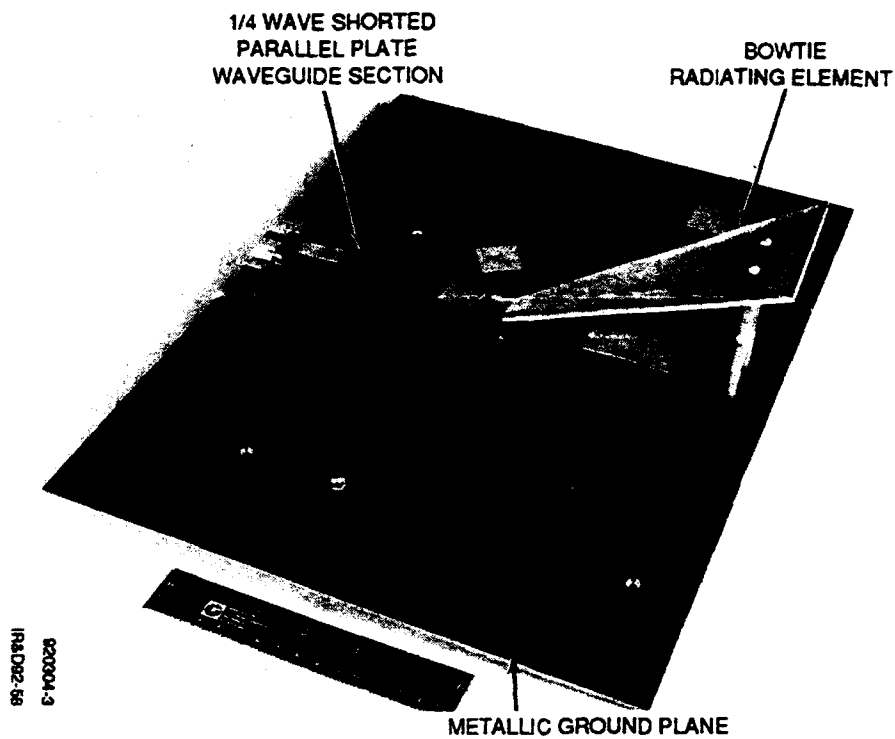
Figure 2. Bowtie Horn Antenna Element

COAXIAL FEED CABLE

MICROSTRIP
SLOTTED LINE

FLARED
RADIATING ELEMENT

HIGH IMPEDANCE
SLOTLINE CAVITY
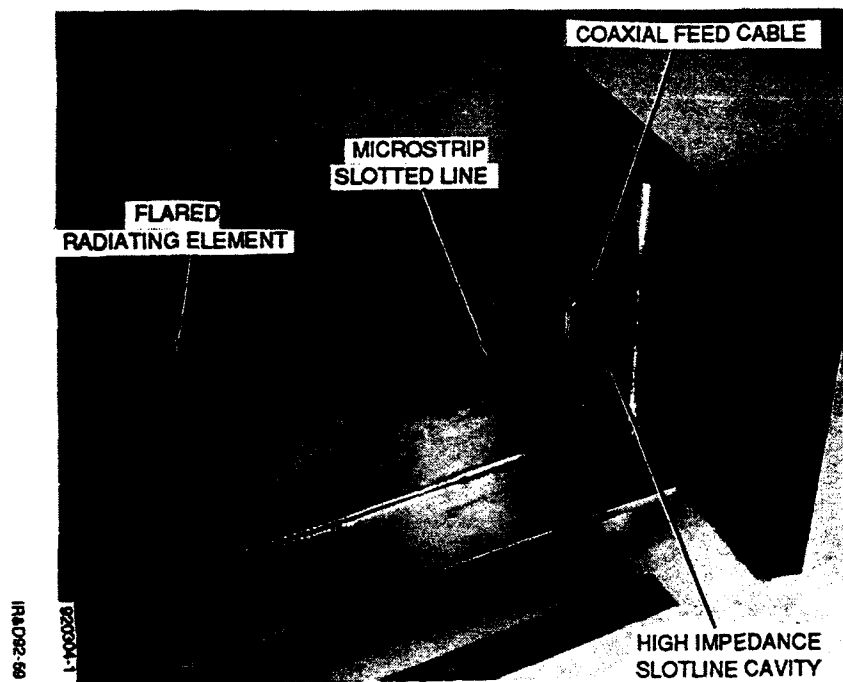
Figure 3. Flared Notch Antenna Element

408
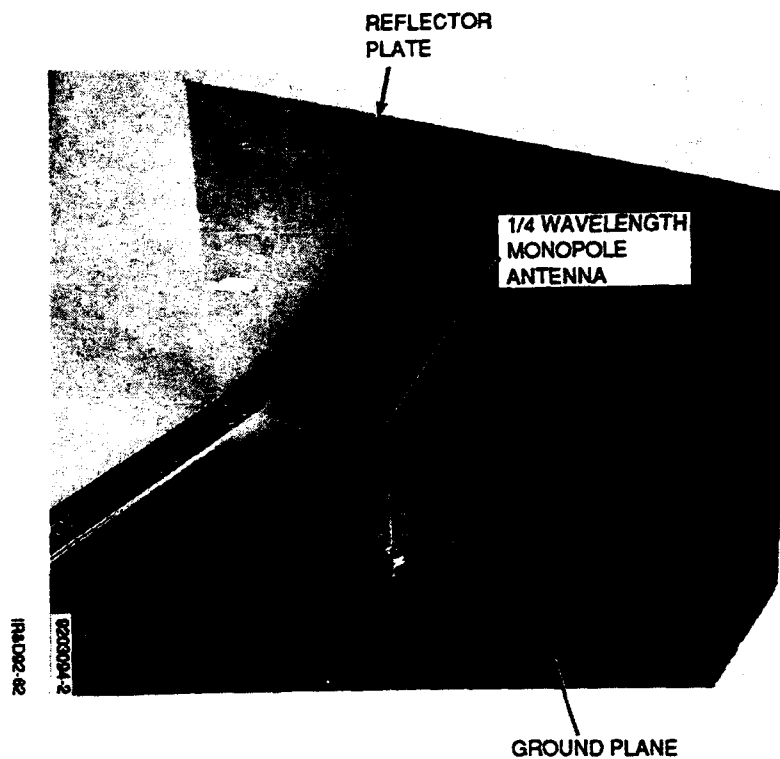
Figure 4. Quarter Wave Stub Antenna Element

The 10.5-inch height and 11.0-inch depth constraints, imposed by the user, presented severe difficulties in narrowing the elevation beam width sufficiently to produce the required values of antenna gain. Consequently, techniques employing metallic reflectors to create radiator images, which would effectively produce an electrical antenna array larger than the limited volume, appeared advantageous. This resulted in the selection of the single broadband monopole, together with a quasi vertical and a quasi horizontal metallic reflector. This design, further enhanced by a Teflon end-fire director, minimizes elevation beam width and maximizes gain by taking advantage of the three images created by the reflecting planes. See Figure 5 for an illustration of this principle.
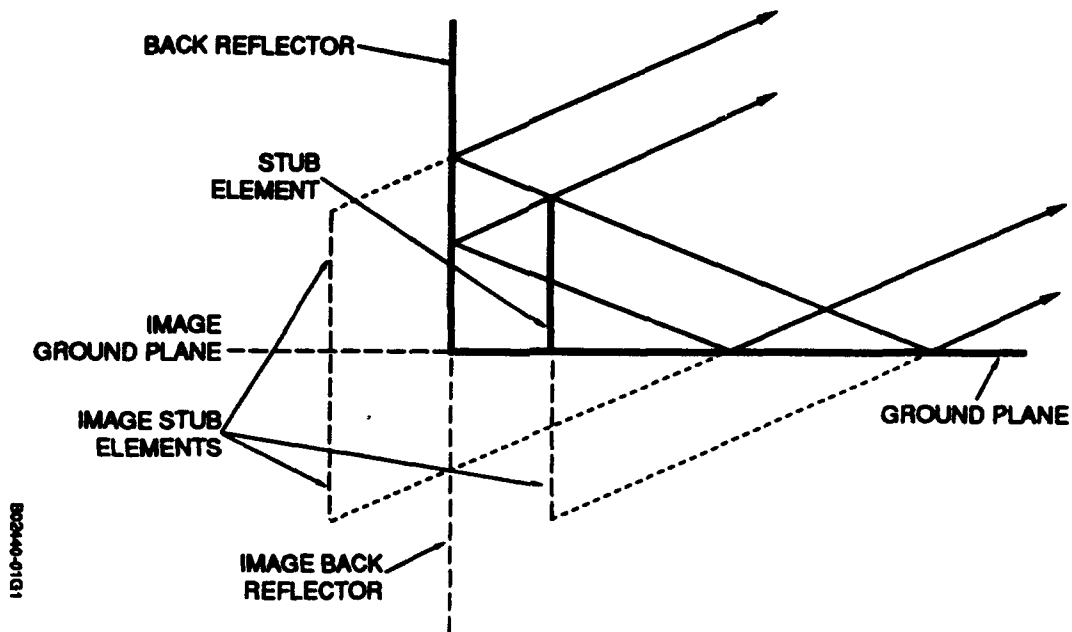
Figure 5. Computer Simulation of Single Stub Over Ground Plane with Reflector

An additional benefit of the single monopole element is its simplicity and its ability to sustain both the maximum peak and average RF powers. A four-element array utilizing this design is seen in Figure 6.

The three rejected candidate designs are discussed in the following paragraphs and compared to the chosen monopole.

2.1 Log-periodic Monopole Array (See Ref. 1 and Figure 1)

The depth constraint forced an apex angle of 30 degrees onto the log periodic array configuration, resulting in an excessive elevation beam width of 77 degrees as measured on Norden's LP models during the '91 IR&D effort. See Figure 7.
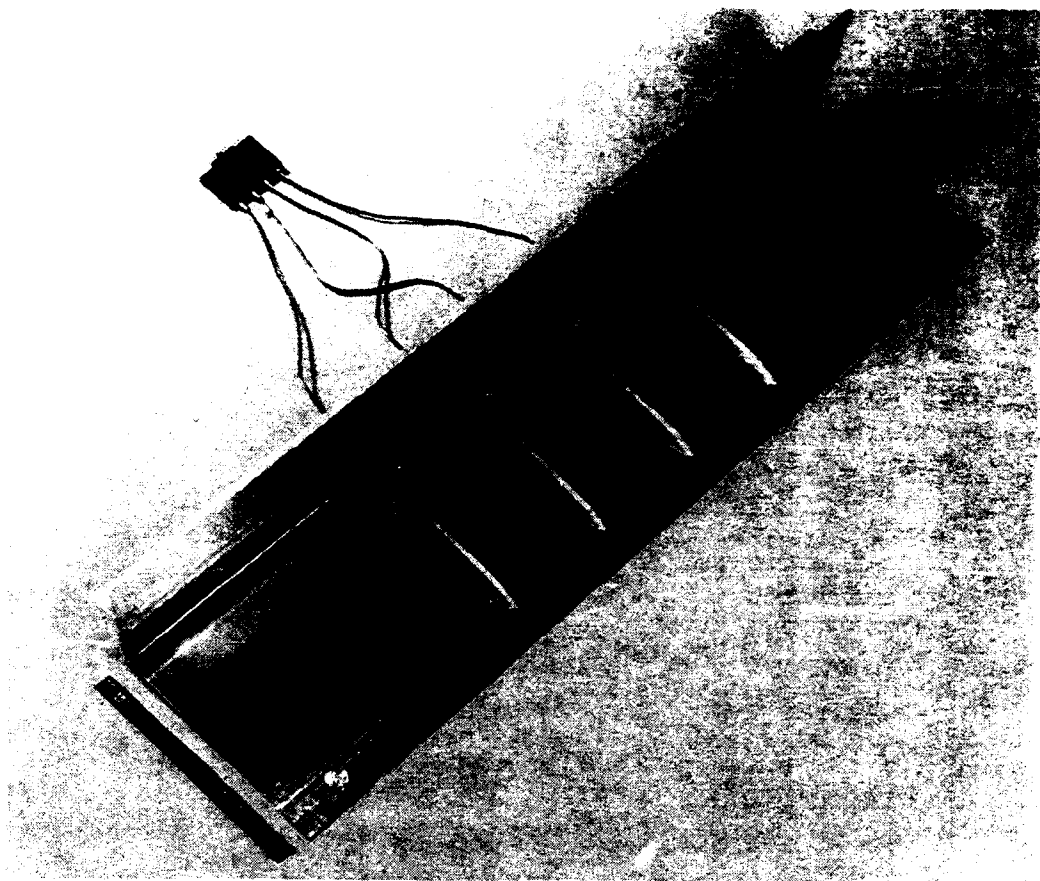
Figure 6. Four-Element Array with Stripline Combiner

The active region of the log periodic array becomes proportionately smaller and moves towards the LP antenna apex at higher frequencies, causing the effective antenna size to decrease. This prevents taking advantage of the total available volume at the higher frequencies, resulting in less than the maximum available gain.

A second disadvantage is that the transmission line losses of an LP antenna exceed those of a monopole by about 0.4 dB, due to the much longer transmission line path inherent in the log-periodic configuration.
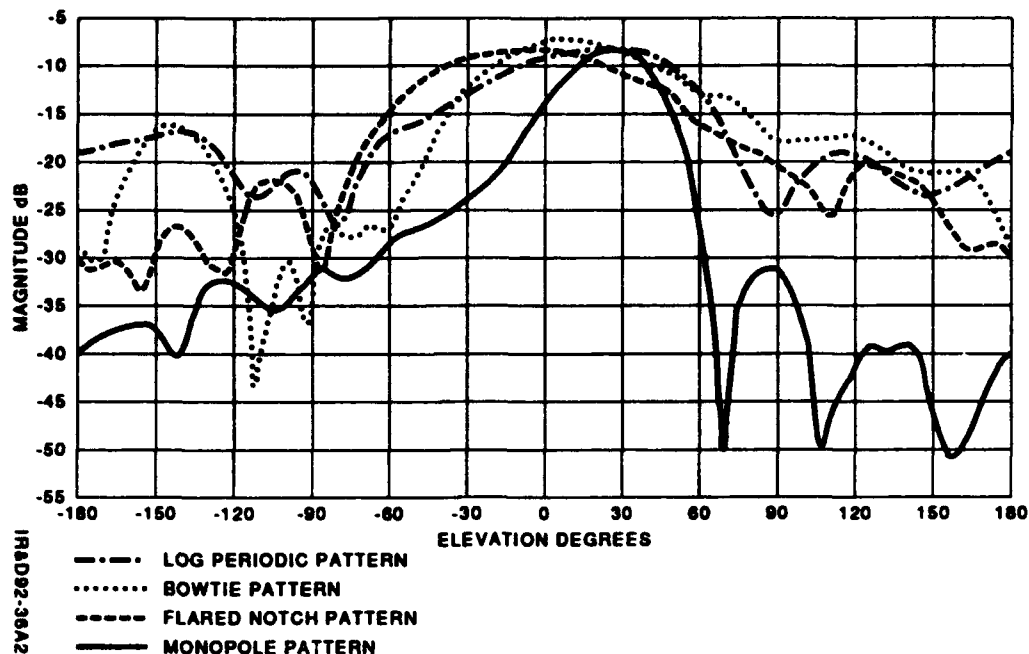
Figure 7. Representative Antenna Element Patterns at f_{min} +1.0 GHz

The close spacing between the current-carrying antenna elements in the vicinity of the apex of the log-periodic configuration present a risk to safe operation at the maximum RF power.

2.2 Flared Bow-Tie-Horn (See Ref. 1 and Figure 2)

Experimental results during Norden's '91 IR&D program showed that the currents traveling on the outside of the flared horn preclude meeting both sidelobe and backlobe requirements. Adding absorber at the outside flared surface would introduce substantial insertion loss and RF power dissipation. Thus, two serious drawbacks are encountered: Reduced antenna gain and antenna overheating/fire-hazard.

2.3 Dual Flared Notch (See Figure 3)

Absence of images in the vertical reflector plane broadens the flared notch elevation beam width, relative to a monopole with two reflecting planes. A detailed comparison of the elevation beam widths, between NRL data and measurements of the Norden IR&D monopole antenna model (See Figure 4) is given in Table 1.

Table 1. Elevation Patterns

Frequency		3 dB BW of NRL Dual Flared Notch (deg.)	3 dB BW of Norden Monopole (deg.)	Improvement in Gain Monopole v. Notch (dB)
f_{min}		89	74	+0.8
f_{min}	+ 0.1	86	63	+1.3
	+ 0.2	78	65	+0.8
	+ 0.3	68	56	+0.8
	+ 0.4	62	51	+0.9
	+ 0.6	53	46	+0.6
	+0.8	44	41	+0.3
	+ 1.0	34	40	-0.7

The broad azimuth beam width of the elemental flared notch raises the far-out azimuth sidelobes. The monopole with its three images possesses a narrower elemental azimuth beamwidth and therefore assures lower far-out side lobes.

Since the flared notch forms a lengthy transmission line connecting the feed point to the aperture, an ohmic insertion loss, not present in the monopole, will lower the net gain of the flared notch antenna, especially at the maximum frequencies.

2.4 Test Result Comparison

A prototype of each V-Pol radiating element design was fabricated and evaluated (See Figures 1 thru 4). Far field patterns were measured in Norden's Compact Antenna Range. Representative patterns for the four designs, taken at

413

f_{min} + 1.0 GHz, are shown in Figure 7. Other typical pattern results, taken at f_{min} + 0.6 GHz are summarized in Table 2.

Table 2. Array Element Test Results at f_{min} +0.6 GHz

Element Type	Elevation Beam Width (deg)	Elevation Sidelobe (dB)
Log Periodic	76	-9
Flared Notch	80	-12
Bowtie Horn	74	-9
Monopole	46	-15

After several iterations of optimizing and retesting, it appeared that only the monopole candidate configuration could successfully meet the design criteria of 18 dB gain at beacon frequencies as well as the other wideband requirements.

Next, the original design was modified into the shape of inverted cone, when it became apparent that this configuration had better impedance matching properties over the required pass band. See Figure 8 for an implementation of the conical monopole array.

The distance between the array monopole elements and the quasi-vertical reflecting back-plane is 0.24 wavelengths at present beacon frequencies. This spacing permits optimum phase addition between the conical monopoles and their images, producing minimum element beam width and sidelobes. The length of the monopole elements and the matching network at the base of each are designed to assure lowest VSWR at mid-band without exceeding 2:1 at any of the other frequency bands.
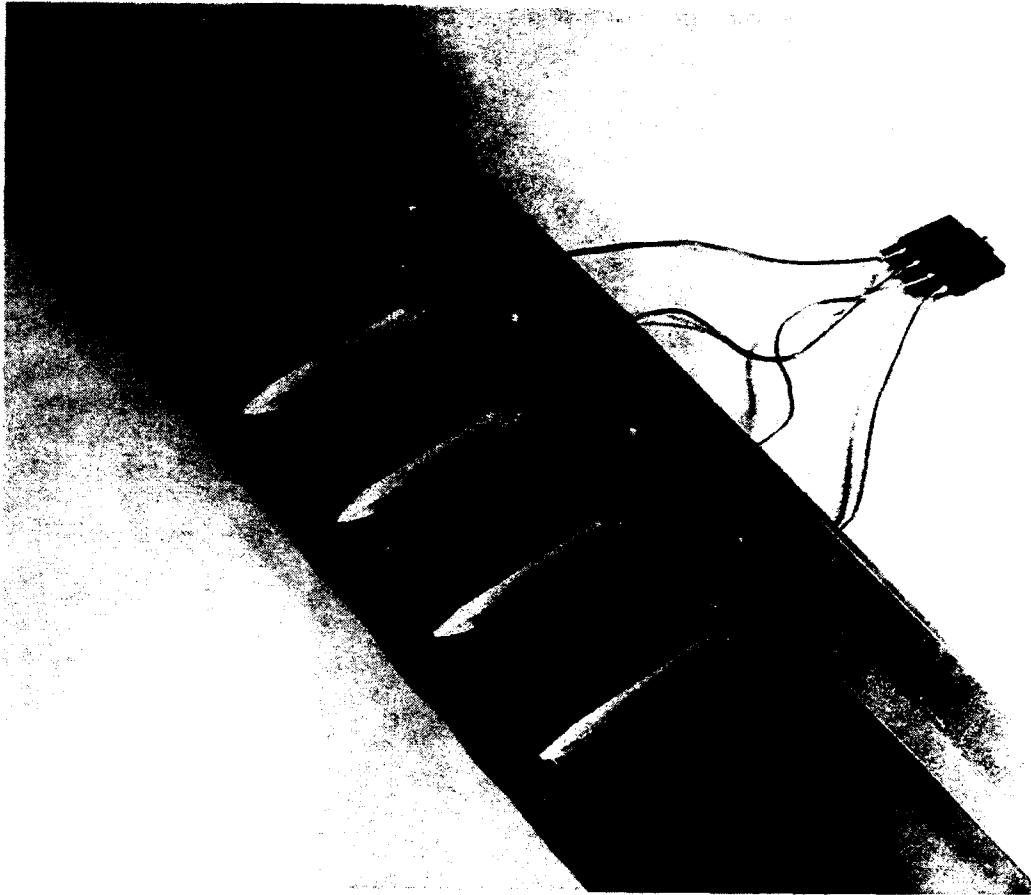
Figure 8. Conical Monopole Array

Teflon slow-wave directors were incorporated into the V-pol array design in order to minimize the elevation beam width and achieve maximum gain at the upper frequencies. The need for improvement in the elevation pattern shape became apparent during IR&D range testing of the prototype monopole array. This effort was detailed in the 1992 Norden IR&D Final Report, Reference 2.

2.5 Conical Monopole VSWR

The impedance of a 42-degree, full apex-angle, conical monopole as shown in Figure 8, was investigated. A 3.9-inch high cone was selected so that the electrical height varies from 70 to 187 electrical degrees. From Reference 4, data for monopole impedance over an infinite ground plane was obtained. This data was verified using a breadboard conical monopole model, a 24 X 24-inch ground plane, and an HP 8510 network analyzer, yielding the Smith chart shown in Figure 9. These results required a matching network consisting of a series, open-circuited stub (2.75 inches long in air and Z_0 = 69 ohms) and a 2.4-inch long airline with Z_0 = 85 ohms, cascaded with the conical monopole, to achieve an optimized VSWR. Table 3 shows the results of attaching the matching network to the 3.9 inch conical monopule over a ground plane. VSWR under 1.15 within the beacon band, under 1.83 in the lower bands and under 1.69 at the upper bands is achieved. Some future adjustments in the matching network need to be made when the effects of the reflecting plane, of mutual coupling and of interaction with the horizontally polarized radiators are included.

Table 3. Detailed VSWR Prediction for Conical Monopole

Freq.		Input R (ohms)	Input X (ohms)	Refl. Coeff. Margn.	VSWR	Insert Loss (dB)
f_{min}		63.602	14.930	0.176	1.43	-0.14
f_{min}	+ 0.1	89.685	-10.862	0.294	1.83	-0.39
	+ 0.2	64.299	-27.615	0.264	1.72	-0.31
	+ 0.3	52.864	-21.860	0.210	1.53	-0.20
	+ 0.4	46.819	-4.556	0.057	1.12	-0.01
	+ 0.5	48.850	4.866	0.051	1.11	-0.01
	+ 0.6	61.497	17.227	0.184	1.45	-0.15
	+ 0.7	74.075	16.441	0.233	1.61	-0.24
	+0.8	84.099	5.740	0.258	1.69	-0.30
	+ 0.9	76.732	-14.535	0.239	1.63	-0.25
	+ 1.0	53.198	-18.203	0.176	1.43	-0.14
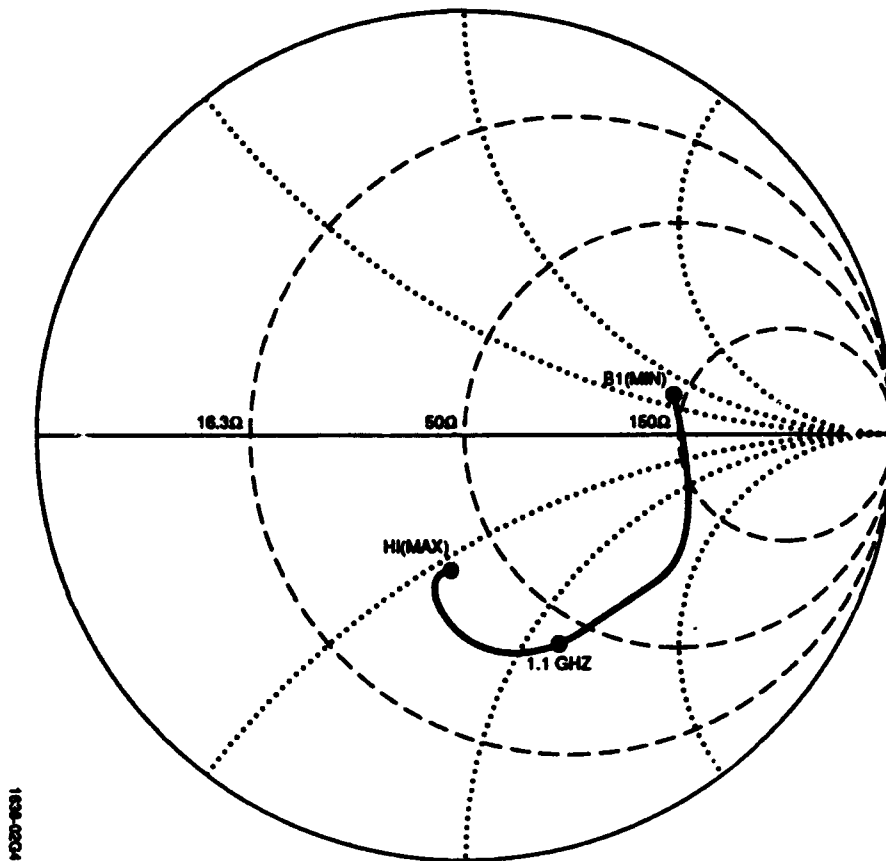
Figure 9. Measured Conical Monopole Input Impedance

Finally, the conical monopole was replaced by a set of radial wires on a conical surface to minimize capacitive integration of the vertically polarized monopoles with a required, horizontally polarized array located near the centerline of the VP array. See Figures 10 and 11 for the final configuration.
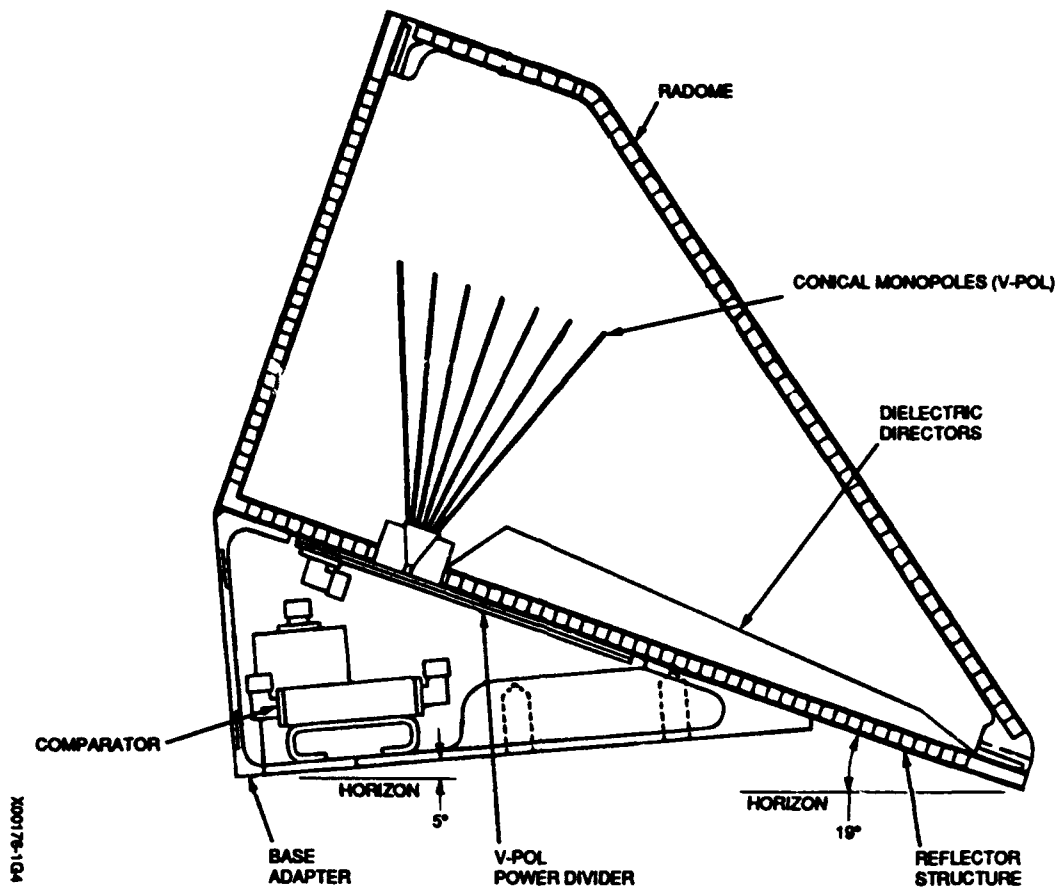
Figure 10.   Cross-sectional View of the Antenna Assembly
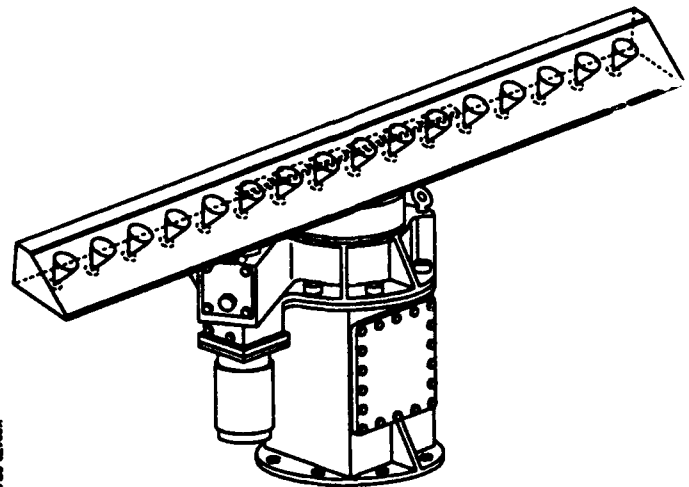
Figure 11.   Beacon Array Mounted on Pedestal

418

3. CONCLUSIONS

The use of the monopole over a ground plane for antennas having a narrow band pass is not new. Its utilization in a beacon system having a wide frequency range, and inducing it to function better than other, more commonly used broadband elements, requires some originality. The array element described above was unique enough to out-perform all other approaches tried, and gave Norden an economical, manufacturable candidate to propose to the beacon user.

4. REFERENCES

The descriptions in this paper are partially based upon a number of readily available references. These are sequentially numbered and referred to in the text as follows:

1. G. Harrison, et al, "A Shipboard IFF Antenna Application," 1991 Norden IR&D Report

2. H. Shnitkin, et al, "A Shipboard IFF Antenna Application," Norden 1992 IR&D Report, No. B02440.

3. W.R. Pickles and J.B.L. Rao, "Broadband Array Antenna of Dual Flared Notch Elements," 1992 Antenna Application Symposium

4. Antenna Engineering Handbook, H. Jasik, pp. 3-10

5. H. Shnitkin, "Getting More Bandwidth from Dipoles," ELECTRONICS, Aug. 1962.

Slot - Fed Microstrip Antennas with a Microstrip Line

Yi Lin Chen

(University of Illinois, Urbana, IL 61801, USA)

Abstract

The cavity model theory is used to analysis the single patch and stacked patch microstrip antennas. The antenna is excited through a slot on the ground plane with a microstrip line. Comparing with full-wave formulation, the cavity model theory can not only provide much physical insight into the antenna operation, but also reduce the computing time by several orders of magnitude. The agreement between theory and experiment is excellent.

Introduction

The compactness of the microstrip antenna would have made it the most attractive ideal antenna if not for its inherent limitation in bandwidth. It has been shown that its bandwidth can only be increased effectively by increasing the antenna thickness. However, when the thickness increases much beyond 0.1 wavelength, the antenna loses its structural superiority as compared with other types of antennas, and , in fact, other conventional designs may even offer substantial better performance.

In this paper, a moderate improvement in bandwidth is attempted by using a double-stacked patch antenna rather than increasing thickness. In particular, for simplicity in large phased array fabrications, the patch is to be excited with a microstrip line through a slot in the common ground plane as shown in Figure 1. Strictly speaking, such a structure can only be analyzed by the so-called rigorous full-wave theory as in [2,3]. Unfortunately, as these references have shown, not only is this approach complex, laborious, and extremely time-consuming in computation, but the theoretical results are generally in poor agreement with the experimental data. A major factor, for the difficulty in obtaining good agreement is the fact that the antenna is a narrow band device and its impedance is very sensitive to the antenna parameters. A small difference between the theoretical and experimental

model can lead to a significantly different final result. Since all practical antenna can only be constructed within a certain tolerance, one may wonder whether a much greater effort expended for the full-wave analysis is truly worthwhile (except perhaps for the purpose of an academic exercise). Following this philosophy, an attempt is made here to modify the simple cavity model theory so that it can be applicable to this structure. Although this technique requires the modification of few antenna parameters, yet each can be determined, based on the physical argument, within a narrow range. As the final results will show, not only the computation time (about a fraction of one second on a workstation) is several orders of magnitude smaller than that of full-wave analysis, the agreement with the measured data is much superior. In application, this theory could provide a close first order solution, from which a final design would readily be reached with some minor iterations.

In the following, we first summarize the modified cavity model theory for a single patch fed with a microstrip line through a slot in the ground plane, then the usefulness of this simple theory is demonstrated with typical examples. Finally, this approach is extended to the stacked patch by assuming the field distribution between the two patches to be the same as that under the bottom excited patch except for a reduction in the field magnitude since the two fields are coupled through their edges. Furthermore, in this study the antenna is intended to operate for two orthogonal polarizations, and therefore only square patches with slot located at the center are considered in detail here. Obviously, the extension of this work to rectangular geometry is straightforward.

Analysis

The cavity model theory assumes [4] that the fields under the patch are independent of z, then electric field E has z component only, magnetic field H has xy components only. The effect of the slot can be modeled by an equivalent magnetic current source M, extending above the slot, from the ground plane to the patch with a uniform density in order to excite the z-independent field. This approximation is expected to be good for thin substrate. Let magnetic current density be

$$\overline{M} = \hat{x}[U(y+\frac{w}{2})-U(y-\frac{w}{2})][U(x+\frac{L}{2})-U(x-\frac{L}{2})]\frac{\cos(\frac{x}{L}\pi)}{wL},$$

where U is unit step function.
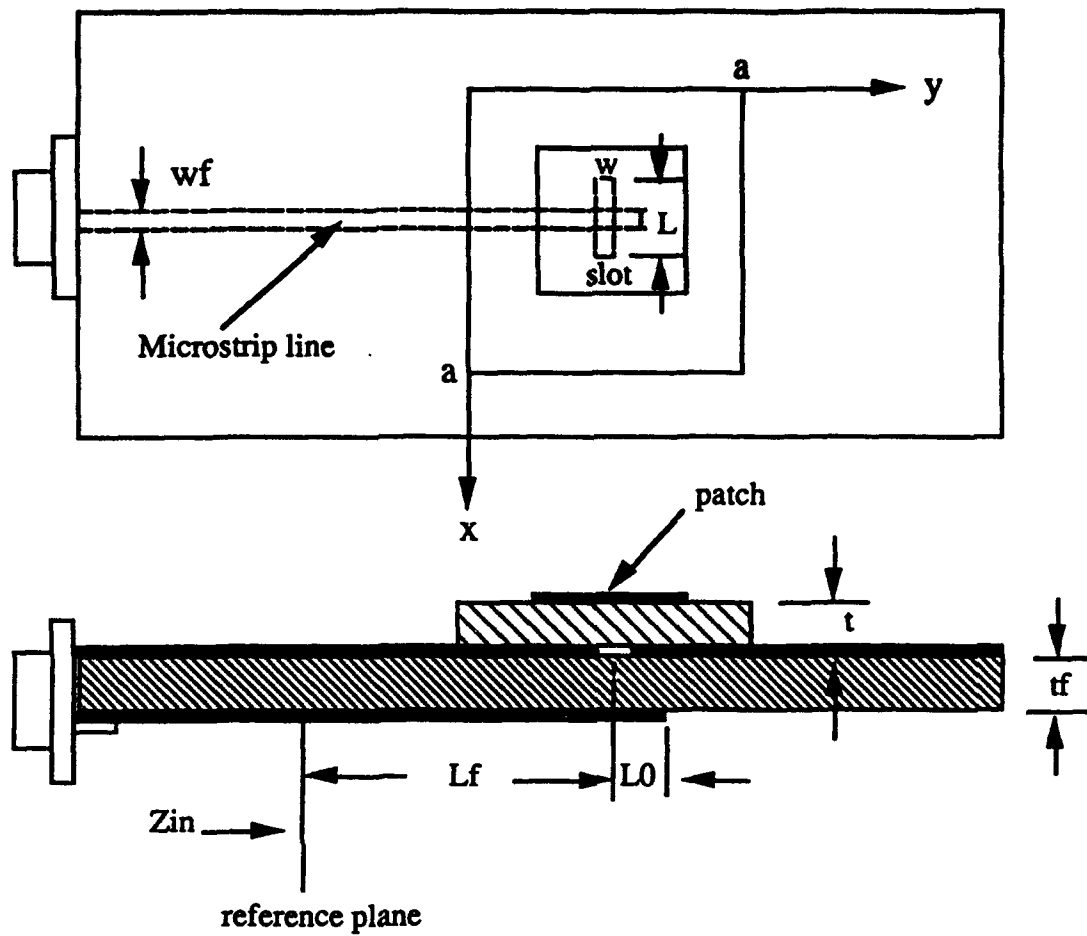
Fig. 1   Geometry of slot fed single patch microstrip antenna.
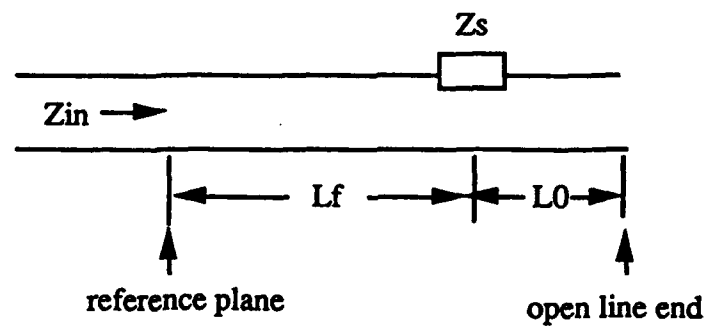
Fig. 2 Equivalent circuit for microstrip feed line.

The E field due to the magnetic current excitation can be found as

$$E_z(x,y) = \sum_{m=0}^{\infty} \sum_{n=0}^{\infty} \frac{c_{mn} g_{mn}}{k^2 - k_{mn}^2} \psi_{mn}(x,y),$$

where

$$c_{mn} = \frac{\frac{4\xi_{mn}}{\pi w}}{(\frac{mL}{a})^2 - 1}$$

$$g_{mn} = \sin\frac{n\pi}{2}\cos\frac{m\pi}{2}\sin\frac{n\pi w}{2b}\cos\frac{m\pi L}{2a}$$

$$\psi_{mn}(x,y) = \xi_{mn}\cos\frac{m\pi}{a}x\cos\frac{n\pi}{b}y$$

$$\xi_{mn} = \sqrt{\frac{\in_m \in_n}{ab}}$$

(1) Single patch excited by a microstrip line through a slot in the ground plane.

The input impedance at the slot center, referred to as slot impedance, can be expressed as:

$$Z_{in} = jk_0\eta_0 tk_m^2\{(-\frac{4L^2}{\pi^3 w^2})[\sum_{m=0,2,}^{\infty} TEMP\frac{\sin(\frac{\pi}{2}B) - \sin(\frac{\pi}{2} - x)B}{B\cos(\frac{\pi}{2}B)}] + \frac{L}{2w}\}^{-1},$$

where

$k_0 = 2\pi f/c$, f is frequency in GHz, c is the speed of light in free space in cm,

$\eta_0 = 377\Omega.$

L,w are the length, width of the slot in cm

$B^2 = (\frac{a}{\pi})^2 k^2 - m^2$, where a is the size of the square patch in cm,

$x = \frac{\pi w}{a}, (0 \le x \le \pi),$

$k = k_0\sqrt{\varepsilon_r}(1 - j0.5/Q),$ whereε_r is the relative dielectric constant of the dielectric substrate. Q is the quality factor of the microstrip patch antenna which can be found in [6].

$$\text{TEMP} = \begin{cases} 1 \text{-------------------------------} m=0 \\[2em] 2[\dfrac{\cos(\dfrac{m\pi L}{2a})}{(\dfrac{mL}{a})^2 - 1}]^2 \text{-------------} m \neq 0 \end{cases}$$

Impedance measurement takes place at reference plane where higher order modes become insignificant. The TRL (THRU-REFLECT-LINE) technique is used for the calibration. The field at the junction of microstrip line and slot is complex and consists of many high-order modes. Therefore, strictly speaking, the traditional method of measuring impedance at the slot center by shorting the line there has no real meaning. The impedance that can be defined and actually measured must take place on the line where only the TEM wave exists. By the same token, the theoretical computation of the impedance at the slot is questionable since the field is nonconservative and voltage can not be uniquely defined. To alleviate these difficulties, first, the comparison of theoretically computed and experimentally measured impedance will be made at a reference plane on the line sufficiently far away from all discontinuities so that high-order fields become insignificant. Second, for theoretical computation, the slot impedance is simply and somewhat arbitrarily defined, as in circuit, to be $|v|^2 / P$. As is well known, in a nonconservative field, the voltage v across the slot can not be uniquely defined. From experimental data, it appears that v could be related to the magnetic current density m by the following relation:

$v = k_m m(wt)$.

where the coefficient $k_m \approx 0.3$ to 0.6, depending on t, w and ε_r. A justification of this relation perhaps could be obtained by static approximation. Based on physical argument, it seems that the narrower is the slot, the more meaningful is this definition. Therefor, this investigation is confined, more or less, to narrow slots. Following this spirit, the coupling between the slot and microstrip line can be regarded as in a series circuit, as shown in fig. 3.

The input impedance at reference plane:

$$Z_{in} = \frac{(z_s + z_{op}) + j\tan(k_f L_f)}{1 + j(z_s + z_{op})\tan(k_f L_f)}$$

For the close agreement with measured data, the patch dimension a, slot length L, and open microstrip line length L_0 have to be slightly modified as,

$a_e \quad a + k_a t, \quad L_e = k_L L, \quad L_{0e} = k_{L0} L_0.$

where $k_a, k_L, k_{L0} \approx 1$.

As is well known, in a non-conservative field, the voltage v across the slot

can not be uniquely defined. From experimental data, it appears that v could be related to the magnetic current density m by the following relation:

$v = k_m m(wt)$.

where the coefficient $k_m \sim 0.3$ to 0.6, depending on t, w and ε_r. A justification of this relation perhaps could be obtained by static approximation.

(2) Stacked patch excited by a microstrip line through a slot in the ground plane.

Assuming the field distribution under the top patches is proportional to that under the lower patch except for a reduction in the field magnitude since the two fields are coupled through their edges.

$E_{z2}(x,y) = \alpha E_{z1}(x,y)$.

where subscript 1 or 2 refers to patch 1 or 2, respectively.

As suggested in [4], in the vicinity of resonant frequency the slot impedance can be viewed as the sum of a resonant model impedance and a reactance, which represents the contribution of all high-order models.

$$Z_s = \frac{|v|^2}{P + j2\omega(W_{E1} - W_{H1})} + jX_{f1},$$

where

$$P = P_{rad} + P_{d1} + P_{d2} + P_{cu1} + P_{cu2}$$

P_{rad} is the radiation power of the stacked patch antenna (lower and upper patches together) .

power loss due to dissipation in dielectric substrate

$$P_d = t\omega\varepsilon_r\varepsilon_0\delta_d \iint_s |E|^2 ds,$$

power loss due to finite conductivity of copper

$$P_{cu} = 2\sqrt{\frac{\omega\mu_0}{2\sigma_c}} \iint_s |H|^2 ds,$$

time average stored electric and magnetic energy

$$W_E = \frac{1}{2}\varepsilon_r\varepsilon_0 t \iint_s |E|^2 ds$$

$$W_H = \frac{1}{2}\mu_0 t \iint_s |H|^2 ds$$

$$\iint_s |E|^2 ds = \frac{32}{(\pi wa)^2} \sum_{m=0,2,}^{\infty} TEMP \sum_{n=1,3}^{\infty} \frac{\sin^2(\frac{n\pi w}{2a})}{(k^2 - k_{mn}^2)(k^2 - k_{mn}^2)^*},$$

$$\iint_s |H|^2 ds = [\frac{32}{(k_0 \eta_0 \pi wa)^2} \sum_{m=0,2,}^{\infty} \text{TEMP} \sum_{n=1,3,}^{\infty} (\sin^2 \frac{n\pi w}{2a})\text{TEMP2}] + \frac{1}{(k_0 \eta_0)^2 2wL},$$

$$\text{TEMP2} = \frac{1/k_{mn}^2}{(k^2/k_{mn}^2 - 1)(k^2/k_{mn}^2 - 1)^*} + 2\,\text{Real}(\frac{1/k_{mn}^2}{(k^2/k_{mn}^2 - 1)})$$

$$k_{mn}^2 = (\frac{m\pi}{a})^2 + (\frac{n\pi}{a})^2$$

feed reactance:

$$X_{f1} = \frac{|v|^2}{2\omega(W_{hm01} - W_{em01})}$$

W_{hm01}, W_{em01} are the energy stored in lower patch due to all modes except mode (0,1).
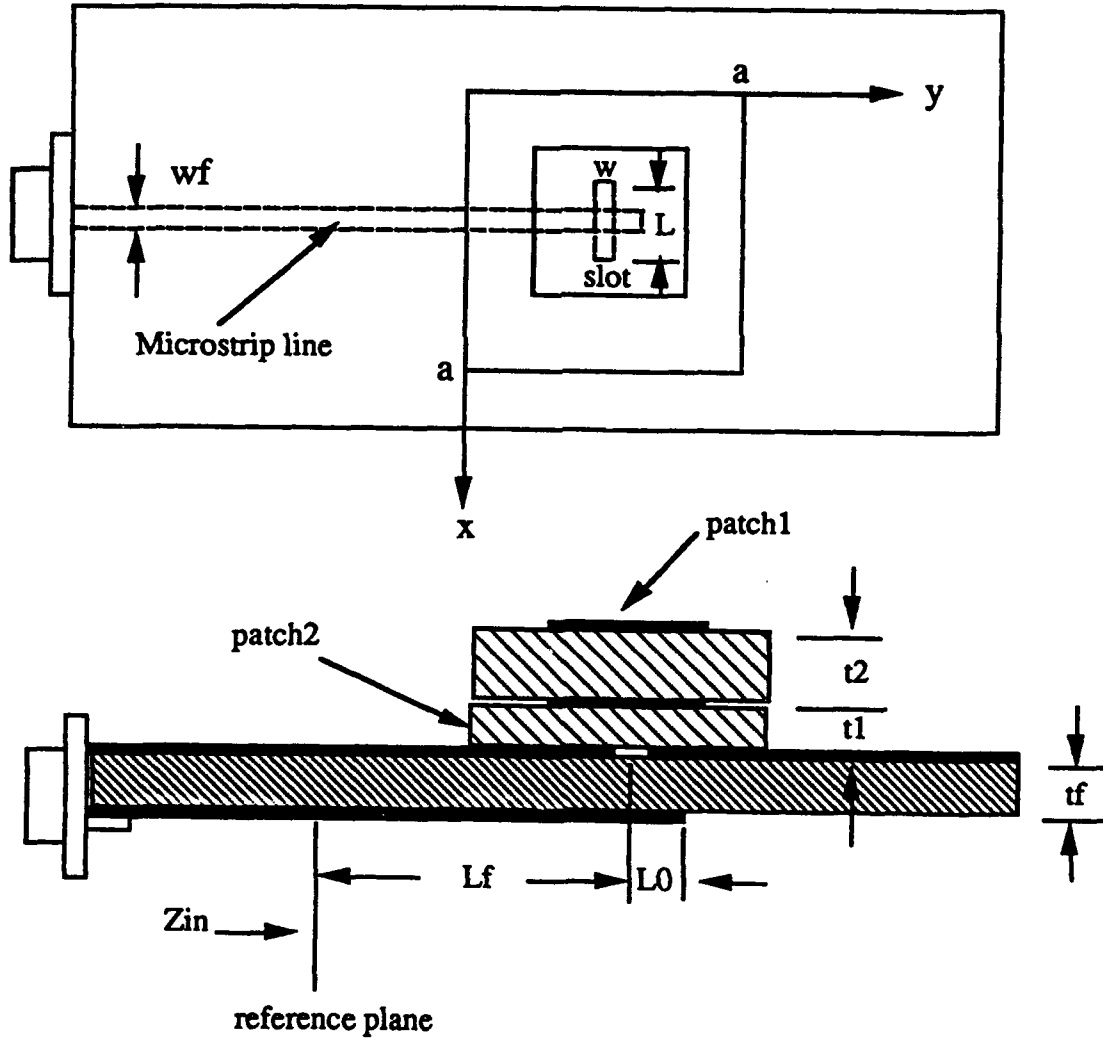
Fig. 3 Geometry of stacked patch slot fed microstrip antenna

426

Computed and Measured Results

It is important to point out that the convergence of summation over n is rather slow. For single patch slot impedance, a close form of summation over n can be obtained. For stacked patch antenna, in order to reach a reasonable accuracy, it is necessary to use a large number of terms, say n larger than 4000.

Impedance measurement takes place at reference plane when higher modes become insignificant. The TRL (THRU-REFLECT-LINE) technique is used for the calibration.

(1). Example 1: Single patch square microstrip antenna:
a=2.8 cm, t= 0.075 cm, L=1.04 cm, w=0.09 cm
Computed and measured results are plotted in Fig. 4.

(2). Example 2: single patch square microstrip antenna:
a=2.8 cm, t=0.15 cm, L=1.2 cm, w=0.09 cm
Computed and measured results are plotted in Fig. 5.

(3). Example 3: stacked patch microstrip antenna,
a1=a2=2.8 cm, t1=0.075 cm, t2=0.475 cm, L=1.4 cm, w=0.09 cm
Computed and measured results are ploted in Fig. 6.

(5). Example 4: stacked patch microstrip antenna,
a1=a2=2.8 cm, t1=0.15 cm, t2=0.31 cm, L=1.5 cm, w=0.09 cm
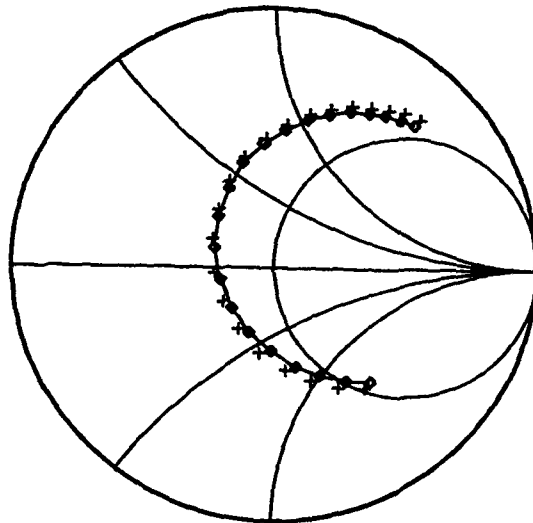
Fig. 4 Computed and measured input impedance of example 1.
+ + --- computed by " sfmaz1.f, ◆—◆   ---- measured
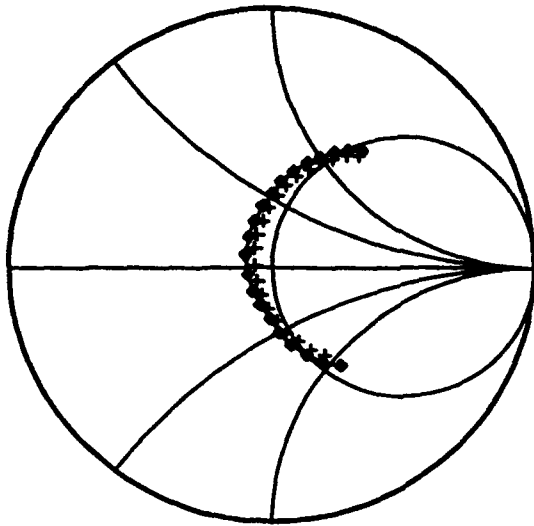
Fig. 5 Computed and measured input impedance of example 2.
+ + --- computed by " sfmaz1.f, ◇-◇ ---- measured
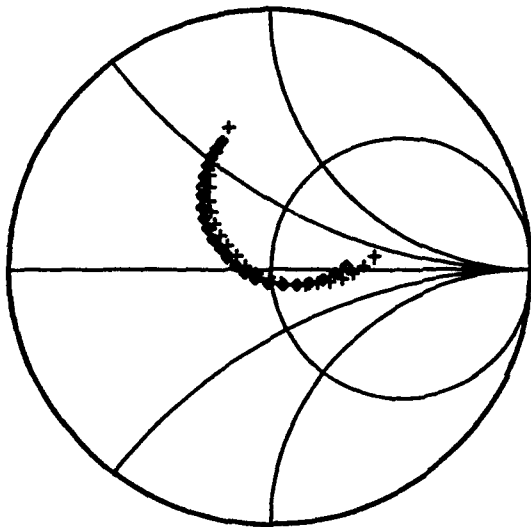
Fig. 6 Computed and measured input impedance of example 3.
+ + --- computed by " sfmaz3.f, ◇-◇ ---- measured
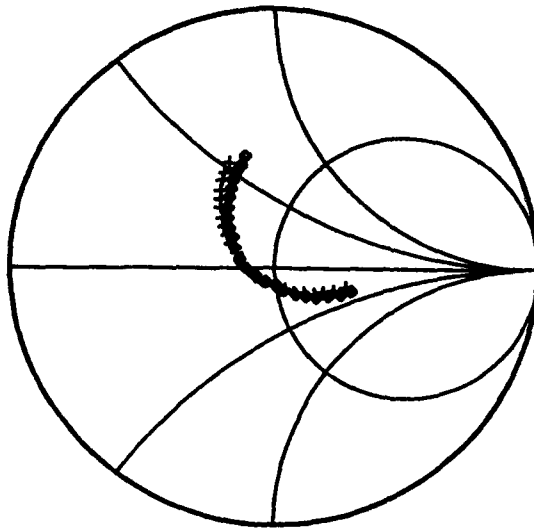
Fig. 7 Computed and measured input impedance of example 4.
╋ ╋ --- computed by " sfmaz3.f, ◇-◇ ---- measured

Conclusion

The cavity model theory is used to predict the impedance of single and stacked patch microstrip antennas in this paper. The agreement between theory and experiment is excellent for the thickness of antenna under a few hundredth of a substrate dielectric wavelength. Comparing with full-wave formulation, cavity model theory not only can provide much physical insight into the antenna operation, but also requires much less computation effort, usually several orders of magnitude smaller.

Acknowledgments

Reference

[1]. C. Harry Chen, P.G. Ingerson, Willian C. Wong, " Slot - coupled patch arrays ", 1991 Antenna Application Symposium.

[2] Frederic Croq, David M. Pozar, " Millimeter - Wave Design of Wide band Aperture - Coupled Stacked Microstrip Antennas ", IEEE, AP, Dec. 1991, pp.1770-1776.

[3] Chen Wu, Jian Wang, etc. " A rigorous Analysis of an Aperture - Coupled Stacked Microstrip Antennas ", Microwave and Optical Technology Letters, vol. 3, No. 11, Nov. 1990, pp. 400-404.

[4] W. F. Richards, " Microstrip Antennas ", Antenna Handbook, Charpter 10, edited by Y. T. Lo and S. W. Lee, Van Norstrand Reinhold Company Inc. New York, 1988.

[5] Rugui Yang, Y.T. LO, " Simple and Effective Analysis for a Slot - Coupled Patch Antenna with a Microstrip Line Feed ", Microwave and Optical Technology Letters, vol. 4, No. 9, August 1991.

[6] S. J. Choi, Y. T. Lo, " Q Factor and Design of CP Microstrip Antennas ", Microwave and Optical Technology Letters, vol. 2, No. 10, October 1989

LINE-OF-SIGHT OF A HELICOPTER MOUNTED ANTENNA

Michael Courtright
Electronic Systems Group
Westinghouse Electric Corp.
Baltimore MD.

Abstract

A fire control radar antenna mounted above the rotor blades of an Apache helicopter is subjected to harsh vibration. This environment causes both bending of the structural members as well as mechanical rotation about the gimbal axes. The sinusoidal motion creates angular Line-of-Sight (LOS) errors and also linear deflection of the RF phase center which results in phase and amplitude modulation of the RF beam, and degraded radar performance. This paper describes the analysis of the beam LOS in a mechanically gimballed feed and reflector antenna mounted above the Apache helicopter. The vibration loads are at discrete sinusoidal frequencies which affects the form of the design requirements and the method of analysis. A description of the flight tests, Finite Element Analysis, LOS equations, and the analytical process is given.

1.0 The Apache Fire Control Radar

The system which is designed to be incorporated in the Apache helicopter consists of the Hellfire missile, and a fire control radar that is designed to rapidly detect enemy tanks, air defense systems, trucks, and aerial targets[1]. The goal is to provide the crew with accurate performance in all weather operations, even through smoke, dust, and haze. With this system, the Apache gunner hands off the target electronically to the missile's radar as soon as it is chosen and is then free

Figure 1: Apache With Radome and Antenna above the Main Rotor

2

to take cover or engage another target[2].

Mounted to a stationary mast above the main rotor as shown in figure 1, the antenna is gimballed in azimuth and elevation allowing the antenna 360° coverage plus up-look and down-look capabilities. The antenna consists of a linefeed and reflector gimballed in elevation. Figure 2 shows how the antenna and the radome rotate together on
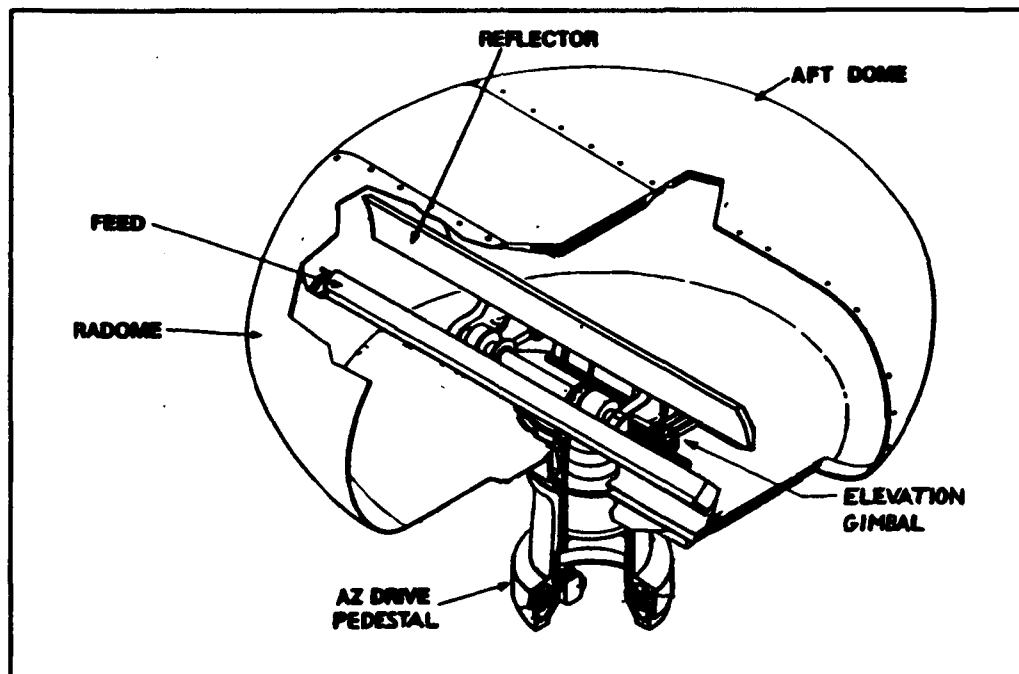
Figure 2: The Antenna Inside the Radome. Linefeed and Reflector are Gimballed in Elevation. The Entire Assembly Rotates in Azimuth.

an azimuth drive pedestal.

Prototype systems have been built and flown with

3

positive results, and production-ready systems are being built and tested and will be flown in the coming year.

2.0 The Vibration Environment

The harsh vibration environment above the rotor affects antenna RF beam stabilization. Antenna beam vibration in azimuth and elevation causes amplitude
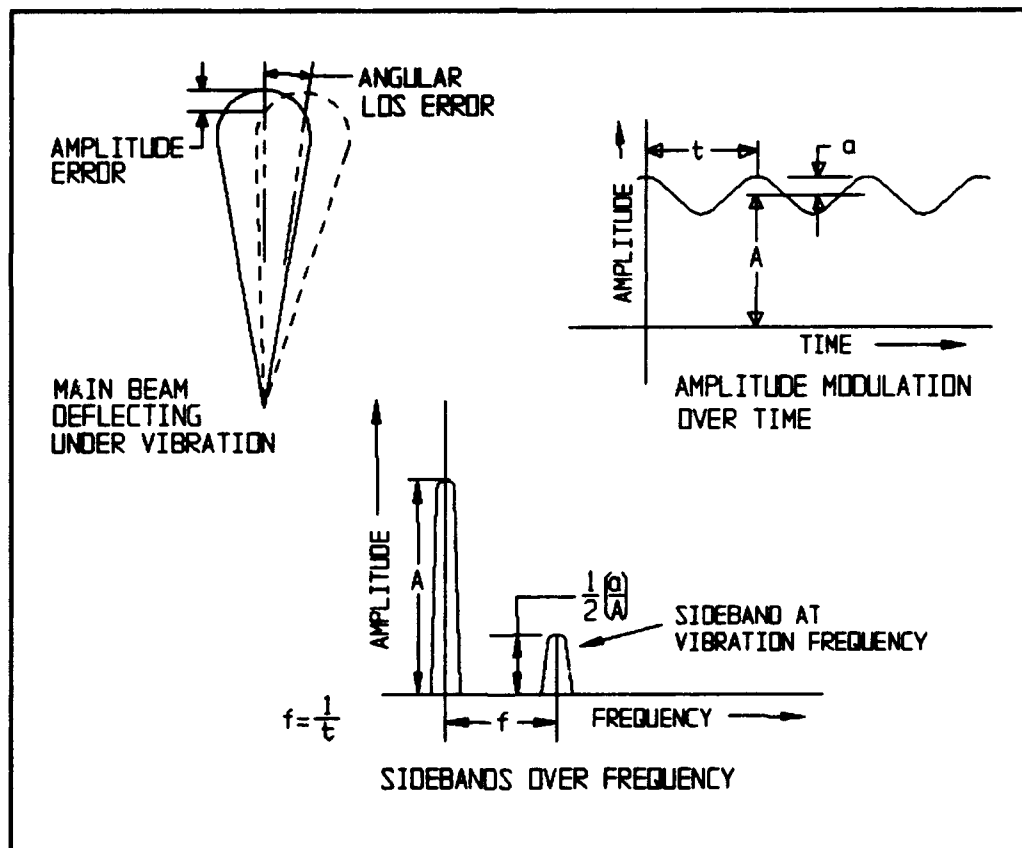
Figure 3: Angular Beam Motion, Amplitude Modulation, and Sidebands. Linear Motion and Resulting Frequency Modulation and Sidebands are Similar.

4

modulation, and the antenna phase center deflects longitudinally along the beam causing frequency modulation. Angular error and the resulting amplitude modulation is shown in figure 3. The linear longitudinal error and resulting frequency modulation are not shown but look similar to the angular case. The system's Moving Target Indicator mode is compromised by excessive motion. Low frequency vibration causes unwanted sideband noise in the signal at frequencies close to the doppler frequencies of the low speed targets. The vibration sidebands can only be filtered out at the expense of filtering out the slow moving targets. The difference in frequencies between the target doppler and the vibration determines the sensitivity of the target detection to the vibration amplitude. The closer the vibration frequency is to the doppler of the minimum allowed target velocity, the more sensitive the system is to the vibration. So less vibration amplitude is permitted at the higher frequencies.

An analysis of the system showed the maximum amplitude of the sidebands which could be filtered, and based on that amplitude, a maximum allowable antenna deflection was derived. There are three separate

5
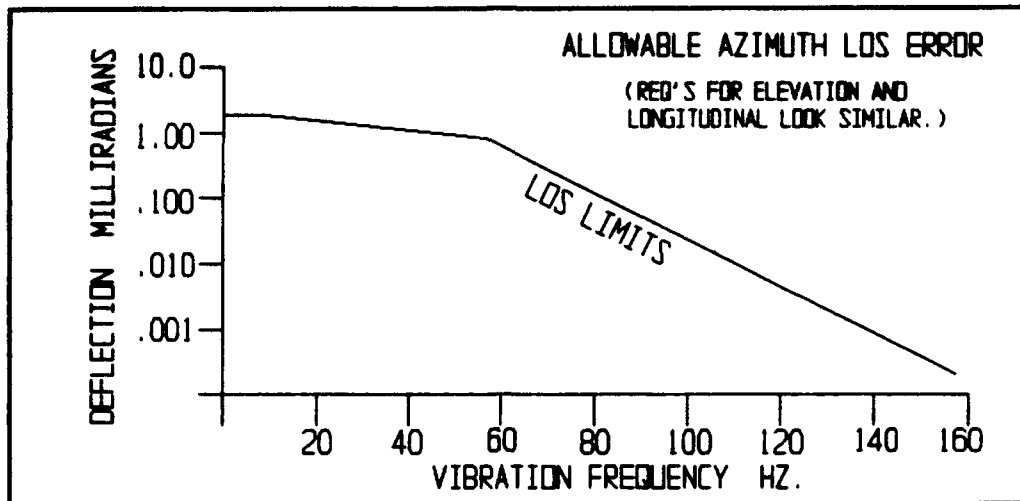
Figure 4: Allowable Azimuth LOS Errors.
Large Deflections Are Permitted at Low Frequencies and
Small Deflections Are Permitted at Higher Frequencies.

requirements: one defining azimuth error, one defining
elevation error, and one defining linear longitudinal
error.

The requirements permit greater deflections at the
lower vibration frequencies but at the higher
frequencies, the deflection limits become tight. The
azimuth LOS requirements are shown in figure 4, and
elevation and longitudinal requirements are similar. In
this analysis, linear motion of the phase center has been
grouped with angular motion under the general heading of
LOS.

These requirements and analysis apply to the main
beam only and not to the sidelobes. They assume that the

6

linefeed and reflector themselves remain rigid and the patterns remain intact under vibration, but that the structure to which they are mounted is deforming causing the main beam to move. The integrity of the linefeed and reflector and therefore the patterns was verified by a separate analysis

3.0 Method of Analysis

The RF beam LOS requirements apply to errors caused by both servo related motion and errors caused by structural bending motion. Errors related to servo are caused by gimbal rotations about the azimuth and elevation bearing axes caused by gimbal imbalance, friction, and spring torque. RF beam errors related to structure are caused by flexing and bending of the pedestal, brackets, and other supporting components. Two computer models were generated to study the system. First, the servo model simulates the motion of the beam caused by gimbal imbalance, friction, and gimbal spring constants. Second, the Finite Element Analysis (FEA) model calculates the motion of the beam caused by the structural bending and twisting.

In order to determine if the three LOS requirements

7

are met, the results of the servo analysis and the results of the structural analysis must be combined. This report only discusses the structural bending errors.

Vibration on top of the helicopter mast occurs at four sinusoidal harmonic frequencies with the rotor speed as the lowest frequency. See figure 5. There is no measurable random or sinusoidal vibration measured other than the four sinusoidal spikes, so the greatest deflections of the antenna will occur at the four spikes and the analysis only investigated those frequencies. The magnitudes of the sinusoids depend on the individual helicopter[3].
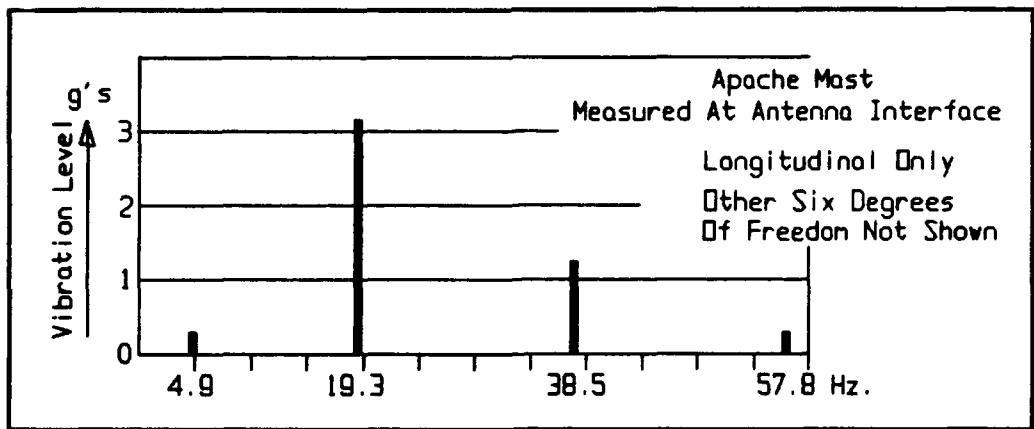
Figure 5: Measured Helicopter Vibration Showing Sinusoidal Spikes at Four Discrete Frequencies.

The vibration magnitudes for this study were taken from a series of flight tests performed on an accurate

8

mock-up of the azimuth drive pedestal and radome assembly
mounted above an Apache helicopter. The vibration at the
bottom and top of the azimuth drive pedestal were
measured with accelerometers. The mock up did not
contain an antenna, so the motion of the linefeed and
reflector could not be measured. Instead, it was
simulated with the computer FEA model. The simulation
was made using ANSYS code with PATRAN pre and post
processing and the antenna model was represented as an
assembly of FEA plate elements and beam elements. Figure
6 shows the Elevation Gimbal Assembly with the linefeed
and reflector, figure 7 shows the model.
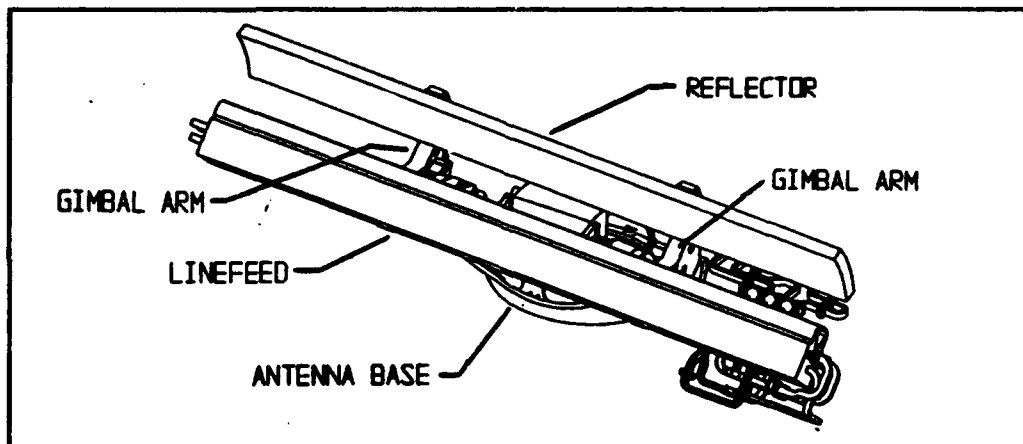
Figure 6: The Antenna

The computer model was excited in 6 degrees of
freedom of motion, at the four input frequencies, and at
the magnitudes measured on the helicopter mockup. The

9
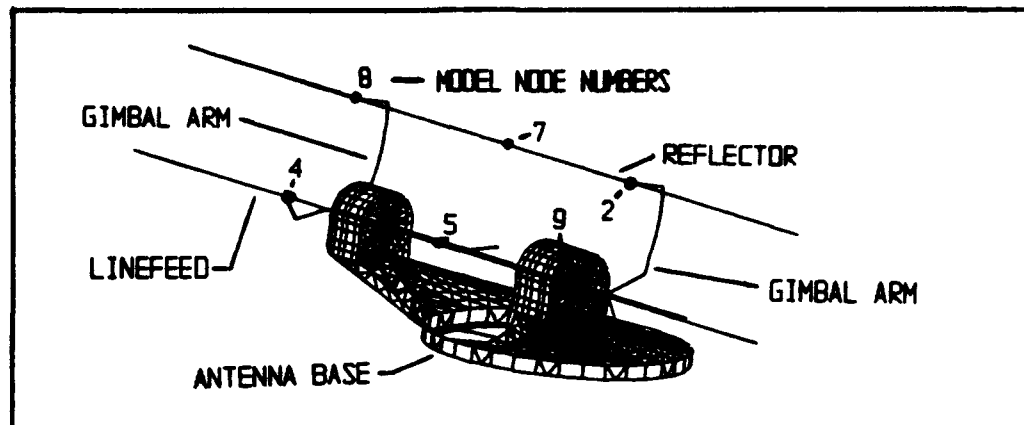
Figure 7: Antenna FEA Model Showing Nodes for Calculating the RF Beam Motion

simulation determined the linear motion of the antenna and the outputs were the maximum cartesian deflections and rotations of the nodes of the model. The maximum deflections of six nodes along the feed and reflector were used to calculate LOS error. Three equations were generated to convert the deflections and rotations of the model nodes into values of RF beam LOS error. One equation is needed for each of the three requirements, and the three equations are developed here.

3.1 Azimuth LOS Error Equation

The azimuth LOS error is caused by the azimuth deflections of the feed and reflector. See figure 8. First, with the reflector stationary, the beam rotation is equal to the rotation of the feed.

10
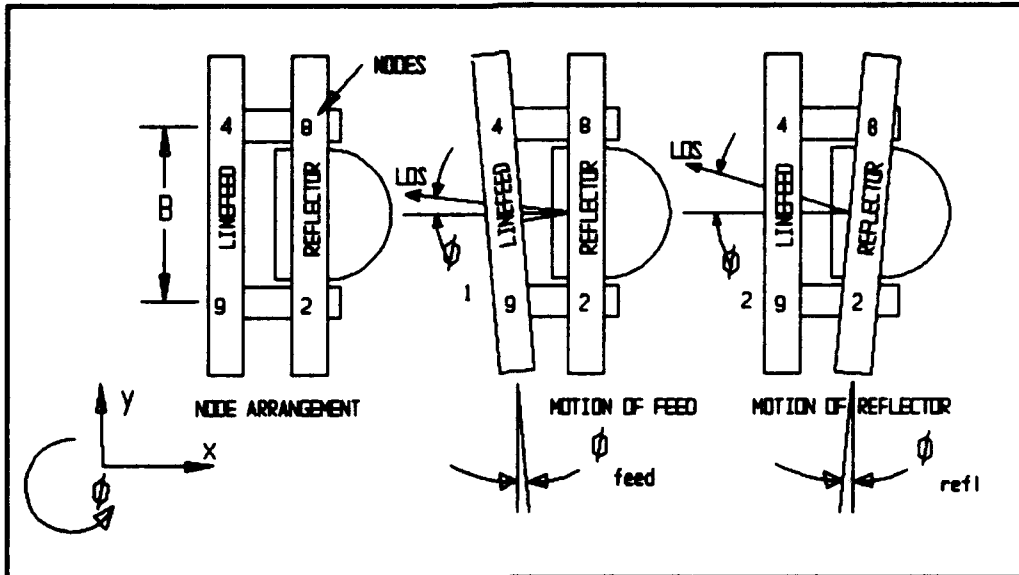
Figure 8: Azimuth Error Due to Feed and Reflector Motion as Calculated at Nodes 4,8,9, and 2.

$$\phi_1 = -\phi_{feed} \tag{1}$$

Second, with the feed stationary, the beam rotates relative to the reflector:

$$\phi_2 = 2*\phi_{refl} \tag{2}$$

Because of the rule of superposition, the two cases are additive. The rotated angles of the feed and reflector are calculated by the deflections in the x direction of four nodes in the model, node numbers: 8, 2, 4, and 9.

$$\phi_{azimuth} = \phi_1+\phi_2 = 2*\phi_{refl}-\phi_{feed} \tag{3}$$

The term B is equal to the distance between the nodes, and using small angle approximation, the angles can be

11

441

substituted for the arc tangents of the angles.

$$\phi_{azimuth} = 2\arctan\left(\frac{X_8 - X_2}{B}\right) - \arctan\left(\frac{X_4 - X_9}{B}\right)$$ (4)

$$\phi_{azimuth} = 2\frac{X_8 - X_2}{B} - \frac{X_4 - X_9}{B}$$

3.2   Elevation LOS Error Equation

The elevation LOS error is caused by two factors: first, the rotation of the feed and reflector as measured at the center of the reflector: node 7.   See figure 9.
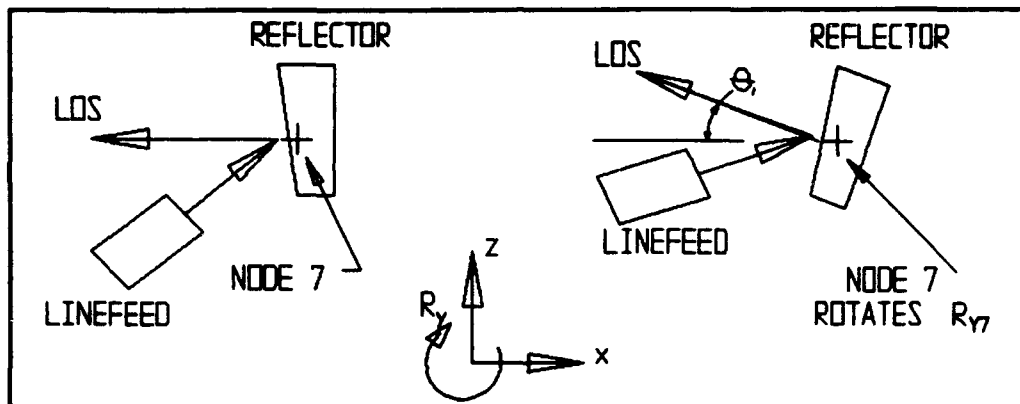
Figure 9: Elevation Error Due to Rotation of Feed and Reflector as Measured at Node 7: R_{Y7}.

$$\theta_1 = R_{Y7}$$ (5)

Second, the elevation LOS error is also caused by the deflection of the linefeed phase center (node 5) with respect to the reflector, and perpendicular to the reflector axis.

12

$$\theta_2 = -.85 * \arctan \frac{D_{phasecntr}}{L}$$
$$\theta_2 = -.85 * \frac{D_{phasecntr}}{L} \tag{6}$$

Equation (6) was determined empirically. $D_{phasecntr}$ is the deflection of the phase center perpendicular the reflector axis and L is the reflector focal length. The total elevation error is the sum of the two components:

$$\theta_{elevation} = \theta_1 + \theta_2 \tag{7}$$

To get θ_2 in terms of the nodes of the computer model (reflector node 7 and feed node 5), the feed displacement must be broken into 2 parts: displacement of phase center due to linear motion of the feed, and displacement of the phase center due to rotation of the feed. With linear displacement, the feed translates vertically relative to the reflector. See figure 10.

$$D_{linear} = Z_5 - Z_7$$

With angular displacement, the phase center is "A" inches from the center of rotation at node 5, so as the feed twists, the phase center is displaced. See figure 11.

13
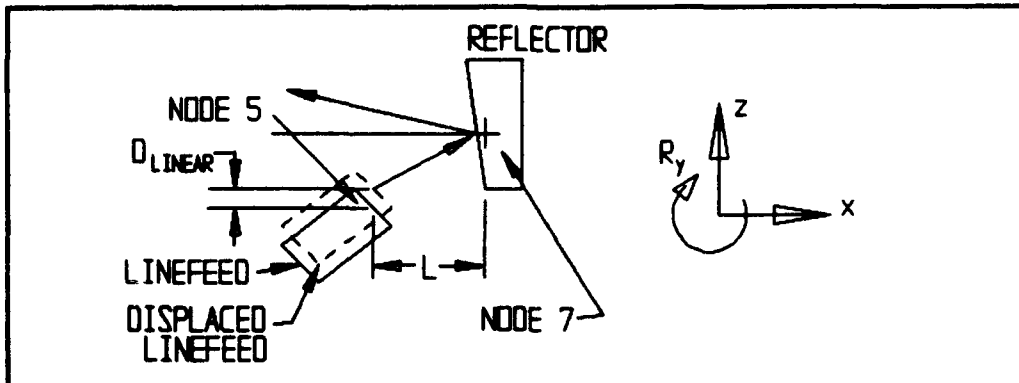
Figure 10: Elevation Error Due to Linear Motion of the Phase Center Relative to the Reflector
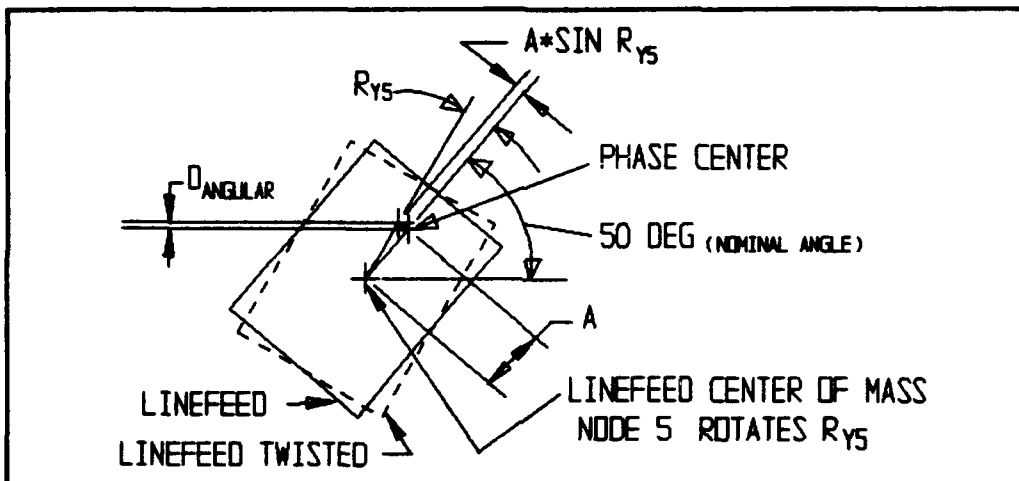
Figure 11: Elevation Error Due to Angular Motion of the Phase Center Relative to the Reflector

$$D_{angular} = -\cos 50° \times A \sin R_{Y5}$$
$$D_{angular} = -\cos 50° \times A \, R_{Y5} \tag{9}$$

The total displacement of the feed phase center with respect to the reflector is $D_{relative}$.

$$D_{relative} = D_{linear} + D_{angular} \tag{10}$$

14

$$D_{relative} = Z_5 - Z_7 - \cos 50° * AR_{Y5} \qquad (11)$$

The difference between $D_{relative}$ and $D_{phasecntr}$ (equation 6) is a coordinate transformation. In equation 6, $D_{phasecntr}$ is the displacement of the feed phase center relative to the reflector, and perpendicular to the reflector axis, in the coordinate system of a tilted reflector. In equation 11, the displacement of the phase center relative to the reflector is in the computer coordinate system. Figure 12 shows the coordinate transformation.
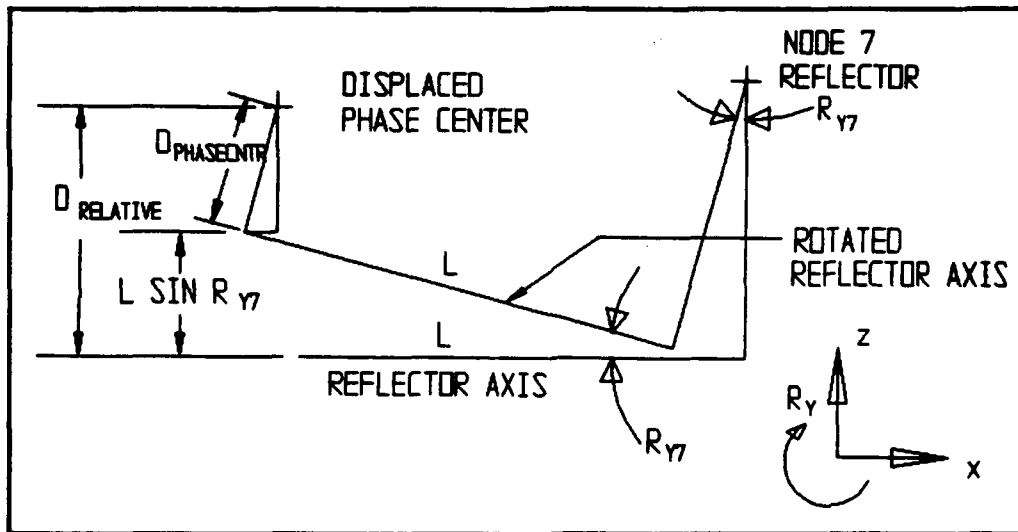
Figure 12: Coordinate Transformation

$$D_{phasecntr} = \frac{1}{\cos R_{Y7}} (D_{relative} - L \sin R_{Y7}) \qquad (12)$$

where L = reflector focal length.

Substitute equation 12 into equation 6:

$$\theta_2 = -.85\frac{(D_{relative} - L\sin R_{Y7})}{L\cos R_{Y7}}$$

$$\theta_2 = -.85\frac{(D_{relative} - L\sin R_{Y7})}{L} \tag{13}$$

Substituting the equation for $D_{relative}$ (11) and the equation for θ_2 (13) into equation 7 yields:

$$\theta_{elevation} = \theta_1 + \theta_2$$

$$\theta_{elevation} = R_{Y7} - .85\frac{L_{relative} - L\sin R_{Y7}}{L}$$

$$\theta_{elevation} = R_{Y7} - .85\frac{Z_5 - Z_7 - \cos 50° * A R_{Y5} - L\sin R_{Y7}}{L} \tag{14}$$

3.3 Longitudinal LOS Error Equation

The linear longitudinal error is equal to the maximum displacement of the reflector and linefeed from nominal plus the maximum displacement of the feed with respect to the reflector along a line connecting the two. See figure 13.

The total linear deflection of the beam is P:

$$P = P_{refl} + P_{feed}$$
$$P_{refl} = X_7$$
$$P_{feed} = \cos 50° (X_7 - X_5) + \sin 50° (Z_5 - Z_7) \tag{15}$$
$$P = X_7 + \cos 50° (X_7 - X_5) + \sin 50° (Z_5 - Z_7)$$

16
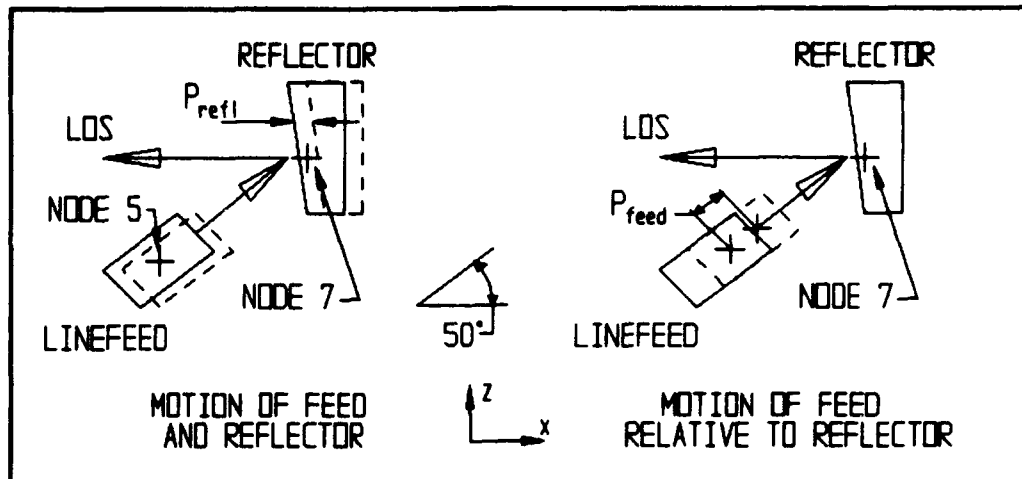
Figure 13: Longitudinal Motion of Feed Phase Center. Total Motion is Sum of Motion of Reflector and Feed Plus Motion of Feed Relative to Reflector.

4.0 The Results of Analysis

The results of the structural analysis show that the requirements will be met. The calculated LOS errors for azimuth are shown in figure 14, and the elevation and longitudinal results look similar. The azimuth and elevation LOS errors are far enough below the permitted levels at all four frequencies that even when the servo errors predicted by the servo model are added , there is still margin.

The longitudinal requirement is met with less margin. However, there are no linear RF beam deflections caused by servo related factors to consider. There are

17

no servo LOS errors to be added to the structural LOS errors so the requirement is met.
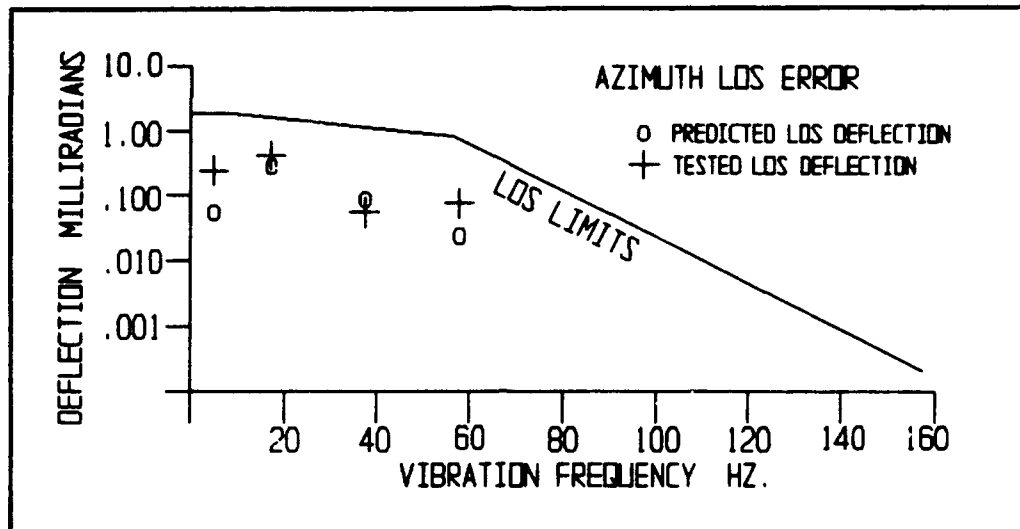
Figure 14: Results of Azimuth Structural Analysis and Tests

5.0 Validation

Tests have been initiated to validate the analysis. A complete pedestal/antenna assembly has been mounted to a shaker table and vibrated at levels expected on the helicopter with accelerometers mounted at the same locations as the nodes of the computer model. The first tests only measured azimuth errors and the results are shown in figure 14. The tests show that, at least in azimuth, the model is correct. The measured deflections correlate very closely to the analysis. Further testing

18

is planned to validate the elevation and longitudinal predictions.

6.0 Acknowledgements:

Thanks are due to Mr. Larry Hunter and Mr. William Yablon, both of Westinghouse Electric Corp. for their assistance in this analysis.

7.0 References:

1. Wilson, J.R. (1993) Does the Apache Longbow Jeopardize the Comanche?, Military and Aerospace Electronics May 17, 1993, vol. 4, No. 5, Pennwell Publ. Westford, Ma.

2. Bond, D.F. (1989) US Army Approves Initial Design Phase of Longbow Radar System for AH-64, Aviation Week and Space Technology, pp 27, McGraw Hill, July 31, 1989.

3. Environmental Test Methods and Engineering Guidelines, Mil-Std-810D, pp 514.4-1 - 514.4-22, July 19, 1983.

19

Measurement Speed and Accuracy in Switched Signal Measurements

John Swanstrom and Robert Shoulders

Hewlett-Packard Company
Santa Rosa Systems Division
1400 Fountaingrove Parkway
Santa Rosa, CA 95403

Abstract

The interdependence of accuracy and speed should be considered when analyzing measurement requirements. Tradeoffs can be made to optimize the measurement when accuracy is of primary importance, or where speed is critical. Several different measurement modes of the HP 8530A Microwave Receiver are presented, each with different measurement speed and accuracy tradeoffs. Examples are given that illustrate which acquisition modes would be appropriate to optimize the acquisition speed and accuracy in a variety of applications.

Keywords

Measurement accuracy, multiple channel measurements

Introduction

Everyone wants more speed; from desktop PCs to antenna measurement systems, higher speed makes jobs easier, and allows tasks to be completed in less time. But achieving higher speed can come with a tradeoff of higher errors. For an antenna measurement system, we would like higher speed to allow us to complete our measurement in less time thus making our time and range more productive. But what if we compromised measurement accuracy? Are we better off with less accurate data that can be taken faster? This paper shows that measurement speed and accuracy are interrelated, and the application determines which is most important. In most applications, accuracy is of primary importance and must not be compromised for increased measurement speed. In some applications, adequate accuracy can be maintained with increases in measurement speed. This paper examines the tradeoffs that can be made between speed and accuracy and how additional measurement speed can be obtained from the HP 8530A Microwave Receiver.

Dynamic Accuracy and Receiver Sensitivity

To achieve high measurement accuracy with multiple channel measurements it is necessary to start with a receiver with good accuracy. Low measurement sensitivity is necessary for minimizing the errors due to noise. Dynamic accuracy (or receiver linearity) is a measure of how accurately the receiver measures signals over its full dynamic range. The HP 8530A microwave receiver achieves its excellent dynamic accuracy through a stable, I/Q detection design that is internally calibrated. Figures 1 and 2 show the worst case amplitude and phase dynamic accuracy specifications for the HP 8530A due to IF residuals and detector inaccuracies. These plots exclude uncertainty due to noise, frequency response, and crosstalk. As can be seen from these curves, the errors due to dynamic accuracy are very small over the wide dynamic range of the receiver.
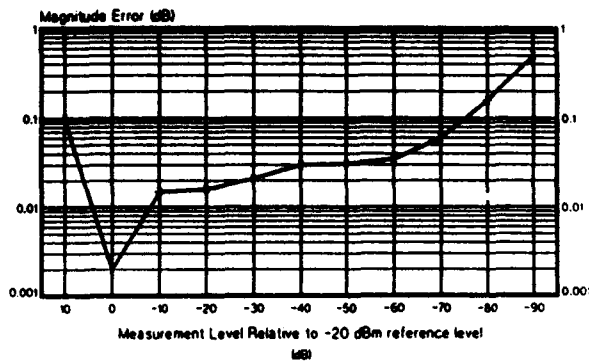
Figure 1: Amplitude Dynamic Accuracy for HP 8530A receiver
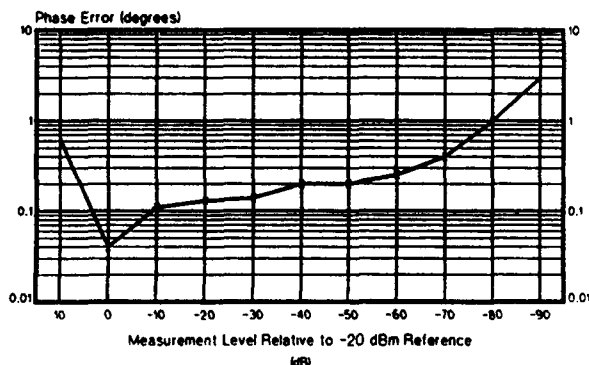
Figure 2: Phase Dynamic Accuracy for HP 8530 receiver

Measuring A Single Signal

The HP 8530A microwave receiver in its fast CW mode can acquire data at 5000 data points per second at full specified performance for signals that have a point-to-point variation of less than 12 dB. Accuracy is preserved by the auto-ranging circuitry which monitors the signal level being presented to the detector. The gain setting is adjusted, between measurements to keep the signal presented to the detector within the most accurate range of the detector. In this

manner, specified accuracy can be maintained over the full 90 dB of dynamic range. This yields the best measurement speed and the dynamic accuracy as shown in figures 1 and 2. An example of this type of measurement is a CW near-field test with a single polarization.

The Challenge of Switched Multiple Test Channels

When using an external PIN switch, (for example switching between the co- and cross-polarized response of an antenna), the signal level presented to the IF chain will likely have a point-to-point variation greater than 12 dB. This presents two challenges to the receiver. Figure 3 shows a simplified block diagram of the HP 8530A microwave receiver. The bandwidth of the 20 MHz crystal filter is 35 KHz with a very high Q filter for rejection of unwanted spurious signals. Therefore, adequate time must be allowed for its transient response before an accurate measurement can be made. Since the transient response is related to the amplitude of the signal prior to switching, the situation that requires the most time is a high level signal being switched to a low level signal, since the residual from the previous signal is large compared to the signal being measured. Figure 4 shows the transient response of the receiver in switching from a high level signal to one 60 dB lower. Note from figure 4 that at 400 microseconds, the residual of the transient is approximately 0.1 dB. This compares to an error due to noise of approximately 1.0 dB (with no averaging) assuming the high level signal was at the compression point of the receiver. The further the high level signal is below the compression point of the receiver, the higher the error due to noise will become.

451
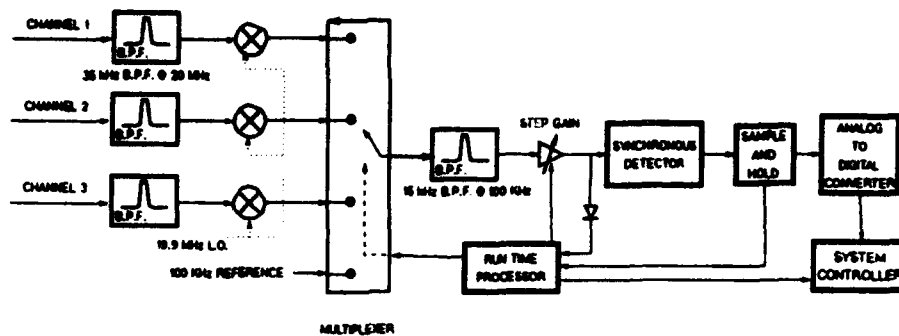
Figure 3: Simplified Block Diagram of HP 8530A IF downconverter and detector
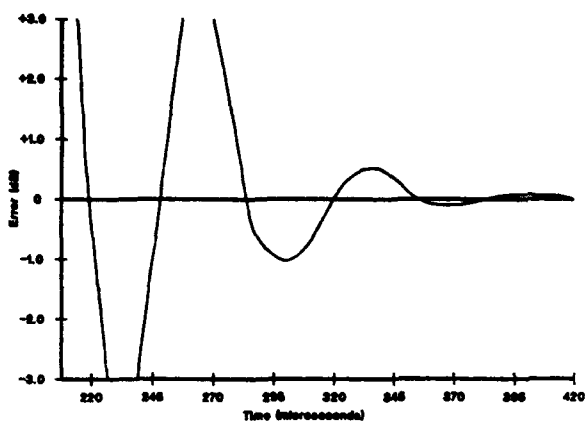
Figure 4: Transient response of the receiver in switching from a high level signal to one 60 dB lower

A Fast Autoranged Data Mode

The second challenge for the receiver for switched signals is the autoranging algorithm. It needs to choose the correct gain stage to place the signal presented to the detector within the most linear portion of the detector's range. A fast autoranged data mode (known as Fast AD) has been implemented in the HP 8530A which allows fast and accurate data to be acquired for multiple channel measurements. This is particularly useful in applications which use PIN switches since it provides high accuracy over the full dynamic range for each channel at a measurement interval of 400 microseconds or 2500 data points per second. It should be noted

that the fast autoranged data mode is not constrained to a certain number of channels. It works equally well for one channel as it does for 64 test channels or more. It is a very useful feature that allows multiple channel data to be acquired accurately at a fast data rate.

Faster Acquisition Time

For a measurement application in which measurement speed is of primary importance, it is possible to increase the data acquisition speed for a multiple channel measurement to an interval shorter than 400 microseconds. The fast parameter time (FASPARMTIME) feature of the HP 8530A allows the user to set the acquisition interval to any value in the range of 200 to 1360 microseconds, allowing up to 5000 data points per second. The data acquisition interval of 400 microseconds was chosen as the default setting for the fast autoranged data mode because it guarantees full specified performance for any signal level change within the receiver measurement range. Selecting a measurement interval less than 400 microseconds may have an effect on measurement accuracy, but the magnitude of this error will depend upon the measurement interval selected and the level change between the two signals. Figures 5 and 6 show the worst case errors due to switching residuals as a function of measurement interval and signal level changes.

452

Error on Low Level Signal due to Switching
Residuals (Fast Autoranged data mode)

Error on Low Level Signal due to Switching
Residuals (Fast IF Multiplexing data mode)
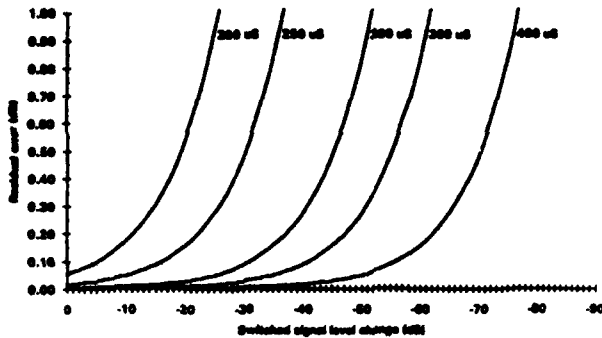
Figure 5: Worst case error on the low level signal due to switching residuals
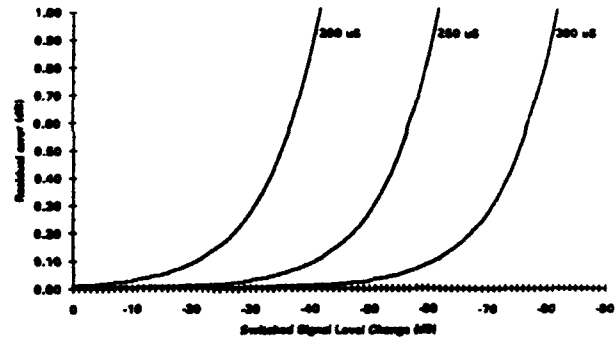
Figure 7: Worst case error on low level signal (fast multiplexed IF mode)

Measurement rate	Maximum error on high level signal (dB)
200 microseconds	0.04
250 microseconds	0.01
300 microseconds	0.0026

Figure 6: Worst case error on the high level signal due to switching residuals

As a practical example, consider measuring an antenna where the co- and cross-polarized responses need to be characterized, and the maximum variation between the two is expected to be 30 dB. Figures 5 and 6 show that if the data is acquired at a 400 microsecond interval, the worst case errors due to switching residuals is <0.0026 dB on the high level signal (co-polarized), and 0.01 dB on the low level signal (cross-polarized). If the measurement interval is decreased to 300 microseconds, the worst case error on the co-polarized signal is 0.0026 dB, and 0.0869 dB on the cross-polarized signal. If the measurement interval is decreased to 200 microseconds, the worst case errors are 0.04 dB on the co-polarized signal, and 1.58 dB on the cross-polarized signal. In this manner, measurement accuracy can be traded for measurement speed to suit the needs of the user.

Internal Parameter Switching

Another data acquisition mode of the HP 8530A receiver, known as fast IF multiplexing, overcomes the problems associated with switched signals through a high Q (reject) filter. By using parallel filters, it is possible to avoid the transient response delay associated with switched signals through a high Q filter. The signals passing through the filters are slowly varying (<12 dB point-to-point) and will not produce significant residual errors. The internal run time processor then cycles through the selected IF inputs (see figure 3). In this mode, up to three test channel can be measured at data rates from 4000 to 5000 data points per second. Figures 7 and 8 illustrate the errors associated with switched IF signals in the fast IF multiplex mode. These errors are due to switching the signals through the 100 KHz filter. This filter is not as high Q as the previous filter (which provides the high spurious rejection) so its settling time is faster. Thus the fast IF multiplex mode provides a greater speed and accuracy combination than the fast autoranged data mode.

Measurement rate	Maximum error on high level signal (dB)
200 microseconds	0.0058
250 microseconds	0.0013
300 microseconds	0.00030

Figure 8: Worst case errors on high level signals (fast multiplexed IF mode)

The fast multiplexed IF mode is useful for fast switching of up to three test channels, at data acquisition rates from 4000 to 5000 data points per second, and at these speeds provides the best accuracy of all the different modes described in this paper.

A typical example of where this mode would be beneficial is in measuring a millimeter-wave monopulse antenna. A separate mixer could be attached to each of the three test ports of the antenna, and accurate multiple channel data could be acquired at 4000 data points per second.

Summary

In this paper we examined the relationships between speed and accuracy within the HP 8530A microwave receiver. For a single channel measurement, fast measurement speed and high accuracy are easily achievable. For multiple channel measurements, more attention needs to be paid to the accuracy-speed tradeoff. Two data modes of the receiver were presented. The fast autoranged data mode allows autoranging of the data to provide high accuracy with PIN switched signals. Data acquisition speeds can range from 2500 to 5000 data points per second in this mode. The fast multiplexed IF data mode allows data acquisition speeds of 4000 data points per second, and very good accuracy for up to three test channels. Data was presented to guide the user in selecting the best data acquisition mode for their particular application. Armed with this knowledge, you are now ready to make fast and accurate measurements!

Conclusions

The conclusions are clear; speed and accuracy are interrelated. When considering measurement speed, you also need to consider measurement accuracy. Different applications will have different accuracy requirements. You should first determine the required accuracy, and then determine the appropriate data acquisition mode and data acquisition speed.

ANTENNA MEASUREMENTS AND DIAGNOSTICS IN A UNIQUE BI-POLAR NEAR-FIELD FACILITY

Yahya Rahmat-Samii, Lawrence I. Williams, and Robert G. Yaccarino

University of California, Los Angeles
Department of Electrical Engineering
Los Angeles, CA 90024

Abstract - A novel customized bi-polar planar near-field antenna measurement technique is presented as an alternative to the plane-rectangular and plane-polar measurement techniques. The bi-polar near-field scanner incorporates an axially rotating test antenna and a rotating probe-carrying arm to sample the near-field on a data grid consisting of concentric circles and radial arcs. This technique offers a large scan plane size with reduced "real estate" requirements and a simple mechanical implementation resulting in a highly accurate and cost-effective antenna measurement and diagnostic system. This paper gives an introduction to the bi-polar near-field technique and a description of the unique hardware implementation at the University of California, Los Angeles (UCLA). It examines the data processing algorithms that have been developed and customized to exploit the unique features of the bi-polar planar near-field measurement technique. The algorithms which have been tailored for the bi-polar configuration include the optimal sampling interpolation (OSI)/fast Fourier transform (FFT), Jacobi-Bessel transform, and Fourier-Bessel transform. Holographic imaging for determination of antenna aperture fields has been incorporated to facilitate antenna diagnostics. Measured results are compared with those produced by a far-field range and a plane-rectangular planar near-field range to verify the implementation and validate the method. Excellent agreement was obtained for both the co-polarized and cross-polarized fields.

I. INTRODUCTION

Much attention has been given to the process of measuring the radiating near-field of microwave and millimeter-wave antennas as a means to determine their far-field radiation pattern and to perform antenna diagnostics [1,2]. The planar near-field measurement technique has enjoyed particular popularity due to the mechanical, theoretical and computational simplicity afforded by measuring on a plane. A new implementation of the planar near-field technique, called bi-polar planar near-field, incorporates an axially rotating test antenna and a probe-carrying arm to sample the near-field on a data grid consisting of concentric circles and radial arcs. This paper provides an introduction to the method, discusses the unique hardware implementation at the University of California, Los Angeles (UCLA), gives an overview of the unique data processing algorithms developed for the bi-polar configuration, and provides a comparative survey of measured results.

A. Plane-rectangular Planar Near-field

The requirement of any planar near-field measurement system is to sample the electromagnetic fields radiating from the antenna under test (AUT) on a planar surface. The arrangement of the measurement samples depends upon the mechanical configuration of the robotic positioner used for the data collection (Fig. 1). The most popular method is the plane-rectangular technique wherein the field probe is positioned in Cartesian coordinates along a raster scan. The plane-rectangular samples lie on a regular, rectangular grid and are directly used for the NF-FF transformation which is performed, almost invariably, using the highly efficient fast Fourier transform (FFT). The field probe maintains its orientation during the translation in the measurement plane and, therefore, probe compensation follows in a straightforward manner [3].

B. Plane-polar Planar Near-field

Rahmat-Samii et. al. [4] introduced the plane-polar technique as an alternative to the traditional plane-rectangular scanning. The plane-polar approach typically incorporates a rectilinearly scanning probe over an axially rotating AUT. Near-field data is collected on concentric rings with measurement samples lying on radial lines (Fig. 1). These samples cannot be directly used in the FFT calculation of the NF-FF transformation which requires a plane-rectangular data arrangement.

In [4], the plane-polar samples were used with the Jacobi-Bessel transform to calculate the far-field. In a subsequent work [5], a simple bivariate Lagrange interpolation scheme was used to recover plane-rectangular samples from the plane-polar ones enabling the rapid determination of the far-field using the FFT.

C. Bi-Polar Planar Near-field

The present work provides another alternative for planar near-field scanning which shares the advantages of plane-polar [4] while providing a simple and cost-effective measurement system. Like plane-polar, the AUT rotates axially providing for data collection on concentric rings. The probe for the bi-polar case, however, no longer translates along a rectilinear path. The probe is attached to the end of a mechanical arm placed above (or in front of) the AUT. This arm sweeps the probe along an arc by rotating about a second axis parallel to the AUT rotation axis (Fig. 2). As the AUT rotates, near-field samples are collected on concentric rings with measurement samples lying on radial arcs (Fig. 3). The combination of AUT rotation and arm rotation yields the desired planar coverage. The name *bi-polar* has been given to this method due to the two rotation axes.

The primary motivation for the bi-polar concept was the desire to develop an inexpensive and simple mechanical implementation of planar near-field scanning while maintaining or improving the accuracy of current systems. The primary feature of the bi-polar scanner is its implicit mechanical simplicity, the distinction being the use of a probe arm with a rotational motion rather than translational probe motion. Plane-polar and conventional plane-rectangular scanning require rectilinearly translating probe motion, typically accomplished by converting a rotational motion, such as that provided by an electric motor, into a linear one. The bi-polar scanner requires only the rotational motion of the AUT and the probe arm. This rotational motion of the arm supplants all linear motion and the associated hardware thus simplifying the design. This feature, along with others offered in the next section, provide a cost-effective, compact and reliable planar near-field scanning system.

Section II of this paper discusses the conceptual aspects of bi-polar scanning emphasizing the mechanical advantages and the bi-polar sample grid. Section III describes the unique bi-polar hardware implementation at UCLA, where a sophisticated antenna measurement facility has been developed. The impact of the bi-polar configuration on the data collection and processing is examined in Section IV. In Section V, measured results for two antennas are compared with

another planar near-field range and an outdoor far-field range. These measurements establish the validity of the technique and manifest the accuracy of the UCLA facility. Conclusions are presented in Section VI.

II. BI-POLAR PLANAR NEAR-FIELD TECHNIQUE

The bi-polar near-field technique has unique features which are discussed in this section. These features are presented in terms of the conceptual description of bi-polar scanning and advantages relative to the other planar techniques.

A. Conceptual Description

The bi-polar scanning configuration is depicted in Fig. 2 and Fig. 3 illustrates the resultant data sample grid. The essence of bi-polar scanning is the rotation of the AUT and the probe-carrying arm. The AUT rotation about axis 1 is described by the angle α and bi-polar arm rotation about axis 2 is described by the angle β. The probe scribes a radial arc in the near-field of the AUT (Fig. 3) as the arm rotates about axis 2. The angles α and β, along with the bi-polar arm length L, completely describe the probe position in the measurement plane. It is possible to position the probe to any location within a circular, planar region of radius 2L. Indeed, it is possible to collect plane-polar or plane-rectangular data with such a configuration through proper selection of α and β. Sampling in incremental, monotonic steps of α and β provide the most efficient data collection, however, since it allows continuous motion of the AUT. In a typical measurement sequence, the AUT is rotated through a full revolution while the measurement receiver samples the near-field in equal increments of α. The probe arm angle β is incremented after each ring of data is collected.

B. Advantages

Plane-rectangular and plane-polar scanning require rectilinear probe motion. Rectilinear motion is typically accomplished using rails with linear reciprocating bearings mounted to a stage. The linear bearings glide along the rails as some linear driving mechanism propels the stage. The rails must have little runout to avoid positional errors and to ensure a truly planar scan surface. The maximum travel of the linear motion is determined by the length of the rails; therefore, a large scan plane requires long rails and a large support structure. The size, weight

458

and cost for a plane-rectangular or plane-polar near-field scanner rapidly increases as the scan plane size increases.

The bi-polar scanner has a mechanical implementation much simpler than that required by plane-rectangular or plane-polar. Only conventional rotary bearings and driving systems are required thus reducing the cost of implementation. The length of the bi-polar arm and its maximum sweep angle β_{max} determine the maximum scan plane size rather than the physical size of the near-field scanner and its support mechanism. The arm's rigidity and bearing quality determine the planar accuracy of the scan. This mechanical simplicity makes for a reliable and cost effective measurement system.

The bi-polar near-field scanner is quite compact when compared with a plane-rectangular scanner capable of similar scan plane size. For the bi-polar scanner, the entire support mechanism need only be slightly larger than the arm and, therefore, the bi-polar scanner is often half the physical size of the plane-rectangular scanner. This compact size reduces the requirements on the anechoic chamber housing the bi-polar scanner. The chamber need only be large enough to accommodate the maximum allowed rotation of the arm. Data points that were sampled within the chamber "rotate" to locations which reside outside the physical limits of the chamber as the AUT rotates. When the entire near-field scan is complete, the actual scan surface can be substantially larger than the chamber itself.

Another feature of the bi-polar scanner is the ease in which the radio-frequency (RF) and control cables between the probe and the RF source/receiver may be mounted. It is important to support these delicate cables carefully in order to avoid measurement errors as the probe moves. The bi-polar configuration simplifies the mounting since the cables may be attached along the top of the arm preventing the cables from flexing excessively. In contrast, the plane-rectangular and plane-polar scanners often require additional hardware to support the RF cables due to the rectilinear motion of the probe.

III. BI-POLAR HARDWARE IMPLEMENTATION*

The development of a sophisticated antenna measurement facility has been undertaken at UCLA. Particularly, a bi-polar planar near-field range has been constructed where antenna measurements are routinely performed. The scanner

---

* Patent pending.

implementation can be discussed in terms of its three major subsystems: mechanical and robotic, acquisition and control, and RF.

A. Mechanical and Robotic

Fig. 4 contains a photograph of the customized bi-polar near-field scanner that was designed and built at UCLA. Absorbing materials have been removed to display the scanner structure. The apparatus is approximately six feet tall and was constructed with thick-walled steel tubing. It is housed in an 18 x 8 x 7 foot anechoic chamber. The arm is aluminum and is counter-weighted by an aluminum block which can be positioned longitudinally along the tail section of the arm to balance the weight of the probe mechanism. Two rotary stages were used to accomplish the rotational motions of the antenna and the probe arm. These rotary stages are high-precision optical bench positioners with pre-loaded ball bearings and zero-backlash tangent worm drive gears. Alignment of the rotation axes is adjusted by a micrometer-based tilt platform installed between the AUT rotary stage and the base frame (see also Fig. 2). The AUT rotary stage has a removable adjustable pedestal to accommodate different antennas and to provide course adjustment of the probe to AUT distance.

The AUT rotary stage and the probe arm rotary stage are both mounted to the same rigid steel frame. The advantage of this "uni-structure" design is the significant reduction in errors that may be induced during a measurement due to the misalignment of the two rotation axes. For instance, if the AUT center of gravity does not coincide with its axis, the rotating AUT will attempt to deflect the stage mount causing the two rotation axes to misalign. Since this design uses a single, highly rigid frame to mount both stages, a deflection of one axis will induce the same deflection in the other axis and thus, in a relative sense, will induce little to no error. The counter-weight has been included on the arm to balance the probe arm system for the same reason.

On the bi-polar near-field range the AUT rotates, consequently, the probe must generally co-rotate to maintain its orientation. The probe positioning mechanism of the bi-polar near-field range has a vertical positioner for computer-controlled fine adjustment of the probe height and a rotary positioner to maintain probe polarization alignment with the AUT (Fig. 4). The rotary positioner accommodates the two orthogonal probe orientations required in planar near-field scanning to extract the vector transmit characteristic of the AUT.

IV. PROCESSING TECHNIQUES

The acquisition of near-field data via the bi-polar planar near-field measurement technique results in near-field samples located, as illustrated in Fig. 3, at the intersection of concentric, circular rings and radially scribed circular arcs [6]. Near-field to far-field transformation algorithms may then be divided into those which interpolate the bi-polar near-field samples into another format before transformation and those which operate on the samples directly. The optimal sampling interpolation (OSI)/fast Fourier transform (FFT) method resides in the former category while techniques in the latter category include the Jacobi-Bessel and Fourier-Bessel transforms. Holographic imaging for determination of antenna aperture fields has been incorporated to facilitate antenna diagnostics. An overview of the bi-polar near-field data processing methods appears in Fig. 5.

The bi-polar coordinate system of Fig. 3 is defined by the independent coordinates (β, α) where β is the angle the probe arm makes with the positive y-axis and α is an azimuthal-like angle which remains constant along each radially scribed circular arc. The probe arm length L, a parameter of the coordinate system, determines the radius of the radially scribed circular arcs. The scan plane radius a, a parameter of the measurement, is determined by the maximum angular extent of the probe arm β_{max}. A conversion to polar coordinates may be made through use of

$$s = \frac{2L}{a}\sin\left(\frac{\beta}{2}\right)$$ (1a)

$$\phi = \alpha - \frac{\beta}{2}$$ (1b)

where $0 \leq s \leq 1$ is the normalized radial coordinate and $0 \leq \phi \leq 2\pi$ is the azimuthal coordinate measured from the positive x-axis. The non-linear relationship of s and β in (1a) implies, with bi-polar sample acquisition occurring in uniform probe arm angle increments $\Delta\beta$, a sample arrangement consisting of non-uniformly radially spaced, concentric, circular rings. Sample acquisition could, alternatively, occur on uniformly spaced rings if the probe arm were incremented in non-uniform increments derivable from (1a) [6]. In addition, it is seen that α is indeed an azimuthal coordinate, however, it is offset from the conventional polar

B. Acquisition and Control

The bi-polar near-field scanner operation is accomplished using a personal computer (PC) to control the scanner motion and to collect and process the near-field data. Custom software was written to control all hardware. The positioners on the bi-polar scanner are driven by an open loop stepper motor drive system which receives serial commands from the PC. The probe response is acquired using an HP8510B receiver controlled by the PC via the IEEE488 bus. Data is recorded until the entire near-field data set has been acquired.

C. RF

The bi-polar near-field's RF subsystem has been designed for high-precision measurement accuracy. The system is based on a computer-controlled HP8510B receiver which provides measurement of both amplitude and phase with wide dynamic range and high sensitivity and linearity over a broad frequency band. The receiver is operated in the dual source mode with balanced external harmonic mixing to provide both a reference and test channel so that common-mode variations and spurious phenomena are removed from the measured signal. The use of external mixing at the probe provides significant improvement in sensitivity, dynamic range, and signal-to-noise ratio (SNR) since high cable losses at RF frequencies are averted. The use of absorbing materials in the anechoic chamber strongly attenuate unwanted RF reflections and provide for a "quiet" measurement environment. An RF cable is fed through the pedestal and is connected to the AUT using a coaxial rotary joint enabling continuous rotation of the AUT. The probe also has a rotary joint enabling its continuous rotation.

A brief overview of current range capabilities include:

- Frequency coverage 2-26 GHz (expandable to 40 GHz)
- 16 foot scan plane diameter
- 7 foot maximum antenna diameter
- 5 foot maximum antenna depth
- 200 pound maximum antenna weight
- Graphical output including:
    - Far-field cuts, contours, 3-D waterfall
    - Near-field cuts, contours, 3-D waterfall
    - Polarization gray shade, vector, Poincaré sphere
    - Holographic images, color or gray shaded.

azimuthal coordinate ϕ by $\beta/2$, which, of course, is dependent on the probe arm angle.

The OSI/FFT, Jacobi-Bessel, and Fourier-Bessel near-field to far-field processing techniques are all methods for computing, assuming $e^{j\omega t}$ time-dependence where ω is the angular frequency, the radiation integral

$$\underline{D}(u,v) = \frac{1}{2\pi} \iint \underline{b}(\underline{\rho},d) e^{j\underline{\kappa} \cdot \underline{\rho}} \, d\sigma \tag{2}$$

where $\underline{b}(\underline{\rho},d)$ is the near-field, or probe response, collected on a plane at a distance $z=d$ above the antenna aperture plane, $\underline{\rho}$ is a position vector in the plane $z=d$ identifying the location of the near-field probe within the region σ, $\underline{\kappa}(u,v)$ is the projection of the wavenumber vector $\underline{k}$ onto the x-y plane, and (u,v) are spectral coordinates. $\underline{D}(u,v)$ is also commonly referred to as the transmit/receive characteristic or plane wave spectrum since it represents an angular spectrum of plane waves. It may be noted that for planar near-field scanning the radiation integral (2) takes the form of an exact Fourier transform of the near-field. The electric field in the far-field region is found, via asymptotic evaluation of (2), to be simply related to the radiation integral by

$$\underline{E}(\underline{r}) = jk\cos\theta \frac{e^{-jkr}}{r} \underline{t}(u_s, v_s) \tag{3}$$

where k is the wavenumber, $\underline{r}$ is a vector in the spherical coordinate system (r,θ,ϕ), the quantity $\underline{t}(u_s,v_s)$ is the probe-corrected version of $\underline{D}(u_s,v_s)$, and

$$u_s = \sin\theta\cos\phi \tag{4a}$$
$$v_s = \sin\theta\sin\phi \tag{4b}$$

are the saddle points corresponding to the asymptotic evaluation of (2).

"Probe correction" is the term applied to removing the effect of the probe pattern from the near-field measurement. The UCLA implementation of the bi-polar near-field measurement technique utilizes Kerns' approach [3] for performing probe correction with a highly accurate open-ended waveguide probe model [7] for determining the pattern of the probe. In Kerns' approach, the Fourier transform of the measured near-field $\underline{D}(u,v)$ is expressed as the product of

the desired AUT transmit/receive characteristic $\underline{t}(u,v)$ and the known probe pattern $\underline{s}(u,v)$. The use of two probes, where the second probe is typically the same as the first but rotated axially by 90 degrees, is necessary to solve for $\underline{t}(u,v)$. The probe antenna, as in the case of the plane-polar technique, must either co-rotate with the AUT or exhibit first-order azimuthal dependence in its far-field pattern so that the polarization properties of the collected near-field can be properly defined [8].

A. *Optimal Sampling Interpolation/Fast Fourier Transform*

The bi-polar implementation of the optimal sampling interpolation (OSI) is a modification of the algorithm developed for plane-polar near-field sampling interpolation [9]. Standard interpolation approaches, like bivariate Lagrange, are not tailored to represent antenna near-fields and cannot control, apart from increasing the sampling rate, the approximation error. Consequently, the focus of [9] was to both rigorously determine the required number of plane-polar near-field samples, or equivalently the sample spacings (which may be considerably relaxed beyond the universally considered maximum sample spacing of $\lambda/2$), and develop an optimal interpolation algorithm that would accurately recover plane-rectangular samples from a minimum number of plane-polar samples with a given required precision. The near-field to far-field transformation using the plane-rectangular near-field samples may then be performed using an efficient fast Fourier transform (FFT) implementation for computation of (2). An arbitrary far-field point may then be found in "closed-form" via application of the OSI approach to the plane wave spectrum samples.

The essential modification of the OSI algorithm unique to the bi-polar technique is the replacement of the plane-polar's linear domain, which corresponds with the radial direction, with a circular domain for the bi-polar technique corresponding to the probe arm's radially scribed circular arcs. The interpolation of the bi-polar near-field samples into a plane-rectangular format given the surrounding bi-polar samples is then calculated using

$$\underline{b}(\beta,\alpha) = \sum_{n=n_o-q+1}^{n_o+q} \sum_{m=m_o-p+1}^{m_o+p} \underline{b}(n\Delta\beta, m\Delta\alpha)\Omega\left(\Psi_{mn}^1\right)D_{M1'}\left(\Psi_{mn}^1\right)\Omega\left(\Psi_{mn}^2\right)D_{M2'}\left(\Psi_{mn}^2\right) \quad (5)$$

where (n_o, m_o) are the indexes of the near-field sample nearest (on the left) to the desired output sample, $2q$ and $2p$ are, respectively, the number of retained radial

arc and azimuthal samples, $\Delta\beta$ is the angular sample spacing along a radial arc, $\Delta\alpha$ is the azimuthal sample spacing, Ω is the Chebychev convergence function [9], $D_{M1'}$ and $D_{M2'}$ are Dirichlet interpolation functions [9] where M1' is the number of samples in the azimuthal direction and M2' is the number of samples along each radial arc, and

$$\Psi^1_{mn} = \alpha - m\Delta\alpha \tag{6a}$$

$$\Psi^2_{mn} = \beta - n\Delta\beta \tag{6b}$$

A rigorous discussion of sampling requirements in the (β,α) coordinates is found in [6] and is based on sampling requirements in the plane-polar coordinates [9]. The (β,α) coordinates of the desired plane-rectangular output sample at (x,y) may be found from [6, (5)-(6)]. It may also be noted that in the limit as the bi-polar probe arm length L tends to infinity that the bi-polar configuration approaches the plane-polar configuration and (5)-(6) tend to the results reported in [9].

The expressions in (5)-(6) additionally differ from those in [9] in that the number of samples on each ring are assumed to be the same. This implementation results in an oversampled scan plane in the vicinity of the scan plane center, however, direct acquisition of samples according to the sampling criteria in [9] implies a more complicated data acquisition algorithm. The acquisition of extraneous samples causes no significant increase in measurement time since the AUT must rotate through a full revolution despite the number of acquired samples. The unnecessary samples could, in fact, be filtered prior to performing the data processing.

B. Jacobi-Bessel and Fourier-Bessel Transforms

The Jacobi-Bessel [4], [11] and Fourier-Bessel [10] transforms expand the bi-polar near-field in a set of basis functions which allow both the expansion coefficients to be found from orthogonality considerations using numerical integration and the far-field in any observation direction to be found in "closed-form" as a series employing the expansion coefficients and defined functions. The direct expansion of the bi-polar near-field eliminates the need for interpolation of the near-field samples.

The Jacobi-Bessel transform technique expands the bi-polar near-field using harmonic functions in the azimuthal direction and the modified Jacobi polynomials [4], [11] in the radial direction as

$$Q(s,\phi) = \sum_{n=0}^{\infty} \sum_{m=0}^{\infty} \left[\underline{C}_{nm} \cos(n\phi) + \underline{D}_{nm} \sin(n\phi) \right] F_m^n(s) \tag{7}$$

where $\underline{C}_{nm}$ and $\underline{D}_{nm}$ are the vector expansion coefficients. $\underline{Q}(s,\phi)$ is related to the bi-polar near-field $\underline{b}(s,\phi)$ by

$$Q(s,\phi) = \frac{a^2}{2\pi} \underline{b}(s,\phi) e^{jkas[u_o \cos\phi + v_o \sin\phi]} \tag{8}$$

where (u_o, v_o) are the chosen coordinates of the expansion center. The orthogonality relations of the expansion functions allow the expansion coefficients in (7) to be found in the (β, α) coordinate system using the coordinate transform of (1) as

$$\left\{ \begin{matrix} \underline{C}_{nm} \\ \underline{D}_{nm} \end{matrix} \right\} = \frac{\varepsilon_n L^2}{a^2} \int_0^{\beta_{max}} \int_0^{2\pi} \underline{Q}(\beta,\alpha) \left\{ \begin{matrix} \cos(n\alpha) \\ \sin(n\alpha) \end{matrix} \right\} F_m^n(s(\beta)) \sin\beta \, d\alpha \, d\beta \tag{9}$$

where ε_n is related to the Neumann number, $s(\beta)$ is defined in (1a), and β_{max} is determined from (1a) when $s=1$. The expansion coefficients $\underline{C}_{nm}$ and $\underline{D}_{nm}$ are independent of the far-field observation coordinates (u,v) thus once they are computed they may be stored and used to find the far-field at any desired location. The expansion coefficients of (9) may also be equivalently expressed in the conventional polar coordinate system (s,ϕ) using the coordinate transform of (1) however, recalling that the acquisition of bi-polar samples with a constant probe arm angle increment $\Delta\beta$ results in non-uniformly radially spaced, concentric, circular rings of samples, implies that the resultant numerical integration over the radial coordinate s require an integration over non-uniformly spaced samples. Numerical integration directly in the (β,α) coordinate system circumvents this inconvenience. The radiation integral (2) is found [4], [11] as

$$\underline{D}(u,v) = \sum_{n=0}^{\infty} \sum_{m=0}^{\infty} j^n \left[\underline{C}_{nm} \cos(n\Phi) + \underline{D}_{nm} \sin(n\Phi) \right] \sqrt{2(n+2m+1)} \frac{J_{n+2m+1}(kB)}{kB} \tag{10}$$

where

$$kB = ka\sqrt{(u - u_o)^2 + (v - v_o)^2} \qquad (11)$$

$$\Phi = \tan^{-1}\left(\frac{v - v_o}{u - u_o}\right) \qquad (12)$$

The Jacobi-Bessel transform results in the use of integer order Bessel functions having an argument sized to the scan plane radius. It may be noted that all terms of (10) are centered at the expansion center (u_o, v_o) with weightings defined by the expansion coefficients, and that at this location the first term, being the Airy disc function, has a peak whereas all subsequent terms have nulls.

The Fourier-Bessel transform expands the bi-polar near-field as

$$\underline{Q}(s, \phi) = \sum_{m=-\infty}^{\infty} \sum_{n=-\infty}^{\infty} \underline{G}_{mn} e^{-j\left[\frac{m\pi x}{a} + \frac{n\pi y}{a}\right]} \qquad (13)$$

where $\underline{G}_{mn}$ are the vector expansion coefficients. $\underline{Q}(s, \phi)$ is related to the bi-polar near-field $\underline{b}(s, \phi)$ in a manner similar to (8). The orthogonality relations of the expansion functions allow the expansion coefficients in (13) to be found in the (β, α) coordinate system as

$$\underline{G}_{mn} = \frac{L^2}{a^2} \int_0^{\beta_{max}} \int_0^{2\pi} \underline{Q}(\beta, \alpha) e^{j\pi s(\beta)[m\cos\alpha + n\sin\alpha]} \sin\beta \, d\alpha \, d\beta \qquad (14)$$

and must be computed numerically where $s(\beta)$ and β_{max} are defined as before. The Fourier-Bessel transform, in its conventional usage, employs an FFT for coefficient determination, however, the bi-polar sample arrangement makes this unfeasible. The computation time, consequently, for coefficient determination is excessive compared to the Jacobi-Bessel transform due to the fact that more coefficients are generally required [12]. The expansion coefficients $\underline{G}_{mn}$, as in the case of the Jacobi-Bessel transform, are independent of the far-field observation coordinates (u, v). The radiation integral (2) is found [10] as

$$\underline{D}(u, v) = \sum_{m=-\infty}^{\infty} \sum_{n=-\infty}^{\infty} \underline{G}_{mn} \frac{J_1(kB_{mn})}{kB_{mn}} \qquad (15)$$

where

$$kB_{mn} = ka\sqrt{\left(u - u_o - \frac{m\pi}{ka}\right)^2 + \left(v - v_o - \frac{n\pi}{ka}\right)^2} \qquad (16)$$

The Fourier-Bessel transform results in the use of only the Airy disc function having an argument sized to the scan plane radius. It may be noted that each term of (15) is centered at a progressively wider angle from the expansion center (u_o, v_o) with weightings defined by the expansion coefficients.

The convergence properties of (10) and (15) are obviously greatly improved when the first few series terms closely approximate the actual far-field pattern. A judicious choice of the expansion center, which typically corresponds to the expected direction of the far-field pattern main beam, is essential if rapid convergence is to be achieved. The expected direction of the main beam may be determined from either a priori knowledge of the AUT or an examination of the phase of the measured near-field. The inclusion of too many terms in (10) or (15) can also negatively affect convergence since the expansion coefficients in (9) and (14) for large orders cannot be numerically computed accurately. The Jacobi-Bessel and Fourier-Bessel transform techniques are most efficient for circular apertures since the leading term in both (10) and (15) is the Airy disc function, however, this leading term is sized to the scan plane radius and not the AUT radius. A scan plane radius similar to the AUT radius would improve convergence but at the expense of collecting an insufficient amount of near-field samples to properly characterize the far-field pattern at wider angles with respect to the expansion center.

V. EXPERIMENTAL RESULTS, RANGE AND PROCESSING COMPARISONS

A validation of our customized bi-polar implementation was performed through a series of antenna measurement comparisons with other antenna ranges. Two planar waveguide-fed slot array antennas were used for the measurements and are shown in Fig. 6. The first antenna is an X-band (9.3 GHz) waveguide-fed slot array with an elliptical aperture 14.8λ by 8.7λ (Fig. 6 (a)). The 196 elements are located on a 0.689λ (E-plane) by 0.738λ (H-plane) rectangular lattice. The aperture illumination of this array provides for a first sidelobe level of approximately -28 dB (E-plane) and -25 dB (H-plane). The second, larger antenna was also measured and used for inter-range comparison. This antenna, an

X-band (9.375 GHz) waveguide-fed slot array with a 23λ by 21.4λ near-circular aperture, was designed for weather radar applications (Fig. 6 (b)). The 764 elements are located on a 0.704λ (E-plane) by 0.758λ (H-plane) rectangular lattice. The aperture taper provides for a first sidelobe level of approximately -25 dB in both the E-plane and H-plane. The antennas were measured on three ranges: the bi-polar near-field range, a 1000-foot outdoor far-field range and a production plane-rectangular planar near-field range. The plane-rectangular facility incorporates a high-accuracy laser interferometer for full closed-loop probe positioning.

A. Elliptical Aperture Array Results

Fig. 7 (a) and (b) are comparisons of the elliptical array far-field patterns, E-plane and H-plane, respectively, obtained on the bi-polar range versus the plane-rectangular planar near-field range. The bi-polar processing was carried out using 10 by 10 point OSI interpolation/FFT with full probe correction for an open-ended WR-90 waveguide probe. The far-field pattern of the probe used for the correction was a theoretical open-ended waveguide model. The scan plane was 28λ in diameter with a probe height of 3.8λ yielding a valid angle of approximately 60 degrees. The radial spacing was 0.5λ and the azimuthal spacing was 0.8λ on the outermost (28th) ring. Range comparison is excellent to less than -45 dB within the limits determined by the valid angle. Excellent agreement of null position and depth may also be noted. Fig. 8 (a) and (b) are comparisons of the elliptical array patterns, E-plane and H-plane, respectively, obtained on the bi-polar range versus a 1000 foot outdoor far-field range. Error sources contaminating the far-field range measurement have been documented and may explain any slight range comparison discrepancies.

B. Weather Radar Array Results

Fig. 9 (a) and (b) are comparisons of the weather radar array patterns, E-plane and H-plane, respectively, obtained on the bi-polar near-field and plane-rectangular planar near-field ranges. The bi-polar processing was carried out using 10 by 10 point OSI interpolation/FFT with full probe correction. The scan plane was 55λ in diameter with a probe height of 6.7λ yielding a valid angle of approximately 60 degrees. The radial spacing was 0.435λ and the azimuthal spacing was 0.893λ on the outermost (55th) ring. Similar conclusions regarding range comparison may be drawn regarding sidelobe level and null position

469

agreement. This measurement, however, reflects a rather challenging range comparison due to the highly oscillatory, low sidelobe nature of the array. Fig. 10 (a) and (b) are comparisons of the weather radar array patterns, E-plane and H-plane respectively obtained on the bi-polar range versus the 1000 foot outdoor far-field range.

One of the most challenging measurements performed on any antenna range is cross-polarization since the low RF intensity levels are easily corrupted by range errors and antenna misalignment. Slight misalignment of the AUT or probe can significantly affect the measured cross-polarized field intensity hence good inter-range comparisons are generally difficult to achieve. Fig. 11 (a) and (b) are comparisons of the weather radar array cross-polarized patterns, E-plane and H-plane, respectively, measured on the bi-polar and plane-rectangular near-field ranges. The slight rippling of the plane-rectangular measurement occurs at a spatial frequency higher than expected for this size of antenna. It is, therefore, suggested that this artifact is due to a probe/AUT multiple reflection corrupting the plane-rectangular measurement. Nonetheless, both the peak and off-boresight levels and the envelope of the two measurements agree exceptionally well and are considered a superior inter-range comparison.

C. Processing Method Comparison

A comparison of the interpolatory optimal sampling interpolation (OSI)/fast Fourier transform (FFT) and the non-interpolatory Jacobi-Bessel and Fourier-Bessel transforms for near-field to far-field processing has been performed using the elliptical array measured data. A scan plane radius of 23.6λ (55 rings with 166 samples per ring) and a scan plane height of 6.7λ yield a valid angle of approximately 61 degrees ($\sin(\theta)=0.87$). A comparison of a reference H-plane pattern and the H-plane patterns produced by the OSI/FFT, Jacobi-Bessel, and Fourier-Bessel methods for the waveguide-fed slot array is shown in Fig. 12. The reference H-plane pattern was obtained from a plane-rectangular planar near-field measurement facility [6]. The OSI interpolation was performed using a 10 x 10 grid (2p=2q=10) of retained samples and an oversampling factor of $\chi=1.15$. The interpolated plane-rectangular grid contained 128 x 128 samples at a sample spacing of 0.5λ. The Jacobi-Bessel transform was produced using n=m=50 coefficients while the Fourier-Bessel transform utilized n=m=42 coefficients. The E-plane result is shown in Fig. 13.

The near-field to far-field processing techniques, in comparison to the reference results, are seen to exhibit close agreement out to the vicinity of the valid angle. In fact, the H-plane and E-plane results of Figs. 12 and 13, respectively, indicate that all of the processing techniques are capable of accurately representing an irregularly behaving, low sidelobe far-field pattern. Discrepancies near and beyond the valid angle are due to both the valid angle limitation and the inherent limitations of each technique which tend to degrade wide angle accuracy.

D. Holographic Imaging and Diagnostics

The determination of the magnitude and phase of the electric field in the aperture plane of the AUT from measurements made in the near- or far- field is commonly referred to as microwave holographic imaging. Holographic imaging capabilities greatly facilitate antenna diagnostics, for example, "phase-up" and location of defective radiators in an array antenna [13] and surface and feed anomalies for reflector antenna systems [14].

The electric field in the aperture plane of the AUT is found via a standard "back-projection" technique which employs an inverse Fourier transform of the probe-corrected plane wave spectrum $\underline{t}(u,v)$ of (2)-(3) with an appropriate factor to "back-propagate" the electric field from the measurement plane to the AUT aperture plane.

Holographic imaging results have been obtained for the weather radar array. The co-polarized aperture electric field phase is shown in Fig. 14. The holographic image is produced from a 64 x 64 point zero-padded plane wave spectrum resulting in an image consisting of 128 x 128 points at $\lambda/4$ spacing. The image display software increases the image size to 512 x 512 points ($\lambda/16$ spacing) using linear interpolation and then truncates the image to the region of interest. In addition, the image display software sets phase values corresponding to relative magnitude values less than -25 dB to a common value so that rapid phase variation in regions of low intensity may be suppressed. Details of the feeding structure may be noted from the phase image of Fig. 14. In particular, the standing wave main line feed at x=0, and especially the shorts at each end of this feed, exhibit phase values substantially different from the remainder of the array. Phase aberrations peculiar to a number of cross-line feeds are also discernible. Results for the corresponding aperture electric field magnitude image clearly

revealed the tapered aperture illumination producing the 25 dB first sidelobe level far-field pattern.

VI. CONCLUSION

A novel customized bi-polar planar near-field measurement technique has been presented as an alternative to the plane-rectangular and plane-polar techniques. This configuration is mechanically simple, practical, accurate, and is capable of measuring a large scan plane with smaller physical requirements than other planar methods. Part I of this two part paper gave an introduction to the bi-polar planar near-field measurement concept including the unique hardware implementation at UCLA and, most importantly, measured results. The companion paper examines the unique data processing challenges due to the bi-polar measurement grid including near-field to far-field transformation and holographic imaging.

A comparative survey of some recent antenna measurements was presented for two waveguide-fed slot array antennas measured at the UCLA bi-polar near-field range facility and at two other facilities. Direct comparisons with a traditional outdoor far-field range and a plane-rectangular planar near-field range yielded excellent agreement for each of these antennas. The co-polarized far-field patterns agree within small fractions of a decibel even in the low-sidelobe regions. Null depth and location also show excellent agreement. The cross-polarization comparison is equally notable especially with consideration given to the extremely low RF intensity levels and inherent sensitivity to the antenna mounting and range errors. The cross-polarized measurement is often the most challenging of all antenna measurements and is rarely duplicated on inter-range comparisons. These results demonstrate that the bi-polar configuration is capable of highly accurate antenna measurements rivaling other measurement techniques.

A comparison of the OSI/FFT, Jacobi-Bessel, and Fourier-Bessel near-field to far-field processing methods demonstrated that, in comparison to an independent reference, highly accurate results are attainable, within the region defined by the valid angle, with each of these methods, despite their fundamental differences in implementation. In fact, the required number of measurements, requisite storage, and attainable precision are essentially the same for all the discussed methods because the maximum allowable sample spacing for all are fixed by the "effective" bandwidth of the field. These fundamental differences in

implementation, however, provide for a rigorous comparison of the methods and yield a rich spectrum of available data processing algorithms.

The existence of this bi-polar planar near-field range at UCLA provides many unique educational and research opportunities. Electromagnetic theory is often a difficult subject for students to understand. Extending the educational experience from the classroom into the laboratory aids the learning process. Modern antenna measurements, particularly near-field measurements, are an important but often neglected topic in the microwave curriculum despite the importance and pervasiveness of these techniques in industry. The neglect in antenna measurement education is primarily due to the absence of appropriate laboratory resources. The planar near-field technique and the plane wave spectrum method draw heavily upon concepts coveied in linear system theory courses. As such, students are well-prepared to understand the method and can immediately benefit from antenna measurement laboratory experience. Additionally, holographic imaging capabilities provide students with electromagnetic field visualization and valuable insight into antenna radiation in the antenna's aperture, near-field and far-field regions.

REFERENCES

[1] A.D. Yaghjian, "An overview of near-field antenna measurements," IEEE Trans. Antennas Propagat., vol. AP-34, pp. 30-45, January 1986.

[2] Special Issue on Near-field Scanning Techniques, IEEE Trans. Antennas Propagat., vol. AP-36, June 1988.

[3] D.M. Kerns, "Plane-wave scattering-matrix theory of antenna and antenna-antenna interactions," NBS Monograph 162, U.S. Govt. Printing Office, Washington, DC, June 1981.

[4] Y. Rahmat-Samii, V. Galindo-Israel, and R. Mittra, "A plane-polar approach for far-field construction from near-field measurement," IEEE Trans. Antennas Propagat., vol. AP-28, pp. 216-230, March 1980.

[5] M.S. Gatti and Y. Rahmat-Samii, "FFT applications to plane-polar near-field antenna measurements," IEEE Trans. Antennas Propagat., vol. AP-36, pp. 781-791, June 1988.

[6] L.I. Williams, Y. Rahmat-Samii, and R.G. Yaccarino, "The bi-polar planar near-field measurement technique part I: implementation and measurement comparisons," To be published in IEEE Trans. Antennas Propagat.

[7] A.D. Yaghjian, "Approximate formulas for the far fields and gain of open-ended rectangular waveguide," National Bureau of Standards, NBSIR 83-1689, May 1983.

[8] L.I. Williams and Y. Rahmat-Samii, "Bi-polar planar near-field measurements with and without probe co-rotation: an experimental verification," IEEE Antennas Propagat. Soc. Int. Symp. Dig., Ann Arbor, MI, June 1993, pp. 1812-1815.

[9] O.M. Bucci, C. Gennarelli, and C. Savarese, "Fast and accurate near-field-far-field transformation by sampling interpolation of plane polar measurements," *IEEE Trans. Antennas Propagat.*, vol. AP-39, pp. 48-55, January 1991.

[10] R. Mittra, W.E. Ko, and M.S. Sheshadri, "A transform technique for computing the radiation pattern of prime-focal Cassegrainian reflector antennas," *IEEE Trans. Antennas Propagat.*, vol. AP-30, pp. 520-524, May 1982.

[11] V. Galindo-Israel and R. Mittra, "A new series representation for the radiation integral with application to reflector antennas," *IEEE Trans. Antennas Propagat.*, vol. AP-25, pp. 631-641, September 1977.

[12] C.S. Kim and Y. Rahmat-Samii, "Analysis of antennas with elliptical apertures using Fourier-Bessel expansion: a comparative study," in *Progress in Electromagnetics Research*, Elsevier, New York, 1991.

[13] J.J. Lee, E.M. Ferren, D.P. Woollen, and K.M. Lee, "Near-field probe used as a diagnostic tool to locate defective elements in an array antenna," *IEEE Trans. Antennas Propagat.*, vol. AP-36, pp. 884-889, June 1988.

[14] Y. Rahmat-Samii, "Surface diagnosis of large reflector antennas using microwave holographic metrology: an iterative approach," *Radio Science*, vol. 19, pp. 1205-1217, September-October 1984.
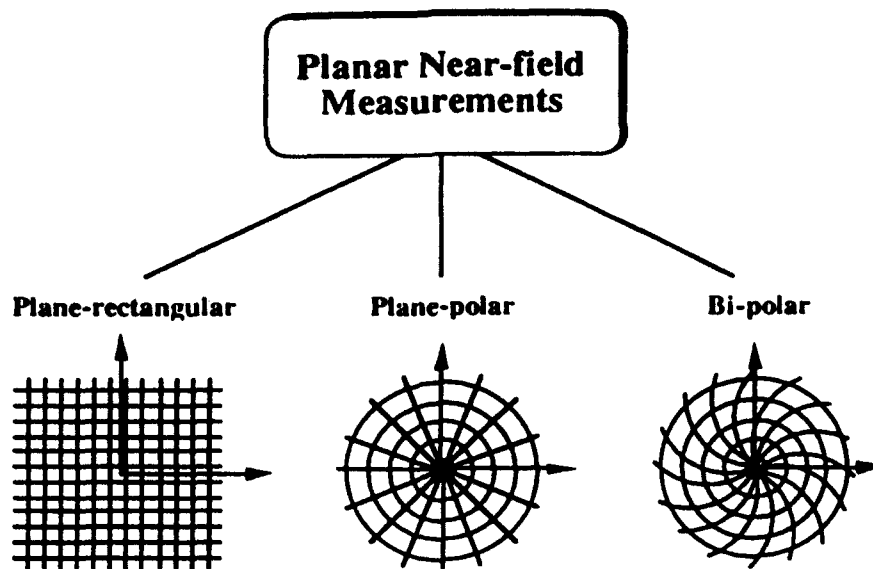
Fig. 1. Planar near-field measurement sample arrangement depends upon the mechanical configuration of the robotic positioner used for the data collection. Current techniques include the plane-rectangular, plane-polar and bi-polar configurations.
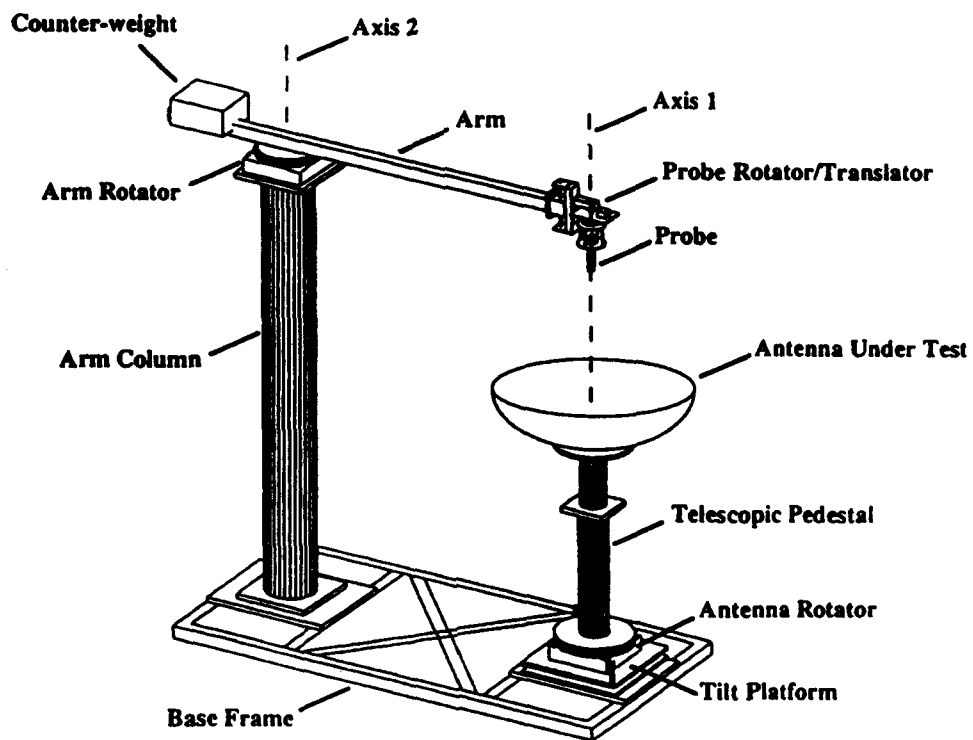
Fig. 2. Bi-polar planar near-field measurement scanner. Essential features include the bi-polar arm and the two axes of rotation.
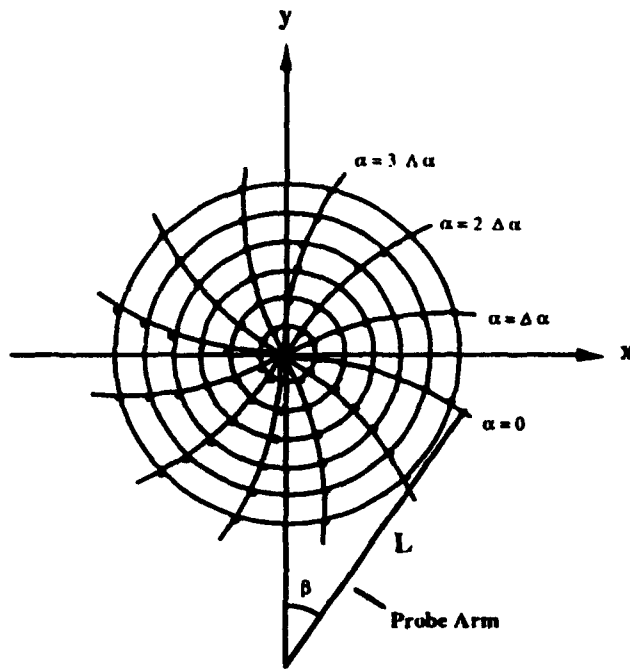
Fig. 3. Bi-polar sampling grid. Measurement rings occur due to the rotation of the test antenna and radial arcs occur due to the rotation of the probe-carrying arm.
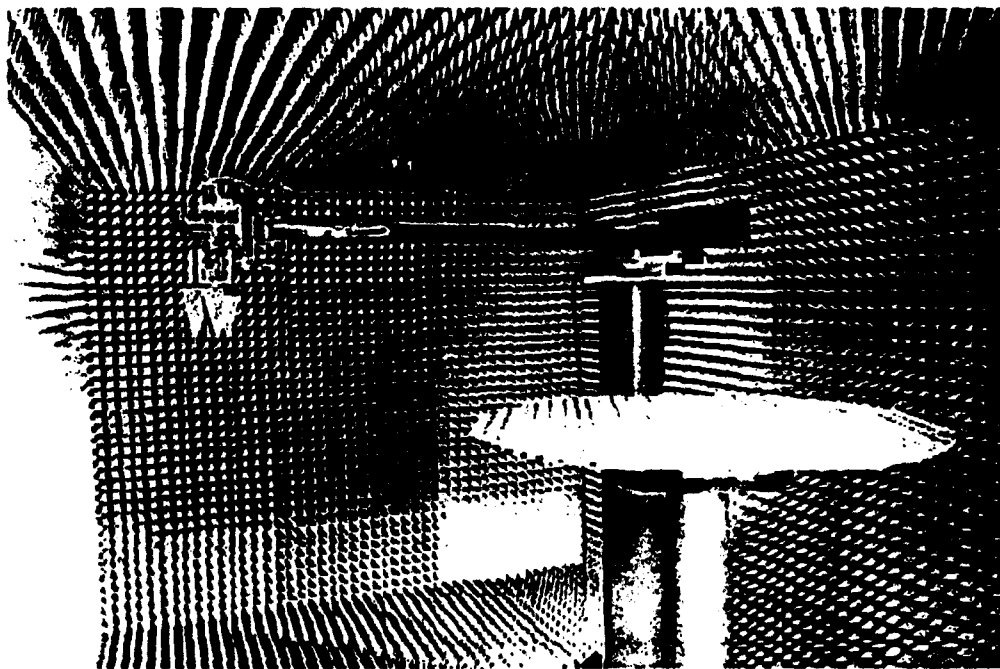
Fig. 4. Bi-polar planar near-field range at the University of California, Los Angeles. This scanner can measure antennas larger than seven feet in diameter on a scan plane 16 feet in diameter.
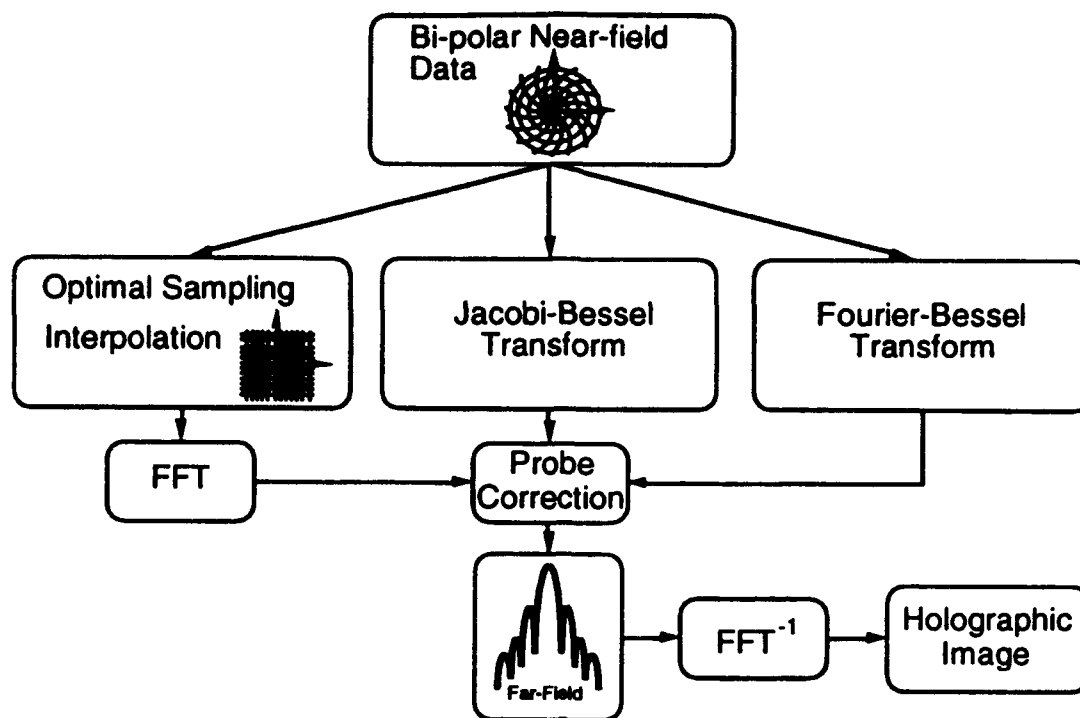
Fig. 5. Overview of bi-polar near-field data processing techniques.
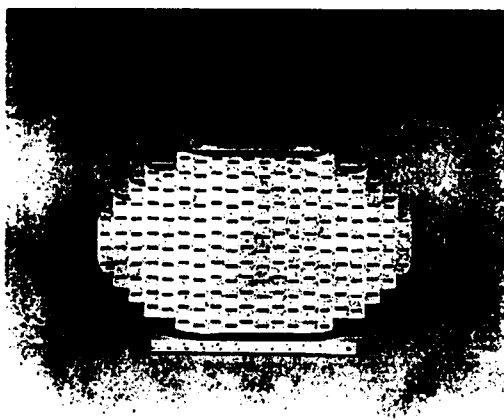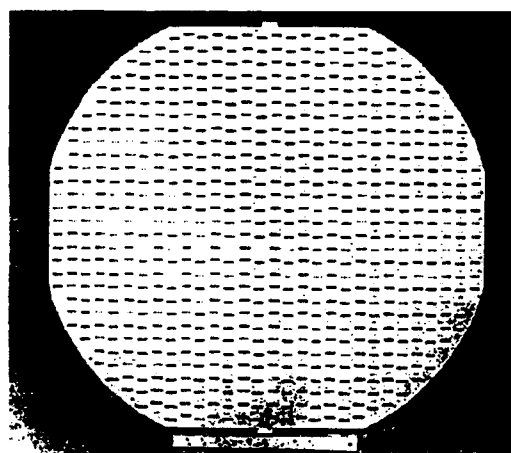
(a)   (b)

Fig. 6. Planar waveguide-fed slot array antennas used for measurement comparisons. The
foreground of each photograph has a foot-long ruler for size comparison.
(a) Elliptical aperture array with a 14.8λ by 8.7λ aperture at 9.3 GHz.
(b) Weather radar array with a near-circular 23λ by 21.4λ aperture at 9.375 GHz.
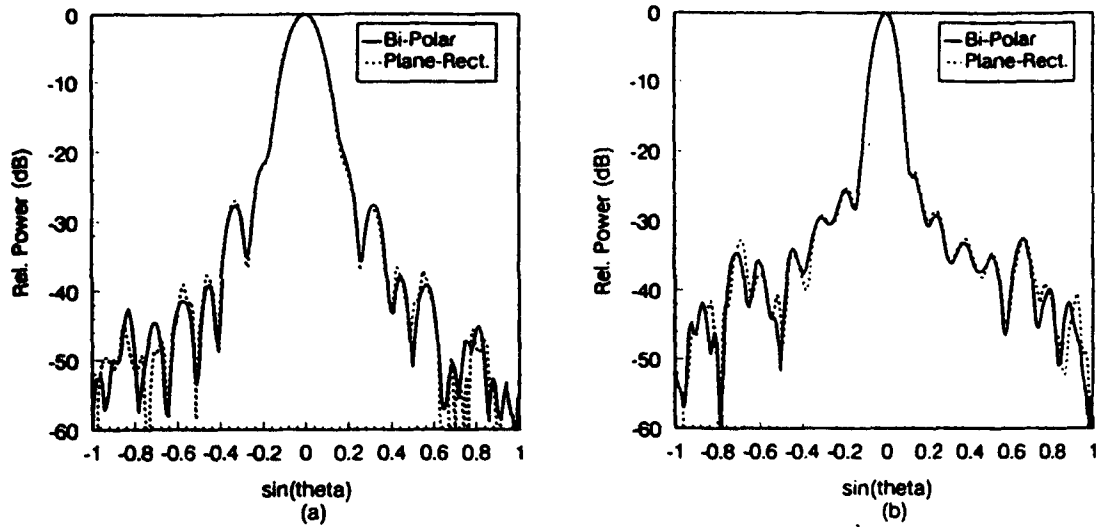
Fig. 7. Comparison of the far-field patterns obtained on the bi-polar range and a plane-
rectangular planar near-field range for the elliptical array of Fig. 6(a).
(a) E-plane. (b) H-plane. Valid angle is sin(θ) = 0.87.
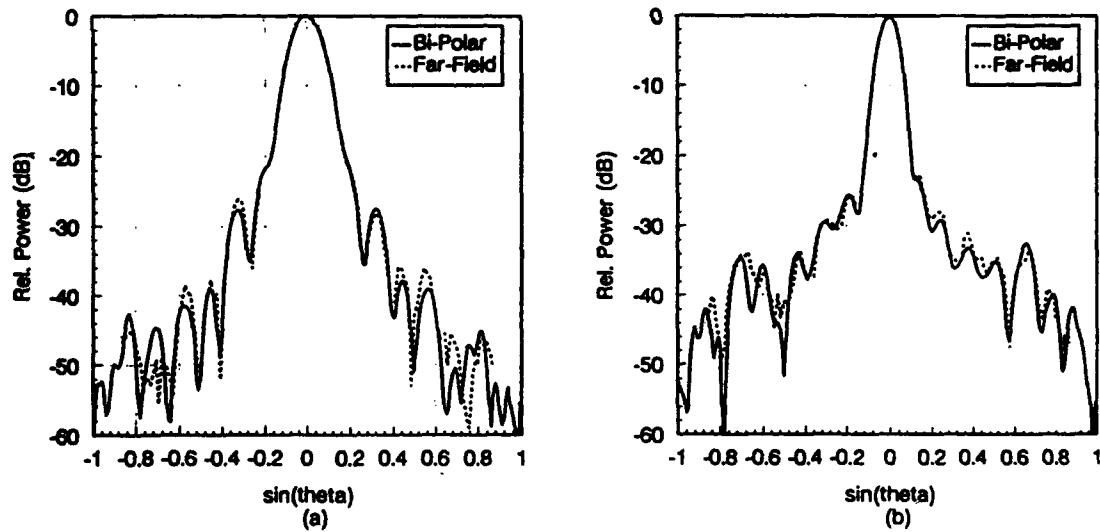
Fig. 8. Comparison of the far-field patterns obtained on the bi-polar range and a 1000 foot
outdoor far-field range for the elliptical array of Fig. 6(a).
(a) E-plane. (b) H-plane. Valid angle is sin(θ) = 0.87.
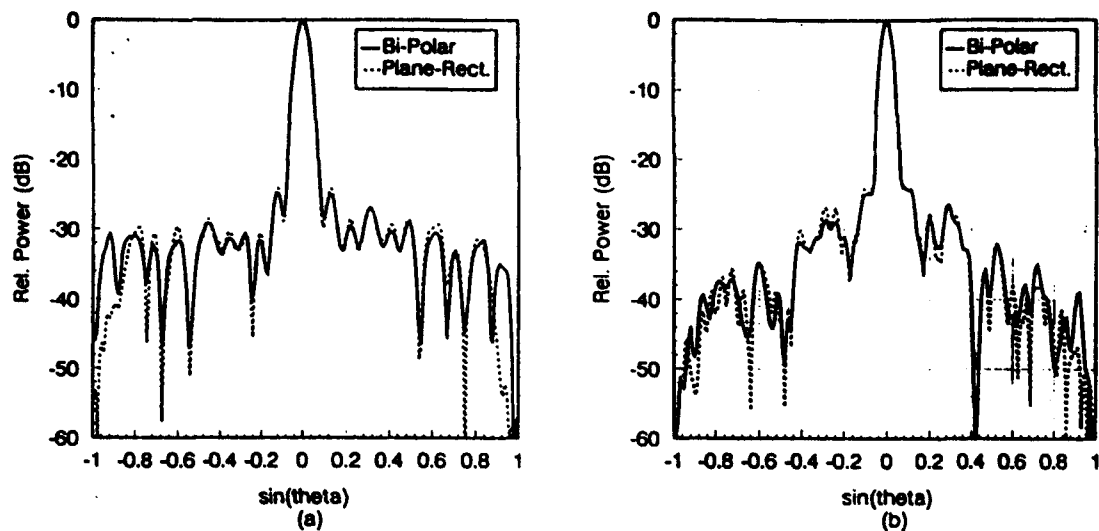
Fig. 9. Comparison of the far-field patterns obtained on the bi-polar range and a plane-rectangular planar near-field range for the weather radar array of Fig. 6(b).
(a) E-plane. (b) H-plane. Valid angle is sin(θ) = 0.87.
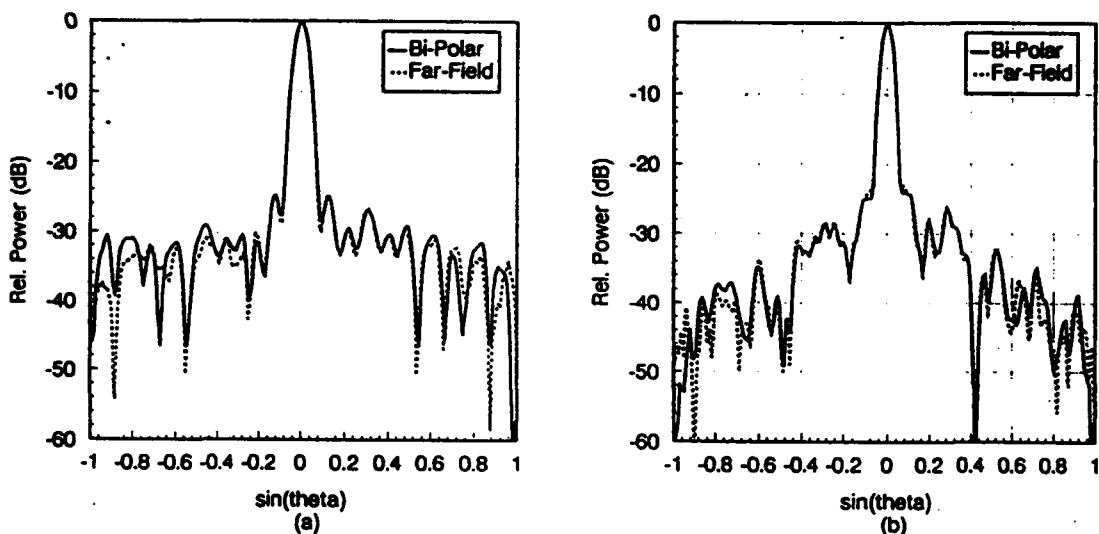
Fig. 10. Comparison of the far-field patterns obtained on the bi-polar range and a 1000 foot outdoor far-field range for the weather radar array of Fig. 6(b).
(a) E-plane. (b) H-plane. Valid angle is sin(θ) = 0.87.
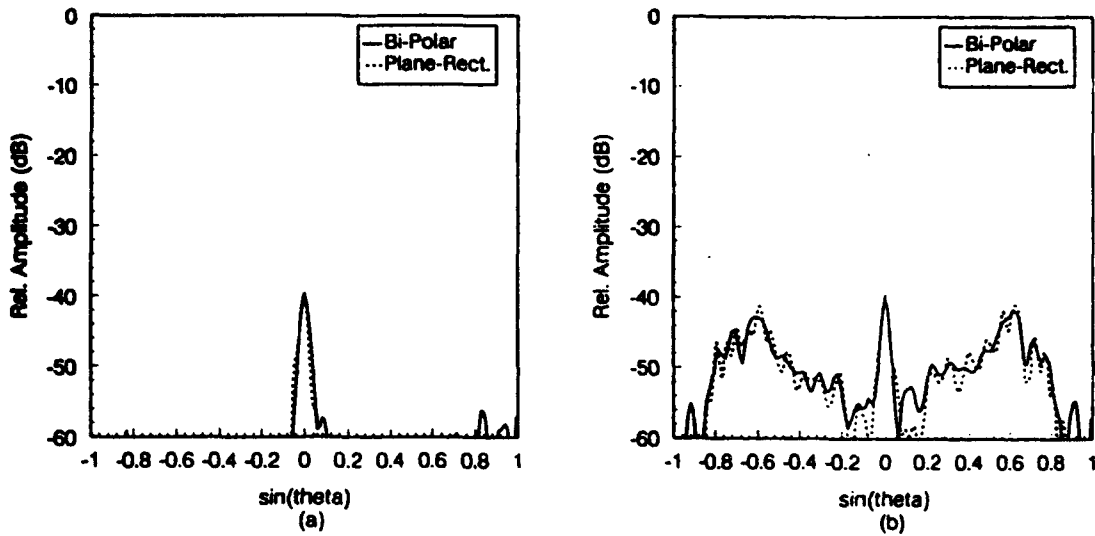
Fig. 11. Comparison of the cross polarized far-field patterns obtained on the bi-polar range and a plane-rectangular planar near-field range for the weather radar array of Fig. 6(b).
(a) E-plane. (b) H-plane. Valid angle is sin(θ) = 0.87.
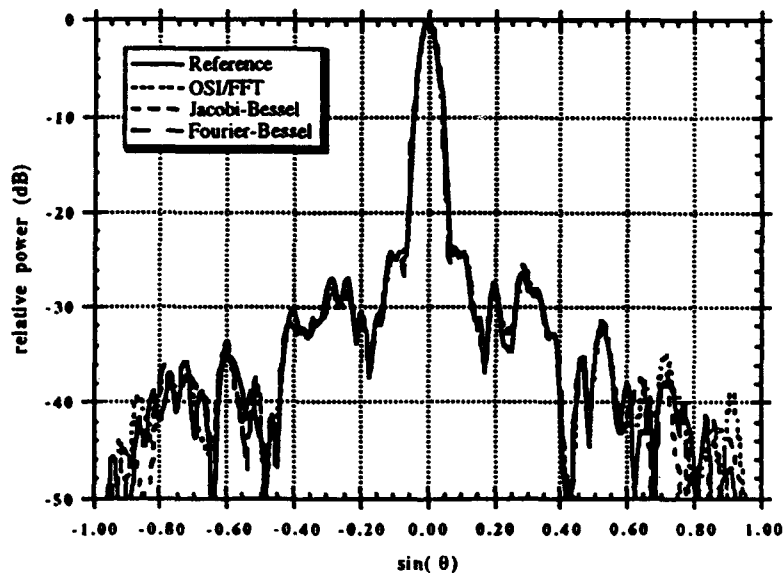
Fig. 12. Comparison of processing methods for the co-polarized, H-plane pattern of the weather radar array of Fig. 6(b). Valid angle is sin(θ)=0.87. The reference pattern is obtained from a plane-rectangular planar near-field measurement facility.
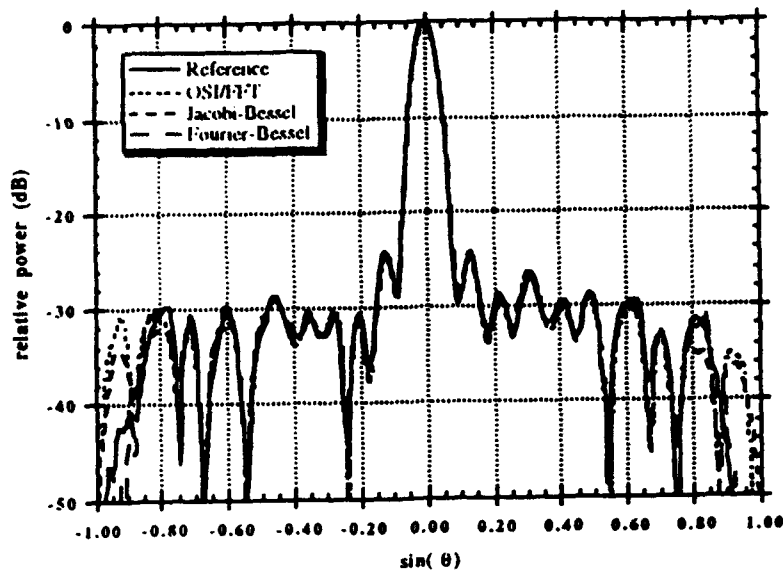
Fig. 13. Comparison of processing methods for the co-polarized, E-plane pattern of the weather radar array of Fig. 6(b). Valid angle is sin(θ)=0.87. The reference pattern is obtained from a plane-rectangular plaanar near-field measurement facility.
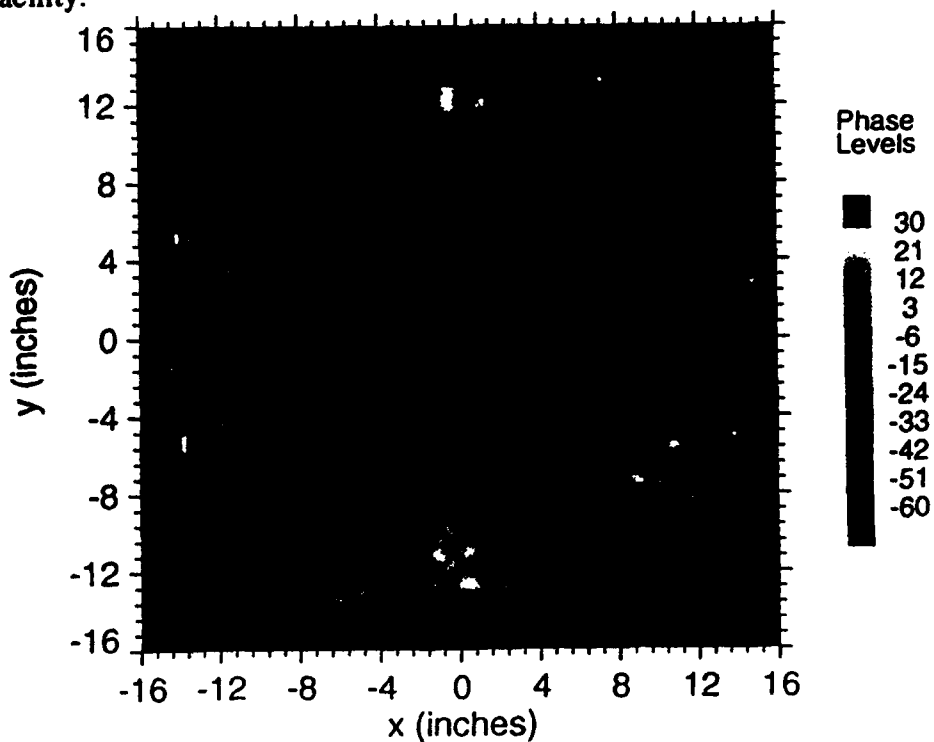
Fig. 14. Holographic image of the aperture electric field phase for the weather radar array.

481

Productivity Gains Using Multiple-Channel, Multiple-Frequency Measurement Techniques for Testing the E2C Antenna

James Scherer, Senior Vice President of
Technology
Robert Magatagan, Senior Scientist
John Miller, Production Test Manager
Gary Amaral, Production Test Supervisor

Loral Randtron Systems
130 Constitution Drive
Menlo Park, CA 94025

John Swanstrom

Hewlett-Packard
Santa Rosa Systems Division
1400 Fountaingrove Parkway
Santa Rosa, CA 95403

Abstract

This paper presents a feasibility study of the productivity improvements that are possible for the production test of the E2C antenna, using multiple-parameter, multiple-frequency measurement techniques. The measurement requirements for the antenna are presented along with the current measurement times. A multiple-channel, multiple-frequency measurement technique is described which will greatly reduce the measurement times. The new measurement times are calculated, and used to determine if the productivity improvements are justified financially.

An economic analysis is include also, which examines the financial impact of the improved productivity, and compares this to the cost of implementing the new measurement system. The financial analysis calculates the payback period, return on investment, net present value, and internal rate of return.

Introduction

The tendency is to leave successful endeavors alone, but not at Randtron. A progressive company, Randtron is concerned with maintaining its productivity and its competitive edge. At Randtron, we produce the E2C antennas, a very successful program for us.

Because the acceptance testing of the E2C antenna consumes a significant portion of test time (and money), we performed a feasibility study, in conjunction with Hewlett-Packard, to determine ways to reduce test time. Reducing the time reduces the cost of producing the antennas, keeps us competitive, and improves the profitability of our company. This paper presents the results of the feasibility study.

The E2C Antenna Program

The E2C antenna is used for airborne early warning and command for the U.S. Navy. It provides electronic surveillance and protection for the U.S. Naval fleet worldwide. The antenna is a large, 24-foot diameter disk that is mounted atop the E2C Hawkeye aircraft, which can be either land or carrier based. Randtron has produced over two hundred E2C antennas since 1972. Our current production averages 20 units per year. We were selected as the sole supplier of E2C antennas because of our ability to produce quality antennas in large volumes at low cost.

Required Antenna Patterns for E2C Antenna

Like all critical flight hardware, the E2C antenna undergoes a complete acceptance test procedure before delivery. The procedure consists of a complete set of antenna patterns, absolute gain measurements, VSWR measurements, a power handling verification, and a measurement of isolation between test channels. The focus of this paper is on the productivity gains that can be made by making improvements in the antenna pattern measurements. Table 1 summarizes the required antenna patterns. There are 185 azimuth patterns, 26 elevation patterns, and 3 relative-phase measurements.

Present Measurement Techniques and Times

Our measurement techniques for the antenna patterns have been the same since 1972. We utilize older measurement instrumentation; a single channel receiver (SA 1742), and a rectangular paper pattern recorder (SA 1520). One pattern (at a single frequency) is produced for each 360 degree rotation of the antenna.

Because of the inertia and momentum associated with large antenna size, the maximum positioner velocity is one revolution per minute. Therefore it takes one minute to acquire the pattern, and one minute to rewind the positioner. We average one azimuth pattern approximately every four minutes. Data acquisition time is 12 hours 20 minutes (185 patterns x 4 minutes/pattern) for the azimuth patterns. For the elevation patterns, the maximum positioner speed is 0.2 degrees/second or 7 minutes per elevation cut. It takes four hours to measure all of the elevation patterns. The absolute gain measurements take four hours, and the relative phase measurements take 1.5 hours to complete. When the measurement overhead is considered, the acceptance testing and data analysis takes 3.5 days to complete. We utilize a four-person crew for the duration of the test.

Technique for Reducing Measurement Time

One of the reasons the data acquisition takes so long is that only one pattern is acquired for each complete rotation of the antenna. If several patterns at different test ports and frequencies could be taken for each rotation of the antenna, this would greatly increase the amount of data acquired in one rotation of the antenna, and significantly reduce the acquisition time. Thus, a multiple-channel, multiple-frequency test technique is indicated. With this technique, at each angular increment of the test antenna, all test ports can be measured at all frequencies. Since the instrumentation is very fast, the data acquisition can be accomplished well before the next angular increment needs to be measured.

Recommended Measurement Technique

Figure 1 shows the instrumentation configuration for measuring the E2C antenna. Key parts of the measurement system are the PIN switches, which allow rapid switching between the test channels, and the fast frequency agility of the system. The PIN switch controller orchestrates all of the data acquisition, and sequences the switching of the PIN switches.

For the E2C antenna, the test sequence is:

- Establish a gain and phase reference at each frequency. This allows each of the subsequently acquired antenna patterns to have a gain and phase reference.

- Measure the sum, difference, auxiliary 1, and auxiliary 2 test channels at their four different operating frequencies at seven different elevation angles.

- Measure the IFF test channel at the required nine different frequencies at seven elevation angles.

- Measure the cross-polarized IFF channel antenna patterns at seven elevation angles.

With this technique, all 185 azimuth patterns are acquired in twenty one rotations of the antenna.

Predicted Data-Acquisition Times

The details for computing the data-acquisition times follow. Frequency switching speeds range from 5-18 msec per frequency depending on the configuration and the size of the frequency step. For this example, telephone line modems are used to communicate frequency changes to the microwave source, and the frequency switching speed is 18 msec. Switching between test channels requires 0.4 msec per channel.

First, measure the sum, difference, auxiliary 1, and auxiliary 2 test channels at four frequencies in one rotation of the antenna.

Acquisition time per angular increment = 78.4 msec.

$$\left[\frac{18msec.}{Freq.} + \left(\frac{0.4msec.}{channel} \right) \times 4chan. \right] \times 4\,freq.$$

Maximum positioner velocity:

$$\frac{0.25\,deg}{78.4\,m\,sec} = 3.2\,deg/sec$$

Time to measure four channels at four frequencies at one elevation angle:

$$\frac{360\,deg}{3.2\,deg/sec} = 112.5\,sec$$

To measure the IFF test channel at nine frequencies at one elevation angle, the acquisition time per angular increment is 165.6 msec, calculated as follows:

$$\left[\frac{18msec}{freq.} + \left(\frac{0.4msec.}{channel} \right) \times 1chan. \right] \times 9\,freq.$$

Maximum positioner velocity:

$$\frac{0.25\,deg}{0.165\,sec} = 1.5\,deg/sec.$$

Time to measure one channel (IFF) at 9 frequencies at one elevation angle:

$$\frac{360\,deg}{1.5\,deg/sec} = 240\,sec.$$

Total data acquisition time for azimuth patterns is: 112.5 sec./rotation x 7 elevation angles + 240 sec./rotation x 7 elevation angles x 2 polarizations = 69 minutes. This would require twenty one rotations of the test antenna.

For elevation patterns, the data acquisition time will be limited by how fast the positioner can move in elevation, which is 0.2 degrees per second due to the gear reduction required in the positioner.

Elevation patterns: Measure all five channels at 13 different frequencies.

Acquisition time per angular increment = 260 msec calculated as follows:

$$\left[\frac{18msec}{freq.} + \left(\frac{0.4msec}{channel} \right) \times 5chan. \right] \times 13\,freq.$$

Maximum positioner velocity (elevation):

$$\frac{0.25\,deg}{0.260\,sec} = 0.96\,deg/sec$$

Maximum positioner velocity is 0.2 deg./sec., so measurement speed is positioner limited.

Time to measure elevation patterns:

$$\frac{80\,deg}{0.2\,deg./sec.} = 400\,sec. \approx 7\,min.$$

Total data acquisition times:
Azimuth patterns: 69 minutes
Elevation patterns: 7 minutes

Data-Acquisition Time vs. Measurement Time

There is a difference between the data-acquisition time and total measurement time. Data-acquisition time is the time it takes the instrumentation to acquire the data, while measurement time is the time it takes to perform the complete test, which includes measurement overhead such as boresighting, breaks for personnel, etc.

For our feasibility study to be valid, it is important to accurately estimate the total measurement time, rather than just data-acquisition times. For the proposed system, we calculated the new data-acquisition times, and then, based on our experience, added our estimates of measurement overhead to arrive at total measurement time.

Data Analysis

Our present method of data analysis is a manual process which takes four hours to complete and utilizes four people. With the new system we are considering, the data-acquisition is done through measurement-automation software and is computer controlled. A software analysis program would be used to analyze all the antenna-pattern data. Automating the data-analysis process will result in a tremendous savings in test time and cost. The four people who laboriously analyze the patterns will be free to perform more profitable tasks, and the analysis which now takes hours to perform will be accomplished in minutes by the computer.

To develop our customized measurement analysis software will require a capital investment. The estimated cost will be included in the financial analysis portion of the feasibility study. The return on this capital investment will be the cost savings realized each time the analysis is completed in minutes instead of hours.

Cost Savings Due To Productivity Improvements

To calculate the cost savings that can be realized, we summarized the factors that contribute to the cost of performing the pattern testing with the current and proposed methods; these cost factors are shown in table 2. The test cost was determined by multiplying the number of test personnel by their hourly cost and then by test time. In this paper, we used industry-standard labor costs rather than Randtron's labor costs. As can be seen from the table, the proposed new method will save $4,697 each time the test is performed.

Required Capital Expenditure

Figure 1 shows the block diagram of the proposed measurement instrumentation which will provide the multiple-parameter, multiple-frequency measurement capability. Note that PIN switches and the PIN switch controller are used to rapidly switch between the multiple test ports. The HP 83621A synthesizers provide the fast multiple-frequency switching.

	Current method	Proposed method
Data acquisition times:		
Azimuth patterns	12 hours 20 minutes	.69 minutes
Elevation patterns	3 hours 45 minutes	7 minutes
Gain measurements	3-4 hours	included
Phase measurements	1.5 hours	included
Data analysis	4 hours	25 minutes
Total measurement time	3.5 days	1.5 days
Number of personnel	4	2
Cost of test	$6,039	$1,342

Table 2: Factors that contribute to the cost of performing the acceptance test

The total price for the measurement instrumentation is $300,410. It is estimated that the cost to change over to the new system will be $10,000, and the cost to write the analysis software will be $40,000. Thus, the total cost to implement the new measurement system is $350,410.

Economic Analysis

Table 3 shows the financial calculations used to determine the economic feasibility of this proposal. Assuming a useful life of seven years, the internal rate of return on the project is 18%, with a payback period of less than 4 years. The return on investment is 24%, and the net present value is $89,000.

Profit Improvement Proposal

The economic analysis clearly indicates that this is a sound financial investment. It has an $89,000 net present value and an 18% internal return on investment. Beyond the savings from reduced test time, which can be easily quantified, there are other benefits; improved quality of the measurements, increased technological capacity, better reliability, greater up-time of the system, and much lower maintenance costs for the new system.

Summary

Randtron has shared a feasibility study which examined how modern measurement techniques can be utilized to reduce test times and costs. The benefits to Randtron are lower costs which will insure our competitive position for the future, and improvement in our long term profitability.

Conclusions

The conclusions are clear: to be competitive in the future, companies need to look for better ways of making measurements today.

References

1. John Swanstrom, "Financially Justifying an Antenna/RCS Measurement System", 11th Annual Meeting and Symposium, Antenna Measurement and Techniques Association, Monterey, CA, October 9-13, 1989, pp. 5-27 to 5-30.

Channel	Frequencies	Azimuth Movement	Elevation Movement	# of patterns
Sum	F1–F4	360/0.5	−9 to 9 by 3	28
Delta	F1–F4	360/0.5	−9 to 9 by 3	28
IFF	F5–F13	360/0.5	−9 to 9 by 3	45
IFF x–pol.	F5–F13	360/0.5	−9 to 9 by 3	28
Sum + Aux 1	F1–F4	360/0.5	−9 to 9 by 9	24
Sum + Aux 2	F1–F4	360/0.5	−9 to 9 by 9	24
Alignmemnt	F1–F4	360/0.5	0	8
Sum	F1–F4	0	−40 to +40	4
Sum	F1–F4	0	−18 to +18	4
IFF	F5–F13	0	−40 to +40	9
IFF	F5–F13	0	−18 to +18	9

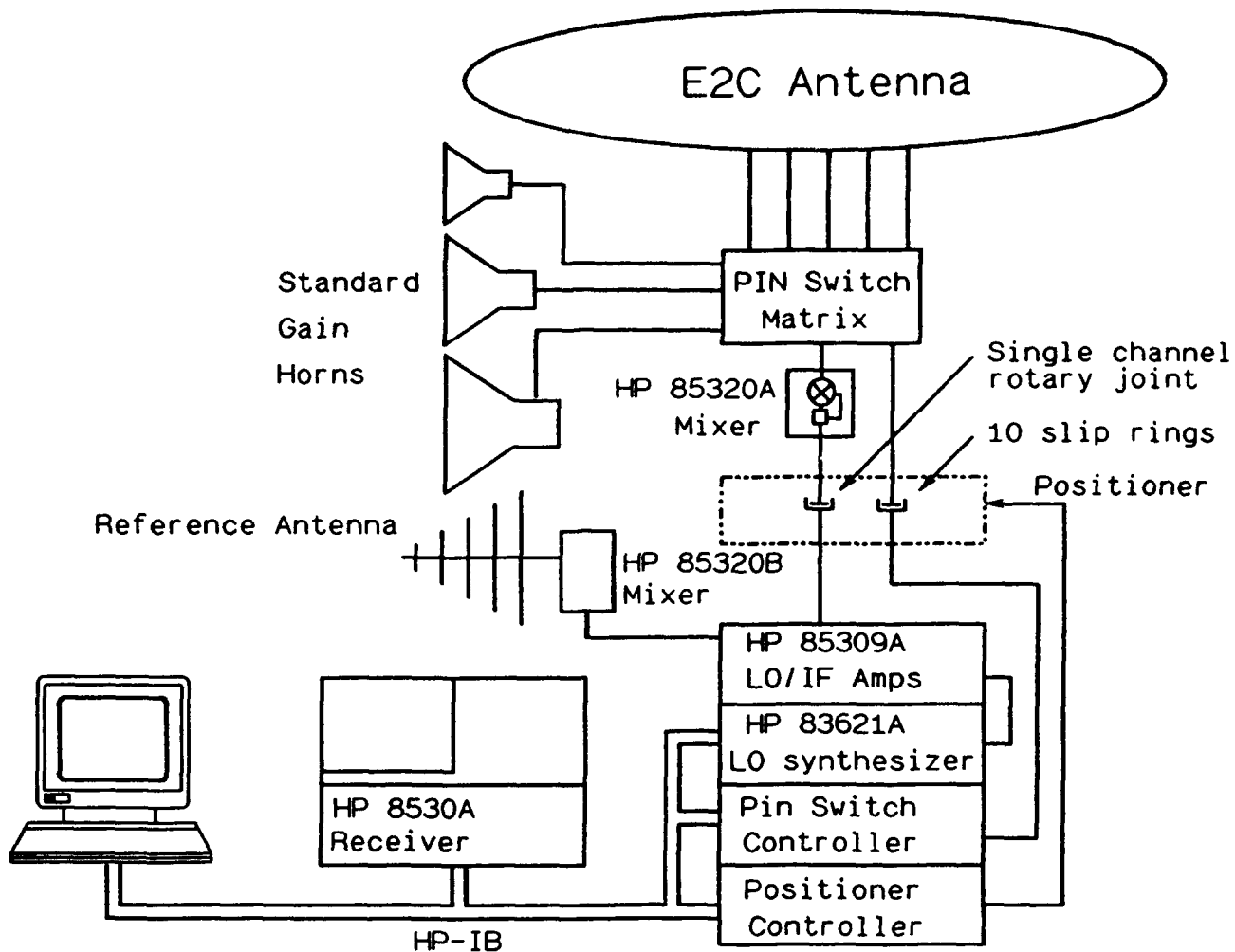Table 1: Required antenna patterns for E2C acceptance test

Figure 1: Proposed instrumentation configuration for measuring E2C antennas

COST OF SAVINGS SUMMARY

	Year 1	Year 2	Year 3	Year 4	Year 5	Year 6	Year 7
Direct Labor Productivity (4% per year inflation)	93942	97700	101608	105672	109899	114295	118867
Cost savings due to maintenance and repair	0	0	0	0	0	0	0
Annual Cost Savings	93942	97700	101608	105672	109899	114295	118867

Depreciation of new equipment

Cost of instrument	300410	
Plus Installation	10000	
TOTAL	310410	
Useful life	3 years	

Method:	Year 1	Year 2	Year 3	Year 4	Year 5	Year 6	Year 7	Total
Sum of Year's Digits	155205	103470	51735					310410
Straight Line	103470	103470	103470					310410
Difference	51735	0	-51735	0	0	0	0	0

Cash Flow Analysis - SYD Depreciation	Initial expense	Year 1	Year 2	Year 3	Year 4	Year 5	Year 6	Year 7	
1. New Measurement System	-300410								
Installation	-10000								
2. Software (non-depreciable)	-40000								
3. Annual Cash Savings		93942	97700	101608	105672	109899	114295	118867	741982
4. Depreciation		155205	103470	51735	0	0	0	0	310410
5. Profit Improvement (3-4)		-61263	-5770	49873	105672	109899	114295	118867	431572
6. Tax (34%)	-13600	-20829	-1962	16957	35928	37366	38860	40415	146734
7. Net Profit Improvement (5-6)		-40434	-3808	32916	69744	72533	75435	78452	284837
8. Cash Flow (3-6)	-338810	114771	99662	84651	69744	72533	75435	78452	595247

Payback period	3.7 years	
Return on Investment	0.24	
Net Present Value @ 10% Interest	89004	
Internal Rate of Return	18.44%	

Table 3: Financial calculations to determine economic feasibility

ADAPTIVE ANTENNA SPACE-TIME PROCESSING TECHNIQUES TO SUPPRESS PLATFORM SCATTERED CLUTTER FOR AIRBORNE RADAR

Edward C. Barile, Thomas P. Guella, David Lamensdorf
The MITRE Corporation
Bedford, MA 01730

Abstract

In order to detect small targets at long ranges, a new airborne, phased array radar will require the use of adaptive filter designs to suppress interfering signals. The platform of the radar will scatter incident signals into the antenna, spreading the angular spectra of those signals to overlap the target signal and increase the false alarm rate. Adaptive space-time processing (STP) provides an optimal, multi-dimensional, matched filter that maximizes the radar's sensitivity in a dynamic interference environment by resolving spectra of the received data simultaneously in spatial angle and Doppler frequency. To reduce the processing requirements of a full STP filter, a suboptimal architecture with fewer degrees of freedom is demonstrated and compared with the optimal architecture.

1.0 Introduction

Surveillance radars require a large power-aperture product to increase their sensitivity for detecting small target signals. This also increases the level of received interference signals from clutter and jammers. These interference signals, which are incident upon the radar antenna from multiple directions, include direct path and multipath via reflections from the radar's platform into the antenna. Receiving antennas with ultra-low sidelobe patterns and adaptive sidelobe cancellers have been proposed for large phased-array radars to suppress the direct path interference signals. However, these techniques have limited benefit for achieving the required interference suppression in the presence of multipath scattering.

For an airborne radar, the aircraft platform is an electromagnetic scatterer in the near-field of the radar antenna that can redirect interference signals into the mainbeam of the antenna from directions that are outside of its mainbeam. Without near-field scattering, a moving target with radial velocity V_T can be distinguished from a clutter signal with the same apparent V_T (or equivalent Doppler frequency) by spatial filtering. Scattering by an obstacle in the near-field creates a spread in the angular spectrum of clutter signals with the same Doppler frequency (figure 1). One component of this angular spectrum can coincide with the target direction, thereby reducing the sensitivity of the radar in that direction and increasing its false alarm rate.

A multidimensional adaptive filter is needed to suppress these signals in order to provide increased sensitivity while operating in the dynamic interference environment of an airborne radar [1,2]. Adaptive space-time processing (STP) provides an optimal matched filter at the output of a phased-array radar to maximize its sensitivity The weights for the adaptive beamforming filter are calculated from data obtained from the received interference signals at all outputs of the array. These signals are monitored as a function of time. By processing the received data from all elements of the array simultaneously in the temporal and spatial dimensions, optimal weights of the adaptive filter are obtained that minimize the sensitivity of the radar for the spatial directions and the Doppler frequencies of the interfering signals, thereby increasing the visibility of a target signal or the signal-to-interference-plus-noise ratio. The adaptive weights are updated periodically to cope with the dynamic interference scenario of a moving airborne radar.

2.0   Application of STP

A demonstration of the impact of near-field scattering is shown in figure 2, where angle-Doppler frequency plots are computed for a linear array with and without near-field scattering. The amplitude of the plot is the power spectral density of the clutter signals received by the array. Two significant features caused by the near-field scattering that reduce the radar's sensitivity are the overall increase in the

clutter signals away from the line representing stationary clutter and a ridge of signals at zero Doppler frequency caused by mainbeam clutter signals (centered around zero Doppler frequency) being spread in angle due to near field scattering.

The application of STP suppresses the excess clutter signals caused by near-field scattering by placing a spatial minimum in the neighborhood of the scatterer for the near field of the receiving antenna pattern. This minimum is illustrated in figure 3 by a plot of the output of the STP for a source in the near field as a function of its cross range position. The near-field scatterer is modeled here as a point and the reflection from the ground clutter is characterized across the clutter cells with a random phase and a constant amplitude that is large enough to create a scenario of clutter-limited receive signals.

The performance improvement provided by STP with a point scatterer in the near-field is demonstrated in figure 4, with the interference including the clutter signals and the effects of the scatterer. The performance improvement is defined here as the ratio of the achievable signal-to-interference-plus-noise ratio to the optimum signal-to-noise ratio (SNR) for the same radar scenario obtained without any interference signals. For one point scatterer, the improvement obtained by using more than two-pulse processing is negligible for large arrays (>14 elements). A model of a larger scatterer is represented by a line of 40 closely spaced point scatterers. The performance improvement, as demonstrated in figure 5, shows that multiple-pulse processing now provides significant benefits for larger scatterers. For these calculations, the number of spatial DOF is equal to the number of elements (width) of the array. The performance approaches an asymptotic value for large arrays beyond which no improvement is obtained. For a large array with a constant power-aperture product, the smaller angular width of the resolution cell containing the target signal reduces the received interference signals in that cell (direct clutter and near-field scattered clutter) while maintaining the same target signal level. Therefore, there is a trade-off between the size of the array and the number of DOF needed to suppress the effects of near-field scattering. For a finite aperture width, but reduced number of spatial DOF, the capability of STP for

490

reducing the effect of near field scattering will depend upon the beamforming architecture that defines the spatial DOF (e.g., beamspace, subarray, sidelobe canceler).

3.0 Predictive Near-Field Nulling

Fully adaptive STP provides the optimal performance for suppressing interference signals plus the effects of near-field scattering. However, as indicated earlier, this generally entails using a large number of DOF with its associated processing throughput. Several techniques have been identified for reducing the number of DOF and, consequently, the processing throughput requirements. These are alternative formulations of algorithms for fully adaptive arrays and suboptimal algorithms. One of the alternatives that appears to be most effective is placing predictive near-field nulls at the known scatterer locations for each column of the array. The elevation patterns of each of the columns will then differ, depending upon their orientation with respect to the scatterer. Horizontal-only spatial DOF plus the temporal DOF can then be applied to suppress the jammer and direct clutter signals plus any residual near field scattering that is not adequately suppressed by the predictive nulling. Figure 6 shows an example of the predicted near-field null created in the elevation plane and its impact on the far-field pattern. There is less degradation in the gain of the elevation pattern when the scatterer is moved away from the line perpendicular to the center of the aperture.

Column-based predictive near-field nulling can be combined with adaptive STP that uses horizontal-only spatial DOF to obtain an optimized performance. The weights for each element in the column can be chosen to minimize an error function, ε, that is the sum of two terms [3]. The first term represents the deviation from the quiescent weights that maximize the elevation gain in the steering direction. The second term minimizes the power received from the near-field scatterer.

$$\varepsilon = \left(\underline{v}(x) - \underline{v}_o\right)^T \left(\underline{v}(x) - \underline{v}_o\right)^* + \alpha \underline{v}^T(x) \underset{S}{\int\int\int} \underline{f}(x,\bar{r}) \underline{f}^H(x,\bar{r}) d\bar{r} \underline{v}^*(x) \qquad (1)$$

$\underline{v}_o$ = quiescent weights (e.g., uniform, Taylor, steered, etc.)

$\underline{v}(x)$ = predictive weights for column at x chosen to produce near-field null and maintain far-field pattern

$\underline{f}$ = vector of near-field scattering response voltages from $\bar{r}$ in the near-field scattering region S

α = relative weight of near-field nulling versus desired far-field pattern

T, H = transpose, Hermitian operations on a vector

The second term in the equation is an integral over the volume of the signals received from the near-field scatterers. Small α de-emphasizes near-field nulling and provides a good far-field pattern. Large α emphasizes near-field nulling at the expense of degradation in the far-field pattern.

An example of the benefit of predictive nulling is shown in figure 7. The low pulse repetition frequency (PRF) example has Doppler frequency foldover or aliasing of the received clutter signal which causes degradation for a small number of columns. For a large number of columns, the number of DOF available with uniform excitation is adequate to suppress the effects of near-field scattering while optimizing the overall performance. The medium PRF has range and Doppler foldover, so the degradation is more pervasive. The performance provided by column-based predictive nulling with horizontal-only spatial DOF has also been demonstrated to approach that achievable with fully adaptive vertical plus horizontal spatial DOF for the same array.

While the location of the near-field scatterers is known relative to the array, small constrained variations of this location can occur with time. The wing and the attached engines of the airplane flex or even vibrate, which is essentially a vertical movement. Predictive nulling can control the width or spatial extent of the near-field null as well as its relative weight, α. These parameters can be optimized to

include the anticipated movement of the scatterer as demonstrated in figure 8. A predicted elevation null width of 1.74λ is applied to an 8-column array with 11 elements per column and the point scatterer is moved vertically through the predicted null. The performance improves significantly when the scatterer is not within the collimated, near-field beam. When the number of columns increases, the number of available DOF becomes adequate to maintain the performance level as the scatterer is moved outside the predicted nulling region. Using more columns also increases the performance level toward its optimum value. However, these extra DOF are also usually required to suppress the direct received interference signals.

4.0   Conclusion

For an airborne phased-array radar, optimal STP and a modification using column-based predictive nulling are demonstrated to suppress the interference effects of ground clutter plus the dispersion created by near-field scattering from the radar's platform. While predictive nulling is suboptimal, it requires fewer adaptive degrees of freedom and its performance approaches the optimal as the size of the array increases.

Acknowledgments

References

1. Brennan, L. E., J. D. Mallett, and I. S. Reed (September 1976) "Adaptive Arrays in Airborne MTI Radar", IEEE Transactions on Antennas and Propagation, Vol. AP-24, No. 5, pp. 607-615

2. Barile, E. C., R. L. Fante, T. P. Guella, J. A. Torres (20-22 April 1993),
   "Performance of Space-Time Adaptive Radar", IEEE 1993 National
   Radar Conference, Lynnfield, MA

3. Shore, R. A. (1986) "Sidelobe Sector Nulling with Minimization of Weight
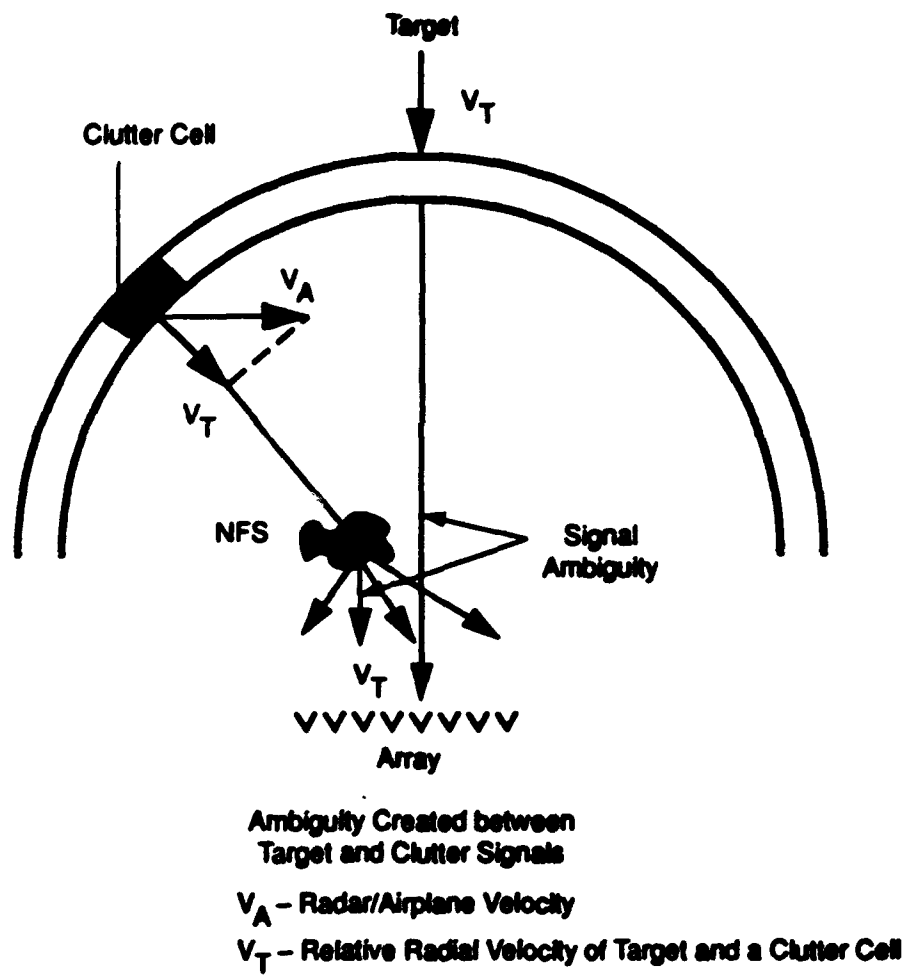   Perturbations", IEEE AP-S International Symposium, Vol. 2, p.591
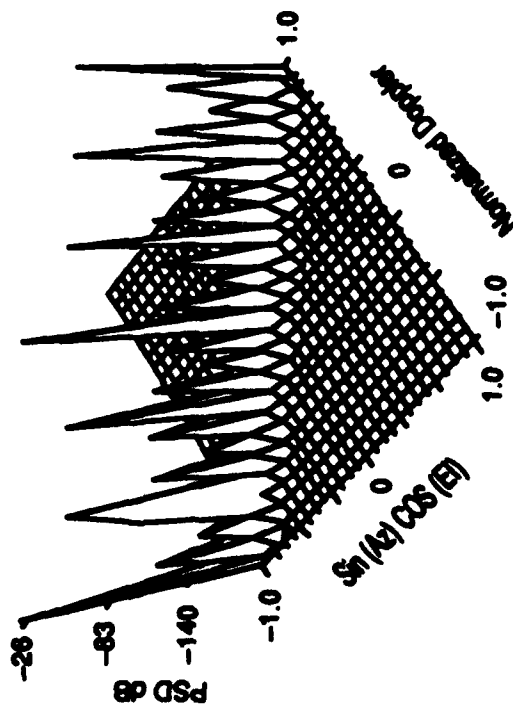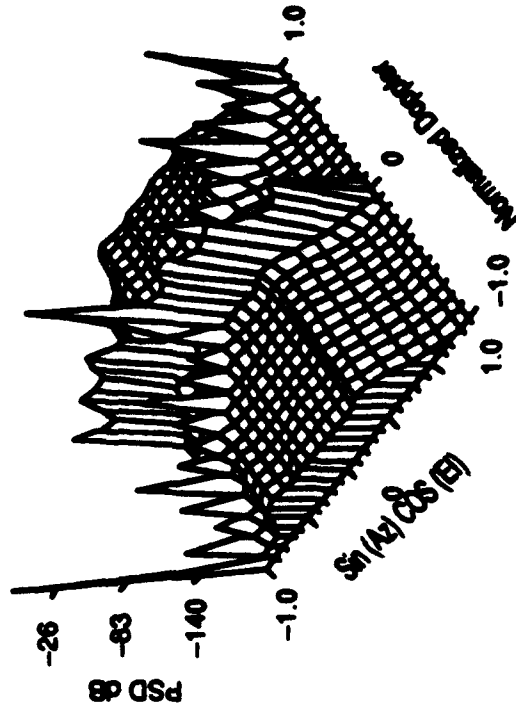
Figure 1. Effect of Near Field Scattering on Airborne Radar

31 Element Array
Near Field Scatterer - .01 sm, 10λ Broadside
Clutter – Constant Γ, Random Phase

PSD dB

−28
−83
−140

Sin (Az) Cos (El)

Normalized Doppler

1.0
0
−1.0

1.0
0
−1.0

Free Space

PSD dB

−28
−83
−140

Sin (Az) Cos (El)

Normalized Doppler

1.0
0
−1.0

1.0
0
−1.0

With Scatterer in Near Field

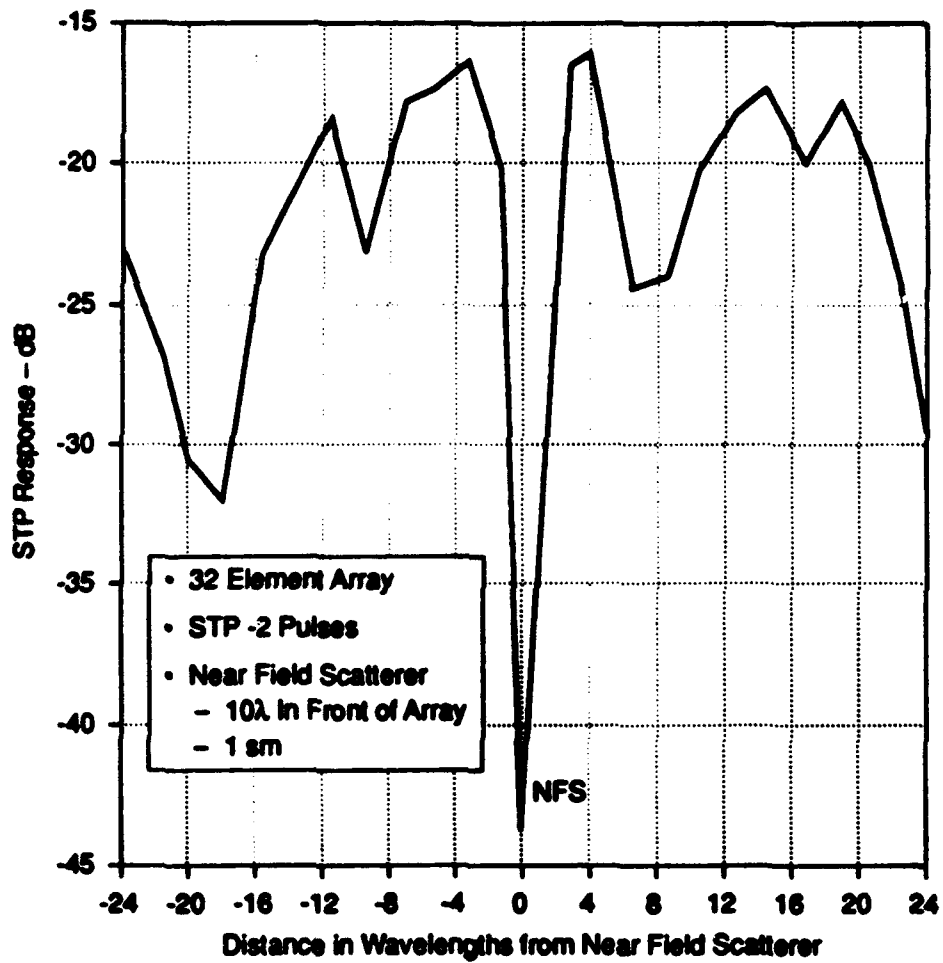Figure 2.   Effect of Near Field Scattering on Clutter Signals Received by Moving Radar

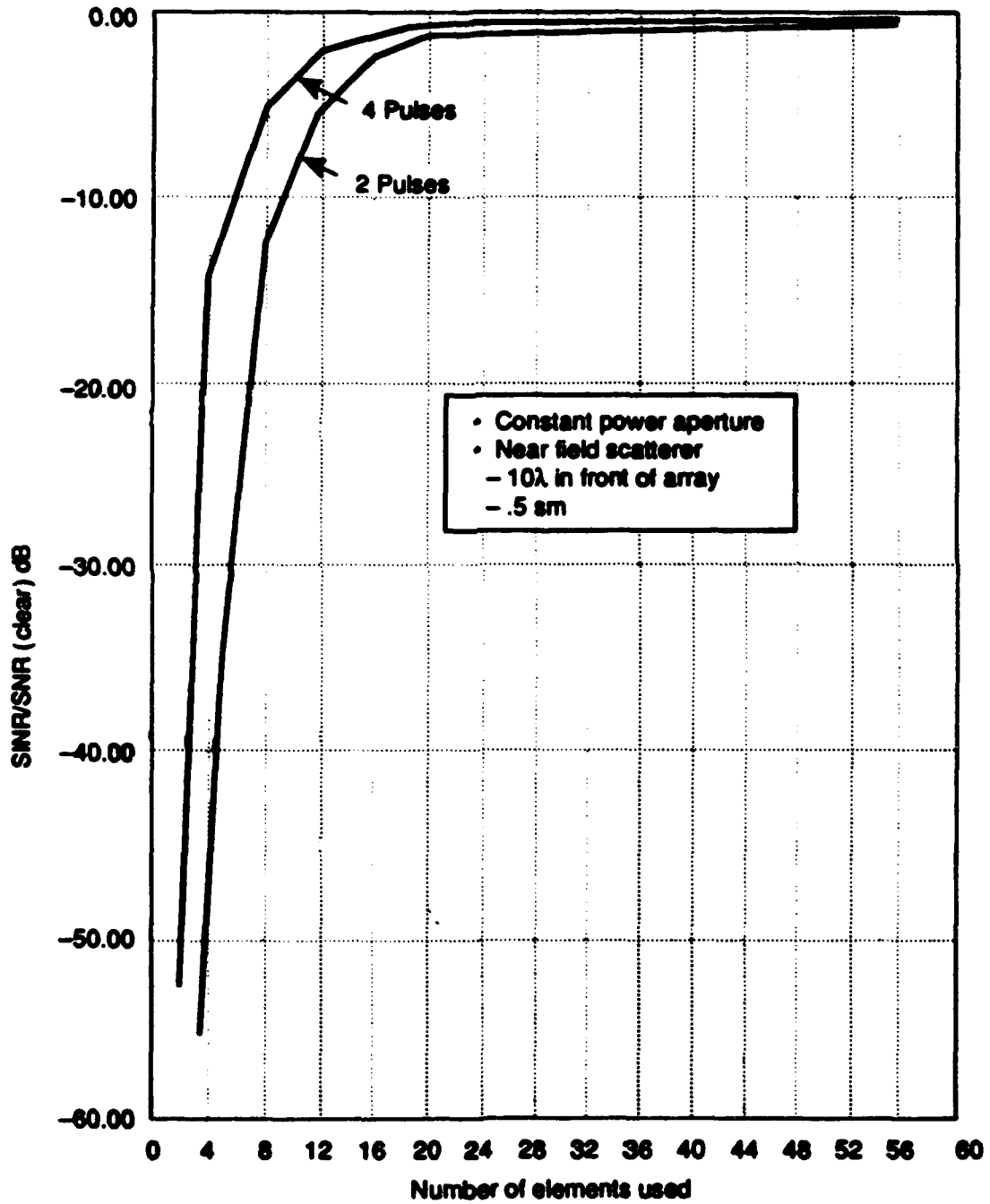**Figure 3. Cross-Range Near-Field Resolution of Point Scatterer**

Figure 4. STP Performance Trade-off for a Point Near Field Scatterer
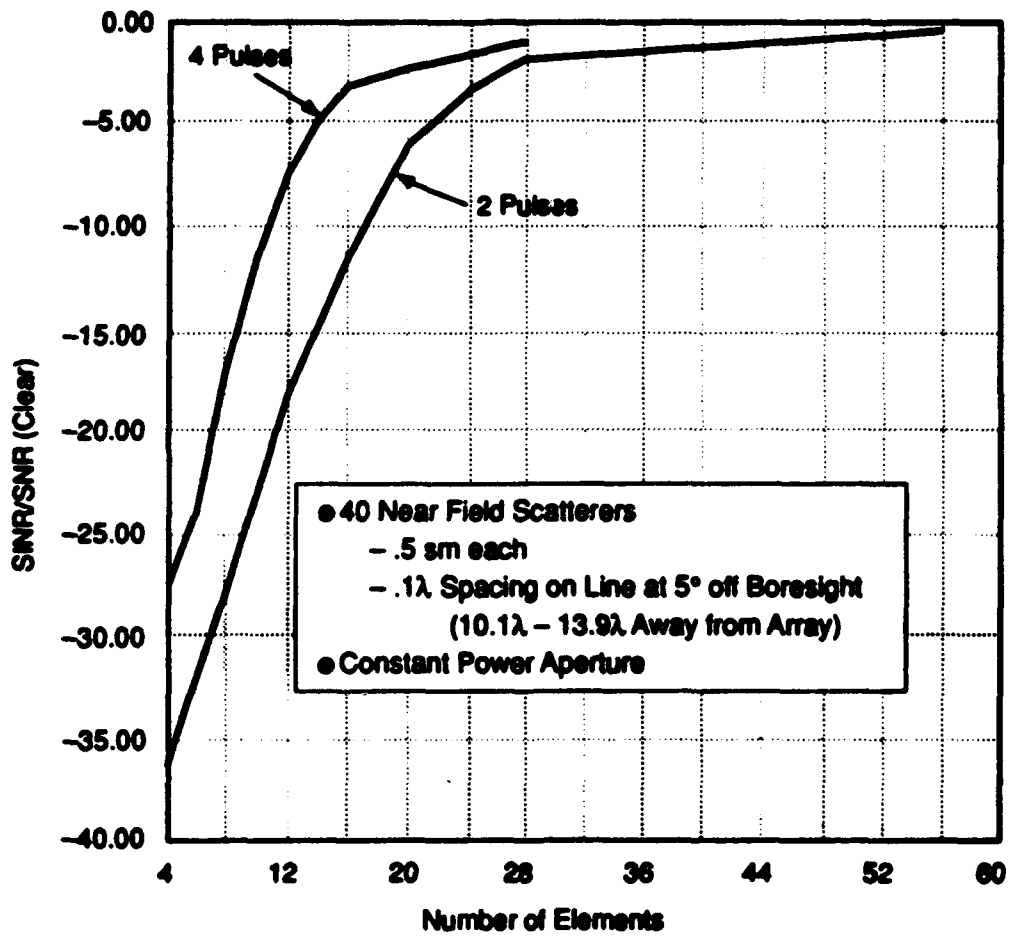
Figure 5. STP Performance Tradeoff for Multiple Point Scatterers

499

- 8 Columns
- 11 Elements/Column
- Scatterer – 10λ in Front of Array, Centered

Elevation Angle - deg

Far Field Pattern

Uniform Excitation

Predictive Null Excitation

Power - dB

Vertical Cross Range Distance in Wavelengths
from Near Field Scatterer

Power - dB

Figure 6. Vertical Array Patterns with Predictive Nulling in Column Subarray for Centered Point
Near Field Scatterer

Figure 7. Effect of Predictive Nulling in Column
Subarray for Point Near-Field Scatterer

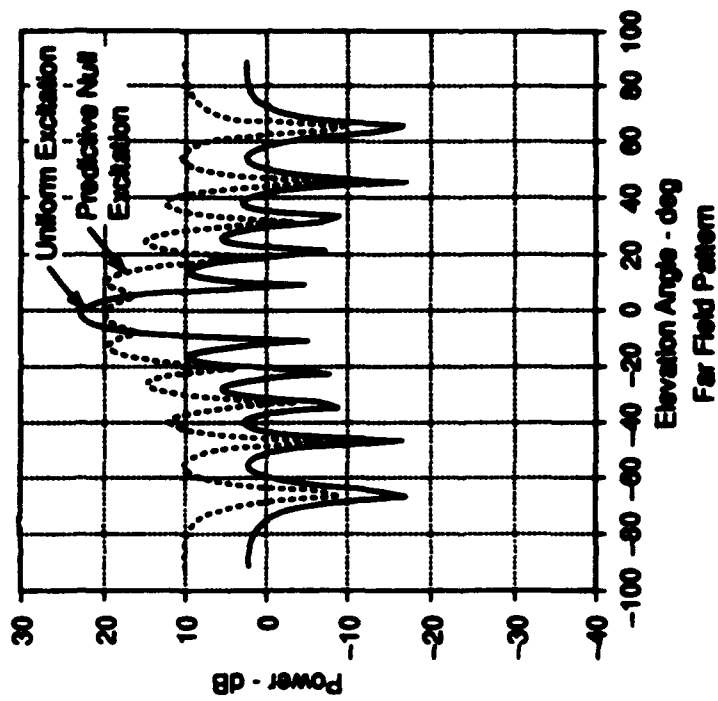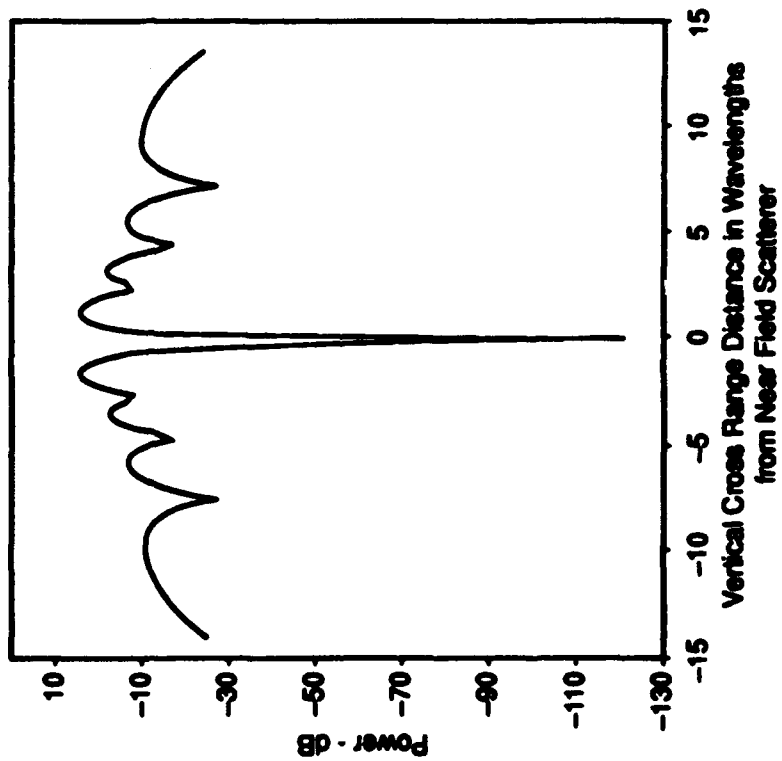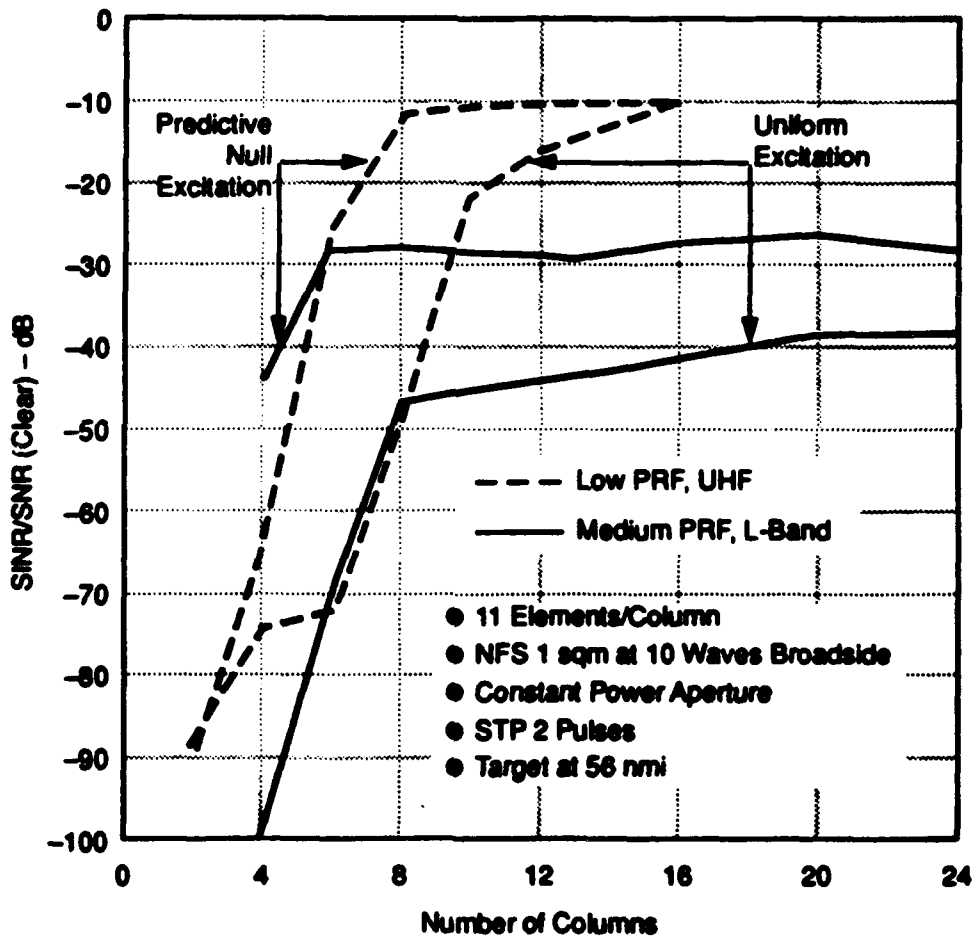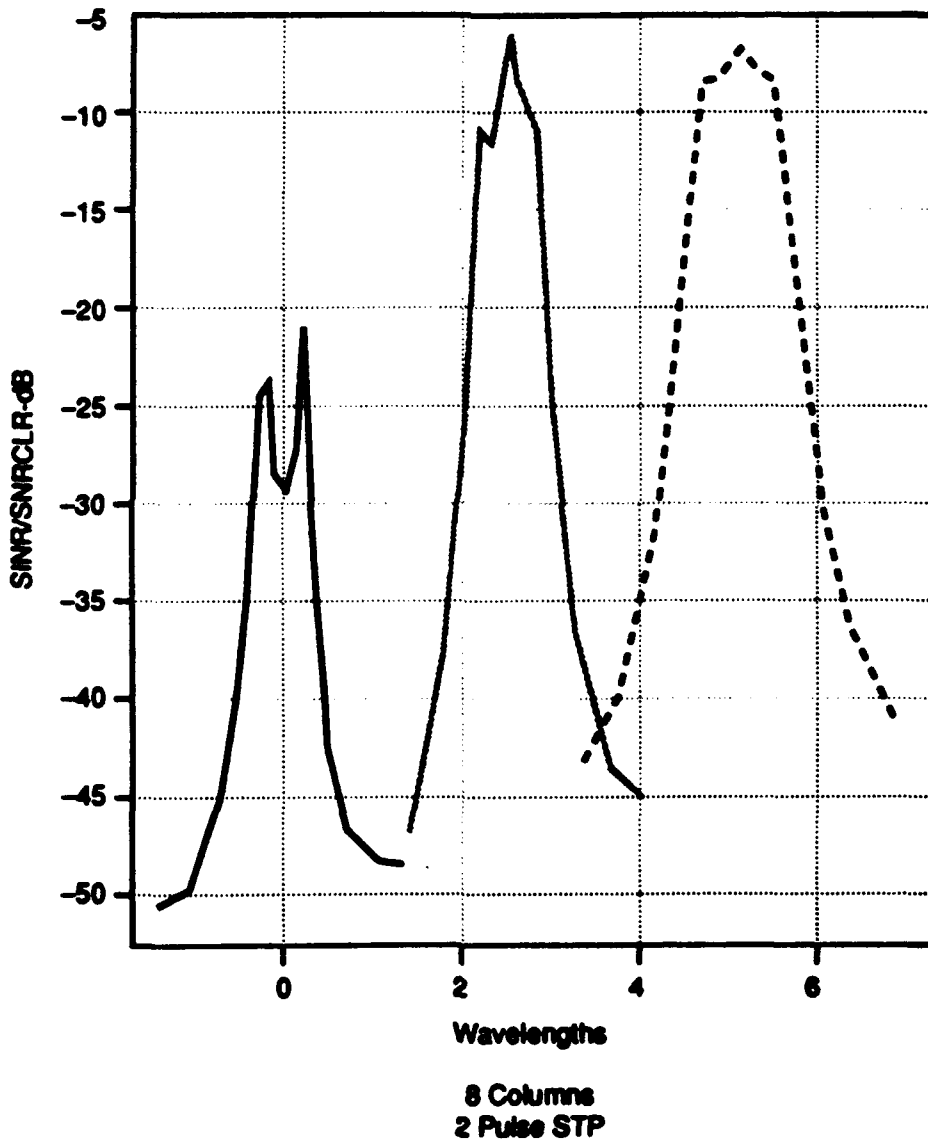Figure 8. Performance with 1.74λ Wide Predictive Null Placed at Each of
Three Locations: 0λ, 2.5λ, and 5λ Vertical Position Relative to Center of Array

CONSTRAINED OPTIMIZATION METHOD

FOR SHAPED BEAM ANTENNA

PATTERN SYNTHESIS

Yihong Qi, Chen Wu, John Litva,

Communications Research Laboratory

McMaster University

Hamilton, Ontario, Canada

Abstract

Advances in techniques for synthesizing and optimizing array patterns are of perennial interest. In this paper we present a constained optimization method for designing shaped beam antenna patterns. The main feature of our method is the inclusion of mutual coupling between the elements during the optimization. This feature alone makes the method of considerable practical interest. Another feature is that the method can be applied to arrays with non-uniform element spacing, thereby allowing elements spacing to be one of the design parameters. This provides more freedom for optimization and better performance can be expected. Since the constrained optimization technique is very flexible, it is expected to be an efficient tool for CAD. Computational results are given to show the effectiveness of the

method. In our examples the main beam are designed to approach $csc^2\theta \times cos\theta$ while the sidelobe level satisfies stringent spcifications. The resulting pattern is shown to approach the desired pattern and that by changing the weights, we can reduce the discrepancy between the desired and achieved pattern.

1 INTRODUCTION

Antenna pattern synthesis has received a great deal of interests over a number of decades. Techniques such as Dolph [1] and Taylor [2] synthesis are considered as classical methods. Schelkunoff [3] developed a general concept of the array polynomial and the relationship between the pattern and polynomial zeros. More recently Elliott[4] and Orchard et al. [5] drived a pattern synthesis procedure based on the Schlkunoff's polynomial representation of the pattern. Pattern synthesis can be realized by finding the position of roots in the complex plane which correspond to a desired pattern. This pattern synthesis technique provides a means of obtaining arbitrary sidelobe topography in the sidelobe region and a balanced ripple in the shaped beam region. The results given in past papers are applicable only to arrays having uniform spacing and isotropic elements.

For more complex pattern synthesis problems, numerical methods and optimization method are more effective then classical technique. Olen and Compton,Jr. [6] gave a pattern synthesis algorithm based on adaptive array theory. Many authors have used optimization methods for pattern synthesis [7],[8],[9]. Sanzgiri and Butler [10] adopted the constrained optimization method to optimize a given

performance index, such as directivity, with a given number of constraints on the sidelobe level. Schjaer-Jacobsen and Madsen [11] used a nonlinear optimization method to synthesize the low sidelobe pattern for nonuniformly spaced linear arrays. Jiao et al. [12] applied a new constrained nonlinear optimization algorithm for synthesizing comformal scanning arrays. As of yet , numerical and optimization technique have not included the effect of mutual coupling on the synthesis process.

In this paper, we concentrate on shaped pattern synthesis techniques and use a newly developed flexible constrained optimization method to solve the synthesis problem. The main feature of this pattern synthesis technique is that the mutual coupling is considered. To the best of the authors' knowledge, none of the existing method for shaped beam pattern synthesis consider the effect of mutual coupling. This is despite the fact that mutual coupling can distort the sidelobe region of the antenna pattern [5]. Two methods are described by Kang and Pozar [13] for correcting pattern synthesis errors due to mutual coupling. One is based on using characteristic modes, other is a point matching technique. Siakavara and Sahalos [14] give a simplified method for considering the influence of mutual coupling on parallel wire antennas, but the mathematical expressions that are provided can only be applied to a one-dimension array. Most of the discussion here will be based on arrays consisting of parallel dipoles or slots. The latter will be treated as magnetic dipoles. We follow Siakavara et al.[14], where the synthesis procedure for practical dipole arrays is divided into two parts. Optimization is performed

by first considering the array to be composed of isotropic elements and then we includeing the effect of mutual coupling by applying a transformation. This means that the time consuming mutual coupling computation need only be carried out once and is completely isolated from the optimization procedure. It will be shown that the method described here can also be used for shaped beam synthesis for planar arrays.

As well this method can also be applied to arrays with non-uniform element spacing, thereby allowing elements spacing to be one of the design parameters. This provides more freedom for optimization and better performance can be expected. Since the constrained optimization technique is very flexible, it is expected to be an efficient tool for CAD. A Sixteen-element wire dipole array is taken as an example to demostrate the synthesis of a $csc^2\theta \times \cos\theta$ pattern.

2 FORMULATION

Consider the parallel dipole array shown in Fig. 1, where the total number of the elements is N. For purposes of analysis, each element is divided into M segments, where M is an odd number. There are N1 rows in the array. By the moment method, the relationship between the currents and the voltages of the segments can be found as following

$$[I] = [Y][V]. \tag{1}$$

If the far-zone field of the nth segment is expressed as

$$\bar{E}_n(\theta, \phi) = \bar{f}(\theta, \phi)e^{jkr_n(\sin\theta\cos\theta_n\cos(\phi-\phi_n)+\cos\theta\cos\theta_n)}, \qquad (2)$$

where $\bar{f}(\theta, \phi)$ is the electric field of a segment with its center at the origion. The variables (r_n, ϕ_n, θ_n) are the spherical coordinates of the nth segment and k is the wave number.

Without any no loss of generality, we assume that the voltage generator is located at the center of a dipole and we suppose M to be an odd number when carrying out the analysis. Then the radiation field of the array can be expressed as

$$\bar{E}(\theta, \phi) = \sum_{i=1}^{N} V_{i'} \sum_{n=1}^{K} Y_{ni'} E_n(\theta, \phi) \qquad (3)$$

where $K = N \times M, Y_{ni}$ is the ni^{th} element of the matrix $[Y]$. and

$$i' = (M+1)/2 + (i-1)M$$

For the planar array, equation (3) yields

$$\bar{E}(\theta, \phi) = \bar{f}(\theta, \phi)\sum_{i=1}^{N} V_{i'} \left[\sum_{n=1}^{N1} e^{jkz_n\cos\theta} \left(\sum_{l=1}^{M1} Y_{l+(n-1)M1,i'} e^{jk\sin\theta\sin\phi y_{l+(n-1)M1}} \right) \right] \qquad (4)$$

where $M1 = K / N1$. Since eq. (4) can be used to obtain the actual field, the time comsuming computation of matix $[Y]$ need only be carried out once for a fixed array. The optimization based on eq. (4) is straightforward.

In practical applications, the pattern shape is generally defined for one particular plane. In the plane $\phi = 0$, which is of interest in many applications, equation (4)

becomes

$$\bar{E}(\theta, \phi) = \bar{f}(\theta, \phi) \sum_{i=1}^{N} V_{i'} \left[\sum_{n=1}^{N1} e^{jkz_n \cos\theta} \left(\sum_{l=1}^{M1} Y_{l+(n-1)M1,i'} \right) \right]. \tag{5}$$

We put

$$\sum_{l=1}^{M1} Y_{l+(n-1)M1,i'} = B_{n,i'} \tag{6}$$

and let

$$[A] = [B][V], \tag{7}$$

where

$$\sum_{i=1}^{N} V_{i'} B_{n,i'} = A_n. \tag{8}$$

Then we have

$$\bar{E}(\theta) = \bar{f}(\theta) \sum_{n=1}^{N1} A_n e^{jkz_n \cos\theta} \tag{9}$$

Equation (9) is the same as the array factor for a linear array. The pattern in the $\phi = 0$ plane is determined only by $[A]$. Therefore, a designated pattern can be derived by the optimization of $[A]$. Note that for a planar array N is larger then N1, thus eq. (7) is an under determined. To solve this probem, the excitation in one row must be specified. This distribution can correspond to either a classical distribution or to some optimized distribution. It is related to the field pattern in $\phi = 90^0$ plane. Suppose the distributions are $a_1, a2, \ldots, a_{M2}$, and $M2 = M1/M$. Then we get

$$[A] = [B'][V'] \tag{10}$$

where

$$B'_{l,q} = \sum_{m=1}^{M2} B_{l,(q-1)M2+m} \, a_m \tag{11}$$

where $[B']$ is a $N1 \times N1$ matrix and $[V']$ is a $N1 \times 1$ matrix.

This means that the we first carry out the optimization on an ordinary linear array to get $[A]$ and then the $[V']$ can be resulted by solving eq. (10). The actual excitation $[V]$ is obtained by the following relation

$$V_{mn} = V'_m a_n \tag{12}$$

where V_{mn} denotes the votage excitation at the element of mth row and nth column.

The $A_j(j = 1, 2, \ldots, N1)$ in eq. (9) are determined by means of a constrained optimization. A measure of how well a synthesized pattern agrees with a desired pattern in the shaped beam region is given by following equation

$$F = \int_\Omega W(\theta)\{\log[E(\theta)E(\theta)^*] - D(\theta)\}^2 d\theta, \tag{13}$$

where Ω denots the shaped beam region, $D(\theta)$ is the desired pattern, *represents complex conjugate, and $W(\theta)$ is the weight.

The sidelobe level in the sidelobe region is given by

$$SLL_i = max\{\log 10[E(\theta)E(\theta)^*] \mid \Omega_i \} \quad i = 1, 2, \ldots, L \tag{14}$$

where Ω_i denotes the sidelobe region.

The optimization problem for the shaped beam array can be expressed as

$$
\left\{
\begin{array}{l}
min\ F \\[1.5ex]
s.t\ SLL_i\ <\ SP_i \\[1.5ex]
0 \leq |A_j| \leq p \quad j = 1, 2, \ldots, N1 \\[1.5ex]
-180^0 \leq \phi_j \leq 180^0 \quad j = 1, 2, \ldots, N1
\end{array}
\right.
\tag{15}
$$

where p is a constraint for excitation amplitudes. ϕ_j is the phase of A_j. SP_i is the design sidelobe level in dB, which is expressed as a negative value.

3   EXAMPLES OF SYNTHESIZED PATTERN

Shaped beam pattern optimization is a nonlinear programming problem with some complex constraints and many simple constraints. In this paper a new direct method is used to solve the problem. The method employes the partial relaxation mutiplier method combined with the regular polyhedron method to improve the convergence. We only relax the sideloble level constraints which are the complex constraints in the problem. The remaining constraints, which are simple, are retained during the minimization process. Thus the problem is solved effectively.

A wire dipole array is taken as an example to illustrate the application of the method. To begin, we consider a sixteen element linear array. For application to a $csc^2\theta \times cos\theta$ pattern, the excitations are optimized to approximate $csc^2(\theta - \pi/2) \times cos(\theta - \pi/2)$ in the shaped beam region $\{\Omega|\theta_2 \leq \theta \leq \theta_3\}$ with $\theta_2 = 100^0$ and $\theta_3 = 140^0$. The sidelobe regions are $\{\Omega_1|0^0 \leq \theta \leq \theta_1 \ , \ \theta_3 \leq \theta \leq 180^0\}$

and $\{\Omega_2|\theta_1 \leq \theta \leq \theta_2\}$, in which $\theta_1 = 67.56^0$, $\theta_2 = 90^0$. The sidelobe levels are $SP_1 = -20dB$ and $SP_2 = -30dB$. The degree to which the synthesized and desired pattern agree is quantified by the size of the ripple in a quantity, which is formed by taking the difference between the two patterns.

The optimization method is now applied to this problem. First an equispaced array is considered in which the element spacing is $\lambda/2$. The influence of mutual coupling is shown in Fig.2, where we see a pattern which is not crrected for mutual coupling and one that is. In this example, $\lambda/2$ wire dipoles were assumed with a wire diameter of 0.0125λ. From Fig.2 it is be seen that mutual coupling results in pattern degradation in the shaped beam region.

We continue the synthesis procedure by putting different weights in the objective function, with the goal of improving the pattern in the shaped beam area. The two pattern shown in Fig.3 demostrate the effect of using different weights. In Fig.3(a), $W(\theta) = 1$ in the shaped beam region, while in Fig.3(b), $W(\theta) = 10$ when $135° \leq \theta \leq 140°$ and $W(\theta) = 1$ elsewhere in shaped beam region.

The optimized pattern for a nonequispaced array is shown Fig.4, in this example an additional constraint is put into the model and the descrepancy between the desired and achieved pattern is controlled to be less then 1dB with no loss in the width of the shaped beam region. This is possible because the optimum results are carried out in an enlarged parameter space.

4 CONCLUSION

The pattern optimization method given in this paper is more flexible then previous techniques. It can be used as a CAD tool for array design. Since mutual coupling is considered in the optimization procedure, the method provides results that can be applied to the design of practical antenna systems. Since the optimization can be carried out in a enlarger parameter space, better array performance can be expected.

References

[1] Dolph, C.L (1946) A current distribution for broadside arrays which optimizes the relationship between beamwidth and sidelobe level, *Proc. IRE*, vol.34, 335-348.

[2] Taylor, T.T. (1955) Design of line source antennas for narrow beamwidth and low sidelobes, *IRE Trans.Antennas Propagat.*, vol.AP-3, 16-28.

[3] Schelkunoff, S.A.(1943) A mathematical theory of linear array, *Bell System Techn.J.*,vol.22, 80-107.

[4] Elliott, R.S. (1982) Improved pattern synthesis for equispaced linear array, *Alta Freq.*, vol.51, 296-300.

[5] Orchard, H.J. , Elliott, R.S. and Stern, G.J. (1985) optimising the synthesis of shaped beam antenna pattern, *Inst. Elec. Eng. Proc., pt.H*,vol.132, no.1.

63-68.

[6] Olen, C.A. and Comptoon, Jr, R.T. (1990) A numerical pattern synthesis algorithm for arrays, *IEEE Trans. Antennas Propagat.*, vol.AP-38, 1666-1676.

[7] Shpak, D.J.and Antoniou,A. (1992) A flexible optimization method for the pattern synthesis of equispaced linear arrays with equiphase excitation, *IEEE Trans. Antennas Propagat.*, vol.AP-40, 1113-1120.

[8] Prasad, S. and Charaan, R. (1984) On the constrained synthesis of array patterns with applications to circular and arc arrays, *IEEE Trans. Antennas Propagat.*, vol.AP-32, 725-730.

[9] Lasdon, L.S. ,Plummer, J.,Buehler, B. and Waren, A.D. (1987) Optimal design of efficient acoustic antenna arrays, *Mathematical Programming* 39,131-155.

[10] Sanzgiri, S.M. and Butler, J.K. (1971) Constrained optimization of the performance indices of arbitrary array antennas, *IEEE Trans. Antennas Propagat.* , vol.AP-19, 493-498.

[11] Jacobsen, H.S. and Madsen, K. (1976) Synthesis of nonuniformly spaced arrays using a general nonlinear minimax optimization method, *IEEE Trans. Antennas Propagat.*, vol.AP-24, 501-506.

[12] Jiao, Y.C. (1990) A study of constrained optimization and its application to optimal design of antennas, *Ph.D dissertation*, Xidian university, Xi'an, China.

[13] Kang, Y.W. and Pozar, D.M. (1985) Correction of error in reduced sidelobe synthesis due to mutual coupling, *IEEE Trans. Antennas Propagat.*, vol.AP-33, 1025-1028.

[14] Siakavara, K. and Sahalos, J.N. (1989) A simplification of the synthesis of parallel wire antenna arrays, *IEEE Trans. Antennas Propagat.*, vol.AP-37, 936-940.
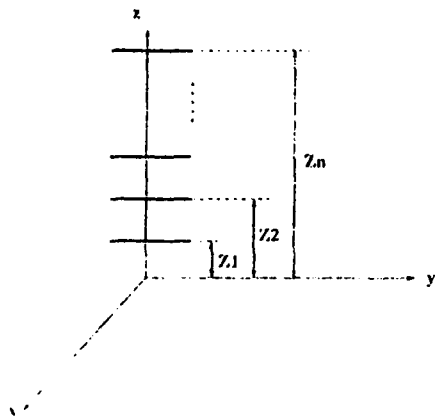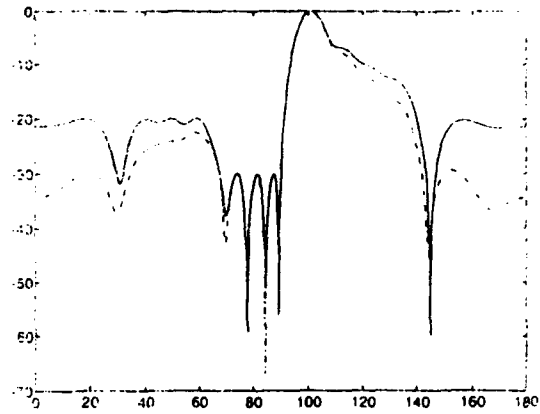
Fig. 1   Array with parallel wire antenna

Fig. 2

.... uncorrected pattern

———— corrected pattern

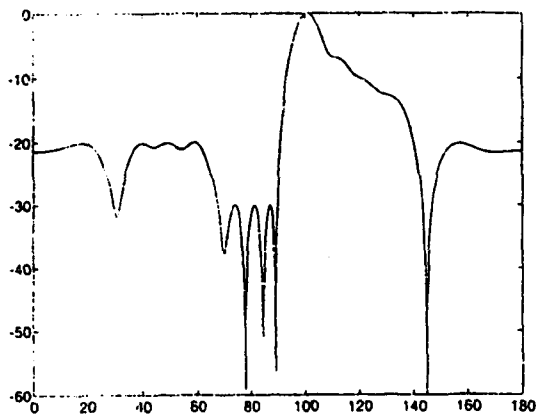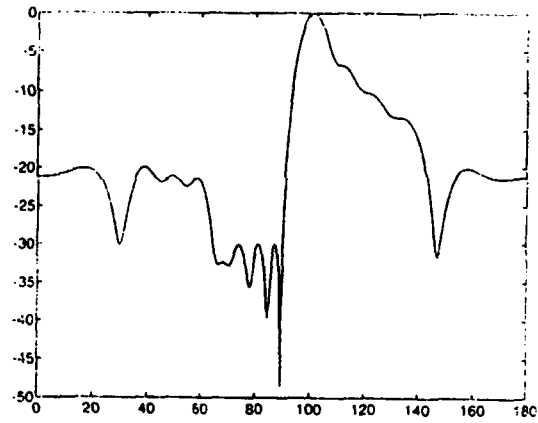Fig. 3(a)

Fig. 3(b)
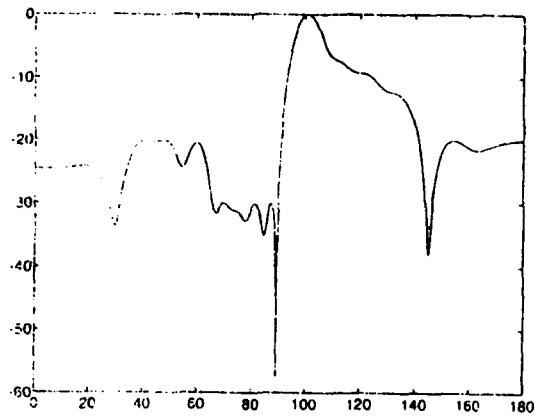

Fig. 4

515

ANTENNA TECHNOLOGY FOR WIDE ANGLE SCANNING

A. J. Zaman and R. J. Acosta
NASA Lewis Research Center, Cleveland, Ohio

Abstract:

Antenna systems for a possible space based, multibeam, wide angle application scenario have been investigated. Key issues and critical subsystem component barrier for each technology alternative have been identified and assessed. Present limitations of a chosen technology that can potentially meet the performance requirement has been discussed.

1. Introduction:

Future space communication and exploration experiments is expected to require antenna systems with wide angle scanning capability. An antenna with a wide field of view (FOV) can communicate simultaneously with several targets without physical movement and thus provide a continuous link between the targets. For example, NASA's Data Distribution Satellite (DDS) concept is conceived for directly distributing space gathered data to users on the ground. A multiple number of links between the DDS and other geosynchronous satellites may be required and adequate steering range must be provided in order to communicate with all potential crosslink users. Future Lunar and Mars exploration missions will also require communication links to be established between the relay satellite and potential low altitude orbiting vehicles. All these missions demand the need for an antenna system that has wide angle beam scanning capability without moving a large and heavy reflector, generally offer low sidelobe characteristics for effective orbit space and frequency spectrum utilization and has potential for multibeam application.

The key purpose of this paper is to look into the technology issues and alternatives involved in the wide angle scanning of space based antenna system. The choice is dependent not only on the performance requirement but also on the cost and complexity consideration. The critical subsystem technology focus and relative performance criterions are assessed for alternative systems. For the purpose of assessment a scan requirement beyond ± 15 BW is considered wide angle. As an example, the following performance requirement was considered for the purpose of system evaluation and trade-off.

Frequency:	32GHz
Beamwidth:	0.5°
Scan range:	±30.0° (±60 Beamwidth)
EIRP:	>45 dBW
Sidelobe/crosspol	<-25 dB

2. Antenna Aperture for Wide Angle Scanning:

The most commonly used aperture types capable of producing beam scanning are reflectors and phased arrays. Of these two, a phased array design is much more complicated than a reflector design. This is due to a large number of array elements and associated beamforming architecture and integration contained in the design. Reflector antennas on the other hand have the advantage of being less expensive and lighter in weight than phased arrays. Therefore, it is desirable to use a reflector antenna if at all possible. The question then comes, "which antenna system is a candidate choice for a given application and performance specification and what are the technology constraints?"

517

2.1 Scanning with Multiple Reflector Systems:

Reflector antennas are traditionally designed for limited scan[1]. Scan performance for a symmetric reflector design is better than for an offset design however, the feed cluster introduces blockage and also there is an inherent 3dB gain loss in the shifted feed design. In order to reduce the large F/D ratio of an offset design required to minimize scan loss, its folded version or the dual reflector system is used.

Dual offset reflectors are good candidates for scanning application because the folded geometry offers packaging and deployment advantages and the second reflector adds a degree of freedom to improve the optical performance. In a standard Cassegrain system very large scanning range can be achieved by either tilting the main reflector, subreflector or both compared to the conventional shifted feed design because of the mirror effect [2]. However, in a large antenna system the main reflector and the associated backing structure are heavy and thus steering requirement introduces an additional mechanical complexity. The steering problem becomes further aggravated when rapid beam movement and highly accurate beam positioning are necessary. So, for a space based system requiring fast and accurate beam positioning, mechanical steering becomes almost prohibitive.

The advantage of using electronic scanning in an unfocussed Gregorian dual reflector system also has its scan limitations since subreflector scan range is magnified by the optics magnification ratio and thus increases the subreflector size and offset height necessary to avoid subreflector blockage. Also the introduction of the feed array reduces the savings in system complexity and cost. Also all dual reflector system offers a limited scan performance (~ 12BW),

518

beyond which pattern degradation becomes excessive due to the introduction of phase error effects.

The unique properties of the spherical surface makes it attractive for the purpose of both multibeam and wide angle scanning, provided that spherical aberration can be corrected to an acceptable level. Spherical reflectors reduce their antenna gain due to phase error caused by spherical aberration. The phase error can be removed by means of a subreflector designed on the basis of path length equalization. Phase corrected offset type spherical reflectors still have the disadvantage of asymmetry in aperture distribution and consequent high cross pol. In Watanabe type of spherical reflectors, the spherical aberration and asymmetrical aperture distribution are compensated by two shaped subreflector and wide angle scanning capability has been reported [3]. This type of tri-reflector system offers high performance and wide angle scanning without main reflector movement. The biggest disadvantage of this system is due to the fact that to scan the beam the entire beam waveguide feed and two subreflector assembly has to be moved around the spherical center keeping their relative position unchanged.

Others have proposed similar tri-reflector system for wide angle scanning feasibility that involves either special phase corrective feed, motion of subreflector assembly or single reflector with novel shaped surface [6,7]. Though tri reflector system offer wide scanning capability, it is best suited for ground station application [4].

2.2 Scanning with Phased Arrays:

Phased array antennas offer rapid electronic beam scanning, real time pattern control, beam agility and reliability through graceful degradation. With individual amplitude and phase excitation control at the radiating element level it is possible to achieve very high performance

goals such as low sidelobe, low cross pol, adaptive control, beam shaping, wide angle scanning and multiple beam with a phased array. Recent advances in MMIC technology have made it possible to incorporate high power generation and low noise pre amplification within the phased array antenna system. Also with the maturity in patch radiating element design and trend towards a low cost T/R module, phased array provide potential advantages of being lightweight, low profile, high performance and realistic [8]. However, present day phased arrays suffer through major drawbacks such as complicated beamforming and feed network, excessive cost of T/R module, in high frequency application difficulty in routing control and bias signal into the array and heat dissipation associated with solid state power amplifiers.

3. Technology Assessment:

For the stated performance specification several reflector and phased array systems were designed [5]. Scan loss at 8° view for each of the reflector designs along with the results of few other reported configurations is compared in Table 1. From the scan loss comparison alone it becomes evident that 30° FOV is too wide a scan to realize with a dual reflector system. Feed array size and subreflector blockage are additional drawbacks. Though tri-reflector design offers very little scan loss, any mechanical steering of the complex feed system or heavy and oversized main reflector will impose extreme difficulty in a space based system and will affect stability of the spacecraft. These considerations mitigate against the use of multiple reflector system for wide angle beam scanning.

Phased array design summary for the two scan cases utilizing practical radiating elements is given in Table 2 and shows that it indeed satisfies the critical design requirements. The details of the design are included in reference [5]. Though phased array system offer wider scanning

520

range and beam versatility, there are practical limitations towards building a successful large phased array with present day technologies. Several critical technology element have been identified that include a) aperture, b) beamforming type, c) subsystem electronics design, d)thermal load/packaging and e) cost. For a high gain phased array of the specified performance type, the number of radiating elements is in the thousands (7000-10000). The element type, ways of constructing the array aperture, beamforming type to distribute RF signal to the array elements, T/R module electronics are a few of the choices available to the array system architect.

A comparison of the three beamforming types is given in Table 3. One of the practical limitation of the otherwise mature RF beamforming is in the generation of a large number of simultaneous beams using the same aperture area. Digital beamforming on the other hand can conceptually provide any number of simultaneous beams and holds the advantage of eliminating all microwave beamformers at the expense of added T/R module complexity. Limitation of digital beamforming is the processing time, available bandwidth and the of state-of-the-art computers to perform numerically intensive operations. Fiber optic feed on the other hand provides wide bandwidth, offer true time delay and increase in data capacity. The principal limitations of this feed type is in the RF to optical conversion loss. Table 4 shows the component technology development in T/R module associated with different beamforming type. Other significantly challenging issues in phased array development are the device integration, thermal management and monolithic fabrication. Thermal load impacts on the development of new packaging technology that can remove hundreds of watts from behind the array face and also places significant burden on HEMT technology for efficient device development.

4. Conclusion:

Phased array technology is capable of meeting the specified requirements for wide angle scanning in a space based system. Availability of efficient power sources, phase shifters and active amplifiers will offer major flexibility in handling cost and system complexity towards building a large phased array. Studies show that at EHF band active monolithic array architecture with one amplifier phase shifter per element can be considered realistic [8]. However, in order to realize this capability, phased arrays need higher average radiated power, wider bandwidth, efficient beamforming and good thermal/mechanical design. These requirements dictate the need for further development in component technology and significant cost reduction of T/R modules.

References:

[1] Lo, Y. T. and S. W. Lee, (1998) Antenna Handbook, VanNostrand Reinhold, New York.

[2] Zimmerman, M., S. W. Lee, B. Houshmand, Y. Rahmat-Samii and R. Acosta (1990) A Comparison of Reflector Antenna Designs for Wide Angle Scanning, Microwave and Optical Technology Letters, pp. 233-235.

[3] Watanabe, F. and Y. Mizuguchi, (1983) An Offset Spherical Tri-Reflect or Antenna, Transaction of the IECE of Japan, vol. E66, no.2.

[4] Nomoto, S., F. Watanabe, Y. Mizuguchi, A. Abe, T. Ino and S. Ohno (1992) A Ku-Band 4-Beam Earth Station Antenna With A 6.5-m Fixed Spherical Reflector, 14th AIAA Conference on Communication Satellite Systems, pp. 702-710.

[5] Chen, Y. L., M. A. Nasir and S. W. Lee (1992) Baseline Antenna Design for Space Exploration Initiative, Final Report, NASA Grant No. NCC3-216.

[6] Werntz, P. C., M. C. Baily, K. Takamizawa and W. L. Stutzman (1992) An Array Fed Tri-Reflector for Wide Angle Beam Scanning, IEEE AP-S, pp. 8-11.

[7] Rappaport, C. M. and W. P. Craig (1991) High Aperture Efficiency Symmetric Reflector Antennas with up to 60- Field of View, IEEE T-AP, vol. 39, no. 3.

[8] Mailloux, R. (1992) Antenna Array Architecture, Proc. IEEE, vol. 80, no. 1.

TABLE 2

Phased Array Application Summary

TABLE 4

Beamforming Technology Assessment

TABLE 1

Multireflector Scan Performance Comparison

TABLE 3

Beamforming Option Comparison

MISSION

OF

ROME LABORATORY

Rome Laboratory plans and executes an interdisciplinary program in research, development, test, and technology transition in support of Air Force Command, Control, Communications and Intelligence (C3I) activities for all Air Force platforms. It also executes selected acquisition programs in several areas of expertise. Technical and engineering support within areas of competence is provided to ESC Program Offices (POs) and other ESC elements to perform effective acquisition of C3I systems. In addition, Rome Laboratory's technology supports other AFMC Product Divisions, the Air Force user community, and other DOD and non-DOD agencies. Rome Laboratory maintains technical competence and research programs in areas including, but not limited to, communications, command and control, battle management, intelligence information processing, computational sciences and software producibility, wide area surveillance/sensors, signal processing, solid state sciences, photonics, electromagnetic technology, superconductivity, and electronic reliability/maintainability and testability.